PhD in Information and Communications Technologies

Curriculum Systems Engineering, Telecommunications, and Hardware/Software Platforms

XXXVIII Cycle

PhD Thesis In

Space-Division Multiplexed Optical Communications

SSD: ING-INF/03

Doctoral Program Coordinator
Prof. Davide Di Ruscio

PhD Candidate
Giammarco Di Sciullo

Supervisor
Prof. Cristian Antonelli

Co- Supervisor
Prof. Antonio Mecozzi

Academic Year 2024/2025

This thesis is dedicated to my family, for their constant support and encouragement.

Abstract

Modern information society is largely enabled by information and communications technologies, whose foundation lies in a worldwide optical fiber network extending over billions of kilometers of fiber that interconnects countries and continents. By harnessing the enormous potential bandwidth of optical fibers, along with the utilization of both polarizations of light, advanced modulation techniques, and coherent detection, data rates up to 100 Tb/s can be achieved over standard single-mode fibers (SMFs), very close to the theoretical capacity of such fibers. With SMFs approaching their transmission capacity limits, the ongoing exponential growth in the demand for larger data rates calls for the development of novel optical transmission technologies.

Multi-band wavelength-division multiplexing (WDM) and space-division multiplexing (SDM) have emerged as two of the most promising technologies to address the impending information capacity crunch driven by the ever-increasing demand for higher transmission capacities. Multi-band WDM leverages the entire available transmission bandwidth of optical fibers, extending well beyond the conventional low-loss spectral region of silica fibers, thereby offering a cost-effective solution to increase the capacity of existing fiber infrastructures. In principle, this approach enables a potential bandwidth increase by up to a factor of 12 compared to current fiber-optic systems, while still relying on the same optical infrastructure. However, the actual capacity increase is smaller then this twelve-fold increase in bandwidth due to system and physical limitations of optical fibers, such as optical amplification, fiber nonlinearities and higher fiber loss outside of the conventional band. In contrast, SDM requires the deployment of novel optical fibers capable of supporting multiple spatial channels within a single fiber cladding. Nevertheless, this approach is also compatible with the use of multi-band WDM. In fact, transmission capacities more than 100 times larger have already been demonstrated

when combining multi-band WDM and SDM, highlighting its significantly greater potential as the leading solution for future fiber-optic systems.

This thesis investigates multi-band WDM and SDM as the key enablers of next generation ultra-high-capacity transmission systems. Multiple aspects are addressed, including transmission experiments and fiber characterizations conducted both in laboratories settings and, most importantly, over field-deployed SDM fiber.

A series of state-of-the-art experiments employing multi-band WDM and SDM transmission are presented. For long-distance transmission, a data rate of 45.7 Tb/s was achieved over 12 053 km of uncoupled-core multi-core fiber (UC-MCF) using an hybrid amplification scheme that seamlessly integrates distributed Raman amplification (DRA) with multi-core amplifiers. For short-reach applications, a record data rate of 1.06 Pb/s was achieved by transmitting signals across the C- and L-bands over 6.3 km of standard-cladding-diameter 15-mode fiber field-deployed in the underground tunnel infrastructure of the city of L'Aquila, Italy. This represents the highest throughput ever reported over any deployed fiber and marks the first petabit-per-second-class transmission on such fibers.

To mitigate modal dispersion (MD) in multi-mode fiber (MMF) transmission, novel mode permutation strategies were proposed and evaluated over distances up to 1178 km of 15-mode fiber, successfully extending the transmission reach while significantly reducing the complexity of the receiver multiple-input multiple-output (MIMO) digital signal processing (DSP). A simple model for simulating propagation in realistic MMFs links with independent fiber spans, whose parameters can be conveniently extracted from the data, was also developed.

Motivated by the desire of using Raman amplification in multi-core fibers (MCFs), we performed the first experimental characterization of stimulated Raman scattering (SRS), a nonlinear optical process in silica-core fibers that can impact the performance of multi-band WDM systems, carried out over a coupled-core multi-core fiber (CC-MCF) also field-deployed in the city of L'Aquila, Italy.

The thesis is structured as follows. In the first part, the theoretical background is presented along with a brief review of propagation effects in optical fibers in the context of lightwave communications systems. In the second part, the most relevant publications among those led by the author of this thesis within his PhD program are appended. In the third part, conclusions and future directions are outlined.

Contents

List of Figures

List of Tables

List of Acronyms

MM multi-mode. 58, 59, 122

MM-EDFA multi-mode erbium-doped fiber amplifier. 58, 59, 61

MMF multi-mode fiber. ii, ix–xi, xiv, 10, 13–15, 27, 42, 47, 48, 51, 54–59, 61, 62, 65, 66, 68, 73, 74, 76–80, 92, 93, 97, 102, 103, 122, 137–142, 144, 145, 147, 152, 157–159, 164, 165

MP mode permutation. ii, xiv, 65, 137–149, 154–159, 164

MPLC multi-plane light converter. xi, 56, 57, 59, 61, 94, 95, 144

MUX multiplexer. xi, 4, 55–59, 61, 94–97, 122, 127, 140

NA numerical aperture. 19, 20

NC-MGP non-cyclic mode-group permutation. xiv, 140–142, 144, 145, 155

NEC Nippon Electric Company. 66

NF noise figure. 127

NLIN nonlinear interference noise. 47

NLSE nonlinear Schrödinger equation. 45, 46

NTT Nippon Telegraph and Telephone. 66

O/E/O optical-electrical-optical. 5, 7, 8

OADM optical add-drop multiplexer. 8

OFC Optical Fiber Communications Conference. 10

OH hydroxyl. ix, 12

OM3 optical multimode cat. 3. 54

OM4 optical multimode cat. 4. 54

OP optical processor. 59, 94, 113, 125, 126, 131, 132, 142, 144

OSA optical spectrum analyzer. xi, xii, 105, 107, 113, 114

OSNR optical signal-to-noise ratio. 70

OXC optical cross-connect. 5

PDL polarization-dependent loss. 33, 37, 42–44

PDM polarization-division multiplexing. 9, 66, 68, 71, 73, 74, 76, 77, 92, 95, 97, 121, 123, 125, 133, 142, 164

PL photonic lantern. x, 56, 57

PM polarization maintaining. 52

PMC polarization-mode coupling. 37–39, 43, 46

PMD polarization-mode dispersion. 9, 39–43, 46

PSD power spectral density. 111, 113

PSP principal states of polarization. 39, 40

Q quadrature. 9

QAM quadrature-amplitude modulated. xiii, 66, 68, 71, 73, 76, 77, 92, 95, 97, 121, 123, 125, 129, 131–134, 164, 165

QKD quantum-key distribution. 54, 65, 74, 75

QoT quality-of-transmission. 70

QPSK quadrature phase-shift keying. 68, 71, 74, 142

RC randomly coupled. 122

RC-MCF randomly-coupled multi-core fiber. 15, 51, 122

ROADM reconfigurable optical add-drop multiplexer. 8, 78, 79

RTO real-time oscilloscope. 61, 62, 94, 126, 144

SBS stimulated Brillouin scattering. 48, 49, 105

SDM space-division multiplexing. i, ii, ix, xiii, 10, 13–15, 35, 38, 41, 42, 44, 46, 48, 51, 54–56, 58, 59, 61, 65, 66, 68, 71, 76, 78–80, 92, 102–104, 122, 123, 126, 127, 130, 131, 133, 134, 138, 164, 165

SE spectral efficiency. 9–11, 13, 52

SMF single-mode fiber. i, ix, x, xii, xvii, 10, 11, 13, 14, 17, 26–28, 30, 31, 33, 38, 39, 41, 43, 45, 48, 51, 52, 54–57, 67, 69, 70, 92, 101–103, 105, 108–110, 115, 116, 122, 138, 163, 165

SNR signal-to-noise ratio. 11, 80, 130

SPM self-phase modulation. 45–47

SpRS spontaneous Raman scattering. 108

SRS stimulated Raman scattering. ii, xii, 12, 17, 48, 49, 54, 59, 65, 67, 69, 70, 101–104, 111–116, 164, 165

SSFM split-step Fourier method. 46

TDFA thulium-doped fiber amplifier. 73

TDM time-division multiplexing. 7, 94, 95

TE transverse electric. 25

TEM transverse electro-magnetic. 25

TIR total internal reflection. x, 18, 19

TLS tunable laser source. 92, 94, 123, 142

TM transverse magnetic. 25

TTL transistor-transistor logic. xi, 61, 62

UC-4CF uncoupled-core four-core fiber. 54

UC-8CF uncoupled-core eight-core fiber. 54

UC-MCF uncoupled-core multi-core fiber. ii, ix, 14, 15, 51–53, 65, 67, 70, 71, 74, 75, 77, 78, 164, 165

UWB ultra-wideband. 10, 12

VOA variable optical attenuator. 105, 113

WC weakly coupled. 122

WC-4CF weakly-coupled four-core fiber. 121, 125

WC-MCF weakly-coupled multi-core fiber. xii, 15, 48, 51, 103, 122, 123, 125–127, 133

WDL wavelength-dependent loss. xii, 125, 126

WDM wavelength-division multiplexing. i, ii, xi, xiii, 7–10, 13, 47, 48, 57–59, 66, 70, 74–76, 80, 94, 96, 102, 103, 107, 109, 111, 113, 125–127, 129–133, 147, 163–165

WSS wavelength-selective switch. 58

XPM cross-phase modulation. 47

XT crosstalk. xiv, 80, 125, 127, 151–153, 157

List of Publications

J: Journal publication; **C:** Conference publication.

Publications Appended to the Thesis:

C1 G. Di Sciullo, R. S. Luís, M. van den Hout, Q. Wu, P. Sillard, F. Achten, R. Emmerich, N. Braig-Christophersen, B. J. Puttnam, D. A. Shaji *et al.*, "Petabit-per-Second C+L Band Transmission Over a Field-deployed 15-Mode Fiber Link," in *Optical Fiber Communication Conference (OFC) 2026*, Los Angeles (CA), USA, March 2026, paper M1C.2.

J1 G. Di Sciullo, L. A. Zischler, D. A. Shaji, Q. Wu, R. S. Luís, R. Emmerich, M. van den Hout, B. J. Puttnam, G. Rademacher, C. Lasagni *et al.*, "Characterization of Stimulated Raman Scattering in Field-Deployed Coupled-Core Multi-Core Fibers," in *Journal of Lightwave Technology*, vol. 44, no. 2, pp. 550-557, 15 Jan, 2026.

J2 G. Di Sciullo, B. J. Puttnam, M. van den Hout, R. S. Luís, D. A. Shaji, G. Rademacher, C. Okonkwo, A. Mecozzi, C. Antonelli, and H. Furukawa, "45.7 Tb/s Over 12 053 km Transmission in an All-Multi-Core-Amplified Recirculating Loop," in *Journal of Lightwave Technology*, vol. 43, no. 10, pp. 4635-4641, 15 May, 2025.

J3 G. Di Sciullo, D. A. Shaji, M. van den Hout, G. Rademacher, R. S. Luís, B. J. Puttnam, N. K. Fontaine, R. Ryf, H. Chen, M. Mazur *et al.*, "Enhancing Long-Haul 15-Mode Fiber Performance: Mode Permutation for Reduced Modal Dispersion," in *Journal of Lightwave Technology*, vol. 43, no. 2, pp. 481-491, 15 Jan, 2025.

Publications Not Appended to the Thesis:

C2 A. Marotta, P. A. Robles, P. Gonzalez, L. D'Errico, I. Babiker, C. Centofanti, G. Di Sciullo, C. Antonelli, L. Velasco, S. Tennina *et al.*, "End-to-End Orchestration across MCF Infrastructure: Field Trial of Spatial PON and P2MP Metro Convergence with O-RAN for AR/VR Services with Edge Offload," in *Optical Fiber Communication Conference (OFC) 2026*, Los Angeles (CA), USA, March 2026, paper Th3E.4.

C3 D. A. Shaji, J. Schneck, L. A. Zischler, G. Di Sciullo, R. S. Luís, P. Sillard, H. Furukawa, G. Rademacher, A. Mecozzi, and C. Antonelli, "Raman Gain Profiling and Distributed Raman Amplification in a Field-Deployed 15-Mode Graded-Index Multimode Fiber," in *Optical Fiber Communication Conference (OFC) 2026*, Los Angeles (CA), USA, March 2026, paper M4E.3.

C4 C. Lasagni, L. A. Zischler, P. Serena, A. Bononi, G. Di Sciullo, A. Mecozzi, and C. Antonelli, "Investigation of Wide-band Nonlinear Effects Leveraging a Semi-analytical EGN Model," in *Optical Fiber Communication Conference (OFC) 2026*, Los Angeles (CA), USA, March 2026, paper Tu3A.3.

C5 M. Giacomin, J. M. Traktenberg, M. R. Bolaños, G. Di Sciullo, T. Hayashi, C. Antonelli, G. Vallone, P. Villoresi, and C. Agnesi, "Demonstration of a Cross-Encoded RFI QKD system in a field-deployed multi-core fiber," in *Optical Fiber Communication Conference (OFC) 2026*, Los Angeles (CA), USA, March 2026, paper M1K.5.

C6 M. Ibrahimi, G. S. Sticca, M. Tibaldini, M. Milione, F. Musumeci, G. Di Sciullo, A. Marotta, C. Antonelli, and M. Tornatore, "A Network-Wide Power Analysis of Cladding-Pumped Amplification in Multi-Core Optical Networks," in *Optical Fiber Communication Conference (OFC) 2026*, Los Angeles (CA), USA, March 2026, paper W1H.4.

J4 D. A. Shaji, R. S. Luís, D. Orsuti, L. A. Zischler, B. J. Puttnam, M. S. Neves, B. Boriboon, G. Di Sciullo, Q. Wu, M. Tan *et al.*, "Experimental Evaluation of Transmission of C+L+U bands over an

Unrepeatered Link," in *Journal of Lightwave Technology*, vol. 44, no. 4, pp. 1249-1258, 15 Feb, 2026.

J5 D. A. Shaji, R. S. Luís, B. J. Puttnam, D. Orsuti, M. S. Neves, B. Boriboon, G. Di Sciullo, Q. Wu, S. Gross, A. Ross-Adams *et al.*, "Experimental Demonstration of a Low-Cost Petabit-per-Second SDM Network Node," submitted to *Optics Express* (Under Revision).

J6 L. A. Zischler, C. Lasagni, P. Serena, A. Bononi, G. Di Sciullo, D. A. Shaji, A. Mecozzi, and C. Antonelli, "Closed-form Expression for the Power Profile in Wideband Systems with Inter-channel Stimulated Raman Scattering," in *Journal of Lightwave Technology*, vol. 44, no. 1, pp. 115-124, 1 Jan, 2026.

C7 D. A. Shaji, B. J. Puttnam, R. S. Luís, D. Orsuti, N. K. Fontaine, M. Mazur, L. Dallachiesa, G. Di Sciullo, L. A. Zischler, R. Ryf *et al.*, "Impact of Distributed Raman Amplification on OSNR in Unrepeatered ESCL Transmission," in *2025 IEEE Photonics Conference (IPC)*, Singapore, November 2025, paper WE3.1.

C8 L. A. Zischler, J. Schneck, G. Di Sciullo, D. A. Shaji, B. Kalla, S. Gaiani, R. S. Luís, D. Orsuti, P. Sillard, C. Okonkwo *et al.*, "Evaluation of Inter-Mode-Group Stimulated Raman Scattering on Multi-Mode Fibers," in *2025 IEEE Photonics Conference (IPC)*, Singapore, November 2025, paper MF1.4.

C9 A. Marotta, G. Di Sciullo, C. Antonelli, M. Ibrahimi, G. S. Sticca, F. Musumeci, and M. Tornatore, "Experimental Insights on Fault Localization and Energy Efficiency in Multi-Core Fiber Systems," in *2025 Asia Communications and Photonics Conference (ACP)*, Suzhou, China, November 2025, paper ACP2025-0801-6. [Invited paper]

C10 G. Di Sciullo, L. A. Zischler, D. A. Shaji, R. S. Luís, R. Emmerich, M. van den Hout, B. J. Puttnam, G. Rademacher, C. Lasagni, P. Serena *et al.*, "Stimulated Raman Scattering in Field-Deployed Coupled-Core Multi-Core Fibers," in *Frontiers in Optics + Laser Science 2025 (FiO, LS)*, Denver (CO), USA, October 2025, paper FTu1E.1. [Invited paper]

J7 L. A. Zischler, Ç. Özkan, T. Vosshenrich, Q. Wu, G. Di Sciullo, D. Shaji, C. Lasagni, P. Serena, A. Bononi, A. Ghazisaeidi *et al.*, "Accurate and Effective Model for Coexistence of Classical and Quantum Signals In Optical Fibers," in *arXiv*, arXiv:2510.02807 [quant-ph], 2025.

C11 R. S. Luís, G. Di Sciullo, M. van den Hout, R. Emmerich, N. Braig-Christophersen, Q. Wu, B. J. Puttnam, D. Shaji, F. Graziosi, A. Mecozzi *et al.*, "19.2 THz S+C+L Transmission in a Field Deployed, Randomly-Coupled, Multicore Fiber," in *51st European Conference on Optical Communication (ECOC 2025)*, Copenhagen, Denmark, September 2025, paper M.03.05.2. [Top-scored paper]

C12 C. Lasagni, P. Serena, A. Bononi, G. Di Sciullo, L. A. Zischler, R. S. Luís, A. Mecozzi, and C. Antonelli, "Nonlinear Interference Investigation in Coupled-Core Multi-Core Fibers with Stimulated Raman Scattering and Mode Dispersion," in *51st European Conference on Optical Communication (ECOC 2025)*, Copenhagen, Denmark, September 2025, paper Tu.01.05.2.

C13 D. A. Shaji, B. J. Puttnam, R. S. Luís, D. Orsuti, N. K. Fontaine, M. Mazur, L. Dallachiesa, G. Di Sciullo, L. A. Zischler, R. Ryf *et al.*, "Experimental Evaluation of Throughput Gains from Distributed Raman Amplification in Ultra-Wideband ESCL Transmission," in *51st European Conference on Optical Communication (ECOC 2025)*, Copenhagen, Denmark, September 2025, paper Tu.04.05.2.

C14 G. Di Sciullo, D. A. Shaji, L. A. Zischler, R. S. Luís, R. Emmerich, M. van den Hout, C. Lasagni, P. Serena, A. Bononi, T. Hayashi *et al.*, "Experimental Characterization of Stimulated Raman Scattering in Field-Deployed Coupled-Core Multi-Core Fibers," in *51st European Conference on Optical Communication (ECOC 2025)*, Copenhagen, Denmark, September 2025, paper W.02.01.01.

C15 Q. Wu, G. Di Sciullo, D. A. Shaji, D. Ribezzo, D. Bacco, R. S. Luís, T. Hayashi, L. A. Zischler, A. Marotta, F. Graziosi *et al.*, "Coexistence of Quantum-Key Distribution and Classical Transmission in Space-Division Multiplexed Fiber-Optic Systems: Modelling and Validation over Field-Deployed Multi-Core Fibers," in *51st European

Conference on Optical Communication (ECOC 2025), Copenhagen, Denmark, September 2025, paper W.02.01.183.

C16 Q. Wu, D. Ribezzo, G. Di Sciullo, D. A. Shaji, R. S. Luís, D. Bacco, L. A. Zischler, A. Marotta, F. Graziosi, S. Cocchi *et al.*, "Field Demonstration of Quantum Key Distribution Coexisting with 110-Tb/s Classical Transmission over Multi-Core Fibers," in *51st European Conference on Optical Communication (ECOC 2025)*, Copenhagen, Denmark, September 2025, paper Th.02.03.3. [Top-scored paper]

C17 N. Braig-Christophersen, C. Schmidt-Langhorst, R. Elschner, G. Di Sciullo, M. van den Hout, R. S. Luís, P. Sillard, C. Antonelli, C. Okonkwo, H. Furukawa *et al.*, "Partitioned MIMO Equalization with Mode-Group Specific Interface Resolution for SDM Transmission over 58.9 km 15-mode Fiber," in *51st European Conference on Optical Communication (ECOC 2025)*, Copenhagen, Denmark, September 2025, paper Th.02.04.4.

C18 R. S. Bravo Ospina, A. Ghazisaeidi, S. Gaiani, R. S. Luís, D. Orsuti, B. Kalla, M. van den Hout, P. Sillard, F. Achten, G. Di Sciullo *et al.*, "Rate-Adaptive Partial MIMO Equalization for Mode-Group Selective Transmission over Few Mode Fibers," in *51st European Conference on Optical Communication (ECOC 2025)*, Copenhagen, Denmark, September 2025, paper Th.02.04.5.

J8 L. A. Zischler, C. Lasagni, P. Serena, A. Bononi, G. Di Sciullo, D. Shaji, A. Mecozzi, and C. Antonelli, "Closed-form Expression for the Power Profile in Wideband Systems with Inter-channel Stimulated Raman Scattering," in *arXiv*, arXiv:2508.00093 [eess.SP], 2025.

C19 A. Marotta, C. Centofanti, G. Di Sciullo, C. Antonelli, F. Graziosi and L. Valcarenghi, "A Resilient Passive Optical Network Architecture Based on Dynamic Spatial Aggregation," in *2025 25th Anniversary International Conference on Transparent Optical Networks (ICTON)*, Barcelona, Spain, July 2025, paper Mo.C7.6.

J9 Q. Wu, D. Ribezzo, G. Di Sciullo, S. Cocchi, D. A. Shaji, L. A. Zischler, R. S. Luís, P. Serena, C. Lasagni, A. Bononi *et al.*, "Integration of quantum key distribution and high-throughput classical communications in field-deployed multi-core fibers," in *Light Science and Applications*, vol. 14, no. 274 (2025).

C20 M. Ibrahimi, P. Lobaccaro, G. Di Sciullo, G. S. Sticca, F. Musumeci, R. S. Luís, A. Marotta, C. Antonelli, and M. Tornatore, "Data-Driven Failure Localization in Multi-Core Optical Networks," in *2025 30th OptoElectronics and Communications Conference (OECC) and 2025 International Conference on Photonics in Switching and Computing (PSC)*, Sapporo, Japan, June 2025, paper ThG1-1. [Invited paper]

C21 C. Antonelli, A. Mecozzi, A. Marotta, F. Graziosi, G. Di Sciullo, D. A. Shaji, L. A. Zischler, Q. Wu, M. Mazur, N. K. Fontaine *et al.*, "Space-Division Multiplexed Transmission in Deployed Fibers," in *2025 30th OptoElectronics and Communications Conference (OECC) and 2025 International Conference on Photonics in Switching and Computing (PSC)*, Sapporo, Japan, June 2025, paper WD1-1. [Invited paper]

C22 D. A. Shaji, R. S. Luís, B. J. Puttnam, D. Orsuti, M. S. Neves, B. Boriboon, G. Di Sciullo, Q. Wu, S. Gross, A. Ross-Adams *et al.*, "Experimental Demonstration of a Low-Cost Petabit-Per-Second SDM Network Node," in *2025 Conference on Lasers and Electro-Optics Europe & European Quantum Electronics Conference (CLEO/Europe-EQEC)*, Munich, Germany, June 2025, paper CI-1.2. [Invited paper]

J10 N. Hoghooghi, M. Mazur, N. K. Fontaine, Y. Liu, D. Lee, C. McLemore, T. Nakamura, T. Hayashi, G. Di Sciullo, D. Shaji *et al.*, "Ultrastable optical frequency transfer and attosecond timing in deployed multicore fiber," in *Optica*, vol. 12, pp. 894-899 (2025).

C23 G. Di Sciullo, D. A. Shaji, M. van den Hout, G. Rademacher, R. S. Luís, B. J. Puttnam, N. K. Fontaine, R. Ryf, H. Chen, M. Mazur *et al.*, "Reduction of Modal Dispersion through Mode Permutation in Multi-Mode Fiber Transmission," in *Optical Fiber Communication Conference (OFC) 2025*, San Francisco (CA), USA, March 2025, paper M4F.1. [Invited paper]

C24 H. Chen, N. K. Fontaine, R. Ryf, G. Di Sciullo, L. Dallachiesa, K. Kim, C. Tran, M. Mazur, X. Xu, J. E. Simsarian *et al.*, "Reconfigurable Multi-Port Multi-Wavelength Coherent Receiver," in *Optical*

Fiber Communication Conference (OFC) 2025, San Francisco (CA), USA, March 2025, paper M2D.1. [Top-scored paper]

J11 M. van den Hout, R. S. Luís, B. J. Puttnam, G. Di Sciullo, T. Hayashi, A. Inoue, T. Nagashima, S. Gross, A. Ross-Adams, M. J. Withford *et al.*, "Reaching the pinnacle of high-capacity optical transmission using a standard cladding diameter coupled-core multi-core fiber," in *Nature Communications*, vol. 16, no. 3833 (2025).

J12 D. Orsuti, B. J. Puttnam, R. S. Luís, M. S. Neves, M. van den Hout, G. Di Sciullo, D. A. Shaji, B. Boriboon, G. Rademacher, J. Sakaguchi *et al.*, "S/C/L-Band Transmission in Few-Mode MCF With Optical Frequency Comb Regeneration via Single-Mode Core Seed Distribution," in *Journal of Lightwave Technology*, vol. 43, no. 4, pp. 1786-1793, 15 Feb, 2025.

C25 G. Di Sciullo, Q. Wu, R. S. Luís, B. J. Puttnam, G. Rademacher, R. Ryf, T. Hayashi, H. Furukawa, A. Mecozzi, and C. Antonelli, "Stimulated Raman scattering in WDM transmission over randomly-coupled multi-core fibers," in *2024 IEEE Photonics Conference (IPC)*, Rome, Italy, November 2024, paper ThG2.5.

C26 G. Di Sciullo, M. van den Hout, B. J. Puttnam, R. S. Luís, D. A. Shaji, G. Rademacher, C. Okonkwo, A. Mecozzi, C. Antonelli, and H. Furukawa, "Performance Comparison of QAM Modulation Formats on an All-4-Core Recirculating Loop," in *2024 IEEE Photonics Conference (IPC)*, Rome, Italy, November 2024, paper ThG2.4.

C27 Q. Wu, D. Ribezzo, G. Di Sciullo, D. A. Shaji, T. Hayashi, R. S. Luís, D. Bacco, Y. Zhu, W. Hu, A. Mecozzi *et al.*, "Integration of Quantum Key Distribution and Classical Communications Over Field-Deployed Uncoupled-Core Four-Core Fiber," in *2024 IEEE Photonics Conference (IPC)*, Rome, Italy, November 2024, paper ME4.3.

C28 Q. Wu, D. Ribezzo, G. Di Sciullo, D. A. Shaji, T. Hayashi, R. S. Luís, D. Bacco, Y. Zhu, W. Hu, A. Mecozzi *et al.*, "Co-existence of Quantum Key Distribution and Classical Transmission in a Field-Deployed Uncoupled-Core Four-Core Fiber," in *50th European Conference on Optical Communication (ECOC 2024)*, Frankfurt, Germany, September 2024, paper W2A.178.

C29 M. van den Hout, G. Di Sciullo, R. S. Luís, B. J. Puttnam, N. K. Fontaine, R. Ryf, H. Chen, M. Mazur, D. T. Neilson, P. Sillard *et al.*, “Long-Distance Space-Division-Multiplexed Transmission Using High-Mode-Count Multi-Mode Fibers,” in *50th European Conference on Optical Communication (ECOC 2024)*, Frankfurt, Germany, September 2024, paper W3B.3. [Invited paper]

C30 C. Antonelli, A. Mecozzi, A. Marotta, F. Graziosi, G. Di Sciullo, D. A. Shaji, Q. Wu, D. Ribezzo, M. Mazur, N. K. Fontaine *et al.*, “Space-Division Multiplexed Transmission from the Lab to the Field,” in *50th European Conference on Optical Communication (ECOC 2024)*, Frankfurt, Germany, September 2024, paper Tu3B.4. [Invited paper]

J13 N. Hoghooghi, M. Mazur, N. K. Fontaine, Y. Liu, D. Lee, C. McLemore, T. Nakamura, T. Hayashi, G. Di Sciullo, D. A. Shaji *et al.*, “Enabling a multifunctional telecommunications fiber optic network: Ultrastable optical frequency transfer and attosecond timing in deployed multicore fiber,” in *arXiv*, arXiv:2410.13801 [physics.optics], 2024.

C31 B. J. Puttnam, D. Orsuti, R. S. Luís, M. S. Neves, M. van den Hout, G. Di Sciullo, G. Rademacher, J. Sakaguchi, C. Antonelli, C. Okonkwo *et al.*, “Wideband S, C, + L-Band Comb Regeneration in Large-Scale Few-Mode MCF Link with Single-Mode Seed Channel,” in *Optical Fiber Communication Conference (OFC) 2024*, San Diego (CA), USA, March 2024, paper Th4A.6. [Post-deadline paper]

C32 N. Hoghooghi, M. Mazur, N. K. Fontaine, Y. Liu, T. Hayashi, G. Di Sciullo, D. A. Shaji, A. Mecozzi, C. Antonelli, and F. Quinlan, “Towards international clock comparisons on a telecom network: ultra-stable optical frequency transfer over deployed multi-core fiber,” in *Optical Fiber Communication Conference (OFC) 2024*, San Diego (CA), USA, March 2024, paper Th4A.5. [Post-deadline paper]

C33 C. Antonelli, A. Mecozzi, A. Marotta, F. Graziosi, G. Di Sciullo, D. Ribezzo, M. Mazur, N. K. Fontaine, L. Dallachiesa, R. Ryf *et al.*, “Field Transmission Performance of Multi-core and Few-Mode Fibers,” in *Optical Fiber Communication Conference (OFC) 2024*, San Diego (CA), USA, March 2024, paper W3J.1. [Invited paper]

C34 G. Di Sciullo, B. J. Puttnam, M. van den Hout, R. S. Luís, D. A. Shaji, G. Rademacher, C. Okonkwo, A. Mecozzi, C. Antonelli, and H. Furukawa, “45.7 Tb/s over 12 053 km Transmission with an All-Multi-Core Recirculating-Loop 4-Core-Fiber System,” in *Optical Fiber Communication Conference (OFC) 2024*, San Diego (CA), USA, March 2024, paper Th3E.2.

C35 M. van den Hout, R. S. Bravo Ospina, R. S. Luís, B. J. Puttnam, G. Di Sciullo, T. Hayashi, A. Inoue, T. Nagashima, S. Gross, A. Ross-Adams *et al.*, “Experimental Analysis of Receiver Failure For 19-Core Randomly Coupled Core Fibre Transmission,” in *Optical Fiber Communication Conference (OFC) 2024*, San Diego (CA), USA, March 2024, paper W2A.28.

J14 B. J. Puttnam, R. S. Luís, D. Orsuti, G. Rademacher, G. Di Sciullo, M. van den Hout, J. Sakaguchi, C. Antonelli, C. Okonkwo, L. Palmieri *et al.*, “Experimental demonstration of a multi-core fiber seeded comb optical network (MCF-SCON),” in *Journal of Optical Communications and Networking*, vol. 16, no. 7, pp. C69-C75, July 2024.

J15 A. Gatto, P. Parolari, R. S. Luís, G. Rademacher, B. J. Puttnam, R. Emmerich, C. Schubert, G. Ferri, F. Achten, P. Sillard, P. Martelli, G. Di Sciullo *et al.*, “Partial-MIMO Based Mode-Group Transmission and Routing in a Field-Deployed 15-Mode Network: Throughput, DSP Resources and Network Flexibility,” in *Journal of Lightwave Technology*, vol. 42, no. 14, pp. 4720-4732, 15 July, 2024.

J16 R. S. Luís, B. J. Puttnam, G. Rademacher, M. van den Hout, G. Di Sciullo, D. Orsuti, C. Okonkwo, C. Antonelli, J. Sakaguchi, and H. Furukawa, “Wideband Unrepeatered Transmission Using Doped Tellurite-Fiber Amplifiers,” in *Journal of Lightwave Technology*, vol. 42, no. 13, pp. 4410-4416, 1 July, 2024.

J17 M. van den Hout, G. Di Sciullo, R. S. Luís, B. J. Puttnam, N. K. Fontaine, R. Ryf, H. Chen, M. Mazur, D. T. Neilson, P. Sillard *et al.*, “Transmission of 273.6 Tb/s Over 1001 km of 15-Mode Multi-Mode Fiber Using C-Band Only 16-QAM Signals,” in *Journal of Lightwave Technology*, vol. 42, no. 3, pp. 1136-1142, 1 Feb, 2024.

C36 B. J. Puttnam, M. van den Hout, G. Di Sciullo, R. S. Luís, G. Rademacher, J. Sakaguchi, C. Antonelli, C. Okonkwo, and H. Furukawa, "22.9 Pb/s data-rate by extreme space-wavelength multiplexing," in *49th European Conference on Optical Communications (ECOC 2023)*, Glasgow, UK, October 2023, paper Th.C.2.1. [Post-deadline paper]

C37 G. Di Sciullo, M. van den Hout, G. Rademacher, R. S. Luís, B. J. Puttnam, N. K. Fontaine, R. Ryf, H. Chen, M. Mazur, D. T. Neilson *et al.*, "Reduction of modal dispersion in a long-haul 15-mode fiber link by means of mode permutation," in *49th European Conference on Optical Communications (ECOC 2023)*, Glasgow, UK, October 2023, paper We.A.1.2.

C38 M. van den Hout, B. J. Puttnam, G. Di Sciullo, R. S. Luís, G. Rademacher, C. Antonelli, C. Okonkwo, and H. Furukawa, "Transmission of 138.9 Tb/s over 12 345 km of 125µm cladding diameter 4-core fiber using signals spanning S, C, and L-band," in *49th European Conference on Optical Communications (ECOC 2023)*, Glasgow, UK, October 2023, paper M.A.5.5.

C39 B. J. Puttnam, R. S. Luís, G. Rademacher, G. Di Sciullo, M. van den Hout, J. Sakaguchi, C. Antonelli, C. Okonkwo, and H. Furukawa, "C + L-band seeded comb regeneration for MCF networks," in *49th European Conference on Optical Communications (ECOC 2023)*, Glasgow, UK, October 2023, paper Th.B.2.5. [Top-scored paper]

C40 R. S. Luís, B. J. Puttnam, G. Rademacher, M. van den Hout, G. Di Sciullo, C. Okonkwo, C. Antonelli, J. Sakaguchi, and H. Furukawa, "40.5 Tb/s, 312.9 km, unrepeatered transmission using erbium-doped tellurite fiber amplifiers," in *49th European Conference on Optical Communications (ECOC 2023)*, Glasgow, UK, October 2023, paper Th.B.6.5.

C41 G. Di Sciullo, M. van den Hout, G. Rademacher, R. S. Luís, B. J. Puttnam, N. K. Fontaine, R. Ryf, H. Chen, M. Mazur, D. T. Neilson *et al.*, "Modal Dispersion Mitigation in a long-haul 15-Mode Fiber link through Mode Permutation," in *2023 IEEE Photonics Society Summer Topicals Meeting Series (SUM)*, Sicily, Italy, July 2023, paper WC1.3.

J18 R. S. Luís, G. Rademacher, B. J. Puttnam, G. Di Sciullo, A. Marotta, R. Emmerich, N. Braig-Christophersen, R. Stolte, F. Graziosi, A. Mecozzi *et al.*, "Demonstration of a 15-Mode Network Node Supported by a Field-Deployed 15-Mode Fiber," in *Journal of Lightwave Technology*, vol. 41, no. 12, pp. 3695-3703, 15 June, 2023.

C42 G. Rademacher, M. van den Hout, R. S. Luís, B. J. Puttnam, G. Di Sciullo, T. Hayashi, A. Inoue, T. Nagashima, S. Gross, A. Ross-Adams *et al.*, "Randomly Coupled 19-Core Multi-Core Fiber with Standard Cladding Diameter," in *Optical Fiber Communication Conference (OFC) 2023*, San Diego (CA), USA, March 2023, paper Th4A.4. [Post-deadline paper]

C43 M. van den Hout, G. Di Sciullo, G. Rademacher, R. S. Luís, B. J. Puttnam, N. K. Fontaine, R. Ryf, H. Chen, M. Mazur, D. T. Neilson *et al.*, "273.6 Tb/s Transmission Over 1001 km of 15-Mode Fiber Using 16-QAM C-Band Signals," in *Optical Fiber Communication Conference (OFC) 2023*, San Diego (CA), USA, March 2023, paper Th4B.5. [Post-deadline paper]

C44 R. S. Luís, G. Di Sciullo, G. Rademacher, B. J. Puttnam, A. Marotta, R. Emmerich, N. Braig-Christophersen, R. Stolte, F. Graziosi, A. Mecozzi *et al.*, "Colorless and Directionless ROADM for Meshed Coupled-Core Multicore Fiber Networks," in *Optical Fiber Communication Conference (OFC) 2023*, San Diego (CA), USA, March 2023, paper Th4C.3. [Post-deadline paper]

C45 A. Gatto, P. Parolari, R. S. Luís, G. Rademacher, B. J. Puttnam, R. Emmerich, C. Schubert, G. Ferri, F. Achten, P. Sillard, P. Martelli, G. Di Sciullo *et al.*, "Partial MIMO-based Mode Division Multiplexing Transmission over the First Field-Deployed 15-Mode Fiber in Metro Scenario," in *Optical Fiber Communication Conference (OFC) 2023*, San Diego (CA), USA, March 2023, paper M2B.3.

C46 P. Parolari, A. Gatto, R. S. Luís, G. Rademacher, B. J. Puttnam, R. Emmerich, C. Schubert, G. Ferri, F. Achten, P. Sillard, P. Martelli, G. Di Sciullo *et al.*, "Demonstration of Multi-Hop Mode-Group Routing in a Field-Deployed Multi-Mode Fiber Network," in *Optical Fiber Communication Conference (OFC) 2023*, San Diego (CA), USA, March 2023, paper M4G.3.

C47 R. S. Luís, G. Rademacher, B. J. Puttnam, G. Di Sciullo, A. Marotta, R. Emmerich, N. Braig-Christophersen, R. Stolte, F. Graziosi, A. Mecozzi *et al.*, “Demonstration of a Spatial Super Channel Switching SDM Network Node on a Field Deployed 15-Mode Fiber Network,” in *48th European Conference on Optical Communications (ECOC 2022)*, Basel, Switzerland, September 2022, paper Th3C.5. [Post-deadline paper]

C48 G. Rademacher, R. S. Luís, B. J. Puttnam, G. Di Sciullo, R. Emmerich, N. Braig-Christophersen, A. Marotta, L. Dallachiesa, R. Ryf, A. Mecozzi *et al.*, “Characterization of the First Field-Deployed 15-Mode Fiber Cable for High Density Space-Division Multiplexing,” in *48th European Conference on Optical Communications (ECOC 2022)*, Basel, Switzerland, September 2022, paper Th3B.1. [Post-deadline paper]

Part I

Thesis Background

Chapter 1

Introduction

Glass fibers were first fabricated in the 1920s, but their use became practical only in the 1950s, when the use of a cladding layer significantly improved their guiding properties. While before 1970 their use in communication was considered impractical due to extremely high losses of about 1000 dB/km, the situation drastically changed in 1970, when losses were reduced below 20 dB/km. By 1979, further advancements lowered losses to only 0.2 dB/km in the 1550 nm spectral region, thus leading to a revolution in the field of lightwave technology with the start of the fiber-optic communications era [1].

Today, it is very well acknowledged that the overwhelming majority of the global data traffic exchanged between cities, countries, and continents – whether separated by land, sea, or even by the ocean – is carried by billions of kilometers of optical communication cables deployed around the world and offering a huge transmission capacity [2, 3]. To cost-effectively meet the ever-increasing demand for higher data rates, particularly driven by video, cloud and artificial intelligence (AI) services, the research community has consistently been able to deliver a hundred-fold increase in the per-fiber capacity every decade, reaching data rates as high as 100 Tb/s on a single optical fiber. This incredible progress has been enabled by continuous device inventions, system innovation, and the introduction of novel communications technologies.

This chapter provides an overview of optical telecommunications systems and highlights the current research challenges in this field, thereby motivating the research presented in this thesis.

1.1 Optical Fiber Networks

To appreciate the importance of optical fibers, it is useful to provide a brief overview of optical fiber networks, which ultimately provide connectivity between end users through a fiber-based infrastructure.

Conceptually, an optical fiber network can be divided into three main layers. The first is the access network, which includes the technologies used by an Internet service provider (ISP) to deliver Internet connectivity – via fifth generation (5G) cellular networks, copper cables, coaxial cables, or optical fiber-to-the-home (FTTH) links – to end-user equipment such as mobile phones or customer premise equipments (CPEs). The second layer is the metropolitan (metro) network, which interconnects cities in a specific region or country. Above this layer lies the global network, responsible for interconnecting metro networks across continents.

Although these layers connect different types of locations, they also provide distinct characteristics and capabilities. Two of the most important differences are the traffic capacities they must support and the distances they must cover. As data traffic is progressively aggregated from the access network through the metro and ultimately to the global network, the requirements in terms of link capacity increase accordingly. Similarly, while access and metro networks typically span distances ranging from a few kilometers to several hundred kilometers, global network links can extend up to 10 000 km, as in the case of some of the longest submarine systems deployed worldwide.

In today's telecommunication network architecture, the transport network provides high-capacity connectivity between all nodes in the network [4], with large cities and large communication hubs forming their primary nodes. Instead of deploying dedicated physical connections between every node pair, the transport network provides virtual channels between endpoints, each of which occupies only a fraction of the available transmission capacity. To be cost-efficient, these lower-rate channels are multiplexed (i.e., aggregated) into a single higher-capacity channel using a multiplexer (MUX), as illustrated in Fig. 1.1(a). Depending on the link length, the signal may need to be periodically regenerated to compensate for transmission impairments (e.g., fiber loss), as illustrated in Fig. 1.1(b). At the destination node, the aggregated data channels are de-multiplexed into the lower-rate tributaries to implement logical connections between nodes, depending on the specific topology of the transport network. In linear network topologies, such as bus or ring structures (typical for metropolitan networks), these lower-rate channels can either be terminated (or,

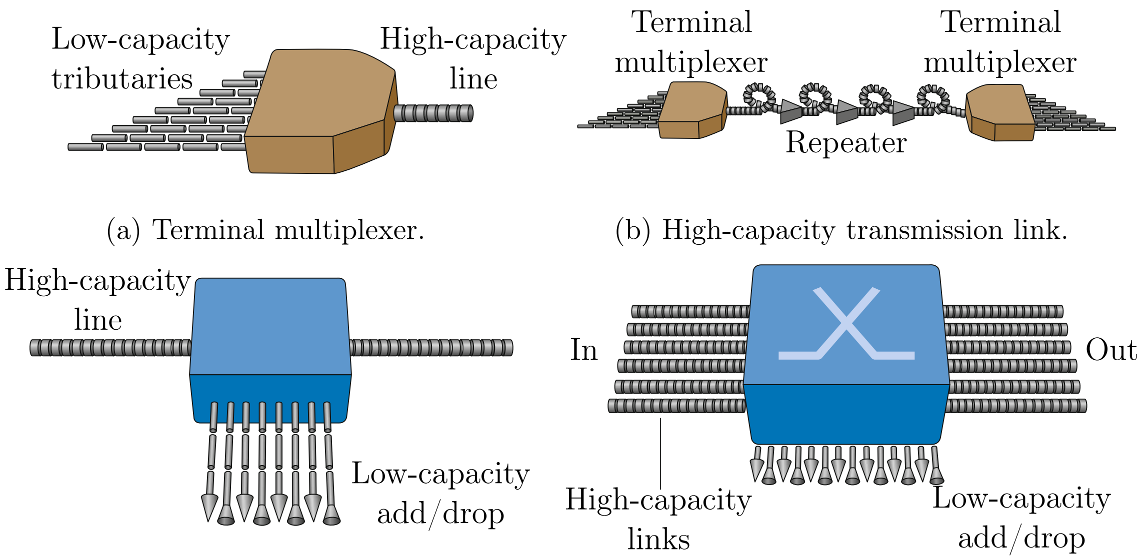

(a) Terminal multiplexer. (b) High-capacity transmission link.

(c) Add/drop multiplexer. (d) Optical cross-connect.

Figure 1.1: Optical fiber network components. From [4, Fig. 1.1a–d].

technically, *dropped*) at that node, or simply *passed through*. In addition, traffic originating at that node must be added to the high-capacity output line alongside the passed-through traffic. This functionality is provided by an add/drop multiplexer, as illustrated in Fig. 1.1(c). In meshed network topologies (typical for national and global networks), each node can be connected to multiple other network nodes, rather than only to the two nearest neighbors used for linear and ring networks. In these networks, the switching element becomes more sophisticated, as it is no longer limited to dropping channels from all incoming links, but also has to switch/route lower-rate channels between output links to provide connectivity across the network. This functionality is provided by an optical cross-connect (OXC), illustrated in Fig. 1.1(d).

Another essential building block in any optical telecommunication system is the transponder, originating from the amalgamation of the words transmitter and responder. As the terms suggests, a transponder integrates the transmitter and receiver functionalities and is able to translate an optical signal from one wavelength to another across two links in the network using optical-electrical-optical (O/E/O) conversion. The transponder ports can support different optical interface classes, depending on link distance, wavelength range, and capacity requirements. The O/E and E/O conversions inside a transponder are performed by another very similar device called transceiver, an amalgamation of the words transmitter and receiver, which is able to simultaneously transmit and receive signals. A transponder can then be seen as a combination of a client- and network-side optical transceivers separated by an

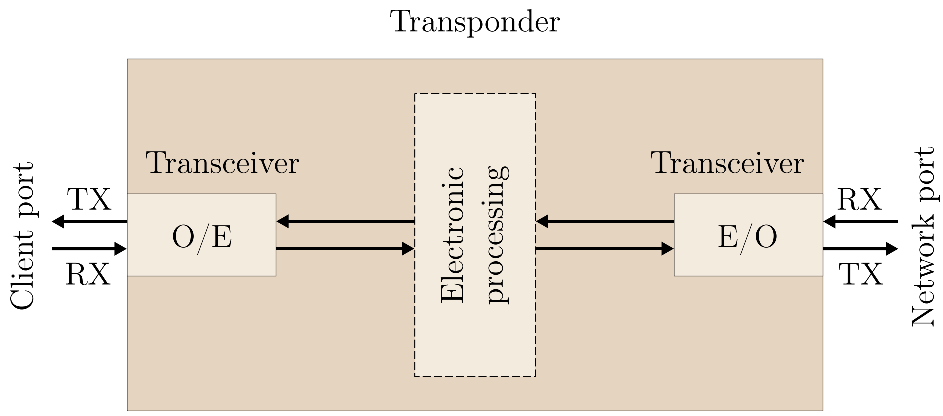

Figure 1.2: Optical transponder basic block digram. Adapted from [4, Fig. 4.1].

electronic processing block, as illustrated in Fig. 1.2. As a consequence, the transponder can be equipped with transceivers tailored to different transmission requirements at the two ends. All the optical fiber network components illustrated in Fig. 1.1 can be built from a transponder by adjusting the number of input and output ports. For example, a multiplexer can be seen as a transponder with multiple low-capacity ports on the client side and a single high-capacity port on the network side. Similarly, an add/drop multiplexer corresponds to a transponder with multiple low-capacity ports on the client side and two high-capacity ports on the network side.

1.2 The Evolution of Optical Transport Networks

With the concept of optical fiber networks outlined in the previous section, we can now review the evolution of optical telecommunication systems over the past decades in response to the ever-increasing demand for data transmission capacities. Some of the record data rates achieved in laboratory *'hero'* transmission experiments from 1996 are reported in Fig. 1.3. The figure illustrates an exponential increase in achieved data rates over the last 30 years and highlights the main technologies that have enabled this capacity scaling. Although exponential growth will eventually saturate, many examples in information and communications technologies have shown that it can be maintained for decades, and in some cases even for a century [5]. This trend is also notable in commercial products, whose records in terms of per-fiber and per-carrier data rates are reported in Fig. 1.4. The huge increase in fiber-optic capacity has been driven by the advent of various novel technologies, along with the use of multiplexing across a number of physical domains available in optical fibers. In what follows, we

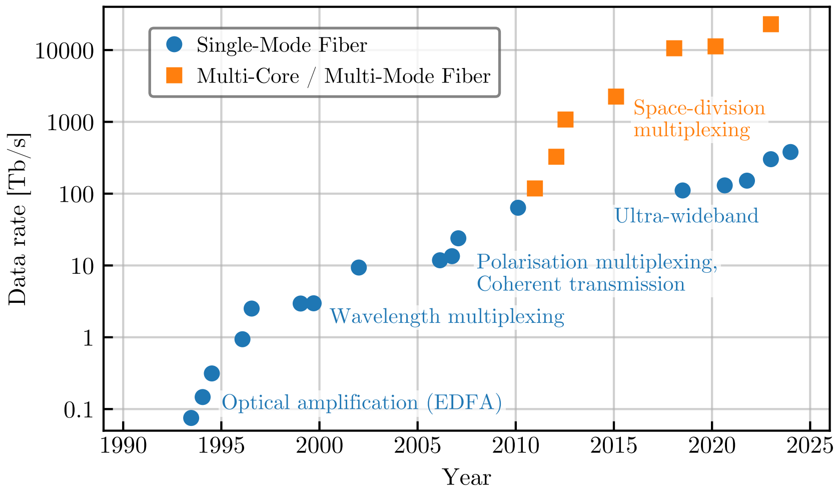

Figure 1.3: Evolution of data rates in optical transmission systems. After [7, Fig. 1], with additional points from [8, 9].

outline some of the main developments in optical telecommunications systems by categorizing them into four major eras of transmission [5, 6].

1. The era of regeneration (1977 - 1995) The first optical telecommunication systems were based on intensity-modulation direct-detection (IM/DD), in which the transmitter modulated lights by adjusting its output power across a number of defined levels, while the receiver detected these power changes to retrieve the transmitted information. As a result, these systems could only exploit time as the sole physical multiplexing domain, resulting in what is generally referred to as time-division multiplexing (TDM). To traverse long distances, the optical signal had to be *regenerated* every fiber span. Since this regeneration required an O/E/O conversion, the capacity of such systems was highly constrained by the interface rate of the transceivers [5].

Figure 1.4 illustrates the evolution of commercial interface rates, which improved of approximately 20% per year for more than three decades. At the same time, research demonstrations were growing at a slightly lower rate, around 14% per year. By the mid-1990s, data rates in these systems reached the order of tens of gigabits per second.

2. The era of amplified dispersion-managed systems (1995 – 2008) This era began with the invention of practical optical amplifiers, and in particular of the erbium-doped fiber amplifiers (EDFAs), which became the driving technology enabling cost-efficient wavelength-division multiplexing (WDM) systems. The commercialization of EDFAs allowed an all-optical amplification of wideband signals, removing the need for O/E/O conversion in signal regeneration. At the same time,

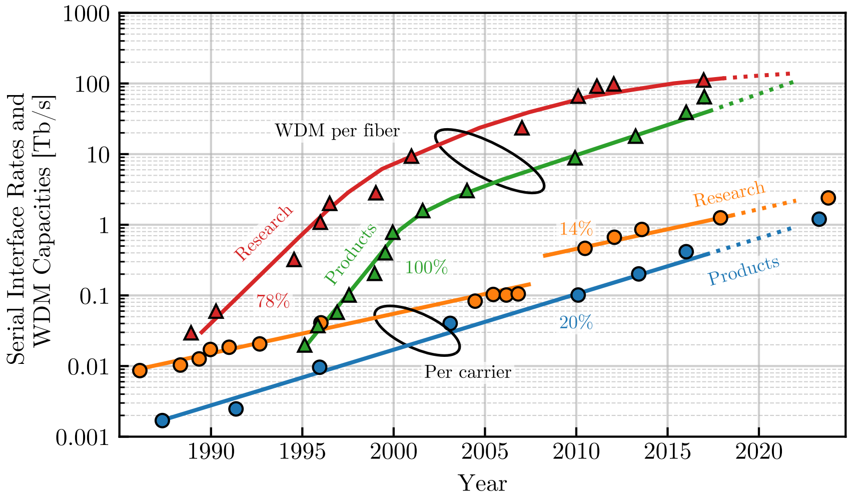

Figure 1.4: Evolution of research and commercial product data rates in terms of both the per-fiber capacity and the per-carrier interface rate. After [10–12], with additional points from [13, 14].

the development of WDM systems allowed multiple optical signals placed at different wavelengths to simultaneously propagate through the same fiber, with the receiver performing filtering and subsequent reception of a single wavelength channel. However, the advent of EDFAs alone was not sufficient to guarantee a growth rate of approximately 100% per year in commercial WDM systems. Indeed, this resulted from a combination of several inventions in the early 1990s. One of the most significant was the introduction of dispersion management, a powerful technique in which transmission fibers with opposite dispersion values are concatenated so that the overall chromatic dispersion (CD) of a link is nearly zero at the receiver side. Here, CD is a phenomenon causing the transmitted signal to spread in time, leading to temporal overlap between multiple signals (see also Section 2.3.2). Another limiting factor for the rise of WDM systems was the limited capacity of electronic switches and routers. This bottleneck was overcome with the introduction of optical add-drop multiplexers (OADMs), and later the more advanced reconfigurable optical add-drop multiplexers (ROADMs) in the early 2000s, which removed the need for O/E/O conversion in add-drop multiplexers by performing the functions of aggregation, disaggregation and switching of low-rate channels directly in the optical domain.

By 2008, research records for these type of systems had broke the 10 Tb/s barrier, with commercial products requiring nearly a decade to reach these capacities. However, these experiments also revealed a reduction in the growth rate of optical fibers. At that time, systems had already reached the maximum usable bandwidth of practical single-band EDFAs, and increasing the per-signal bandwidth was limited by the frequency granularity of the available optical filters. The continuous scaling of WDM capacity required more efficient modulation formats to increase spectral efficiency (SE), defined as the ratio between the data rate (in bit/s) and the occupied bandwidth (in Hz). In this context, coherent transmission schemes proved to be a more efficient alternative. Although IM/DD schemes are still in use today in access and intra-data-center networks, this transition marked the end of the era of amplified dispersion-managed systems in metro and global networks.

3. The era of amplified coherent systems (2008 – present) Coherent systems were studied as early as the 1980s because of their enhanced sensitivity compared to IM/DD systems, allowing lower power levels for signal detection and thus enabling longer repeater spacing. However, at that time, difficulties related to analog frequency and phase locking made them unsuitable for commercial fiber-optic systems. Moreover, the success of EDFAs in the early 1990s, which made signal regeneration obsolete, further postponed the development of coherent technologies [11].

Due to the need for higher SE, coherent technologies were studied again in the mid-2000s. Using a free-running local oscillator (LO) laser, digital coherent receivers beat the optical signal down to baseband and convert the full optical signal field – i.e., both real and imaginary components, also referred to as the in-phase (I) and quadrature (Q) components – in both polarizations of light into the digital electronic domain. Access to the full optical field enables *quadrature modulation* (I/Q) and *polarization-division multiplexing* (PDM), resulting in a factor of four increase in SE. In 2008, the first intradyne transponder operating at 40 Gb/s was commercialized [15], with current systems now providing data rates of up to 1.6 Tb/s per single wavelength [16]. Moreover, access to the full optical field in the digital domain enabled adaptive digital compensation of CD, polarization-mode dispersion (PMD) and even distortion arising from fiber nonlinearities.

The continuous but slower growth in fiber capacity since the early 2000s (see Fig. 1.3) raised concerns that transmission systems might be approaching a fundamental limit. These concerns have motivated numerous studies on the capacity of the fiber channel in the nonlinear transmission regime, often referred to as *nonlinear Shannon capacity* [17–19]. Within this framework, the achievable throughput initially follows the linear Shannon limit for additive white Gaussian noise (AWGN) channels, whereas it becomes much more challenging to predict its evolution in the nonlinear transmission regime [20]. Using this approach, an achievable throughput of approximately

100 Tb/s has been estimated for a single-mode fiber (SMF) system operating in the C-band over long-haul transmission distances on the order of a few thousand kilometers [18]. As shown in Fig. 1.3, laboratory demonstrations have already achieved data rates around this value, while Fig. 1.4 indicates that commercial products have also approached the 100 Tb/s threshold per single optical fiber.

4. The era of space-division multiplexing (actively researched since 2008)
The continuous exponential growth of global traffic at approximately 45% per year, combined with interface rates and fiber capacities scaling at only about 20% per year (see Fig. 1.4), reveals a critical disparity. This issue was already anticipated as early as 2005, in a talk from Emmanuel Desurvire discussing the *capacity exhaustion* of SMFs [21], and later in 2009, during a plenary presentation at the European Conference on Optical Communications (ECOC) by Andrew Chraplyvy, who warned of the impending *information capacity crunch* [22]. These terms describe a situation where the rate at which traffic demand grows exceeds the rate at which the optical transport network can increase its supported throughput. Soon, network operators will no longer be able to meet the enormous capacity requirements of emerging applications, such as video streaming, cloud and AI services, simply by adding more WDM channels or by increasing the SE. Instead, network operators will be forced to deploy new optical fiber cables, thereby increasing the number of parallel systems running within their infrastructures. However, this approach fails to reduce the energy consumption (and thus the cost) per transmitted bit, in contrast with the exponentially decreasing trend in cost per bit observed over the past decades [23].

To address this issue, several research initiatives were launched around 2008 to develop new technologies capable of increasing the per-fiber capacity while simultaneously reducing the cost per bit [24, 25]. Two of the most promising approaches proposed to overcome the 100 Tb/s barrier of conventional SMF systems were: (i) the exploitation of the remaining transmission bands available in silica-core fibers, summarized in Table 1.1, and referred to as multi-band or ultra-wideband (UWB) WDM transmission, and (ii) the utilization of the last remaining physical dimension in the optical domain, leading to what is now known as space-division multiplexing (SDM). By 2011, post-deadline papers at the Optical Fiber Communications Conference (OFC) had already demonstrated successful SDM transmission using both multi-mode fiber (MMF) and multi-core fiber (MCF) technologies [27–31], achieving aggregate data rates around 109 Tb/s with such fibers [28].

Table 1.1: Spectral bands in single-mode fiber assigned by the International Telecommunication Union. From [12, 26].

Band	Description	Range [nm]	Bandwidth [THz]
O-band	Original	1260 – 1360	17.5
E-band	Extended	1360 – 1460	15.1
S-band	Short wavelength	1460 – 1530	9.4
C-band	Conventional	1530 – 1565	4.4
L-band	Long wavelength	1565 – 1625	7.1
U-band	Ultra-long wavelength	1625 – 1675	5.5

1.3 Multi-Band WDM and SDM Systems

In the linear transmission regime, the fiber-optic channel can be modeled as an AWGN channel, whose capacity is given by the well-known Shannon formula [32]. The full exploitation of the fiber channel capacity requires leveraging the five physical dimensions available in optical fibers, namely *time*, *frequency*, *quadrature*, *polarization*, and *space*. In this regime, the capacity formula for a fiber supporting N spatial dimensions, each with two orthogonal polarizations, is given by

$$C = N \cdot B \cdot 2 \cdot \log_2 (1 + \text{SNR}), \tag{1.1}$$

where B is the system bandwidth in hertz (Hz), and the logarithmic term, which depends on the signal-to-noise ratio (SNR), describes the maximum achievable SE of a single-polarization complex optical signal.

All the attempts to enhance the SNR by reducing amplifier noise, lowering fiber loss, or mitigating fiber nonlinearities, only yield logarithmic (and thus minor) improvements. In contrast, increasing the system bandwidth (B), or equivalently the number of parallel spatial paths (N), provides a linear increase in system capacity. For instance, deploying two parallel systems results in a two-fold capacity increase, whereas achieving an equivalent gain would require a 12.3 dB (i.e., 17 times) increase in SNR.

1.3.1 Multi-Band Wavelength-Division Multiplexing Transmission

As mentioned before, increasing the system bandwidth (B) provides a linear increase in system capacity, provided that the underlying system components can support such

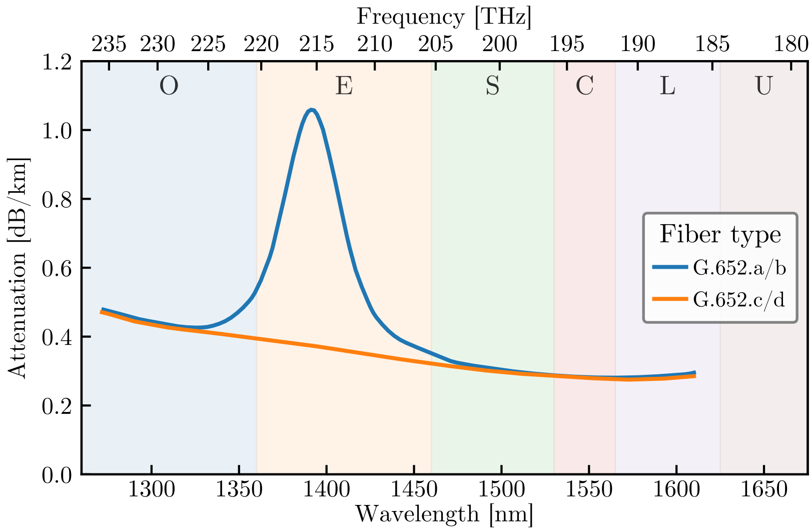

Figure 1.5: Maximum attenuation of standard single-mode fibers (G.652a/b) and zero water peak fibers (G.652c/d) as a function of wavelength (bottom x-axis) and frequency (top x-axis), for the different optical transmission bands. The high attenuation peak around 1380 nm in G.652a/b fibers is characteristic of hydroxyl (OH)-group absorption of light within the fiber. After [12, Fig. 1.8].

spectral extension. As an example, Fig. 1.5 illustrates typical wavelength-dependent attenuation coefficients across the low-loss spectral window of commercial optical fibers, while also highlighting the optical transmission bands specified by the International Telecommunication Union (ITU) [26] and summarized in Table 1.1. From Table 1.1, a bandwidth increase by approximately a factor of 12 can be achieved when operating deployed fibers from the O-band up to the U-band (1260 nm–1675 nm, i.e., 56 THz), rather than using only the C-band (1530 nm–1565 nm, i.e., 4.4 THz), as is done in the overwhelming majority of today's commercially deployed systems. Although, according to Eq. (1.1), such a twelve-fold increase in bandwidth could theoretically lead to a similar capacity increase, this is unlikely in practice due to several fundamental and implementation-related limitations typical of ultra-wideband systems [33]. In realistic conditions, a capacity increase by a factor of five is more feasible, as also demonstrated in [9, 34]. Some of the main limiting factors include higher fiber loss and the lower efficiency (i.e., higher noise) of amplifiers outside of the C-band. Moreover, since it is unlikely that a single amplifier can cover all bands, band-couplers are typically required to multiplex and de-multiplex the signals of different bands, introducing additional performance penalties. Stimulated Raman scattering (SRS), a nonlinear phenomenon that transfers power from shorter to longer wavelengths, is another impairment particularly relevant in multi-band systems (see also

Section 2.4.3).

From these considerations, it becomes evident that bandwidth extension is attractive only for a limited number or specific use cases, and that wavelength parallelism does not represent true parallelism in the sense that different subsystems are used rather than a single system replicated multiple times – a key aspect to bring down costs through integration and volume production [11]. Although multi-band WDM systems can indeed provide a short-term capacity increase for already deployed fiber cables – with the deployment of new optical components being considerably cheaper than laying new fibers – they can not meet the long-term, cost-effective capacity scaling requirements needed for growth factors of 100 and even 1000.

1.3.2 Space-Division Multiplexing Transmission

As evident from the previous discussions on the limitations of bandwidth scaling, increasing capacity through spatial parallelization (N), which provides a linear increase according to Eq. (1.1), represents the most promising long-term approach to substantially scale system capacities, complementing multi-band WDM. Moreover, SDM does not necessarily require the deployment of novel optical fiber types, as long as the spatial dimension is exploited to reduce costs through integration. For instance, in submarine systems, massive SDM implementations with approximately 50 parallel fibers per direction enables higher-capacity and lower-cost systems, due to the lower SE required by such system architectures [11, 35–37].

A schematic of the main fiber types suitable for SDM is illustrated in Fig. 1.6. Single-mode fibers, illustrated in Fig. 1.6(a), represent the most basic form of SDM fibers, as they do not require the deployment of new fiber types. In fact, multiple SMFs can be grouped into bundles and can be used in parallel to take advantage of the spatial dimension while relying on commercially available standard fibers. However, integration remains one of the most effective ways to reduce the overall system cost, as seen across many other technologies (e.g., multi-core processors). In optical communication systems, integration can be introduced across all its subsystems, such as transponder arrays and optical switch arrays. In particular, novel fiber types can bring integration down to the transmission medium level, providing multiple parallel transmission paths within a more compact fiber structure.

Multi-mode fibers, illustrated in Fig. 1.6(b), are designed to guide multiple spatial modes co-propagating within a single fiber core, while maintaining the standard 125 µm cladding diameter of SMFs. For example, a core diameter of 28 µm supports the propagation of 15 fiber modes [38], whereas a 50 µm core can guide approximately

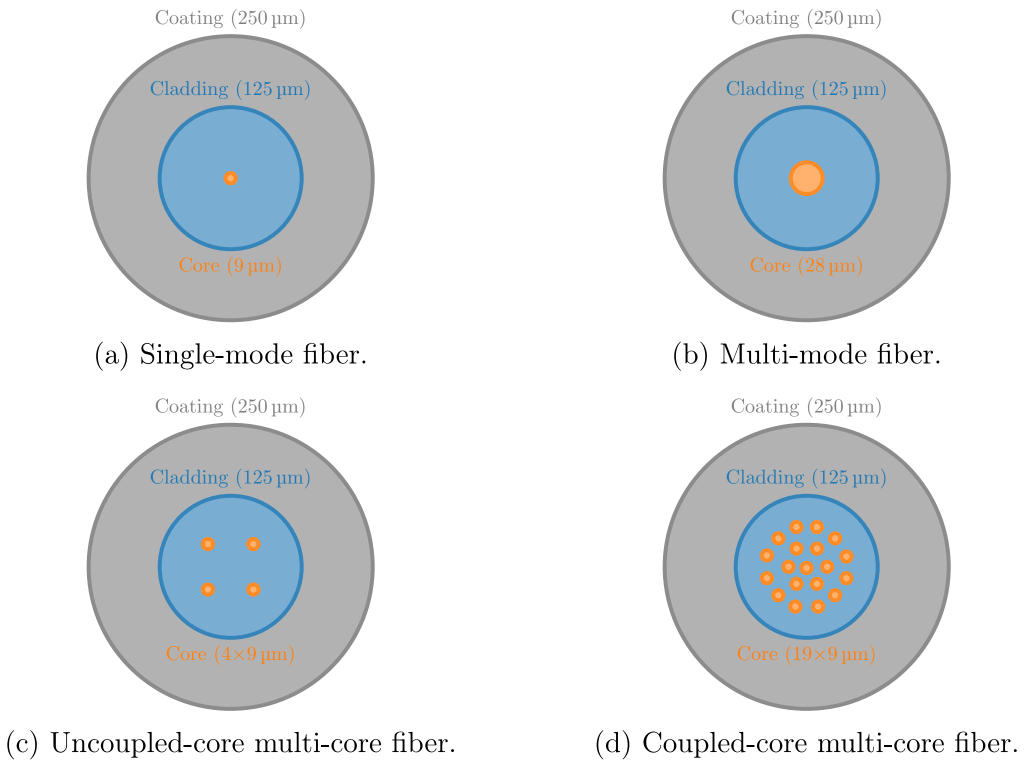

Figure 1.6: Schematic of different fiber types suitable for space-division multiplexing (SDM). (a) Single-mode fibers grouped into bundles represent the most basic form of an SDM system. (b) Multi-mode fibers support multiple spatial modes co-propagating within a single enlarged core. (c) Uncoupled-core multi-core fibers contain multiple single-mode cores within a common fiber cladding, spaced sufficiently apart to ensure negligible inter-core interference. (d) Coupled-core multi-core fibers also contain multiple single-mode cores within a common fiber cladding, but they are spaced closely enough to experience strong inter-core coupling. After [12, Fig. 1.9].

55 fiber modes [39, 40]. For different reasons, fibers guiding up to hundreds of modes have been used for many years in early short-reach optical communication links (on the order of a few kilometers) employing IM/DD [41], mainly due to their practical advantages over SMFs at the time. In fact, their larger core diameter made light coupling inside the fiber easier and relaxed the alignment tolerances during splicing and connectorization processes. Moreover, MMFs enabled the use of cheaper light sources in the 850 nm range, such as light emitting diodes (LEDs), rather than expensive lasers required by SMFs, while also simplifying manufacturing and installation. However, as transmission distances and data rates started to increase in the early 1980s, MMFs were gradually replaced by SMFs, due to the suppression of modal dispersion (MD) in the latter. The interest in such fibers reemerged after the mid-2000s in the context of SDM, with the goal of individually addressing all the supported

fiber modes [42]. Notably, MMFs intended for SDM, and designed to have improved modal properties, have recently been used to demonstrate transmission capacities exceeding 1 Pb/s both in laboratory settings [43–45] and, within this thesis work, after field-deployment (see Chapter C1).

Multi-core fibers were first introduced in 1979 [46, 47]. Given their many degrees of freedom, they can be divided into two main categories depending on whether there is weak or strong interaction between cores, generally referred to as inter-core coupling or inter-core crosstalk (IC-XT). Specifically, uncoupled-core multi-core fibers (UC-MCFs) exhibit very week inter-core coupling (i.e., negligible IC-XT), whereas coupled-core multi-core fibers (CC-MCFs) are purposely designed to ensure strong coupling between cores. In general, and similarly to MMFs, MCFs restarted to gain interest after the mid-2000s as strong candidates to overcome the capacity limit of current optical communication systems with SDM [48]. Uncoupled-core multi-core fibers, also referred to as weakly-coupled multi-core fibers (WC-MCFs) [49] and illustrated in Fig. 1.6(c), were introduced in 1994 [50], and have since become one of the strongest candidates for next-generation SDM transmission medium. In UC-MCFs, multiple single-mode cores (with diameters of approximately 9 µm) are arranged within a common 125 µm cladding. To ensure negligible inter-core coupling, these cores need to be spaced sufficiently apart. For instance, a core spacing (technically referred to as core pitch) of approximately 40 µm is required for a four-core MCF designed for operation from the O-band up to the L-band, whereas a core pitch of approximately 30 µm is required for an eight-core MCF optimized for operation in the O-band only [51]. Coupled-core multi-core fibers, also referred to as randomly-coupled multi-core fibers (RC-MCFs) [52] and illustrated in Fig. 1.6(d), are purposely designed to enforce strong inter-core coupling, for example by reducing the core pitch. This enables CC-MCFs to simultaneously achieve ultra-low loss and high spatial channel density compared to the other SDM fibers. Moreover, they can significantly suppress the accumulation of both MD [53–55] and mode-dependent loss (MDL) [56–58], which are among the main limiting factors in MMF transmission.

Chapter 2

Lightwave Propagation in Optical Fibers

The previous chapter introduced the reader to the evolution of optical communication systems from the first generation, deployed as early as the 1970s, to the high-capacity coherent optical transmission systems that today carry the huge amount of information generated by the modern society. The fundamental capacity limit of standard single-mode fibers (SMFs) has also been addressed, and two of the most promising approaches to overcoming this limit have also been outlined. This chapter focuses on how optical fibers can be used to convey information.

First, the principle of guiding light in optical fibers is described using ray optics. This is followed by a more rigorous analysis of optical field propagation based on Maxwell's equation, ultimately deriving the well-known characteristic equation of step-index fibers, including its simplification under the regime of weak guidance. The origin of both linear and nonlinear transmission effects are discussed in Sections 2.3 and 2.4. In addition, Section 2.4.3 provides a brief introduction to stimulated Raman scattering (SRS), a nonlinear optical phenomenon that is further detailed in Chapter J1, where its first comprehensive characterization in coupled-core multi-core fibers (CC-MCFs) is reported.

2.1 Optical Fiber Geometry

Optical fibers are made of glass (SIO_2) and are as this as a human hair (approximately 125 µm), which makes them surprisingly flexible. An optical fiber consists of a thin cylindrical strand of glass, the core, surrounded by a cladding whose refractive index is slightly lower than that of the core. Fibers with such an abrupt refractive-index change at the core-cladding interface are known as step-index fibers. Another common

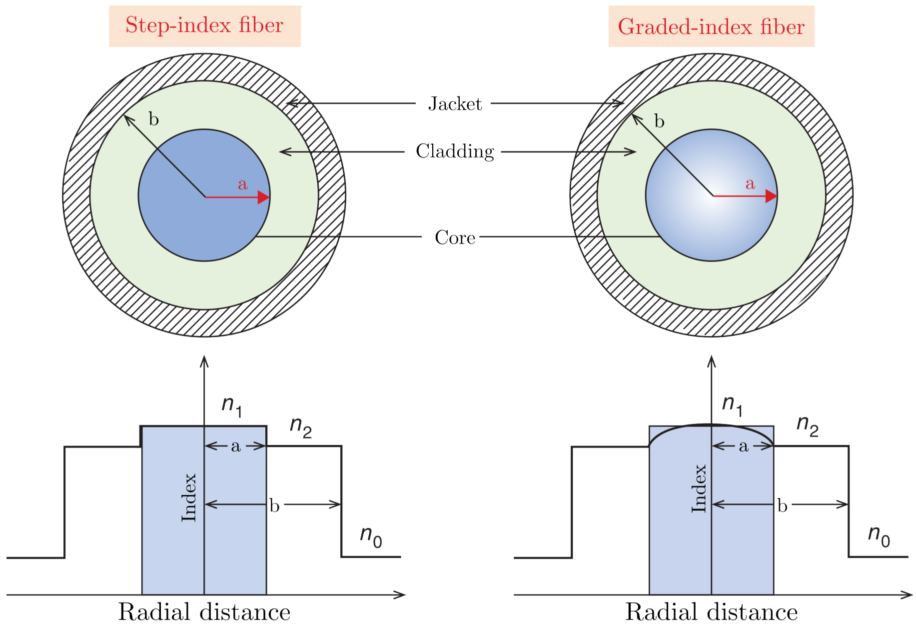

Figure 2.1: Cross sections and refractive index profiles for step-index and graded-index fibers [1].

fiber type is known as graded-index fiber, characterized by a gradual decrease of the refractive index within the core. Figure 2.1 illustrates the cross section and the refractive index profiles of these two types of optical fibers.

The fiber's ability to guide light can be understood intuitively with reference to the effect of total internal reflection (TIR) in the framework of ray optics. For an ideal, straight step-index fiber, the condition for TIR at the core-cladding interface follows directly from Snell's law, illustrated in Fig. 2.2 and described by the relation

$$n_{\text{core}} \sin(\alpha) = n_{\text{clad}} \sin(\beta), \tag{2.1}$$

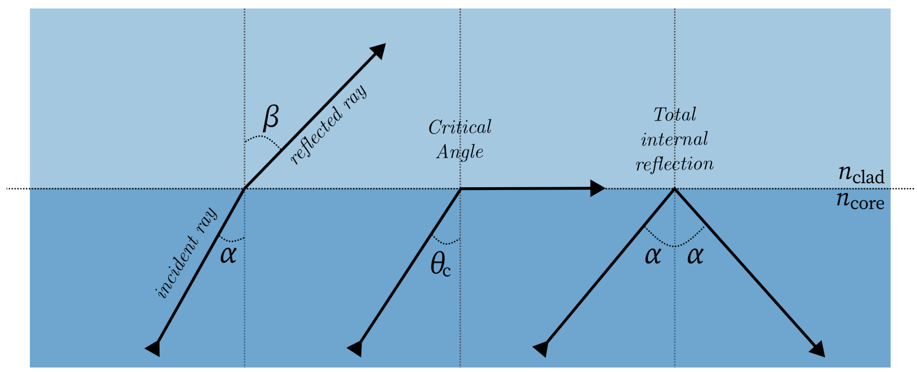

Figure 2.2: Refraction of light, critical angle and total internal reflection at the core-cladding interface of an optical fiber. The core has refractive index n_{core} and the cladding has refractive index n_{clad}, with $n_{\text{core}} > n_{\text{clad}}$.

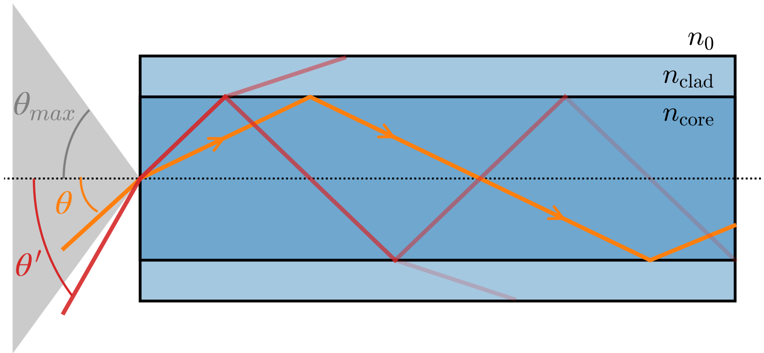

Figure 2.3: Total internal reflection in an ideal, straight step-index fiber, where the core index n_{core} is slightly larger than the cladding index n_{clad}. After [12, Fig. 2.2].

which yields

$$\sin(\beta) = \frac{n_{\text{core}}}{n_{\text{clad}}} \sin(\alpha). \tag{2.2}$$

By imposing $\sin(\beta) > 1$, a condition for which the refracted angle β becomes imaginary, the condition for TIR is found to be given by $\alpha > \arcsin(n_{\text{clad}}/n_{\text{core}}) = \theta_c$. The critical angle θ_c, illustrated in Fig. 2.2, represents the smallest impinging angle at the core-cladding interface for having TIR. With reference to the straight step-index fiber illustrated in Fig. 2.3, light rays entering the fiber with an external incidence angle θ are guided under the condition of TIR if and only if the incident angle θ satisfy

$$\theta \leq \theta_{\text{max}} \simeq \sqrt{n_{\text{core}}^2 - n_{\text{clad}}^2}. \tag{2.3}$$

A more rigorous description is obtained by defining the numerical aperture (NA) of the fiber as the sine of the acceptance-cone half-angle:

$$\text{NA} = \sin(\theta_{\text{max}}) = \sqrt{n_{\text{core}}^2 - n_{\text{clad}}^2} \simeq \bar{n}\sqrt{2\Delta}, \tag{2.4}$$

where $\Delta = (n_{\text{core}} - n_{\text{clad}})/\bar{n}$ and $\bar{n} = (n_{\text{core}} + n_{\text{clad}})/2$, which for $n_{\text{core}}^2 - n_{\text{clad}}^2 \ll 1$ yields the approximation for θ_{max} in Eq. (2.3).

One might aim for an optical fiber with a very large NA to facilitate the coupling of light from a source into the fiber. However, this leads to an undesired effect known as modal dispersion (MD). This phenomenon arises because different rays propagate along paths of different lengths, therefore arriving at the fiber output at different times, even if they enter the fiber simultaneously and travel at the same speed [1]. Because of this effect, an optical pulse may broaden considerably as it propagates through the fiber. The extent of this broadening can be estimated by considering the

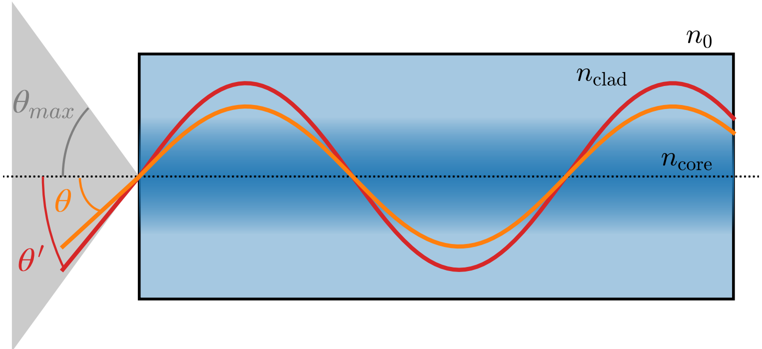

Figure 2.4: Ray trajectories inside a graded-index fiber. The gradual decrease of the refractive index from the core center to the core-cladding interface ensures that rays following different trajectories arrive at the fiber output at nearly the same time. After [12, Fig. 2.4].

shortest and longest ray paths. The shortest path corresponds to the ray entering with an impinging angle $\theta = 0$ and has a length L (fiber length), while the longest path corresponds to $\theta = \theta_{\text{max}}$ and has length $L/\sin(\theta_{\text{max}})$. The resulting MD is

$$\Delta T = T_{\text{max}} - T_{\text{min}} = \frac{1}{v}\left[\frac{L}{\sin(\theta_{\text{max}})} - L\right] = \frac{L}{v}\frac{n_{\text{core}} - n_{\text{clad}}}{n_{\text{clad}}} \simeq \frac{L\Delta}{v}, \tag{2.5}$$

with $v \simeq c/n_{\text{core}}$ the speed of flight inside the fiber core. From Eq. (2.4), increasing Δ improves coupling efficiency (larger NA), whereas from Eq. (2.5), decreasing Δ reduces MD. Thus a trade-off needs to be found between acceptance and dispersion.

Graded-index fibers help reduce the impact of MD because their refractive index decreases gradually from its maximum value n_{core} at the core center to its minimum value n_{clad} at the core-cladding interface. This effect can be understood by analyzing the ray trajectories inside a graded-index fiber, as illustrated in Fig. 2.4. Oblique rays spend a larger portion of their path in regions of lower refractive index than n_{core}, where they travel faster. As a result, rays that follow different trajectories may arrive at the fiber output at nearly the same time.

2.2 Fiber Modes

A rigorous study of propagation in optical fibers requires an understanding of fiber modes. As with all electromagnetic phenomena, the propagation of the electromagnetic field in optical fibers is governed by Maxwell's equations, which in this context take the form

$$\nabla \cdot \vec{\boldsymbol{d}} = 0, \tag{2.6}$$

$$\nabla \cdot \vec{\boldsymbol{h}} = 0, \tag{2.7}$$

$$\nabla \times \vec{\boldsymbol{e}} = -\mu_0 \mu_r \frac{\partial \vec{\boldsymbol{h}}}{\partial t}, \tag{2.8}$$

$$\nabla \times \vec{\boldsymbol{h}} = \frac{\partial \vec{\boldsymbol{d}}}{\partial t}, \tag{2.9}$$

where $\vec{\boldsymbol{e}}$ and $\vec{\boldsymbol{h}}$ denote the electric and magnetic fields, respectively, and $\vec{\boldsymbol{d}} = \epsilon_0 \vec{\boldsymbol{e}} + \vec{\boldsymbol{p}}$ is the dielectric displacement field vector, with $\vec{\boldsymbol{p}}$ denoting the polarization density vector. Assuming that, in silica glass, polarization follows changes in the electric field instantaneously, the polarization vector can be approximated as

$$\vec{\boldsymbol{p}} = \epsilon_0 \left(\chi^{(1)} \vec{\boldsymbol{e}} + \chi^{(2)} \vec{\boldsymbol{e}}^2 + \chi^{(3)} \vec{\boldsymbol{e}}^3 + \dots \right). \tag{2.10}$$

Here $\chi^{(k)}$ is the k-th order dielectric susceptibility, which is in general a tensor of rank $k+1$. In the reference case of an ideally straight fiber with instantaneous material response, the polarization vector reduces to $\vec{\boldsymbol{p}} = \epsilon_0 \chi^{(1)} \vec{\boldsymbol{e}}$, where $\chi^{(1)}$ is the (linear) dielectric susceptibility, and $\vec{\boldsymbol{d}} = \epsilon_0 \epsilon_r \vec{\boldsymbol{e}}$, where $\epsilon_r = \chi^{(1)} + 1$ is the relative dielectric constant. Inside optical fibers, the relative permittivity is related to the refractive index through $\epsilon_r = n^2$ and $\mu_r = 1$. By defining the Fourier Transform pair as

$$F(\omega) = \int_{-\infty}^{+\infty} f(t)\, e^{i\omega t}\, dt, \quad f(t) = \int_{-\infty}^{+\infty} F(\omega)\, e^{-i\omega t}\, \frac{\mathrm{d}\omega}{2\pi}, \tag{2.11}$$

Maxwell's equations in the frequency domain take the form

$$\nabla \cdot \vec{\boldsymbol{D}} = 0, \tag{2.12}$$

$$\nabla \cdot \vec{\boldsymbol{H}} = 0, \tag{2.13}$$

$$\nabla \times \vec{\boldsymbol{E}} = i\omega\mu_0 \vec{\boldsymbol{H}}, \tag{2.14}$$

$$\nabla \times \vec{\boldsymbol{H}} = -i\omega \vec{\boldsymbol{D}}, \tag{2.15}$$

with $\vec{\boldsymbol{D}} = \epsilon_0 \epsilon_r \vec{\boldsymbol{E}}$ in the case of an ideal, straight fiber. It is important to note that Eq. (2.12) is strictly valid only for step-index fibers, whereas for graded-index fibers it reduces to $\nabla \cdot \left(n^2 \vec{\boldsymbol{E}} \right) \simeq 0$.

While Eqs. (2.12) to (2.15) provide the general framework for studying wave propagation in optical fibers, fiber modes can be conveniently studied by considering a monochromatic excitation of a single fiber mode ($\omega = \omega_0$). A fiber mode is characterized by a transverse field distribution that remains unchanged during propagation, such that a solution to the general equations can be written in the form

$$\vec{\boldsymbol{E}}(x, y, z, \omega)\big|_{\omega=\omega_0} = A(\omega_0)\, \vec{\boldsymbol{F}}(x, y, \omega_0)\, e^{i\beta(\omega_0)z}, \tag{2.16}$$

$$\vec{\boldsymbol{H}}(x, y, z, \omega)\big|_{\omega=\omega_0} = A(\omega_0)\, \vec{\boldsymbol{G}}(x, y, \omega_0)\, e^{i\beta(\omega_0)z}, \tag{2.17}$$

where z is the longitudinal coordinate along the fiber, β is the propagation constant in the fiber, and $A(\omega_0)$ is the mode excitation at the fiber input. The functions $\vec{\boldsymbol{F}}$ and $\vec{\boldsymbol{G}}$ describe the transverse profiles of the electric and magnetic fields, respectively, each consisting of three components whose dependence on the x and y coordinates remains unchanged during propagation (propagation eigenstates), while their dependence on the longitudinal coordinate z is determined by the $e^{i\beta(\omega_0)z}$ term in Eqs. (2.16) and (2.17). The frequency dependence for the latter quantities is implicitly assumed in what follows.

The z-components of the electric and magnetic mode profiles play a special role in mode analysis, since all other components can be expressed as a function of them. To see this, it is convenient to decompose the lateral profiles as $\vec{\boldsymbol{F}} = \vec{\boldsymbol{F}}_t + F_z\hat{\boldsymbol{z}}$ and $\vec{\boldsymbol{G}} = \vec{\boldsymbol{G}}_t + G_z\hat{\boldsymbol{z}}$, where the subscript t denotes the transverse components laying in the fiber cross-section (the (x, y) plane). Substituting $\vec{\boldsymbol{E}} = \vec{\boldsymbol{F}}e^{i\beta z}$ and $\vec{\boldsymbol{H}} = \vec{\boldsymbol{G}}e^{i\beta z}$ in Eq. (2.14) one obtains

$$\begin{aligned}\nabla \times \vec{\boldsymbol{E}} &= \left(\nabla_t + \hat{\boldsymbol{z}}\frac{\partial}{\partial z}\right) \times \left(\vec{\boldsymbol{F}}_t e^{i\beta z} + \hat{\boldsymbol{z}} F_z e^{i\beta z}\right) \\ &= \left[\nabla_t \times \vec{\boldsymbol{F}}_t + (\nabla_t F_z) \times \hat{\boldsymbol{z}} + i\beta\hat{\boldsymbol{z}} \times \vec{\boldsymbol{F}}_t\right] e^{i\beta z} \\ &= i\omega\mu_0 \left(\vec{\boldsymbol{G}}_t + G_z\hat{\boldsymbol{z}}\right) e^{i\beta z}.\end{aligned} \tag{2.18}$$

Multiplying both sides of Eq. (2.18) by $\hat{\boldsymbol{z}}\times$, the latter expression reduces to

$$\nabla_t F_z - i\beta\vec{\boldsymbol{F}}_t = i\omega\mu_0\hat{\boldsymbol{z}} \times \vec{\boldsymbol{G}}_t, \tag{2.19}$$

and, by a similar substitution to Eq. (2.15)

$$\nabla_t G_z - i\beta\vec{\boldsymbol{G}}_t = -i\omega\epsilon_0\epsilon_\mathrm{r}\hat{\boldsymbol{z}} \times \vec{\boldsymbol{F}}_t. \tag{2.20}$$

From these equations, one can readily obtain

$$\vec{\boldsymbol{F}}_t = \frac{i\beta}{\omega^2\mu_0\epsilon_0\epsilon_\mathrm{r} - \beta^2}\left(\nabla_t F_z - \frac{\omega\mu_0}{\beta}\hat{\boldsymbol{z}} \times \nabla_t G_z\right), \tag{2.21}$$

$$\vec{\boldsymbol{G}}_t = \frac{i\beta}{\omega^2\mu_0\epsilon_0\epsilon_\mathrm{r} - \beta^2}\left(\nabla_t G_z + \frac{\omega\epsilon_0\epsilon_\mathrm{r}}{\beta}\hat{\boldsymbol{z}} \times \nabla_t F_z\right), \tag{2.22}$$

demonstrating the assumption on the key role of the z-components of the electric and magnetic mode profiles.
The solution for F_z is obtained by applying the curl of Eq. (2.14) and using Eq. (2.15), which leads to the well-known Helmholtz equations, fundamental for the analysis of fiber modes

$$\nabla^2 \vec{\boldsymbol{E}} + k^2 n^2 \vec{\boldsymbol{E}} = 0, \tag{2.23}$$

$$\nabla^2 \vec{\boldsymbol{H}} + k^2 \vec{\boldsymbol{H}} = 0, \tag{2.24}$$

where $k^2 = \omega^2/c^2$ is the propagation constant in vacuum and c is the speed of light. As in the previous case, Eq. (2.23) is strictly valid only for step-index fibers, whereas for graded-index fibers it provides a good approximation when the refractive index profile varies smoothly and the refractive index difference between core and cladding is small. Substituting $\vec{\boldsymbol{E}} = \vec{\boldsymbol{F}} e^{i\beta z}$ and $\vec{\boldsymbol{H}} = \vec{\boldsymbol{G}} e^{i\beta z}$ in Eqs. (2.23) and (2.24) one readily obtains

$$\nabla^2 \vec{\boldsymbol{F}} + \left(k^2 n^2 - \beta^2\right) \vec{\boldsymbol{F}} = 0, \tag{2.25}$$

$$\nabla^2 \vec{\boldsymbol{G}} + \left(k^2 n^2 - \beta^2\right) \vec{\boldsymbol{G}} = 0. \tag{2.26}$$

The component F_z is the solution of Eq. (2.25) with F_z replacing $\vec{\boldsymbol{F}}$. Given the circular symmetry of the optical fiber, $F_z(x, y)$ can be expressed in polar coordinates as $F_z(\rho, \phi)$. Applying separation of variables $F_z(\rho, \phi) = \Psi(\rho) f(\phi)$, and substituting into Eq. (2.25) yields

$$\frac{\mathrm{d}^2\Psi}{\mathrm{d}\rho^2} + \frac{1}{\rho}\frac{\mathrm{d}\Psi}{\mathrm{d}\rho} + \left(k^2 n^2 - \beta^2 - \frac{\ell^2}{\rho^2}\right)\Psi = 0, \tag{2.27}$$

$$\frac{\mathrm{d}^2 f}{\mathrm{d}\phi^2} + \ell^2 f = 0, \tag{2.28}$$

where ℓ is an integer constant introduced by the separation of variables, since $f = \exp\left(\pm i\ell\phi\right)$ must be periodic with a period of 2π. At this point, determining Ψ requires specifying the refractive-index profile of the fiber.

2.2.1 Step-Index Fiber Modes

As illustrated in Fig. 2.3, a step-index fiber has the refractive index n equal to n_{core} in the core and to n_{clad} in the cladding, with $n_{\text{core}} > n_{\text{clad}}$. In this case, Eq. (2.27) takes the form of a Bessel equation whose solution depends on the sign of $k^2n^2 - \beta^2$. When

$$h^2 = k^2 n_{\text{core}}^2 - \beta^2 > 0, \tag{2.29}$$

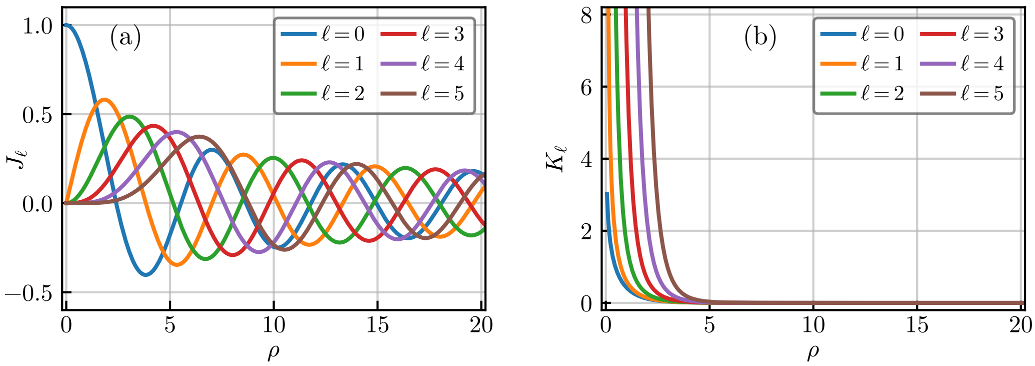

Figure 2.5: (a) Bessel function of first kind and order ℓ and (b) modified Bessel function of second kind and order ℓ.

Equation (2.27) represents a Bessel function of the first kind and order ℓ (J_ℓ) which does not have singularities in $\rho = 0$ and is therefore suitable for the core region ($n = n_{\text{core}}$). Conversely, when

$$q^2 = \beta^2 - k^2 n_{\text{clad}}^2 > 0, \tag{2.30}$$

Equation (2.27) is a modified Bessel function of the second kind and order ℓ (K_ℓ) which does not diverge for $\rho \to +\infty$ and is therefore suitable for the cladding region ($n = n_{\text{clad}}$). These Bessel functions are illustrated for different orders ℓ in Fig. 2.5. From the expressions of h and q, it is possible to see that $kn_{\text{clad}} < \beta < kn_{\text{core}}$. Given the fiber core radius a, the radial function $\Psi(\rho)$ can thus be expressed as

$$\Psi(\rho) = \begin{cases} J_\ell(h\rho), & \rho < a, \\ K_\ell(q\rho), & \rho > a. \end{cases} \tag{2.31}$$

Having $F_z(\rho, \phi) = \Psi(\rho)e^{-i\ell\phi}$ and $G_z(\rho, \phi) = \Psi(\rho)e^{i\ell\phi}$, with $\Psi(\rho)$ given in Eq. (2.31), substitution in Eqs. (2.16) and (2.17) yields

$$E_z(\rho, \phi, z) = \begin{cases} f_a \frac{J_\ell(h\rho)}{J_\ell(ha)} e^{i(\beta z - \ell\phi)}, & \rho < a, \\ f_a \frac{K_\ell(h\rho)}{K_\ell(ha)} e^{i(\beta z - \ell\phi)}, & \rho > a, \end{cases} \tag{2.32}$$

and

$$H_z(\rho, \phi, z) = \begin{cases} g_a \frac{J_\ell(h\rho)}{J_\ell(ha)} e^{i(\beta z + \ell\phi)}, & \rho < a, \\ g_a \frac{K_\ell(h\rho)}{K_\ell(ha)} e^{i(\beta z + \ell\phi)}, & \rho > a. \end{cases} \tag{2.33}$$

Furthermore, starting from $F_z(\rho, \phi)$ and $G_z(\rho, \phi)$, the components of $\vec{\boldsymbol{F}}_t$ and $\vec{\boldsymbol{G}}_t$ can be obtained directly by applying Eqs. (2.21) and (2.22). It can be verified that by doing so, $\vec{\boldsymbol{F}}_t$ and $\vec{\boldsymbol{G}}_t$ take the form of a linear combination of the two constants f_a

and g_a.

Imposing the boundary conditions for the electromagnetic fields at the core-cladding interface shows that the only condition to be satisfied is the continuity of the ϕ-component of $\vec{\boldsymbol{F}}_t$ and $\vec{\boldsymbol{G}}_t$ at the core-cladding interface ($\rho = a$). This requirements leads to a 2×2 homogeneous linear system for f_a and g_a. A non-trivial solution exists only when the determinant of the coefficients matrix of the system is zero, yielding the well-known characteristic equation of optical fibers [59]

$$\begin{aligned}\ell^2 \left(\frac{\beta}{k}\right) \left[\left(\frac{1}{ha}\right)^2 + \left(\frac{1}{qa}\right)^2\right]^2 = &\left[\frac{n_{\text{core}}^2 J_\ell'(ha)}{haJ_\ell(ha)} + \frac{n_{\text{clad}}^2 K_\ell'(qa)}{qaK_\ell(qa)}\right] \\ &\times \left[\frac{J_\ell'(ha)}{haJ_\ell(ha)} + \frac{K_\ell'(qa)}{qaK_\ell(qa)}\right].\end{aligned} \tag{2.34}$$

This equation is typically solved numerically for β.

Starting from the expressions $h^2 = k^2 n_{\text{core}}^2 - \beta^2$ and $q^2 = \beta^2 - k^2 n_{\text{clad}}^2$, one can notice that the quantity

$$V = \sqrt{(ha)^2 + (qa)^2} = a\sqrt{n_{\text{core}}^2 - n_{\text{clad}}^2}k, \tag{2.35}$$

only depends on the fiber parameters and is referred to as normalized frequency. This quantity is useful for solving Eq. (2.34) numerically, as for example one can write

$$qa = \sqrt{V^2 - (ha)^2}, \qquad ha < V. \tag{2.36}$$

Moreover, since both $ha < V$ and $qa < V$, increasing V allows more solutions to exist, each corresponding to different fiber modes.

Modes with $\ell = 0$

When $\ell = 0$, Eq. (2.34) simplifies to

$$\left[\frac{n_{\text{core}}^2 J_0'(ha)}{haJ_0(ha)} + \frac{n_{\text{clad}}^2 K_0'(qa)}{qaK_0(qa)}\right] \left[\frac{J_0'(ha)}{haJ_0(ha)} + \frac{K_0'(qa)}{qaK_0(qa)}\right] = 0. \tag{2.37}$$

In this equation, only one of two brackets can be zero (not both simultaneously) for an electromagnetic field to propagating inside the fiber. This implies that, in the more general case, transverse electro-magnetic (TEM) modes do not exist in optical fibers:

- If the first bracket is zero, the mode is a transverse magnetic (TM) mode;
- If the first bracket is zero, the mode is a transverse electric (TE) mode.

In both cases, no TE or TM modes propagate inside the fiber when the normalized frequency $V < 2.405$.

Modes with $\ell > 0$

When $\ell > 0$, modes are labeled $\mathrm{HE}_{\ell,m}$ or $\mathrm{EH}_{\ell,m}$ depending on whether the magnetic (H) or the electric field (E) dominates, respectively. The index m denotes the solution order related for a given ℓ. In this case, a particular mode, $\mathrm{HE}_{1,1}$, can propagate inside the fiber even when $V < 2.405$. Consequently, the $\mathrm{HE}_{1,1}$ mode is referred to as the *fundamental mode*. An optical fiber that supports only the fundamental mode is referred to as SMF. In general, to ensure single-mode operation at a specific wavelength one typically designs the fiber such that $V < 2.405$, a condition which can be achieved by reducing the fiber core radius a or reducing the numerical aperture $\sqrt{n_{\text{core}}^2 - n_{\text{clad}}^2}$.

2.2.2 Linearly Polarized Modes

As described in the previous section, extracting the characteristics of fiber modes directly from their analytical expressions is rather complicated. However, this problem is greatly simplified in the practically relevant regime of weak guidance of the optical fiber [60]. A fiber is said to be weakly guiding when the refractive-index difference between core and cladding is very small, $\Delta n = n_{\text{core}} - n_{\text{clad}} \ll n_{\text{core,clad}}$, typically with $\Delta n / n_{\text{core,clad}}$ of the order of 0.1%. The key observations of this regime are:

1. The longitudinal components of the mode fields are much smaller than the corresponding transverse components, that is
$$\begin{aligned} |F_z| &\ll |\vec{\boldsymbol{F}}_t|, \\ |G_z| &\ll |\vec{\boldsymbol{G}}_t|. \end{aligned} \tag{2.38}$$
2. The mode polarization is approximately linear and nearly constant across the entire fiber section.

Following an approach similar to that presented in the previous section for the general case, one can obtain the weak-guidance equivalent of Eq. (2.34) as

$$ha \frac{J_{\ell+1}(ha)}{J_\ell(ha)} = \sqrt{V^2 - (ha)^2} \frac{K_{\ell+1}\left(\sqrt{V^2 - (ha)^2}\right)}{K_\ell\left(\sqrt{V^2 - (ha)^2}\right)}. \tag{2.39}$$

The solutions of Eq. (2.39) define the linearly polarized (LP) modes, denoted as $\mathrm{LP}_{\ell,n}$, where n denotes the solution order for a given ℓ. For $\ell = 0$, $\mathrm{LP}_{0,n}$ modes are two-fold degenerate (with respect to polarization) whereas for $\ell > 0$, $\mathrm{LP}_{\ell,n}$ modes are four-fold

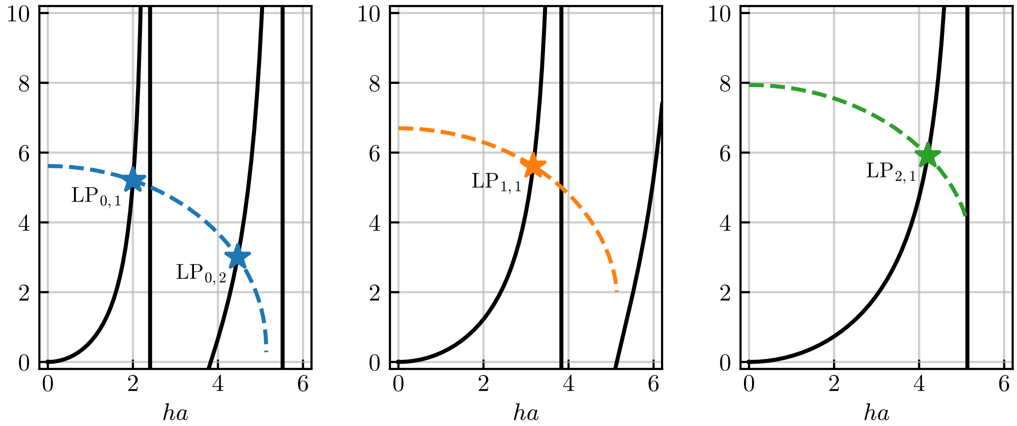

Figure 2.6: A graphical approach for solving Eq. (2.34) in the case of an optical fiber with $a = 9.88\,\mu$m, $n_{\text{core}} = 1.4692$, $n_{\text{clad}} = 1.4636$, $\lambda = 1550\,$nm and $V = 5.135$.

degenerate (with respect to polarization and to their dependence on ϕ).
Equation (2.39) always admits a solution for $\ell = 0$. Therefore, under the weak-guidance regime, the fundamental mode is the LP$_{0,1}$ mode. Figure 2.6 shows a graphical approach for solving Eq. (2.39). The black curves correspond to the left-hand side of the equation while the blue, orange and green curves illustrate the right-hand side of the equation for different values of ℓ. Before proceeding to the discussion of the main phenomena affecting pulse propagation in fibers, it is worth noting that in an SMF the electromagnetic field can always be expressed as a superposition of an x-polarized LP$_{0,1x}$ mode and a y-polarized LP$_{0,1y}$ mode. This property becomes especially interesting when introducing the Jones formalism for analyzing the light polarization state in optical fibers, as discussed in Section 2.3.4.

2.3 Linear Propagation Effects in Fibers

The previous section reviewed how light is guided in optical fibers and described the optical field distributions they support based on the fiber's physical parameters. However, in practice, the optical field evolves as it propagates along the fiber. This section examines some of the main linear propagation effects that alter, and potentially distort, the optical field during transmission.

2.3.1 Waveguide and Material Dispersion

As introduced in Section 2.1, MD in multi-mode fibers (MMFs) can cause significant pulse broadening due to the different speeds associated with the different supported modes. In SMFs, this form of dispersion disappears because the optical pulse propagates through a single mode that carries the whole energy. However, pulse broadening does not completely disappear. In fact, even in the ideal case of a perfectly uniform fiber – characterized by the absence of perturbations to its geometrical structure – distortion of the propagating waveform arises from the frequency dependence of the propagation constant, $\beta(\omega)$. This phenomenon is known as *waveguide dispersion* and is typically accompanied by additional dispersion originating from the frequency dependence of the fiber refractive index, $n(\omega)$, known as *material dispersion* [1, 61]. The combination of waveguide and material dispersion results into the phenomenon of group-velocity dispersion (GVD), often referred to simply as chromatic dispersion (CD), which is of particular interest when determining how optical pulses evolve during propagation in optical fibers.

2.3.2 Chromatic Dispersion

To build an intuitive understanding of CD, one can consider the transmission of a baseband signal $e_{\text{in}}(t)$ through an optical fiber. At the fiber input, this signal modulates a laser source at the optical carrier frequency ω_0, which for the present analysis can be regarded simply as an oscillator of the form $e^{-i\omega_0 t}$. The modulation process can then be expressed as

$$e_{\text{in}}(t)\, e^{-i\omega_0 t} \quad \overset{\mathscr{F}}{\longleftrightarrow} \quad E_{\text{in}}(\omega - \omega_0) \tag{2.40}$$

where $E_{\text{in}}(\omega - \omega_0)$ denotes the spectrum of the modulated signal, centered at the carrier frequency ω_0 and having a bandwidth $B \ll \omega_0$.

Substituting $A(\omega) = E_{\text{in}}(\omega - \omega_0)$ in Eq. (2.16), the electric field propagating inside the fiber can be expressed as

$$\vec{\boldsymbol{E}}(x, y, z, \omega) = E_{\text{in}}(\omega - \omega_0)\, \vec{\boldsymbol{F}}(x, y, \omega)\, e^{i\beta(\omega)z}. \tag{2.41}$$

Transforming back to the time domain using Eq. (2.11) yields

$$\begin{aligned} \vec{\boldsymbol{e}}(x, y, z, t) &= \int_{-\infty}^{+\infty} E_{\text{in}}(\omega - \omega_0)\, \vec{\boldsymbol{F}}(x, y, \omega)\, e^{i\beta(\omega)z} e^{-i\omega t}\, \frac{\mathrm{d}\omega}{2\pi} \\ &\simeq \vec{\boldsymbol{F}}(x, y, \omega_0) \int_{-\infty}^{+\infty} E_{\text{in}}(\omega - \omega_0)\, e^{i\beta(\omega)z} e^{-i\omega t}\, \frac{\mathrm{d}\omega}{2\pi}, \end{aligned} \tag{2.42}$$

where the last approximation follows from the fact that $\vec{\boldsymbol{F}}(x, y, \omega)$ is almost constant within the signal bandwidth, that is

$$\vec{\boldsymbol{F}}(x, y, \omega) \simeq \vec{\boldsymbol{F}}(x, y, \omega_0), \tag{2.43}$$

for $B \ll \omega_0$.

By using a first-order Taylor expansion of $\beta(\omega)$ within the signal bandwidth, i.e.,

$$\beta(\omega) \simeq \beta_0 + \beta_1 (\omega - \omega_0), \qquad \beta_i = \frac{\partial^i \beta}{\partial \omega^i}|_{\omega=\omega_0}, \tag{2.44}$$

and performing some straightforward algebra, Eq. (2.42) reduces to

$$\vec{\boldsymbol{e}}(x, y, z, t) = e_{\text{in}}(t - \beta_1 z)\, \vec{\boldsymbol{F}}(x, y, \omega_0)\, e^{i(\beta_0 z - \omega_0 t)}, \tag{2.45}$$

from which the following two important quantities can be identified.

- **Phase accumulation:**

$$\phi_a = \beta_0 z, \qquad v_p = \frac{\omega_0}{\beta_0} = \frac{c}{n_{\text{eff}}}, \tag{2.46}$$

  representing the phase shift (and the corresponding phase velocity) experienced by the propagating envelope or, equivalently, to the spectral component centered at frequency ω_0.

- **Group delay:**

$$t_g = \beta_1 z, \qquad v_g = \frac{1}{\beta_1}, \tag{2.47}$$

  representing the delay (and the corresponding group velocity) associated to the propagating envelope.

By considering a second-order Taylor expansion of $\beta(\omega)$, i.e.,

$$\beta(\omega) \simeq \beta_0 + \beta_1 (\omega - \omega_0) + \frac{1}{2}\beta_2 (\omega - \omega_0)^2, \tag{2.48}$$

the integral in Eq. (2.42) reduces to

$$\vec{\boldsymbol{e}}(x, y, z, t) = \\ = \vec{\boldsymbol{F}}(x, y, \omega_0)\, e^{i(\beta_0 z - \omega_0 t)} \int_{-\infty}^{+\infty} E_{\text{in}}(\omega - \omega_0)\, e^{-i\left[t - \beta_1 z - \frac{\beta_2(\omega - \omega_0) z}{2}\right](\omega - \omega_0)} \frac{\mathrm{d}\omega}{2\pi}, \tag{2.49}$$

suggesting the existence of a frequency-dependent group delay t_g. In other words, this result shows that different spectral components of $\vec{\boldsymbol{E}}(x, y, z, \omega)$ propagate with slightly different group velocities inside the fiber, leading to GVD or CD.

Starting from Eqs. (2.42) and (2.48), it is also possible to obtain the following envelope propagation equation in the time domain

$$\frac{\partial}{\partial z} e(z, t) = i\beta_0 e(z, t) - \beta_1 \frac{\partial}{\partial t} e(z, t) - i\frac{\beta_2}{2}\frac{\partial^2}{\partial t^2} e(z, t). \tag{2.50}$$

For $\beta_2 = 0$, the solution of Eq. (2.50) is given in Eq. (2.45), showing that propagation introduces a phase accumulation $\beta_0 z$ and a group delay $\beta_1 z$. Therefore, the first two terms on the right-hand side of Eq. (2.50) can be removed by applying the transformation

$$e(z,t) = e'(z,\tau)\, e^{i\beta_0 z}, \qquad \tau = t - \beta_1 z, \tag{2.51}$$

which removes the frequency-independent part of the group delay. The resulting propagation equation for $e'(z,\tau)$ becomes

$$\frac{\partial}{\partial z} e'(z,\tau) = -i\frac{\beta_2}{2}\frac{\partial^2}{\partial \tau^2} e'(z,\tau), \tag{2.52}$$

and its solution is readily found in the frequency domain, yielding

$$E(z,\omega) = e^{i\frac{\beta_2}{2}\omega^2 z} E(0,\omega), \tag{2.53}$$

where primes have been dropped for simplicity.

The coefficient β_2 describes GVD or CD, as implied by

$$\beta_2 = \frac{\partial \beta_1}{\partial \omega} = -\frac{1}{v_g^2}\frac{\partial v_g}{\partial \omega}. \tag{2.54}$$

An intuitive understanding of this effect can be developed by considering a signal of bandwidth B propagating inside the fiber, so that different narrow spectral sub-bands of the signal travel at different group velocities. As an example, let's consider the particular case of $\beta_2 < 0$, which implies

$$\frac{\partial v_g}{\partial \omega} > 0, \tag{2.55}$$

so that group-velocity increases with frequency. In this situation, the signal undergoes temporal spreading. The extent of pulse broadening accumulated over a fiber of length L can be estimated as the delay difference between the slowest and fastest spectral components, that is

$$\begin{aligned} \Delta T &= T_{\text{slowest}} - T_{\text{fastest}} = \\ &= \frac{L}{v_g(\omega_0 - B/2)} - \frac{L}{v_g(\omega_0 + B/2)} \\ &= L\left[\beta_1(\omega_0 - B/2) - \beta_1(\omega_0 + B/2)\right] \\ &\simeq -L\beta_2 B = L|\beta_2|B. \end{aligned} \tag{2.56}$$

The parameter β_2 has the unit of [s^2/m] and is generally referred to as chromatic dispersion parameter. A typical value for β_2 in SMFs is $\sim -21\ \mathrm{ps}^2/\mathrm{km}$. In some optical systems the signal bandwidth is expressed in wavelength units rather than frequency and, in such cases, Eq. (2.56) becomes

$$\Delta T = -L\beta_2 \frac{2\pi c}{\lambda^2} B_\lambda = L\left(-\beta_2 \frac{2\pi c}{\lambda^2}\right) B_\lambda = LDB_\lambda, \tag{2.57}$$

where D (unit [ps/(nm · km)]) is the wavelength-domain equivalent dispersion parameter. In SMFs D typically has values of ~ 17 ps/(nm · km). The case described above, where group-velocity increases with frequency ($\beta_2 < 0$), is known as anomalous dispersion and is typical in communication fibers around 1550 nm. The opposite case, where group-velocity decreases with frequency ($\beta_2 > 0$), is known as normal dispersion and is characteristic of some special fibers at 1550 nm, e.g. dispersion compensating fibers (DCF).

The discussion on CD is concluded by introducing third-order dispersion (or, more in general, higher-order dispersion). These effects are usually negligible but become relevant near the zero-dispersion frequency (or wavelength), where $\beta_2 \simeq 0$ (or equivalently $D \simeq 0$). In such cases, a higher-order Taylor expansion of $\beta(\omega)$ is required, introducing additional time-derivative terms in the time-domain propagation equation of Eq. (2.50). When $\beta_2 \simeq 0$, the coefficient β_3 plays a major role in the analysis of CD. It is therefore useful to define the dispersion-slope parameter

$$S = \frac{\mathrm{d}D}{\mathrm{d}\lambda} = \beta_3 \left(\frac{2\pi c}{\lambda^2}\right)^2, \tag{2.58}$$

which characterizes the impact of third-order dispersion, especially over very long propagation distances.

2.3.3 Fiber Loss

Another important phenomenon to consider when dealing with pulse propagation in fibers is fiber loss. In practice, the optical power of a pulse propagating inside a fiber – given by the absolute squared value of the electric filed properly normalized, in the absence of other propagation effects (e.g., CD) – decreases exponentially with distance z. This can be expressed as

$$I(z,t) = I(0,t)\, e^{-\alpha z}. \tag{2.59}$$

Fiber loss is unavoidable and can be understood by examining the polarization vector $\vec{\boldsymbol{P}}(\omega)$ in the frequency domain

$$\vec{\boldsymbol{P}}(\omega) = \epsilon_0 (\epsilon_\mathrm{r} - 1)\, \vec{\boldsymbol{E}}(\omega) = \epsilon_0 \left[n^2(\omega) - 1\right] \vec{\boldsymbol{E}}(\omega) = \epsilon_0 \tilde{\chi}^{(1)}(\omega)\, \vec{\boldsymbol{E}}(\omega). \tag{2.60}$$

In what follows, the superscript $\chi^{(1)}$ is omitted for simplicity. Returning in the time domain, the polarization vector $\vec{\boldsymbol{p}}(t)$ becomes

$$\vec{\boldsymbol{p}}(t) = \epsilon_0 \chi(t) \otimes \vec{\boldsymbol{e}}(t), \tag{2.61}$$

showing that the dielectric susceptibility ($\chi(t)$) acts as the impulse response of the fiber atoms and molecules to the electric field. For $\chi(t)$ to represent an impulse response, it must satisfy the causality constraint, that is

$$\chi(t) = 0, \qquad \text{for } t < 0. \tag{2.62}$$

Imposing this condition when applying the inverse Fourier transform to Eq. (2.60), leads to the conclusion that the real and imaginary parts of the frequency-domain susceptibility, $\tilde{\chi}_{\mathrm{R}}(\omega)$ and $\tilde{\chi}_{\mathrm{I}}(\omega)$, are related to each other through the Kramers-Kronig relations and neither part can vanish without the other vanishing too [62]. Starting from Eq. (2.60), one observes that

$$n^2(\omega) = \tilde{\chi}(\omega) + 1. \tag{2.63}$$

Since $\tilde{\chi}(\omega)$ is complex, the refractive index

$$n(\omega) = \sqrt{[1+\tilde{\chi}_{\mathrm{R}}(\omega)] + i\tilde{\chi}_{\mathrm{I}}(\omega)} \simeq \underbrace{\sqrt{1+\tilde{\chi}_{\mathrm{R}}(\omega)}}_{n_{\mathrm{eff}}(\omega)} + \underbrace{\frac{i\tilde{\chi}_{\mathrm{I}}(\omega)}{2\sqrt{1+\tilde{\chi}_{\mathrm{R}}(\omega)}}}_{\Delta n_{\mathrm{eff}}(\omega)} \tag{2.64}$$

is also complex, with its imaginary part accounting for gain and/or loss. Assuming

$$\beta(\omega) = \frac{\omega}{c} n(\omega) \simeq \frac{\omega}{c} n_{\mathrm{eff}}(\omega) + \frac{\omega}{c}\Delta n_{\mathrm{eff}}(\omega) = \frac{\omega}{c} n_{\mathrm{eff}}(\omega) + \frac{i}{2}\underbrace{\frac{\omega\,\tilde{\chi}_{\mathrm{I}}(\omega)}{c\,n_{\mathrm{eff}}(\omega)}}_{\alpha(\omega)}, \tag{2.65}$$

the frequency-domain equivalent propagation equation in Eq. (2.52) becomes

$$\frac{\partial E(z,\omega)}{\partial z} = \left(-\frac{\alpha}{2} + i\frac{\beta_2}{2}\omega^2\right) E(z,\omega). \tag{2.66}$$

The solution of Eq. (2.66) is given by

$$E(z,\omega) = E(0,\omega)\, e^{i\frac{\beta_2}{2}\omega^2 z} e^{-\frac{\alpha}{2}z}, \tag{2.67}$$

where the first exponential term corresponds to CD (see Eq. (2.53)), while the second describes fiber loss. In the time domain, if CD is negligible ($\beta_2 \simeq 0$), Eq. (2.67) reduces to the power attenuation expression in Eq. (2.59).

2.3.4 Polarization Effects

A very important class of propagation effects depends on the state of polarization of light. A brief but comprehensive description of these effects is provided here. To this end, a new representation for the electromagnetic field propagating inside the optical fiber is first introduced.

As previously anticipated in Section 2.2.2, in an optical fiber (say, a SMF) the electromagnetic field can always be expressed as a superposition of an x-polarized $LP_{0,1x}$ mode and a y-polarized $LP_{0,1y}$ mode [63]. This yields

$$\vec{\boldsymbol{e}}(x,y,z,t) = \frac{F_{\mathrm{LP}_{01}}(x,y,\omega_0)}{\mathscr{N}(\omega_0)}\mathrm{Real}\left\{\left[e_x(z,t)\,\hat{\boldsymbol{x}} + e_y(z,t)\,\hat{\boldsymbol{y}}\right]e^{i\omega_0 t}\right\}, \tag{2.68}$$

where $e_x(z,t)$ and $e_y(z,t)$ are the complex envelopes of the electric field associated with the two polarization components, and $\mathscr{N}(\omega_0)$ is a normalization coefficient ensuring that the power carried by the x- (or y-) polarized mode is $|e_x(z,t)|^2$ (or $|e_y(z,t)|^2$). This representation follows from the following assumptions

$$\vec{\boldsymbol{F}}_{\mathrm{LP}_{01x}}(x,y,\omega_0) = F_{\mathrm{LP}_{01}}(x,y,\omega_0)\,\hat{\boldsymbol{x}}, \qquad \vec{\boldsymbol{F}}_{\mathrm{LP}_{01y}}(x,y,\omega_0) = F_{\mathrm{LP}_{01}}(x,y,\omega_0)\,\hat{\boldsymbol{y}}. \tag{2.69}$$

Because of this structure, the electric field can be conveniently represented as a two-dimensional column vector

$$|\boldsymbol{e}(z,t)\rangle = \begin{pmatrix} e_x(z,t) \\ e_y(z,t) \end{pmatrix}, \tag{2.70}$$

whose components corresponds to the complex envelopes of the electric field appearing in Eq. (2.68). This representation is related to the Jones vector and provides a full characterization of the optical field not only in the weakly guiding approximation – where the components correspond directly to the x and y polarized fields – but also in the most general case where the longitudinal field component is non-negligible [63]. More rigorously, when propagation is characterized by the absence of polarization-dependent loss (PDL), it is convenient to introduce the normalized Jones vector as the Fourier transform of Eq. (2.70), yielding

$$|\boldsymbol{s}(z,\omega)\rangle = \frac{|\boldsymbol{E}(z,\omega)\rangle}{||\boldsymbol{E}(z,\omega)\rangle|} = \frac{|\boldsymbol{E}(z,\omega)\rangle}{\sqrt{\langle\boldsymbol{E}(z,\omega)\,|\boldsymbol{E}(z,\omega)\rangle}} = \begin{pmatrix} s_x(z,\omega) \\ s_y(z,\omega) \end{pmatrix}, \tag{2.71}$$

where the bra $\langle\boldsymbol{E}|$ indicates the corresponding complex conjugate row vector, i.e., $\langle\boldsymbol{E}(z,\omega)\,| = \left(E_x^*(z,\omega)\,, E_y^*(z,\omega)\right)$, and where

$$s_x = \frac{E_x(z,\omega)}{\sqrt{|E_x(z,\omega)\,|^2 + |E_y(z,\omega)\,|^2}}, \qquad s_y = \frac{E_y(z,\omega)}{\sqrt{|E_x(z,\omega)\,|^2 + |E_y(z,\omega)\,|^2}}. \tag{2.72}$$

From Eq. (2.71), the polarization state is fully determined by the relation between the complex-valued scalars s_x and s_y.

Starting from the Jones notation, which fully characterizes the optical field through a two-dimensional complex column vector, it is possible to introduce the Stokes notation, which provides an alternative description based on the use of real-valued three-dimensional column vectors and that is isomorphic to the Jones representation. By denoting with $\vec{\boldsymbol{S}}$ the Stokes vector of unit length corresponding to the Jones vector $|\boldsymbol{s}\rangle$, its components are defined as [64]

$$\begin{aligned} S_1 &= |s_x|^2 + |s_y|^2 = \langle \boldsymbol{s}|\boldsymbol{\sigma}_1|\boldsymbol{s}\rangle, \\ S_2 &= 2\mathrm{Real}\left(s_x^* s_y\right) = \langle \boldsymbol{s}|\boldsymbol{\sigma}_2|\boldsymbol{s}\rangle, \\ S_3 &= 2\mathrm{Imag}\left(s_x^* s_y\right) = \langle \boldsymbol{s}|\boldsymbol{\sigma}_3|\boldsymbol{s}\rangle, \end{aligned} \tag{2.73}$$

where the Pauli matrices are

$$\boldsymbol{\sigma}_1 = \begin{pmatrix} 1 & 0 \\ 0 & -1 \end{pmatrix}, \qquad \boldsymbol{\sigma}_2 = \begin{pmatrix} 0 & 1 \\ 1 & 0 \end{pmatrix}, \qquad \boldsymbol{\sigma}_3 = \begin{pmatrix} 0 & i \\ -i & 0 \end{pmatrix}. \tag{2.74}$$

The Stokes vector length is equal to $|\vec{\boldsymbol{S}}| = \sqrt{S_1^2 + S_2^2 + S_3^2} = \sqrt{\langle \boldsymbol{s}|\boldsymbol{s}\rangle} = 1$, thus the light polarization state in the Stokes' space is represented through a point on a sphere of unit radius referred to as the Poincaré sphere. Given the relation between the two isomorphic Jones and Stokes spaces, it is easy to see that linear polarization states lie on the equator of such sphere, horizontal and vertical polarization correspond to the directions $\pm\hat{\boldsymbol{S}}_1$, while the $\pm 45°$ linear states correspond to $\pm\hat{\boldsymbol{S}}_2$. Circular polarization states are located at the north and south poles of the sphere, i.e., along $\pm\hat{\boldsymbol{S}}_3$. All remaining points on the sphere correspond to elliptical polarization states. This is summarized in Fig. 2.7.

By defining the projection operator in the Jones space as [64]

$$|\boldsymbol{p}\rangle\langle\boldsymbol{q}| = \begin{pmatrix} p_x q_x^* & p_x q_y^* \\ p_y q_x^* & p_y q_y^* \end{pmatrix}, \tag{2.75}$$

and recalling that an Hermitian 2×2 matrix can always be expanded in terms of the identity matrix $\mathbf{I}$ and the three Pauli matrices with real-valued coefficients, the relation between the Jones and Stokes vectors can be written as

$$|\boldsymbol{s}\rangle\langle\boldsymbol{s}| = \frac{1}{2}\left(\mathbf{I} + \vec{\boldsymbol{S}} \cdot \vec{\boldsymbol{\sigma}}\right), \tag{2.76}$$

where $\vec{\boldsymbol{S}}$ is the Stokes vector and $\vec{\boldsymbol{\sigma}}$ is a column vector collecting the three Pauli matrices, so that $\vec{\boldsymbol{S}} \cdot \vec{\boldsymbol{\sigma}} = S_1\boldsymbol{\sigma}_1 + S_2\boldsymbol{\sigma}_2 + S_3\boldsymbol{\sigma}_3$. Equation (2.76) can be used to demonstrate the relation between scalar products in the Jones and Stokes spaces

$$|\langle \boldsymbol{s}_1|\boldsymbol{s}_2\rangle|^2 = \frac{1}{2}\left(1 + \vec{\boldsymbol{S}}_1 \cdot \vec{\boldsymbol{S}}_2\right). \tag{2.77}$$

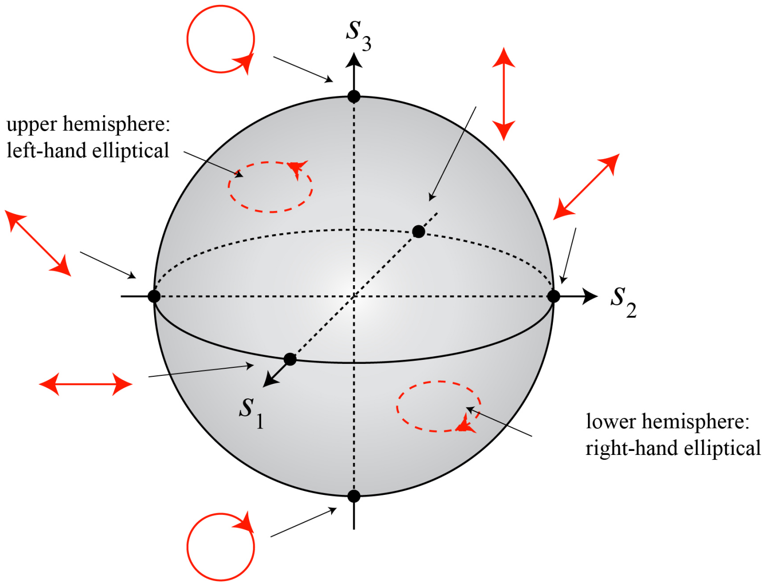

Figure 2.7: The Poincaré sphere representing the relationship between light polarization states in the Jones and Stokes spaces. Points on the equator represent linear polarization states, points on the poles represent circular polarization states while all the others represent elliptical polarization states. From [65].

From the latter equation, one can find that orthogonal polarization states in the Jones space, satisfying $\langle \boldsymbol{s}_1 | \boldsymbol{s}_2 \rangle = 0$, correspond to anti-parallel vectors in the Stokes space, that is $\vec{\boldsymbol{S}}_1 \cdot \vec{\boldsymbol{S}}_2 = -1$. This explains why, for example, x (or 45°) and y (or -45°) light polarization states, that are orthogonal in the Jones space, are represented by opposite points on the Poincaré sphere, represented by the vectors $\pm\hat{\boldsymbol{S}}_1$ (or $\pm\hat{\boldsymbol{S}}_2$), in the Stokes space.

In the more general case of space-division multiplexing (SDM) fibers with N available spatial dimensions, a complete description of the electric field requires a $2N$-dimensional vector, accounting for both polarization components of each spatial dimension. The generalized Jones vector $|\boldsymbol{s}(z,\omega)\rangle$ (often referred to as the hyper-polarization vector [63]) is defined as

$$|\boldsymbol{e}(z,t)\rangle = \begin{pmatrix} e_{1x}(z,t) \\ e_{1y}(z,t) \\ \vdots \\ e_{Nx}(z,t) \\ e_{Ny}(z,t) \end{pmatrix}, \qquad |\boldsymbol{s}(z,\omega)\rangle = \frac{|\boldsymbol{E}(z,\omega)\rangle}{||\boldsymbol{E}(z,\omega)\rangle|}, \tag{2.78}$$

where $|\boldsymbol{e}\rangle$ and $|\boldsymbol{s}\rangle$ now denote $2N$-dimensional column vectors. The generalization of the Stokes representation follows from extending the Pauli-matrix formalism. Since

$|\boldsymbol{s}\rangle\langle\boldsymbol{s}|$ is a $2N \times 2N$ Hermitian matrix, Eq. (2.76) can be generalized to

$$|\boldsymbol{s}\rangle\langle\boldsymbol{s}| = \frac{1}{2N}\left(\boldsymbol{I} + \vec{\boldsymbol{S}} \cdot \vec{\boldsymbol{\Lambda}}\right), \tag{2.79}$$

where $\vec{\boldsymbol{S}}$ is the generalized Stokes vector and $\vec{\boldsymbol{\Lambda}}$ is a column vector collecting the generalized Pauli matrices $\boldsymbol{\Lambda}_n$. These matrices must be Hermitian, traceless, and must satisfy the trace-orthogonality condition

$$\operatorname{tr}\{\boldsymbol{\Lambda}_m\boldsymbol{\Lambda}_n\} = 2N\delta_{n,m}. \tag{2.80}$$

These matrices form a basis for all traceless Hermitian $2N \times 2N$ matrices and span a space of dimension $D = 4N^2 - 1$. Using Eqs. (2.79) and (2.80), one obtains the following generalized relations between the Jones and Stokes spaces [63]

$$S_n = \langle\boldsymbol{s}|\boldsymbol{\Lambda}_n|\boldsymbol{s}\rangle, \qquad n = 1, \ldots, D, \tag{2.81}$$

$$\vec{\boldsymbol{S}} = \langle\boldsymbol{s}|\vec{\boldsymbol{\Lambda}}|\boldsymbol{s}\rangle, \tag{2.82}$$

$$|\langle\boldsymbol{s}_1|\boldsymbol{s}_2\rangle|^2 = \frac{1}{2N}\left(1 + \vec{\boldsymbol{S}}_1 \cdot \vec{\boldsymbol{S}}_2\right). \tag{2.83}$$

We note that although the Stokes vectors corresponding to two orthogonal Jones vectors satisfy $\vec{\boldsymbol{S}}_1 \cdot \vec{\boldsymbol{S}}_2 = -1$, this condition does not imply that the two vectors are anti-parallel in the multi-dimensional representation.

2.3.4.1 Polarization-Mode Coupling

Linear polarization effects result from manufacturing imperfections and deployment-related issues that cause the fiber to loose its ideal circular symmetry. In practice, real fibers exhibit random variations in the shape and size of the core along their lengths. This situation can be modelled by the following relation between the polarization vector $\vec{\boldsymbol{P}}(z,\omega)$ and the electric field $\vec{\boldsymbol{E}}(z,\omega)$

$$\vec{\boldsymbol{P}}(z,\omega) = \epsilon_0\tilde{\chi}(\omega)\vec{\boldsymbol{E}}(z,\omega) + \epsilon_0\tilde{\chi}_P(\omega)\vec{\boldsymbol{E}}(z,\omega), \tag{2.84}$$

where $\tilde{\chi}_P(\omega)$ is a traceless 2×2 tensor accounting for perturbations to the ideal, isotropic susceptibility. By treating the second term in Eq. (2.84) as a perturbation in the derivation of the propagation equation, and neglecting the main effects introduced in the previous chapter (CD and fiber loss), the evolution of the electric field inside the fiber can be written as [64]

$$\frac{\partial|\boldsymbol{E}(z,\omega)\rangle}{\partial z} = \frac{i}{2}\mathbf{B}(z,\omega)|\boldsymbol{E}(z,\omega)\rangle, \tag{2.85}$$

with $|\boldsymbol{E}(z,\omega)\rangle$ the Fourier transform of Eq. (2.70). In the absence of PDL, which implies unitary propagation, the 2×2 matrix $\mathbf{B}$ in Eq. (2.85) is Hermitian and traceless. Equation (2.85) shows that the two components of the electric field in the frequency domain ($E_x(z,\omega)$ and $E_y(z,\omega)$) undergo a unitary mixing, resulting into a phenomenon referred to as polarization-mode coupling (PMC). Since the matrix $\mathbf{B}$ is traceless and Hermitian, it can be expanded using a linear combination of the three Pauli matrices with real-valued coefficients. Consequently, Eq. (2.85) can be rewritten as

$$\frac{\partial|\boldsymbol{E}(z,\omega)\rangle}{\partial z} = i\frac{\vec{\boldsymbol{\beta}}(z,\omega)\cdot\vec{\boldsymbol{\sigma}}}{2}|\boldsymbol{E}(z,\omega)\rangle, \tag{2.86}$$

where $\vec{\boldsymbol{\beta}}(z,\omega)$ is a real-valued three-dimensional row vector known as birefringence vector and $\vec{\boldsymbol{\sigma}}$ represents a three-dimensional column vector whose components are the Pauli matrices. Moving to the Jones space, that is by normalizing $|\boldsymbol{E}(z,\omega)\rangle$ as in Eq. (2.71), the PMC-evolution can be expressed by means of a unitary matrix $\mathbf{U}(z,\omega)$ through

$$|\boldsymbol{s}(z,\omega)\rangle = \mathbf{U}(z,\omega)\,|\boldsymbol{s}(0,\omega)\rangle. \tag{2.87}$$

The evolution operator $\mathbf{U}(z,\omega)$ satisfies

$$\frac{\partial\mathbf{U}(z,\omega)}{\partial z} = i\frac{\vec{\boldsymbol{\beta}}(z,\omega)\cdot\vec{\boldsymbol{\sigma}}}{2}\mathbf{U}(z,\omega). \tag{2.88}$$

which follows by substituting Eq. (2.87) into Eq. (2.86) in the Jones space.

In the most general case, Eq. (2.88) does not admit a closed-form solution. However, its solution can be approximated numerically by iteratively applying

$$\mathbf{U}(z+\Delta z,\omega) \simeq e^{i\frac{\vec{\boldsymbol{\beta}}(z,\omega)\cdot\vec{\boldsymbol{\sigma}}}{2}\Delta z}\mathbf{U}(z,\omega), \tag{2.89}$$

which corresponds to modelling the fiber as a concatenation of birefringence plates, each characterized by a different birefringence vector $\vec{\boldsymbol{\beta}}(z,\omega)$. In the special case where the birefringence is constant along the fiber, Eq. (2.88) admits the following closed-form solution

$$\mathbf{U}(z,\omega) = e^{i\frac{\vec{\boldsymbol{\beta}}(\omega)\cdot\vec{\boldsymbol{\sigma}}}{2}z}. \tag{2.90}$$

Although PMC can be analyzed in the Jones space using the previous approach, it is often more conveniently studied in the Stokes space, where the unitary evolution of the field polarization state corresponds to a rotation of the Stokes vector on the Poincaré sphere. By denoting with $\mathbf{R}(z,\omega)$ the Stokes-space rotation matrix, which is isomorphic to $\mathbf{U}(z,\omega)$, these two quantities are related by [64]

$$\mathbf{R}\vec{\boldsymbol{\sigma}} = \mathbf{U}^{\dagger}\vec{\boldsymbol{\sigma}}\mathbf{U}, \tag{2.91}$$

with $\mathbf{R}(z,\omega)$ generally referred to as Müller matrix. Differentiating the Stokes vector $\vec{\boldsymbol{S}}(z,\omega) = \langle \boldsymbol{s}(z,\omega) | \vec{\boldsymbol{\sigma}} | \boldsymbol{s}(z,\omega) \rangle$ with respect to z, and using Eqs. (2.87) and (2.88), yields [64]

$$\frac{\partial \vec{\boldsymbol{S}}(z,\omega)}{\partial z} = \vec{\boldsymbol{\beta}}(z,\omega) \times \vec{\boldsymbol{S}}(z,\omega). \tag{2.92}$$

Equation (2.92) shows that the birefringence vector $\vec{\boldsymbol{\beta}}(z,\omega)$ acts as the local rotation axis for the motion of the field Stokes vector and that its modulus corresponds to the local angular velocity. The general solution can be written as

$$\vec{\boldsymbol{S}}(z,\omega) = \mathbf{R}(z,\omega)\, \vec{\boldsymbol{S}}(0,\omega), \tag{2.93}$$

which in the case of constant birefringence along the fiber simplifies to

$$\vec{\boldsymbol{S}}(z,\omega) = \exp\left(z\vec{\boldsymbol{\beta}}(\omega)\times\right)\vec{\boldsymbol{S}}(0,\omega), \tag{2.94}$$

where $\vec{\boldsymbol{\beta}}(\omega)\times$ denotes the 3×3 matrix representing the vector product with $\vec{\boldsymbol{\beta}}(\omega)$. It is important to note that $\vec{\boldsymbol{\beta}}(z,\omega)$ is random in nature and, as a result, PMC also varies randomly along the propagating direction z.

2.3.4.2 Mode and Polarization Coupling in SDM Fibers

In an SDM fiber supporting N spatial dimensions, PMC continues to play a significant role. In this context, however, the coupling between the two polarization components of a given spatial dimension also extends to the two polarizations of all other spatial dimensions. This gives rise to the phenomenon of mode coupling, which is described by a $2N \times 2N$ unitary matrix $\mathbf{U}(z,\omega)$ whose evolution obeys (see also Eq. (2.88))

$$\frac{\partial \mathbf{U}(z,\omega)}{\partial z} = i\frac{\vec{\boldsymbol{\beta}}(z,\omega)\cdot\vec{\boldsymbol{\Lambda}}}{2N}\mathbf{U}(z,\omega), \tag{2.95}$$

where the D-dimensional vector $\vec{\boldsymbol{\beta}}(z,\omega)$ accounts for both propagation-constant mismatches among the spatial channels and the local mode coupling. As in the single-mode case, Eq. (2.95) does not admit a closed-form solution except when the generalized birefringence vector is constant along the fiber. In that special case, the result of Eq. (2.90) generalizes to

$$\mathbf{U}(z,\omega) = e^{i\frac{\vec{\boldsymbol{\beta}}(\omega)\cdot\vec{\boldsymbol{\Lambda}}}{2N}z}. \tag{2.96}$$

However, $\vec{\boldsymbol{\beta}}(z,\omega)$ is random in nature and, as a result, mode and polarization coupling also varies randomly along the propagating direction z [66].

The Stokes-space representation remains analogous to the SMF case (see Eqs. (2.92) and (2.93)). However, the matrix $\mathbf{R}$ now represents a transformation in the $D \times D$

Stokes space. Although such a transformation still represents a rotation, in an hyper-space it no longer provides the same intuitive geometrical interpretation as in the SMF case.

2.3.4.3 Polarization-Mode Dispersion

As introduced in the previous section, the birefringence vector depends on both distance (z) and frequency (ω). Its dependence on frequency gives rise to polarization-mode dispersion (PMD), which takes the form of frequency-dependent random PMC. Polarization-mode dispersion can be understood in different ways depending on the viewpoint [64]. In the frequency-domain view, for a fixed input polarization, the output polarization varies with frequency. In the time-domain view, and in a first-order approximation, a pulse traveling through the fiber experiences a mean time delay and some distortion that depend on the input pulse polarization.
In order to see this, it is useful to recall that the frequency derivative of $\mathbf{U}(z,\omega)$ must be of the same form of Eq. (2.88). In fact, differentiating the unitary condition $\mathbf{U}\mathbf{U}^{\dagger} = \mathbf{I}$ with respect to ω, shows that $(\partial\mathbf{U}/\partial\omega)\,\mathbf{U}^{\dagger}$ is anti-Hermitian and traceless. From this observation one obtains [64]

$$\frac{\partial\mathbf{U}(z,\omega)}{\partial\omega} = i\frac{\vec{\boldsymbol{\tau}}(z,\omega)\cdot\vec{\boldsymbol{\sigma}}}{2}\mathbf{U}(z,\omega)\,, \tag{2.97}$$

where $\vec{\boldsymbol{\tau}}(z,\omega)$ is known as the PMD vector.

The frequency domain view of PMD can be easily understood by considering the PMD vector $\vec{\boldsymbol{\tau}}(z,\omega)$ in Eq. (2.97) as the frequency-domain equivalent of the birefringence vector $\vec{\boldsymbol{\beta}}(z,\omega)$ in Eq. (2.88), previously introduced for the analysis of PMC. Since the birefringence vector represents the local rotation axis of the field Stokes vector as the field propagates along the optical fiber at a fixed optical frequency ω, it is easy to extend this result to the PMD vector, representing the local rotation axis of the Stokes vector when the position z is fixed and the optical frequency ω is varied. This is illustrated in Fig. 2.8, where the PMD vector $\vec{\boldsymbol{\tau}} = \vec{\boldsymbol{\tau}}(z,\omega_0)$ represents the local rotation axis of the optical field in the frequency domain, in close proximity of the reference frequency ω_0. Under this definition, the orientation $\hat{\boldsymbol{\tau}}(z,\omega)$ determines the so called output principal states of polarization (PSP), while the magnitude $\tau(z,\omega) = |\vec{\boldsymbol{\tau}}(z,\omega)|$ corresponds to the differential group delay (DGD).

To illustrate the time domain view of the PMD previously introduced, it is convenient to consider the special case in which the PMD vector is approximately constant

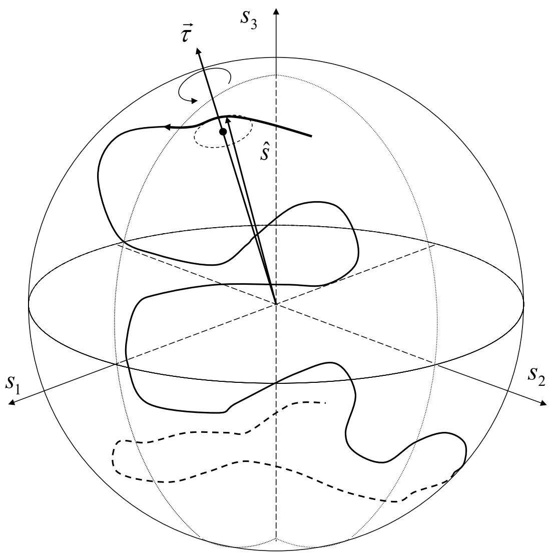

Figure 2.8: The trajectory that the field polarization state at a given position z along the link draws on the Poincaré sphere as a function of the optical frequency ω. The PMD vector $\vec{\boldsymbol{\tau}}$ represents the local rotation axis.

within the signal bandwidth, that is $\vec{\boldsymbol{\tau}}(z,\omega) \simeq \vec{\boldsymbol{\tau}}(z,\omega_0)$. Under this assumption, the solution of Eq. (2.97), expressed in terms of its eigenvalues, takes the form [64]

$$\mathbf{U}(z,\omega) = e^{i\tau(z,\omega_0)/2}|\boldsymbol{\tau}\rangle\langle\boldsymbol{p}|+e^{-i\tau(z,\omega_0)/2}|\boldsymbol{\tau}_\perp\rangle\langle\boldsymbol{p}_\perp|, \tag{2.98}$$

where $\tau(z,\omega_0) = |\vec{\boldsymbol{\tau}}(z,\omega_0)|$ is the DGD. The vectors $|\boldsymbol{\tau}\rangle$ and $|\boldsymbol{\tau}_\perp\rangle$ are orthogonal Jones vectors associated with the Stokes vectors $\pm\vec{\boldsymbol{\tau}}/\tau$ (output PSP), while $\langle\boldsymbol{p}|$ and $\langle\boldsymbol{p}_\perp|$ are the associated input PSP. Light launched inside the fiber along one of the input PSP will be aligned with the corresponding output PSP at the fiber output, with this output polarization states being insensitive to first-order variations in ω. This interpretation is consistent with Fig. 2.8. In fact, when the output field polarization is aligned with respect to $\pm\vec{\boldsymbol{\tau}}$ (output PSP), no rotation occurs in the close proximity of the reference frequency. The time domain effect of PMD on a pulse $f(t)$ launched with input polarization $|\boldsymbol{u}\rangle$ follows directly from the application of Eq. (2.98). The resulting output field is

$$f(t)\,|\boldsymbol{u}\rangle \rightarrow \langle\boldsymbol{p}|\boldsymbol{u}\rangle f\left(t-\tau_0-\frac{\tau}{2}\right)|\boldsymbol{\tau}\rangle + \langle\boldsymbol{p}_\perp|\boldsymbol{u}\rangle f\left(t-\tau_0+\frac{\tau}{2}\right)|\boldsymbol{\tau}_\perp\rangle, \tag{2.99}$$

showing that two replicas of the input pulse $f(t)$ appear at the fiber output, each aligned with one of the output PSP and delayed by $\tau_0 \pm \tau/2$. The term τ_0 accounts for a polarization-independent delay that is always accumulated during propagation. The delay τ between the maximum and minimum mean time delays is the DGD. The output PSP $|\boldsymbol{\tau}\rangle$ and $|\boldsymbol{\tau}_\perp\rangle$ are therefore called slow and fast PSP, respectively.

This result is only valid when the PMD vector can be considered constant within the signal bandwidth, a condition known as first-order PMD approximation. To assess the validity of this approximation, it is necessary to obtain a complete description of PMD as a stochastic process in the frequency domain. Since this chapter provides only an introduction to polarization effects, we present the basis for such analysis by defining the PMD dynamic evolution equation. This equation is derived by equating the frequency derivative of Eq. (2.88) with the z-derivative of Eq. (2.97), resulting in [64]

$$\frac{\partial \vec{\boldsymbol{\tau}}\left(z,\omega\right)}{\partial z} = \frac{\partial \vec{\boldsymbol{\beta}}\left(z,\omega\right)}{\partial \omega} + \vec{\boldsymbol{\beta}}\left(z,\omega\right) \times \vec{\boldsymbol{\tau}}\left(z,\omega\right), \tag{2.100}$$

which describes the evolution of the PMD vector along the propagation distance z. Since $\vec{\boldsymbol{\beta}}\left(z,\omega\right)$ is inherently random, Eq. (2.100) defines a stochastic process, whose bandwidth can be characterized by evaluating the PMD vector frequency correlation function [67].

2.3.4.4 Modal and Polarization Dispersion in SDM Fibers

In the case of SDM systems, the temporal dispersion between the two polarization components of a given spatial dimension extends to the two polarizations of all other spatial dimensions, giving rise to the more general phenomenon of MD. The extension of Eq. (2.97) to the multi-dimensional case is straightforward. In fact, the three-dimensional PMD vector can be replaced with its generalized D-dimensional counterpart, yielding

$$\frac{\partial \mathbf{U}\left(z,\omega\right)}{\partial \omega} = i\frac{\vec{\boldsymbol{\tau}}\left(z,\omega\right) \cdot \vec{\boldsymbol{\Lambda}}}{2N}\mathbf{U}\left(z,\omega\right), \tag{2.101}$$

where the D-dimensional vector $\vec{\boldsymbol{\tau}}\left(z,\omega\right)$ generalizes the PMD vector and is commonly referred to as MD vector [63]. Although its evolution is also governed by Eq. (2.100), provided that each vector is assumed to be its multi-dimensional generalization, a major difference with respect to the SMF case arises from the mismatch in propagation constants of the different spatial modes. This mismatch can be modeled by introducing a generalized birefringence vector

$$\vec{\boldsymbol{\beta}}\left(z,\omega\right) = \vec{\boldsymbol{\beta}}_d\left(\omega\right) + \vec{\boldsymbol{\beta}}_r\left(z,\omega\right), \tag{2.102}$$

where $\vec{\boldsymbol{\beta}}_d$ accounts for both propagation-constant mismatch and deterministic coupling among spatial modes, while $\vec{\boldsymbol{\beta}}_r$ represents random mode coupling [63]. Using this definition, the evolution equation for the generalized MD vector becomes

$$\frac{\partial \vec{\boldsymbol{\tau}}\left(z,\omega\right)}{\partial z} = \frac{\partial \vec{\boldsymbol{\beta}}_d\left(\omega\right)}{\partial \omega} + \frac{\partial \vec{\boldsymbol{\beta}}_r\left(z,\omega\right)}{\partial \omega} + \left[\vec{\boldsymbol{\beta}}_d\left(\omega\right) + \vec{\boldsymbol{\beta}}_r\left(z,\omega\right)\right] \times \vec{\boldsymbol{\tau}}\left(z,\omega\right). \tag{2.103}$$

The second term on the right-hand side has a negligible effect on the evolution of the MD vector and is typically omitted [63, 68]. The effectiveness with which the random mode coupling affects the evolution of the MD vector determines the two relevant regimes of weak and strong mode coupling. In the case of weak coupling, the most relevant metric is the largest DGD, also known as the delay spread of the fiber, with MD growing linearly with propagation distance. A different situation arises in the regime of strong spatial coupling. In this regime, the MD bandwidth becomes much narrower compared to the typical bandwidth of coherent optical signals (on the order of a few tens of GHz), even after a short propagation distance. As a consequence, the first-order PMD approximation becomes no longer valid. In this case, MD is accurately characterized by the intensity impulse response (IIR) duration, defined as the mode-averaged output power measured when exciting a single mode at the fiber input with a spectrally flat signal with a bandwidth exceeding the MD bandwidth. The resulting IIR waveform has a Gaussian shape, with a duration that grows with the square root of the propagation distance and is proportional to the root-mean-squared length of the generalized PMD vector $\vec{\boldsymbol{\tau}}$. The IIR duration is particularly important as it determines the temporal window that must be accommodated within the receiver's multiple-input multiple-output (MIMO) digital signal processing (DSP), and directly impacts the complexity of SDM receivers. This aspect is further examined for MMF transmission systems in Chapter J3.

2.3.4.5 Polarization-Dependent Loss

As introduced in the previous chapter, fiber loss is always present in optical fibers. This phenomenon arises from the fact that the relation between the polarization vector and the electric field is equivalent to that of a causal linear system. As a consequence, the real and imaginary parts of the dielectric susceptibility, $\tilde{\chi}_{\mathrm{R}}(\omega)$ and $\tilde{\chi}_{\mathrm{I}}(\omega)$, are not independent but are related through the Kramers-Kronig relations. The same results hold in the presence of polarization effects, since the quantity $\tilde{\chi}_P(\omega)$ in Eq. (2.84) also consists of real and imaginary parts. This gives rise to PDL, a phenomenon in which different field polarization states experience different attenuations as they propagate through the fiber. By including both the real and imaginary parts of $\tilde{\chi}_P(\omega)$ within the perturbative framework introduced in Section 2.3.4.1, the evolution equation for the electric field in the presence of PDL becomes

$$\frac{\partial|\boldsymbol{E}(z,\omega)\rangle}{\partial z} = \frac{\mathbf{A}(z,\omega) + i\mathbf{B}(z,\omega)}{2}|\boldsymbol{E}(z,\omega)\rangle, \tag{2.104}$$

where $\mathbf{A}(z,\omega) = \vec{\boldsymbol{\alpha}}(z,\omega) \cdot \vec{\boldsymbol{\sigma}}$ is an Hermitian and traceless matrix describing the local loss, while $\mathbf{B}(z,\omega) = \vec{\boldsymbol{\beta}}(z,\omega) \cdot \vec{\boldsymbol{\sigma}}$ is an Hermitian and traceless matrix describing local coupling and dispersion.

Although PMC and PMD are unitary propagation effects, meaning that the field power spectral density is preserved during propagation, PDL is non-unitary and therefore degrades the performance of fiber-optic communications systems at a fundamental level. Given

$$|\boldsymbol{E}(z,\omega)\rangle = \mathbf{T}(z,\omega)\,|\boldsymbol{E}(0,\omega)\rangle, \tag{2.105}$$

where $\mathbf{T}(z,\omega)$ is the system transfer matrix describing propagation from $z=0$ to z, the field power spectral density at position z is

$$\langle \boldsymbol{E}(z,\omega)\,|\boldsymbol{E}(z,\omega)\rangle = \langle \boldsymbol{E}(0,\omega)\,|\mathbf{T}^{\dagger}(z,\omega)\,\mathbf{T}(z,\omega)\,|\boldsymbol{E}(0,\omega)\rangle. \tag{2.106}$$

From Eq. (2.106), it is clear that the quantity of interest for characterizing PDL is the Hermitian matrix $\mathbf{T}^{\dagger}\mathbf{T}$, which can in turn by expanded as

$$\mathbf{T}^{\dagger}(z,\omega)\,\mathbf{T}(z,\omega) = \gamma_0\left[\boldsymbol{I} + \vec{\boldsymbol{\Gamma}}(z,\omega)\cdot\vec{\boldsymbol{\sigma}}\right], \tag{2.107}$$

where $\vec{\boldsymbol{\Gamma}}(z,\omega)$ is known as the PDL vector. Polarization states aligned with $\pm\vec{\boldsymbol{\Gamma}}(z,\omega)$ experiences attenuations of $\gamma_0(1+\Gamma)$ and $\gamma_0(1-\Gamma)$, respectively, corresponding to the maximum and minimum attenuation levels, with

$$\Gamma = |\vec{\boldsymbol{\Gamma}}(z,\omega)| \leq 1. \tag{2.108}$$

A common figure of merit for the PDL of a fiber-optic link is the power ratio, in dB, between the most and least attenuated polarization states, given by

$$\rho = 10\log_{10}\left(\frac{1+\Gamma}{1-\Gamma}\right), \tag{2.109}$$

where ρ in SMFs rarely exceeds a few dB. Since ρ is typically random in nature, its probability density function depends on the distribution of PDL sources along the link. When the link contains a very large number of PDL elements that can be treated as continuously distributed, and when the mean PDL is sufficiently small, the probability density function is well approximated by a Maxwellian distribution [69]. Although such approximation holds in most practical cases, the exact expression for the probability density function is available in [70]. Conversely, when the link comprises only a few dominant PDL sources, the probability density function is approximated by the "hinge model" [71, 72].

2.3.4.6 Mode-Dependent Loss in SDM Fibers

Extending the concept of PDL to fibers supporting N spatial dimensions is straightforward. In particular, Eq. (2.107) remains valid, provided that the three-dimensional PDL vector $\vec{\mathbf{\Gamma}}$ is replaced by its D-dimensional generalized counterpart, and the vector $\vec{\boldsymbol{\sigma}}$ is replaced by the vector of generalized Pauli matrices $\vec{\mathbf{\Lambda}}$. Under these assumptions, one obtains

$$\mathbf{T}^{\dagger}(z,\omega)\,\mathbf{T}(z,\omega) = \gamma_0\left[\mathbf{I} + \vec{\mathbf{\Gamma}}(z,\omega)\cdot\vec{\mathbf{\Lambda}}\right]. \tag{2.110}$$

In these more general settings, the matrix $\vec{\mathbf{\Gamma}}(z,\omega)\cdot\vec{\mathbf{\Lambda}}$ has $2N$ eigenvalues, representing the mode-dependent loss (MDL) and/or gain experienced by the spatial-polarization modes. Consequently, the MDL figure of merit is generalized as

$$\rho = 10\log_{10}\left(\frac{1+\Gamma_{\mathrm{max}}}{1+\Gamma_{\mathrm{min}}}\right), \tag{2.111}$$

where Γ_{max} and Γ_{min} denote the largest and smallest eigenvalues of $\vec{\mathbf{\Gamma}}(z,\omega)\cdot\vec{\mathbf{\Lambda}}$, respectively.

2.4 Nonlinear Propagation Effects in Fibers

This chapter ends with an introduction to the study of nonlinear effects experienced by a signal propagating through the fiber-optic channel. These effects originate from the dependence of the fiber-glass refractive index on the optical power, and become significant at high transmit power levels. Some of the key nonlinear effects affecting propagation in both single-mode and SDM fibers are reviewed.

2.4.1 Self-Phase Modulation

It can be shown that the response of optical fibers becomes nonlinear when the electromagnetic fields reaches sufficiently high intensities. This nonlinear behavior originates from the intrinsic properties of the glass medium and becomes relevant at elevated signal power levels [73, 74]. To see this effect, it is useful to analyze the polarization vector $\vec{\boldsymbol{p}}(t)$, as introduced in Eq. (2.61) for a linear medium in which both chromatic dispersion and loss have already been accounted for. The key observation is that the polarization vector of Eq. (2.61) also consists of a nonlinear term, referred to as the Kerr term, for which here we consider only the instantaneous contribution

$$\vec{\boldsymbol{p}}(t) = \epsilon_0\chi(t)\otimes\vec{\boldsymbol{e}}(t) + \epsilon_0\chi^{(3)}|\vec{\boldsymbol{e}}(t)|^2\vec{\boldsymbol{e}}(t). \tag{2.112}$$

Neglecting polarization effects, the equations describing pulse propagation in the presence of fiber loss, CD, and instantaneous Kerr nonlinearity can be written as

$$\begin{aligned}\frac{\partial e_x}{\partial z} &= -\frac{\alpha}{2}e_x - i\frac{\beta_2}{2}\frac{\partial^2 e_x}{\partial t^2} + i\gamma\left(|e_x|^2 e_x + \frac{2}{3}|e_y|^2 e_x + \frac{1}{3}e_y^2 e_x^*\right),\\ \frac{\partial e_y}{\partial z} &= -\frac{\alpha}{2}e_y - i\frac{\beta_2}{2}\frac{\partial^2 e_y}{\partial t^2} + i\gamma\left(|e_y|^2 e_y + \frac{2}{3}|e_x|^2 e_y + \frac{1}{3}e_x^2 e_y^*\right),\end{aligned} \tag{2.113}$$

where the dependence of the electrical field components on the propagation distance z and time t is implicitly assumed. The two coupled equations in Eq. (2.113) are commonly referred to as coupled nonlinear Schrödinger equations (NLSEs). The nonlinearity coefficient γ is defined as

$$\gamma = \frac{\omega_0}{c}\frac{n_2}{A_{\text{eff}}}, \tag{2.114}$$

where ω_0 is the signal carrier frequency, n_2 is the nonlinear index coefficient, and A_{eff} is the effective area of the fiber. A typical value for γ in SMFs is approximately 1.3 $\text{W}^{-1}\text{km}^{-1}$. In general, the coupled NLSEs do not admit closed-form analytical solutions, except for specific classes of input waveforms and/or for specific settings of the involved parameters. An instructive example can be found when only one polarization component is excited at the fiber input (say, e_x) and chromatic dispersion is neglected, that is by setting $\beta_2 \simeq 0$ in Eq. (2.113). In this case, the solution reduces to

$$e(z,t) = e(0,t)\, e^{-\frac{\alpha}{2}z} e^{i\gamma|e(0,t)|^2 z_{\text{eff}}}, \tag{2.115}$$

$$z_{\text{eff}} = \frac{1-e^{-\alpha z}}{\alpha}. \tag{2.116}$$

The quantity z_{eff} is referred to as effective length of the fiber and it approaches $1/\alpha$ as $z \to \infty$, while it reduces to z in the lossless limit $\alpha \to 0$. Equation (2.115) shows that the nonlinear effect results in the introduction of a phase term

$$\Phi_{\text{SPM}}(t) = \gamma|e(0,t)|^2 z_{\text{eff}}, \tag{2.117}$$

which is known as self-phase modulation (SPM). Since fiber loss is always present in reality (i.e., $\alpha > 0$), for propagation distances $z \gg 1/\alpha$ the effective length saturates and the SPM-induced phase shift approaches

$$\Phi_{\text{SPM}}(t) = \gamma|e(0,t)|^2/\alpha. \tag{2.118}$$

Thus, when the peak launch power is sufficiently small, the SPM contribution becomes negligible. Self-phase modulation is also responsible for an instantaneous frequency shift

$$\delta\omega = -\frac{\mathrm{d}\Phi_{\mathrm{SPM}}\left(t\right)}{\mathrm{d}t}, \tag{2.119}$$

which is proportional to the intensity profile of the input waveform. For a pulse-like waveform, this results in a negative (red-) shift in the leading edge and a positive (blue-) shift in the trailing edge of the pulse, producing spectral broadening. Although this analysis neglects CD, it provides an intuitive understanding of how the nonlinear term affects propagation even in the presence of CD.

As the NLSEs of Eq. (2.113) do not admit analytical solutions for arbitrary input pulses $e\left(z,t\right)$, numerical techniques are employed, with the most widely used being the split-step Fourier method (SSFM) [74].

2.4.1.1 The Manakov Equation

It is important to note that the presence of random PMC in optical fibers leads to a significant simplification of the NLSEs in Eq. (2.113). This simplification stems from the fact that PMC scrambles the state of polarization of the propagating field on a length scale that is much shorter than the scale over which nonlinear effects become non-negligible. Indeed, nonlinear effects typically accumulate over distances of several tens of kilometers, whereas the instantaneous state of polarization uniformly covers the Poincaré sphere over distances of the order of meters. As a result, the equation governing nonlinear propagation in the presence of random PMC reduces to

$$\frac{\partial|\boldsymbol{e}\rangle}{\partial z} = -\frac{\alpha}{2}|\boldsymbol{e}\rangle - i\frac{\beta_2}{2}\frac{\partial^2|\boldsymbol{e}\rangle}{\partial t^2} + i\frac{8}{9}\gamma\langle\boldsymbol{e}|\boldsymbol{e}\rangle|\boldsymbol{e}\rangle, \tag{2.120}$$

where $|\boldsymbol{e}\rangle = |\boldsymbol{e}\left(z,t\right)\rangle$ denotes the bi-dimensional column vector defined in Eq. (2.70), and γ is the nonlinearity coefficient defined for the fundamental mode. This equation is known as the Manakov equation [75], and it can be further extended to account for the effect of PMD [76]. Generalized versions of the Manakov equation have been shown to accurately describe nonlinear propagation in fibers for SDM with N spatial modes [77–79]. In the case of a single group of quasi-degenerate spatial modes (i.e., modes with nearly identical propagation constants), and in the absence of MD, Eq. (2.120) generalizes to

$$\frac{\partial|\boldsymbol{e}\rangle}{\partial z} = -\frac{\alpha}{2}|\boldsymbol{e}\rangle - i\frac{\beta_2}{2}\frac{\partial^2|\boldsymbol{e}\rangle}{\partial t^2} + i\kappa\gamma\langle\boldsymbol{e}|\boldsymbol{e}\rangle|\boldsymbol{e}\rangle, \tag{2.121}$$

where $|\boldsymbol{e}\rangle$ is now a $2N$-dimensional vector collecting the polarization components of the N spatial modes. The dimensionless coefficient κ, accounting for the averaging of the nonlinear interactions over the strongly-coupled spatial and polarization modes is given by [77]

$$\kappa = \sum_{n,h} \frac{C_{nhhn} C_{nhnh}}{2N\,(2N+1)}, \tag{2.122}$$

where the constants C depend on the overlap integrals of the spatial mode profiles [78]. The summation indexes n and h are used to span all combinations of modes. In the case of multiple groups of degenerate spatial modes (i.e., groups with different propagation constants), Eq. (2.120) is conveniently rewritten by using separate hyper-polarization vectors for the electric field in each mode group (MG). The coupled Manakov equations for a reference multi-mode fiber (MMF) with two MGs of $2N_A$ and $2N_B$ spatial and polarization modes each are given by [77]

$$\begin{aligned}\frac{\partial|\boldsymbol{e}_1\rangle}{\partial z} &= -\frac{\alpha}{2}|\boldsymbol{e}_1\rangle - i\frac{\beta_2}{2}\frac{\partial^2|\boldsymbol{e}_1\rangle}{\partial t^2} + i\gamma\left(\kappa_{11}\langle\boldsymbol{e}_1|\boldsymbol{e}_1\rangle + \kappa_{12}\langle\boldsymbol{e}_2|\boldsymbol{e}_2\rangle\right)|\boldsymbol{e}_1\rangle,\\ \frac{\partial|\boldsymbol{e}_2\rangle}{\partial z} &= -\frac{\alpha}{2}|\boldsymbol{e}_2\rangle - i\frac{\beta_2}{2}\frac{\partial^2|\boldsymbol{e}_2\rangle}{\partial t^2} + i\gamma\left(\kappa_{21}\langle\boldsymbol{e}_1|\boldsymbol{e}_1\rangle + \kappa_{22}\langle\boldsymbol{e}_2|\boldsymbol{e}_2\rangle\right)|\boldsymbol{e}_2\rangle.\end{aligned} \tag{2.123}$$

The dimensionless coefficients κ_{jj} and κ_{jl} are given by

$$\begin{aligned}\kappa_{jj} &= \sum_{n,h=1}^{2N_j} \frac{C_{nhhn} C_{nhnh}}{2N_j\,(2N_j+1)},\\ \kappa_{jl} &= \sum_{n=1}^{2N_j}\sum_{h=1}^{2N_l} \frac{C_{nhhn} C_{nhnh}}{4N_j N_l},\end{aligned} \tag{2.124}$$

and it can be seen that $\kappa_{jl} = \kappa_{lj}$.

2.4.2 Cross-Phase Modulation and Four-Wave Mixing

When multiple information-carrying signals are transmitted in different frequency channels, various forms of nonlinear interactions arise due to the Kerr nonlinearity of the fiber. In wavelength-division multiplexing (WDM) systems, the most important inter-channel nonlinear effect is cross-phase modulation (XPM), which results from the interaction between pairs of channels. Additional nonlinear effects, arising in the form of four-wave mixing (FWM), originate from the interactions between three or more channels. In the analysis of coherent WDM system performance, the combined impact of SPM, XPM, and FWM is conveniently described in terms of additive noise, commonly referred to as nonlinear interference noise (NLIN) [80, 81].

2.4.3 Stimulated Raman Scattering

Stimulated Raman scattering (SRS) is another important nonlinear phenomenon that can be exploited to turn optical fibers into broadband amplifiers [82]. However, SRS can severely impair the performance of wideband WDM systems by causing a unidirectional power transfer from higher-frequency (shorter-wavelength) channels to lower-frequency (longer-wavelength) ones. Under the continuous wave (CW) assumption, a simple model describing the signal power evolution in the presence of SRS is

$$\frac{\partial I_s}{\partial z} = -\alpha_s I_s + \frac{g_{\mathrm{R}}}{kA_{\mathrm{eff}}} I_s I_p, \tag{2.125}$$

where I_s and I_p are the signal and pump field intensities, respectively. The term α_s is the fiber loss coefficient at the signal frequency, as discussed in Section 2.3.3. The Raman gain coefficient g_{R} originates from the imaginary part of the third-order nonlinear susceptibility, $\chi^{(3)}$, and it depends on both the fiber core composition (varying significantly with the use of different dopants) and the frequency separation between the pump and the Stokes waves. The normalization factor k accounts for polarization: $k = 1$ is used for co-polarized and $k = 2$ is used for depolarized pump and signal. The term A_{eff} denotes the effective area of the pump-signal interaction within the fiber core. The normalized Raman gain spectrum for fused silica fibers is shown in Fig. 2.9 [83]. As observed, the Raman gain peak occurs at a pump-signal frequency separation of approximately 13.2 THz. Moreover, Eq. (2.125) can be extended to describe the interaction among multiple WDM channels, which is a key aspect in C-band and multi-band transmission systems [84].

Stimulated Raman scattering has been extensively studied in WDM systems using standard SMFs [82, 84–91], while its study in SDM transmission is still at its preliminary stage. In particular, the impact of SRS in multi-band WDM transmission over weakly-coupled multi-core fibers (WC-MCFs) has been shown to be similar in magnitude to that observed in SMFs [92, 93], and some preliminary investigations have also been conducted in MMF systems [94]. In contrast, the study of the impact of SRS in WDM transmission over CC-MCFs has received very little attention to date. The first comprehensive characterization has been reported in [95] and is introduced in Chapter J1.

2.4.4 Stimulated Brillouin Scattering

Stimulated Brillouin scattering (SBS) is another important nonlinear phenomenon in optical fibers, occurring at input power levels much lower than those required

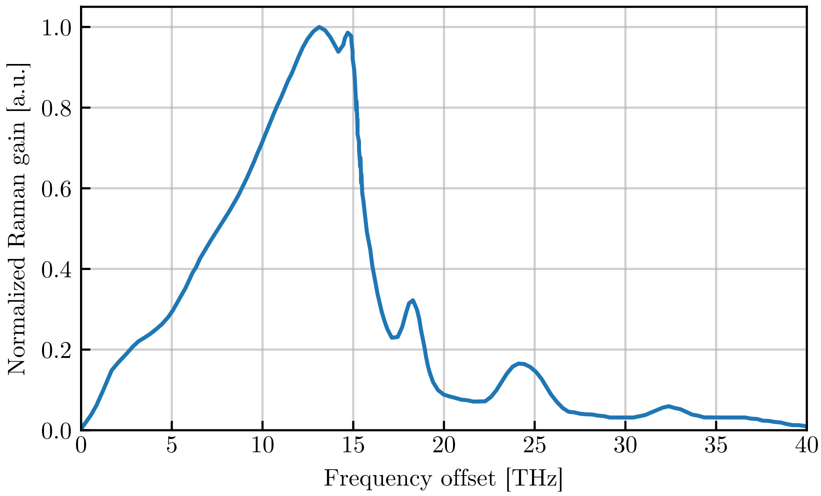

Figure 2.9: Normalized Raman gain for a fused-silica fiber. The strongest Raman gain occurs at a frequency offset of approximately 13.2 THz and decays beyond 15 THz. After [83].

for SRS. Since SBS produces a backward-propagating Stokes wave carrying most of the input power, it limits the allowable channel power in optical communication systems. This phenomenon arises from a nonlinear interaction among the pump and Stokes waves, and an acoustic wave generated (thermally) through the process of electrostriction [96]. The acoustic wave induces a periodic modulation of the material density, which in turn locally modifies its refractive index. This refractive index perturbation, induced by the pump field, leads to Bragg scattering of the pump light in the backward direction, with a Stokes frequency down-shift roughly three orders of magnitude smaller than that of SRS (approximately 10 GHz). In coherent transmission systems, however, SBS is generally not a predominant impairment, since it requires a strong, narrow-band optical tone to be present, whereas joint amplitude and phase modulation significantly suppress the carrier's power spectral density.

Chapter 3

SDM Fibers and Components

This chapter is devoted to introducing the main fiber designs that are suitable for space-division multiplexing (SDM), along with the main devices and technologies required for SDM transmission.

3.1 Spatially-Diverse Fibers

Spatially-diverse fibers can be divided into two main categories: multi-core fibers (MCFs) and multi-mode fibers (MMFs), as well as combinations of the two. It is worth noting that such fibers are not strictly required for implementing SDM, as the use of parallel SMFs combined with the integration of one or more subsystems can also be regarded as SDM. Nevertheless, both MCFs and MMFs are well-established technologies and have been proposed for a variety of applications, spanning from short-reach interconnects to long-haul transmission. The reminder of this section provides a more detailed description of these two fiber types.

3.1.1 Multi-Core Fibers

As the name suggests, MCFs are characterized by the presence of multiple fiber cores within the same cladding structure. Depending on the spacing between these cores, which defines the resulting propagation regime, MCFs can be divided into two main categories: uncoupled-core multi-core fibers (UC-MCFs) (also known as weakly-coupled multi-core fibers (WC-MCFs)) and coupled-core multi-core fibers (CC-MCFs) (also known as randomly-coupled multi-core fibers (RC-MCFs)).

In UC-MCFs, the fiber is engineered so that the interference between neighboring cores, generally referred to as inter-core crosstalk (IC-XT), is sufficiently weak to be treated as additive noise. As a result, each fiber core can be treated as an independent spatial channel, enabling the use of conventional coherent transceivers without the need for full-multiple-input multiple-output (MIMO) processing across all fiber cores. This can be achieved using several techniques, such as introducing trenches and holes around the cores, or using heterogeneous cores, where adjacent cores are designed to have different propagation constants. Another effective approach to reduce IC-XT is the use of bidirectional transmission, in which neighboring cores carry signals propagating in opposite directions [97]. The maximum number of cores that can be accommodated within a single cladding is ultimately limited by the cladding diameter. Increasing the cladding diameter above the standard 125 µm allows more cores to be housed within the fiber, resulting in spatial channel densities (defined as core count per unit of facet area) much larger than that of SMFs [98]. However, doing so results in more fragile fibers, with reduced reliability, lower production yield, and decreased compatibility with existing manufacturing, cabling and connectorization processes [99]. Splicing of MCFs is also an important aspect to consider. These fibers can be spliced using equipment designed for polarization maintaining (PM) fibers, although a non-standard cladding diameter would require more sophisticated splicers with customized fiber holders. Moreover, core alignment is generally less accurate than in SMFs, especially for the cores located farther from the fiber center, which are more sensitive to rotational misalignment, leading to increased splicing losses [99]. These practical limitations led to the development of UC-MCFs with the same 125 µm cladding diameter of SMFs, which typically supports up to four trench-assisted cores and achieve IC-XT values around -60 dB/km in the C-band. Notable examples include the fabrication of compatible four-core UC-MCFs by four different vendors as part of a standardization effort [100], and the first field-deployment of four-core and eight-core UC-MCFs in the Italian city of L'Aquila as part of the INCIPICT project [51, 101]. It is important to note that a standardized UC-MCF design has not yet been proposed. Instead, the optimal design typically depends on several parameters, including operating wavelength, target throughput, transmission reach, and the employed digital signal processing (DSP) architecture. In particular, the studies reported in [102–106] investigate fiber design parameters such as core count, refractive index profile, core pitch, cladding diameter, and others, in order to balance the interplay among the impacts of IC-XT, amplified spontaneous emission (ASE) noise, and fiber nonlinearities. As the core count increases, the spectral efficiency (SE) initially grows linearly, with system performance being mainly limited by ASE noise. Beyond an optimal number of cores, however, the SE starts to decrease,

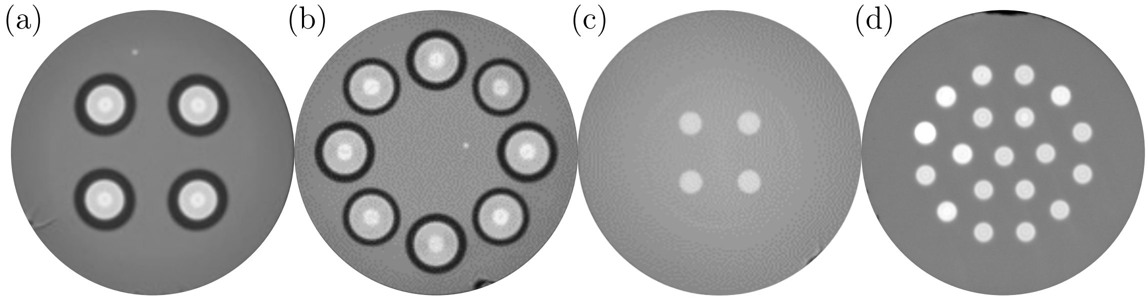

Figure 3.1: Cross sections of the multi-core fibers used in this work: (a) uncoupled-core four-core fiber, (b) uncoupled-core eight-core fiber, (c) coupled-core four-core fiber, and (d) coupled-core 19-core fiber. Drawn to scale, all fibers have a 125 µm cladding diameter.

as performance becomes mainly limited by IC-XT [7]. While good performance has been demonstrated in a number of applications with IC-XT levels of approximately −60 dB/km over moderate transmission reaches, the wavelength dependence of IC-XT may limit the applicability of such designs as optical transmission systems start to exploit multi-band transmission windows. Moreover, since IC-XT grows with wavelengths, a standard 125 µm cladding diameter UC-MCF can support a larger number of cores in the low IC-XT region typical of the O-band [51].

In contrast, CC-MCFs are engineered to operate in the coupled-core regime, where the distance between cores is intentionally reduced so that the IC-XT increases up to the point at which the cores become coupled. As a consequence, a novel receiver implementing full-MIMO processing across all fiber cores is required to undo the coupling accumulated during propagation, and the individual fiber cores can no longer be operated independently. It is important to mention that as the core pitch in MCFs decreases, the coupling level increases until a maximum coupling strength is reached. Further reduction of the core pitch leads to the formation of supermodes and mode groups (MGs) propagating with different group velocities, thereby increasing the total delay spread of the fiber. The strong coupling typical of these fibers is characterized by a delay spread that grows with the square root of propagation distance and by a system intensity impulse response (IIR) that becomes Gaussian-shaped at sufficiently long distances [68]. Since the core pitch is intentionally reduced, CC-MCFs can support a substantially larger number of cores compared to UC-MCFs. In a standard 125 µm cladding diameter, the maximum number of coupled cores that can be accommodated is approximately 19 [107, 108]. The first field-deployment of four-core CC-MCFs is also part of the INCIPICT project [51, 101].

Figure 3.1 shows the cross-section of several MCFs used in the author's work.

Specifically, Fig. 3.1(a) corresponds to an uncoupled-core four-core fiber employed to demonstrate the longest reach ever reported in an all-multi-core amplified recirculating-loop-based transmission system, as described in Chapter J2 [109, 110]. Figure 3.1(b) shows an uncoupled-core eight-core fiber deployed in the city of L'Aquila and used for experimental quantum-key distribution (QKD) co-existence activities in the O-band [111]. Figure 3.1(c) shows a coupled-core four-core fiber, also field-deployed in L'Aquila, used for the first experimental characterization of stimulated Raman scattering (SRS) in CC-MCFs, as reported in Chapter J1 [95]. Finally, Fig. 3.1(d) shows a coupled-core 19-core fiber used to demonstrate the highest reported throughput among standard-cladding diameter MCFs [107].

3.1.2 Multi-Mode Fibers

Multi-mode fibers are characterized by a single core that is either enlarged or has a larger core-cladding refractive index difference compared to SMFs, so that the normalized frequency parameter V becomes large enough to support more than one mode. Since these fibers contain a single core, they typically have a standard cladding diameter of 125 µm. The guided modes can serve as independent spatial channels, and fiber designs supporting more than 100 modes can be realized. Note that any fiber that supports multiple modes is generally referred to as an MMF, while those guiding only a small number of modes are often called few-mode fibers (FMFs). In practice, fibers supporting less than ten modes are referred to as FMFs, although this limit is rather arbitrary. Therefore, through the thesis, we refer to all such fibers simply as MMFs. For example, a graded-index MMF with a core diameter of 28 µm supports the propagation of 15 modes [38], whereas a fiber with a 50 µm core can guide approximately 55 fiber modes [39, 40]. Graded-index MMFs represent the most widely used class of MMFs for SDM. Their design and fabrication processes are very similar to those of commercially available graded-index fibers optimized for operation at 850 nm, such as the OM3 and OM4 fibers commonly deployed in short-reach interconnects.

The modes supported by an MMF are typically organized into MGs, where modes belonging to the same group exhibiting similar propagation constants. Within each MGs, the propagation regime resembles the strong-coupling behavior typical of CC-MCFs, with the undergoing strong mutual mixing. In contrast, modes belonging to different MGs have different propagation velocities and therefore experience no-to-weak coupling, resulting in minor inter-group mixing. As a consequence, full-MIMO processing is required at the receiver to undo the coupling among the modes supported by an MMFs. Due to the group-velocity difference, MMFs exhibit large differential

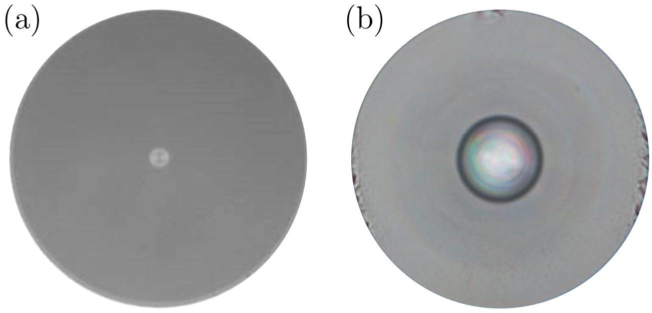

Figure 3.2: Cross sections of (a) the single-mode fiber and (b) the 15-mode multi-mode fiber used in this work. Both fibers share the same 125 µm cladding diameter.

group delay (DGD), which for high mode counts can reach orders of approximately 100 ps/km [112]. While such delay spread is manageable in short-reach applications, in long-haul communication systems extending to up to 10 000 km it could accumulate to approximately 1 µs. Fortunately, the coupling between modes mitigates this accumulated delay spread. As the accumulated delay spread determines both the channel memory and the computational complexity of the receiver DSP, several techniques have been proposed to enhance coupling between different MGs [113–117]. A comprehensive study on system-level mode-permutation techniques for increasing inter-MG coupling in a 15-mode MMF, and thereby reducing the receiver DSP complexity, is presented in Chapter J3. Moreover, the potential for ultra-high-capacity short-reach transmission over the first field-deployed 15-mode MMF – installed in the Italian city of L'Aquila as part of the INCIPICT project – is discussed in Chapter C1. This demonstration represents the first petabit-per-second-class transmission over any field-deployed fiber at the time of writing. The cross-section of the 15-mode MMF used in these two works is shown in Fig. 3.2(b), alongside a reference SMF (Fig. 3.2(a)).

3.2 Components for SDM

The deployment of SDM transmission systems requires the development of novel optical components capable of operating over multiple spatial channels simultaneously, such as amplifiers that can simultaneously amplify all cores of an MCF. Moreover, spatial multiplexer (MUX) and demultiplexer (DeMUX) devices are needed to interface the SMF-based inputs and outputs with the SDM fibers. This section provides an overview of the main components required in an SDM communication system.

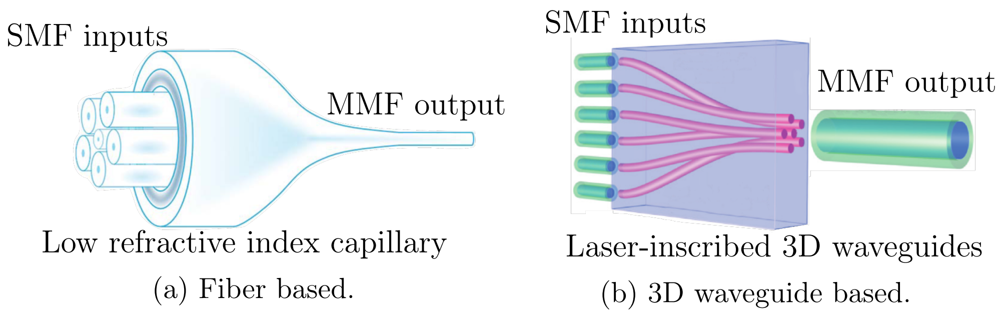

Figure 3.3: Two different photonic lantern implementations: (a) Fiber-based, and (b) 3D-waveguide based. After [12, Fig. 4.1].

3.2.1 Spatial Multiplexers

Spatial MUX and DeMUX devices are needed to convert parallel SMF inputs into a spatially-multiplexed output, and vice versa, respectively. Depending on the specific type of SDM fiber used, these devices are referred to as fan-in/fan-out (FIFO) devices (for MCFs), or mode MUXs/DeMUXs (for MMFs). Fan-in/fan-out are relatively simple devices whose function is to spectrally rearrange the SMF inputs into the spatial core layout of the MCF, and different FIFO techniques are reviewed in [49]. Mode MUXs, on the other hand, couple multiple SMFs into the guided modes of an MMF. These devices are generally divided into two categories: *mode-selective*, when they directly couple a given SMF to a specific fiber mode, and *non mode-selective*, when they map different SMF ends to different orthogonal linear combinations of modes [63]. It is important to note that, in coherent transmission, both categories of mode MUXs can be used without performance penalties, since mode mixing, whether lumped or propagation-induced, is ultimately compensated by MIMO equalization at the receiver. Although mode MUXs can be implemented using various techniques, two of the most promising techniques are photonic lanterns (PLs) and multi-plane light converters (MPLCs), which are briefly illustrated in the following.

Photonic lanterns [118, 119] consist of a set of SMFs which are combined and tapered down to form a MMF. To achieve this, the SMFs are inserted into a low-refractive-index capillary, which ultimately becomes the cladding of the resulting MMF, as illustrated in Fig. 3.3(a). If the taper is adiabatic, PLs can in principle achieve nearly lossless conversions. However, in practice, most fabricated devices exhibit insertion losses below 1 dB. An alternative approach to realize PLs relies on femtosecond laser-inscribed three-dimensional waveguides. In this method, waveguides are written inside a glass substrate and brought gradually close to each other as illustrated in Fig. 3.3(b), so that they almost merge before short, focused laser pulses

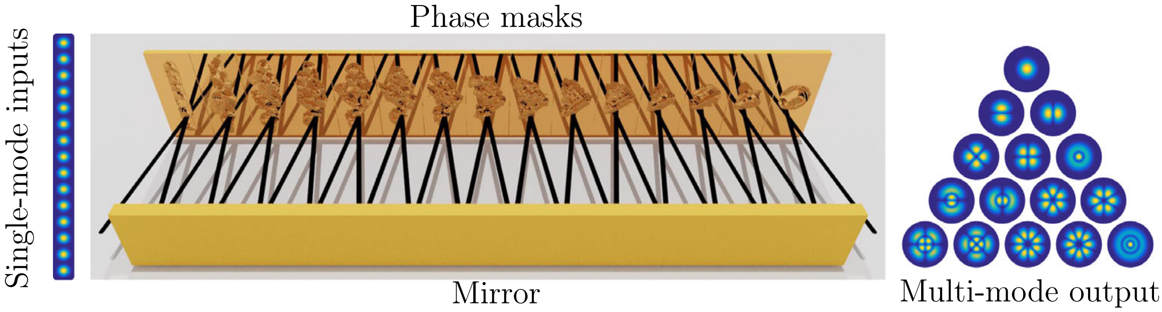

Figure 3.4: Schematic of a multi-plane light converter. Single-mode inputs (left) are converted into higher-order modes by multiple reflections between the two parallel planes. The resulting multi-mode output (right) can then be coupled into a 15-mode multi-mode fiber. After [12, Fig. 4.2].

locally and permanently change the refractive index of the glass substrate. The main advantage of this technique lies in the ability to create arbitrary 3D waveguide geometries. Notably, these structures can also be used as FIFO devices for MCFs.

As an alternative to PLs, MPLCs have been proposed as universal mode-converting devices capable of transforming any arbitrary set of input modes into any desired output mode set [120]. The principle is rather simple: the light from an array of SMFs propagates through an array of phase plates that perform the required mode transformation, with the required number of phase masks determined by the complexity of the desired transformation. For practical alignment, MPLCs are typically implemented using two parallel planes and exploiting reflective geometry, with the light being reflected multiple times between one plane consisting of a substrate with multiple phase masks and a high reflectivity mirror. A schematic on an MPLC of the same kind used in the experiments reported in Chapters C1 and J3 is shown in Fig. 3.4. Using this technique, mode MUXs have been demonstrated for up to 1035 modes [121] and over a broad bandwidth of approximately 200 nm [122].

3.2.2 Networking Components

Networking and routing in modern optical transmission systems are largely based on wavelength-division multiplexing (WDM), a technique that enables multiple data streams to share a single optical fiber by assigning each traffic stream to a distinct, non-overlapping wavelength channel. In a WDM network, end users communicate through optical WDM channels, generally called *lightpaths*, which may span multiple fiber links. Since modern optical networks comprise a huge number of nodes (say, K), each equipped with only W transceivers ($W \ll K$), only a limited amount of lightpaths can be simultaneously established on the network. Consequently, a key networking challenge is: given a set of lightpaths to be established on the network and a constraint on the number of wavelengths, determine both the routing of these lightpaths and the assignment of wavelengths to them so that the maximum number of lightpaths may be established [123].

Compared to conventional WDM optical networks, SDM transmission systems introduce an additional dimension (i.e., space) that can potentially be exploited for networking and routing [124, 125]. However, depending on the level of coupling between spatial paths, routing may be constraint. Spatial paths that do not couple during propagation can be routed independently towards their destinations, for example by using a separate wavelength-selective switch (WSS) per each spatial lane. In contrast, spatial paths that couple during transmission must be routed to the same receiver so that the coupling can be undone using MIMO equalization. Consequently, for CC-MCFs and MMFs, this generally means that the spatial dimension cannot be freely used for routing. Still, limited routing of individual MGs might be implemented with minor penalties [126, 127]. Spatial channels at the same wavelength that are routed together through the optical network are referred to as spatial superchannels. These can be switched either using a dedicated switching element capable of handling all spatial paths simultaneously [128], or by first demultiplexing the spatial paths and then routing them using standard single-mode WSSs. The latter approach, however, requires careful alignment of the spatial paths to avoid introducing artificial modal dispersion (MD).

3.2.3 Amplifiers

As discussed in the previous chapter, optical fibers exhibit propagation losses that must be compensated by optical amplification to enable long-distance transmission. For SDM fiber, signal amplification can be implemented in several ways. The simplest approach is to use spatial MUX/DeMUX pairs on either side of an array of standard single-mode erbium-doped fiber amplifiers (EDFAs), which already provides some benefits by sharing components and control circuitry among them [4]. A more integrated alternative is the direct use of MCFs and MMFs as the gain medium in multi-mode (MM) and multi-core (MC) EDFAs, respectively. This removes the need for MUX/DeMUX devices and enables the use of free-space optics shared among the spatial paths, as an example for gain-flattening filtering isolation.

Both MC-EDFAs and MM-EDFAs can be divided into two main categories: core-pumped and cladding-pumped. As the name suggests, the difference between them lies in how the pump power is injected inside the erbium-doped region of the SDM fiber. In core-pumped MC-EDFAs, the pump power can be controlled independently for each core [129]. An amplifier of this type is used in the experiment reported in Chapter J2. In contrast, cladding-pumped MC-EDFAs use a tapered pump-delivery fiber that is wrapped around the erbium-doped MCF. This enables the use of a single, cost-effective, high-power multi-mode pump laser shared across all cores. However, since all cores are pumped at the same time, this approach may result in a larger power consumption compared to conventional single-core amplification schemes. Designing MM-EDFAs is more challenging. For core-pumped MM-EDFAs, the pump light should first be passed through a mode MUX, so as to control the pump power injected into each mode [130]. For cladding-pumped MM-EDFAs, achieving uniform gain across all spatial modes is very difficult, and precise control of the doping profile is required to minimize mode-dependent gain (MDG) [131]. Moreover, as both MCFs and MMFs exhibit SRS (see also Chapter J1), Raman amplification can also be used [132, 133].

3.3 Space-Division Multiplexed Transmission

To conclude this section, a system-level overview of an SDM system is provided, focusing on the experimental setup of the transmission experiment described in Chapter J3. Although a detailed description of the experimental setup is provided in Section J3.3, the focus here is on a system-level perspective, highlighting the design and implementation of a recirculating-loop-based, long-haul SDM transmission system operating in the C-band. The experimental setup is illustrated in Fig. 3.5.

This setup emulates a C-band WDM system by generating a spectrally-flattened noise spectrum using a C-band single-mode EDFA, in combination with an optical processor (OP). The OP is also programmed to produce a notch in the spectrum to accommodate a three-channel sliding test-band for signal reception and performance evaluation. Since the signal propagates over a 15-mode MMF, which would in principle require 15 independent test-bands, a practical approach is adopted whereby a single-mode test-band is split into 15 tributaries. These tributaries are then injected through the fiber using an MPLC-based mode-MUX. To ensure that the replicas are uncorrelated with respect to the fiber delay spread, thereby resembling different test-bands relative to the fiber memory length, each tributary is optically delayed using fiber spools. In the reference case shown in Fig. 3.5, the fiber spools have lengths of multiples of 30 m. Although it is convenient to use spools with lengths that are multiples of a common basic value, it is not strictly required. Moreover, the use of

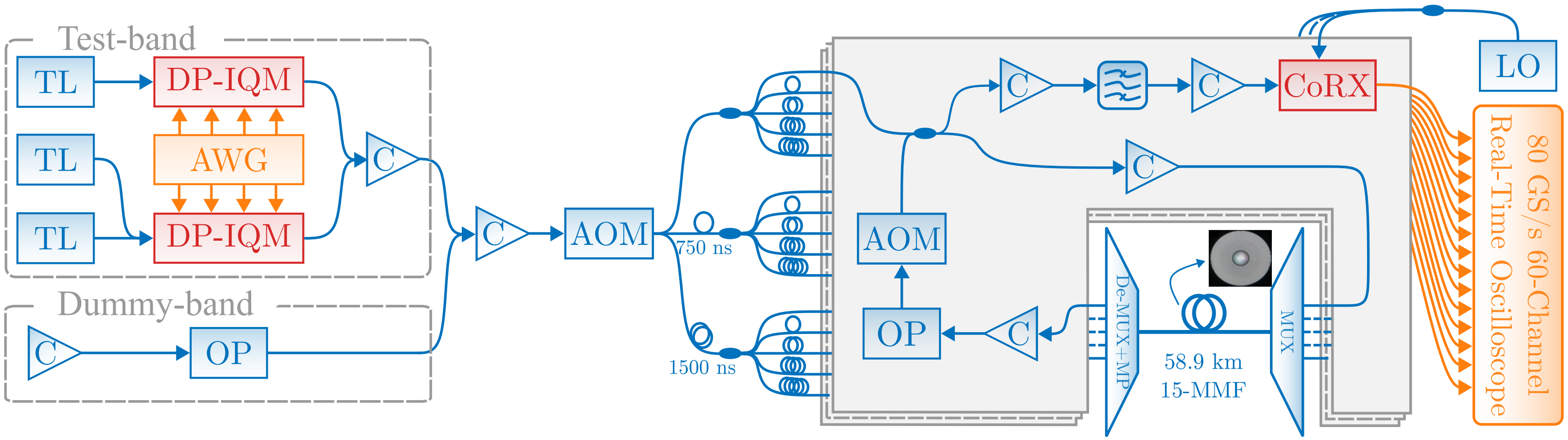

Figure 3.5: Experimental setup of a recirculating-loop-based, long-haul 15-mode fiber link.

slightly different fiber lengths can be advantageous when performing offline digital signal processing (DSP), particularly for cross-correlation between the transmitted signal and the received one. Before injection into the 15-mode MPLC mode-MUX, each of the 15 uncorrelated tributaries is amplified using single-mode EDFAs. After propagation over 58.9 km of 15-mode MMF, an MPLC mode-DeMUX separates the signals back into the single-mode domain. These signals are then amplified again using an array of single-mode EDFAs and recirculated to the fiber input via parallel power couplers. For signal reception, the signals from each mode are amplified again both before and after the test-band is selected using optical filters. Finally, the channel under test is detected using 15 parallel coherent receivers (Coh. RXs) sharing the same local oscillator (LO), whose electrical outputs are digitized by a 60-channel, 80 GSa/s real-time oscilloscope (RTO) and stored for offline DSP. Since the 15 signals couple during propagation, either strongly within MGs or weakly between MGs, full-MIMO processing is required to compensate for this coupling. As coupling occurs among all polarizations of all spatial modes, a 30×30 MIMO equalizer is implemented. Two key aspects of the experimental system are signal amplification and signal recirculation. In the reference configuration shown in Fig. 3.5, signal amplification is performed exclusively in the singe-mode domain due to current unavailability of efficient MM-EDFAs. Furthermore, signal recirculation represents a practical means of emulating long-haul transmission without requiring prohibitively large fiber availability. However, this approach is not without limitations, as the parallel recirculating loops require careful path-length alignment to avoid artificially increasing the effective delay spread of the fiber, especially in the presence of coupling between spatial paths. Since the realization and operation of recirculating loops play an important role in long-haul experimental setups, a more detailed description of the loop architecture and timing is provided in the following section. In future practical deployed systems, one would expect a concatenation of SDM fiber spans separated simply by SDM amplifiers, without the need for arrays of single-mdoe EDFAs.

3.3.1 Recirculating Loop in SDM Transmission

To enable signal recirculation, a set of fast optical switches is placed at both inputs of the parallel power couplers that direct the signal into the fiber and towards the receiver chain. In the reference case shown in Fig. 3.5, these optical switches are implemented using acousto-optic modulators (AOMs). These switches, together with all other measurement equipment (e.g., the RTO), are controlled and synchronized using an electronic control box that typically generates transistor-transistor logic

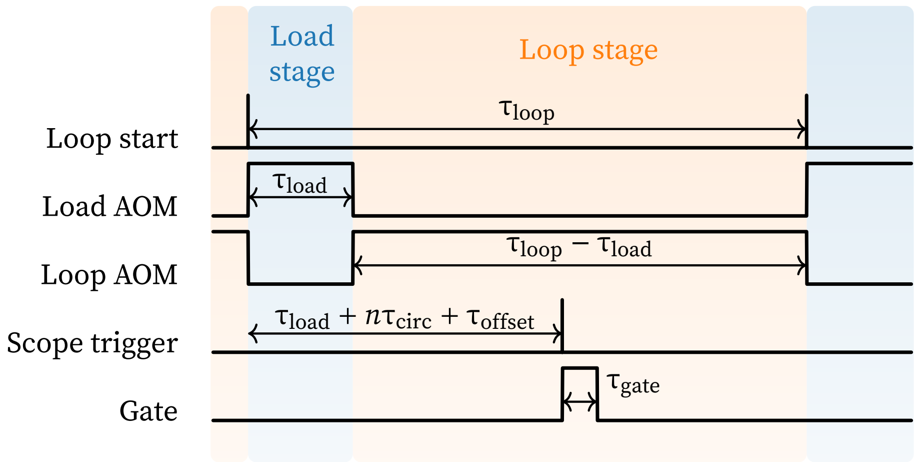

Figure 3.6: Time digram illustrating the transistor-transistor logic trigger signals from the electronic control box to synchronize the recirculating loop. Figure from [12, Fig. 5.3].

(TTL) trigger signals. These signals are summarized in Fig. 3.6. Following the signal path from the transmitter in Fig. 3.5, the signal first passes through an AOM acting as a *loading switch*, before entering the *split and delay* stage. The outputs of this stage are connected to one input of the power couplers responsible for signal loading and recirculation within the parallel single-mode loops, therefore referred to as *loop couplers*. In addition, the amplified signals at the MMF output are routed through a second array of AOMs, referred to as *loop switches*, whose outputs are connected to the second input of the loop couplers. The operation of the recirculating loops can be divided into two stages: *load* and *loop*, as visualized in Fig. 3.6. During the loading stage, the load AOM is closed (signal transmitted through the switch) and the loop AOM is opened (signal is not transmitted through the switch), so that the transmitter fills the parallel loops with the optical signal. The duration of this stage, denoted as τ_{load}, must be at least equal to the propagation time through the fiber. Subsequently, the load AOM is opened and the loop AOM is closed, causing the optical signal to recirculate within the loop. After a duration τ_{loop}, the procedure is repeated. Since during the loop stage the signal is both recirculated and sent to the receiver chain, a trigger signal is required for the RTO to acquire the received signal at the correct time, corresponding to a specific number of recirculations n. This trigger is typically sent $\tau_{\text{load}} + n\tau_{\text{circ}} + \tau_{\text{offset}}$ seconds after the start of the load stage. Here, τ_{circ} denotes the time required for a single recirculation, while τ_{offset} is introduced to position the trigger between successive recirculation periods, thereby preventing loop artifacts from affecting the measurement. A gate signal is also provided by the electronic control box to enable other laboratory equipment to perform measurements corresponding to a specific recirculation. Finally, since optical signals are continuously fed to the receiver chain and optical amplifiers are present throughout the system, it is crucial to eliminate, or at least to minimize, optical transients. In particular, situations in which the signal at the input of an EDFAs is temporally absent and then reintroduced abruptly can generate strong output-power transients, which can potentially degrade system performance and damage the receiving equipment. Such conditions are avoided through accurate time synchronization of the system.

Chapter 4

Thesis Contribution

This thesis investigates space-division multiplexing (SDM) as one of the most promising approaches to meet the continuously increasing demand for larger transmission capacities and to avoid a potential information capacity crunch [22]. Different aspects of SDM are considered, ranging from high-data rate short- and long-distance transmission (see Chapters C1 and J2, respectively) to the experimental characterization of novel optical fiber types both before and after field-deployment The latter is enabled by the first field-deployed SDM fiber testbed, located in the Italian city of L'Aquila. Specifically, the first characterization of stimulated Raman scattering (SRS) in strongly coupled multi-core fibers (MCFs) is presented by the author in Chapter J1. Moreover, mode permutation (MP) techniques used to intentionally introduce strong coupling between modes that would otherwise experience partial coupling, thus reducing the total modal dispersion (MD) of long-haul multi-mode fiber (MMF) systems (introduced in Chapter 2), are reported in Chapter J3. The author's contribution extends beyond the manuscripts appended to the thesis. Collaborations on a number of experiments involving SDM fibers are acknowledged throughout the following sections. Alongside record-breaking transmission experiments over uncoupled-core multi-core fibers (UC-MCFs), coupled-core multi-core fibers (CC-MCFs), and MMFs, networking experiments implementing routing functionalities for spatial super-channels have also been conducted. Significant work has additionally been carried out on the co-existence of classical transmission and quantum-key distribution (QKD) over MCFs with uncoupled cores.

It is important to note that SDM remains in an active research phase, with most SDM demonstrations still confined to laboratory environments. Notable exceptions include the previously mentioned SDM fiber testbed in L'Aquila, Italy [51], where both MCF and MMF cables run through the city-center's underground multi-service tunnel infrastructure, the MCF testbed deployed at the Nippon Telegraph and Telephone (NTT) headquarters in Tokyo, Japan [134], and the first commercialization of a mass-produced ultra-low loss MCF with two uncoupled cores by Sumitomo [135, 136]. In recent months, additional deployed MCFs testbeds have been also opened in India and Portugal [137, 138]. Furthermore, Google and Nippon Electric Company (NEC) have announced the adoption of this 2-core MCF for a segment of their new submarine cable connecting Taiwan and the Philipines to the United States [139]. This represents the first commercial deployment of MCF in an operational optical transmission system, marking a major milestone towards broader adoption of SDM technologies in optical networks.

4.1 Publications Appended to the Thesis

The chapters presented in the second part are based on the following publications or submitted manuscripts. Below, one briefly presents the main contributions of each chapter (publication or manuscript)[1].

C1 G. Di Sciullo, R. S. Luís, M. van den Hout, Q. Wu, P. Sillard, F. Achten, R. Emmerich, N. Braig-Christophersen, B. J. Puttnam, D. A. Shaji *et al.*, "Petabit-per-Second C+L Band Transmission Over a Field-deployed 15-Mode Fiber Link," in *Optical Fiber Communication Conference (OFC) 2026*, Los Angeles (CA), USA, March 2026, paper M1C.2.

This work demonstrates an experimental transmission covering both the C- and L-bands over a field-deployed, 15-mode MMF. The fiber link, with a total length of 6.1 km, is deployed in an underground multi-service tunnel infrastructure located in downtown L'Aquila, Italy. By transmitting 266×15 SDM and wavelength-division multiplexing (WDM) channels, modulated with 35 Gbaud polarization-division multiplexing (PDM) 64-ary quadrature-amplitude modulated (QAM) signals in the C-band and 35 Gbaud PDM-16QAM signals in the L-band, a total capacity of 1.13 Pb/s estimated from the generalized mutual information (GMI) and 1.06 Pb/s after forward error correction (FEC) decoding is achieved. This work represents the first demonstration of C+L-band transmission over a field-deployed MMF, and marks the first petabit-per-second-class transmission over any field-deployed fiber.

[1] **J:** Journal; **C:** Conference.

Author's contribution: The author devised the experimental idea, led in the implementation and calibration of the experimental setup, performed data acquisition and processing, and wrote the manuscript.

J1 G. Di Sciullo, L. A. Zischler, D. A. Shaji, Q. Wu, R. S. Luís, R. Emmerich, M. van den Hout, B. J. Puttnam, G. Rademacher, C. Lasagni *et al.*, "Characterization of Stimulated Raman Scattering in Field-Deployed Coupled-Core Multi-Core Fibers," in *Journal of Lightwave Technology*, vol. 44, no. 2, pp. 550-557, 15 Jan, 2026.

This work reports the first experimental characterization of SRS in CC-MCFs. The 4-core CC-MCF link is field-deployed in an underground multi-service tunnel infrastructure located in downtown L'Aquila, Italy, and has a total length of approximately 69.3 km. The work demonstrates that the effective Raman gain coefficient and its frequency derivative, directly measured over the field-deployed fiber link with two complementary methodologies, are comparable in both magnitude and shape to those observed in a reference single-mode fiber (SMF) of similar length co-deployed within the same fiber infrastructure. The excellent agreement between the two complementary approaches further confirms the validity and accuracy of the experimental findings, also in line with the theory of SRS in the presence of strong inter-core coupling.

Author's contribution: The author devised the experimental concept, led the implementation and calibration of the experimental setup, performed data acquisition and processing, and wrote the manuscript.

J2 G. Di Sciullo, B. J. Puttnam, M. van den Hout, R. S. Luís, D. A. Shaji, G. Rademacher, C. Okonkwo, A. Mecozzi, C. Antonelli, and H. Furukawa, "45.7 Tb/s Over 12 053 km Transmission in an All-Multi-Core-Amplified Recirculating Loop," in *Journal of Lightwave Technology*, vol. 43, no. 10, pp. 4635-4641, 15 May, 2025.

This work experimentally demonstrates a recirculating-loop-based long-haul transmission over a 4-core UC-MCF. The transmission is supported by the first reported all-multi-core-amplified system without the use of fan-in/fan-out (FIFO) devices, relying entirely on 4-core C-band multi-core erbium-doped fiber amplifiers (MC-EDFAs) and distributed Raman amplification (DRA). A total throughput of 49.9 Tb/s estimated from GMI and 45.7 Tb/s after FEC decoding is achieved at a transmission distance of 12 053 km by utilizing 175×24.5 Gbaud

PDM-quadrature phase-shift keying (QPSK) C-band signals on each core. Moreover, a performance comparison between PDM-QPSK, PDM-16QAM and PDM-64QAM is carried out using the same experimental setup over different transmission distances. This work represents the longest transmission reach ever reported for MCF systems relying on a fully integrated multi-core amplification scheme without the use of FIFO devices.

Author's contribution: The author devised the experimental concept, led the implementation and calibration of the experimental setup, performed data acquisition and processing, and wrote the manuscript.

J3 G. Di Sciullo, D. A. Shaji, M. van den Hout, G. Rademacher, R. S. Luís, B. J. Puttnam, N. K. Fontaine, R. Ryf, H. Chen, M. Mazur *et al.*, "Enhancing Long-Haul 15-Mode Fiber Performance: Mode Permutation for Reduced Modal Dispersion," in *Journal of Lightwave Technology*, vol. 43, no. 2, pp. 481-491, 15 Jan, 2025.

This work experimentally investigates the efficacy of mode permutation for mitigating the impact of MD in a 15-mode fiber link for long-haul SDM transmission. By comparing four mode permutation strategies over a recirculating-loop-based 15-mode MMF link for distances of up to 1200 km, and with a fixed MIMO window of 71.4 nm, we demonstrate a reduction in intensity impulse response (IIR) duration from 40 nm to less than 15 ns, while extending the transmission reach from 530 km to 1178 km. The accumulation of mode-dependent loss (MDL) with propagation distance is also investigated. Additionally, we propose a simple model to simulate propagation in realistic MMF links composed of independent fiber spans, by relying on parameters that can be conveniently extracted from experimental data.

Author's contribution: The author devised the experimental concept, participated in the implementation and calibration of the experimental setup, performed all data acquisition and processing, contributed to the definition of the simulation model, and wrote the manuscript.

4.2 Publications Not Appended to the Thesis

The following publications or submitted manuscripts are not covered in the thesis but contain related materials and applications. These works are categorized according to the author's level of contribution.

4.2.1 Publications with Leading Contribution

C10 G. Di Sciullo, L. A. Zischler, D. A. Shaji, R. S. Luís, R. Emmerich, M. van den Hout, B. J. Puttnam, G. Rademacher, C. Lasagni, P. Serena *et al.*, "Stimulated Raman Scattering in Field-Deployed Coupled-Core Multi-Core Fibers," in *Frontiers in Optics + Laser Science 2025 (FiO, LS)*, Denver (CO), USA, October 2025, paper FTu1E.1.[2] [Invited paper]

C14 G. Di Sciullo, D. A. Shaji, L. A. Zischler, R. S. Luís, R. Emmerich, M. van den Hout, C. Lasagni, P. Serena, A. Bononi, T. Hayashi *et al.*, "Experimental Characterization of Stimulated Raman Scattering in Field-Deployed Coupled-Core Multi-Core Fibers," in *51st European Conference on Optical Communication (ECOC 2025)*, Copenhagen, Denmark, September 2025, paper W.02.01.01.[3]

This work reports the first experimental characterization of the effective Raman gain coefficient in a CC-MCF. The analysis is performed on a 69.3 km-long, 4-core CC-MCF link field-deployed in an underground multi-service tunnel infrastructure located in downtown L'Aquila, Italy. By comparing the effective Raman gain coefficient profile directly measured in both the MCF and a reference SMF of similar length, co-deployed in the same infrastructure, we demonstrate for the first time that they are comparable in shape and magnitude, in line with the theory of SRS in the presence of strong inter-core coupling.

Author's contribution: The author contributed to the formulation of the experimental concept, led the implementation and calibration of the experimental setup, performed data acquisition and processing, and wrote the manuscript.

C20 M. Ibrahimi, P. Lobaccaro, G. Di Sciullo, G. S. Sticca, F. Musumeci, R. S. Luís, A. Marotta, C. Antonelli, and M. Tornatore, "Data-Driven Failure Localization in Multi-Core Optical Networks," in *2025 30th OptoElectronics and Communications Conference (OECC) and 2025 International Conference on Photonics in Switching and Computing (PSC)*, Sapporo, Japan, June 2025, paper ThG1-1. [Invited paper]

This work demonstrates machine learning (ML)-assisted soft-failure localization using real data obtained from an MCF-based optical network testbed. The

[2] This work is based on results previously reported in [J1].
[3] Part of this work was later incorporated into [J1].

link consists of two concatenated 12.6 km-long, 4-core UC-MCF strands, field-deployed in an underground multi-service tunnel infrastructure located in downtown L'Aquila, Italy. To emulate varying levels of failure along the two-span link, three emulation stages are implemented. By systematically varying the failure severity, different severity regions are identified at each emulation stage. By applying localization algorithms on an experimentally-obtained dataset containing 36 720 data points (observations), accuracy levels of up to 94% are achieved over temporally-ordered data, using quality-of-transmission (QoT) metrics such as bit-error ratio (BER) and optical signal-to-noise ratio (OSNR).

Author's contribution: The author contributed to the formulation of the experimental concept, let the implementation and calibration of the experimental setup, and performed data acquisition and processing (but not the ML processing).

C23 G. Di Sciullo, D. A. Shaji, M. van den Hout, G. Rademacher, R. S. Luís, B. J. Puttnam, N. K. Fontaine, R. Ryf, H. Chen, M. Mazur *et al.*, "Reduction of Modal Dispersion through Mode Permutation in Multi-Mode Fiber Transmission," in *Optical Fiber Communication Conference (OFC) 2025*, San Francisco (CA), USA, March 2025, paper M4F.1.[4] [Invited paper]

C25 G. Di Sciullo, Q. Wu, R. S. Luís, B. J. Puttnam, G. Rademacher, R. Ryf, T. Hayashi, H. Furukawa, A. Mecozzi, and C. Antonelli, "Stimulated Raman scattering in WDM transmission over randomly-coupled multi-core fibers," in *2024 IEEE Photonics Conference (IPC)*, Rome, Italy, November 2024, paper ThG2.5.[5]

This work reports the first experimental characterization of the frequency derivative of the effective Raman gain coefficient in a CC-MCF. The derivative is estimated by analyzing the spectral distortion (tilt) induced by SRS over a C-band dense WDM system. The analysis is performed on a 69.3 km-long, 4-core CC-MCF link field-deployed in an underground multi-service tunnel infrastructure located in downtown L'Aquila, Italy. By comparing the effective Raman gain coefficient's derivative estimated in both the MCF and a reference SMF of similar length, co-deployed in the same infrastructure, this work demonstrates, for the first time, that they are comparable in magnitude. The results are consistent with the theory of SRS in the presence of strong inter-core coupling.

[4]This work is based on results previously reported in [J3].
[5]Part of this work was later incorporated into [J1].

Author's contribution: The author contributed to the formulation of the experimental concept, led the implementation and calibration of the experimental setup, performed data acquisition and processing, and wrote the manuscript.

C26 G. Di Sciullo, M. van den Hout, B. J. Puttnam, R. S. Luís, D. A. Shaji, G. Rademacher, C. Okonkwo, A. Mecozzi, C. Antonelli, and H. Furukawa, "Performance Comparison of QAM Modulation Formats on an All-4-Core Recirculating Loop," in *2024 IEEE Photonics Conference (IPC)*, Rome, Italy, November 2024, paper ThG2.4.[6]

This work assesses the performance of different modulation formats using the first all-multi-core-amplified recirculating loop, relying on 4-core C-band MC-EDFAs and DRA. In particular, PDM-QPSK, PDM-16QAM and PDM-64QAM signals are transmitted over a 4-core UC-MCF for distances of up to 12 053.6 km. Total decoded throughputs of 45.7 Tb/s after 12 053.6 km, 90.8 Tb/s after 3161.6 km, and 137 Tb/s after 395.2 km are achieved for PDM-QPSK, PDM-16QAM and PDM-64QAM signals, respectively.

Author's contribution: The author contributed to the formulation of the experimental concept, led the implementation and calibration of the experimental setup, performed data acquisition and processing, and wrote the manuscript.

C34 G. Di Sciullo, B. J. Puttnam, M. van den Hout, R. S. Luís, D. A. Shaji, G. Rademacher, C. Okonkwo, A. Mecozzi, C. Antonelli, and H. Furukawa, "45.7 Tb/s over 12 053 km Transmission with an All-Multi-Core Recirculating-Loop 4-Core-Fiber System," in *Optical Fiber Communication Conference (OFC) 2024*, San Diego (CA), USA, March 2024, paper Th3E.2.[7]

This work demonstrates long-haul transmission over 12 053 km of UC-MCF supported by the first all-multi-core-amplified system without the use of FIFO devices. The amplification scheme relies on 4-core C-band MC-EDFAs and DRA. By transmitting 175×24.5 Gbaud PDM-QPSK C-band signals across all four fiber cores, a total throughput of 49.9 Tb/s estimated from GMI and 45.7 Tb/s after FEC decoding is achieved. This represents the longest reach reported to date in SDM transmission experiments relying completely on SDM amplification.

[6]Part of this work was later incorporated into [J2].
[7]Part of this work was later incorporated into [J2].

Author's contribution: The author contributed to the formulation of the experimental concept, led the implementation and calibration of the experimental setup, performed data acquisition and processing, and wrote the manuscript.

C37 G. Di Sciullo, M. van den Hout, G. Rademacher, R. S. Luís, B. J. Puttnam, N. K. Fontaine, R. Ryf, H. Chen, M. Mazur, D. T. Neilson *et al.*, "Reduction of modal dispersion in a long-haul 15-mode fiber link by means of mode permutation," in *49th European Conference on Optical Communications (ECOC 2023)*, Glasgow, UK, October 2023, paper We.A.1.2.[8]

This work experimentally investigates mode permutation schemes to mitigate the impact of MD in a long-haul 15-mode fiber link. The proposed schemes reduce the rate at which the link's IIR duration increases with transmission distance, resulting in a substantial reduction in MIMO DSP complexity. An IIR duration reduction from 40 nm to less than 15 nm, while extending the transmission reach from 530 km to 1178 km, is demonstrated.

Author's contribution: The author contributed to the formulation of the experimental concept, participated in the implementation and calibration of the experimental setup, performed data acquisition and processing, and wrote the manuscript.

C41 G. Di Sciullo, M. van den Hout, G. Rademacher, R. S. Luís, B. J. Puttnam, N. K. Fontaine, R. Ryf, H. Chen, M. Mazur, D. T. Neilson *et al.*, "Modal Dispersion Mitigation in a long-haul 15-Mode Fiber link through Mode Permutation," in *2023 IEEE Photonics Society Summer Topicals Meeting Series (SUM)*, Sicily, Italy, July 2023, paper WC1.3.[9]

This work preliminary investigates mode permutation schemes to mitigate the impact of MD in a long-haul 15-mode fiber link. It shows that mode permutation leads to slower accumulation of MD, evidenced by a square-root dependence of the link's IIR response with transmission distance, in contrast to the linear growth observed without any mode permutation.

Author's contribution: The author contributed to the formulation of the experimental concept, participated in the implementation and calibration of the experimental setup, performed data acquisition and processing, and wrote the manuscript.

[8] Part of this work was later incorporated into [J3].

[9] Part of this work was later incorporated into [J3].

4.2.2 Publications with Substantial Contribution

The following publications are not appended to the thesis but contain related materials and applications.

C11 R. S. Luís, G. Di Sciullo, M. van den Hout, R. Emmerich, N. Braig-Christophersen, Q. Wu, B. J. Puttnam, D. Shaji, F. Graziosi, A. Mecozzi *et al.*, "19.2 THz S+C+L Transmission in a Field Deployed, Randomly-Coupled, Multicore Fiber," in *51st European Conference on Optical Communication (ECOC 2025)*, Copenhagen, Denmark, September 2025, paper M.03.05.2. [Top-scored paper]

This work demonstrates the first experimental transmission covering the S-, C-, and L-bands over a field-deployed, 4-core CC-MCF. The fiber link, field-deployed in an underground multi-service tunnel infrastructure located in downtown L'Aquila, Italy, has a total length of approximately 69.3 km. A record-wide 19.2 THz S+C+L-band signal, composed of 1540×12.25 Gbaud PDM-256QAM channels, was transmitted over each of the four fiber cores. Amplification relied on erbium-doped fiber amplifiers (EDFAs) and thulium-doped fiber amplifiers (TDFAs), in conjunction with bidirectional DRA with single-core pumping per direction, leveraging the strong inter-core coupling to achieve uniform gain across cores. A total capacity of 927.7 Tb/s estimated from the GMI and 863.4 Tb/s after FEC decoding is achieved. This work represents the first demonstration of S+C+L-band transmission in a standard cladding CC-MCF, the first use of DRA in such fibers, and the widest reported bandwidth along with the highest reported throughput of any field-deployed fiber. It is worth noting that an even higher capacity was later achieved in the 15-mode MMF experiment also presented and appended in this thesis, although it is unpublished at the time of writing.

Author's contribution: The author partially contributed to the formulation of the experimental concept, participated in the implementation and calibration of the experimental setup, and assisted in the data acquisition and processing.

C16 Q. Wu, D. Ribezzo, G. Di Sciullo, D. A. Shaji, R. S. Luís, D. Bacco, L. A. Zischler, A. Marotta, F. Graziosi, S. Cocchi *et al.*, "Field Demonstration of Quantum Key Distribution Coexisting with 110-Tb/s Classical Transmission over Multi-Core Fibers," in *51st European Conference on Optical Communication*

(ECOC 2025), Copenhagen, Denmark, September 2025, paper Th.02.03.3.[10] [Top-scored paper]

This work demonstrates the coexistence of QKD with classical communication channels in the C-band. The experimental analysis is performed over a 4-core UC-MCF link field-deployed in an underground multi-service tunnel infrastructure located in downtown L'Aquila, Italy, for varying transmission distances. The core dedicated to the quantum channel is operated in counter-propagating configuration with respect to the cores used for classical transmission. In the latter, full C-band dense WDM transmission is performed only at the maximum transmission distance of 25.2 km, yielding a total throughput of 110 Tb/s estimated based on GMI and 99.3 Tb/s after FEC decoding.

Author's contribution: The author contributed marginally to the formulation of the experimental concept, supported the implementation and calibration of the experimental setup, and led the classical transmission, data acquisition, and processing.

C17 N. Braig-Christophersen, C. Schmidt-Langhorst, R. Elschner, G. Di Sciullo, M. van den Hout, R. S. Luís, P. Sillard, C. Antonelli, C. Okonkwo, H. Furukawa *et al.*, "Partitioned MIMO Equalization with Mode-Group Specific Interface Resolution for SDM Transmission over 58.9 km 15-mode Fiber," in *51st European Conference on Optical Communication (ECOC 2025)*, Copenhagen, Denmark, September 2025, paper Th.02.04.4.

This work demonstrates partitioned MIMO equalization for PDM-QPSK signals transmitted over a 58.9 km-long, 15-mode MMF link. The conventional 30×30 MIMO equalizer is partitioned into five sub-equalizers corresponding to the different mode groups of the fiber, with lower-resolution inter-partition interfaces introduced to account for inter-group coupling. Different inter-partition interface resolutions are investigated and analyzed to minimize the performance degradation arising from partitioned-MIMO-related information penalties, while simultaneously achieving a significant reduction in the computational complexity of the MIMO DSP.

Author's contribution: The author participated in the implementation and calibration of the experimental setup and performed data acquisition (but not data processing).

[10] This work is based on results previously reported in [J9].

J9 Q. Wu, D. Ribezzo, G. Di Sciullo, S. Cocchi, D. A. Shaji, L. A. Zischler, R. S. Luís, P. Serena, C. Lasagni, A. Bononi *et al.*, "Integration of quantum key distribution and high-throughput classical communications in field-deployed multi-core fibers," in *Light Science and Applications*, vol. 14, no. 274 (2025).

This work proposes an analytical model for inter-core spontaneous Raman scattering (IC-SpRS) noise in MCF systems supporting the coexistence of QKD and classical transmission in the C-band. In addition, the model is experimentally validated for varying transmission distances and, for the first time, such coexistence is demonstrated over a 4-core UC-MCF link field-deployed in an underground multi-service tunnel infrastructure located in downtown L'Aquila, Italy. By injecting the quantum channel in a counter-propagating configuration with respect to the classical communication channels, the contributions of the individual classical cores to the Raman noise are analyzed and found to be in good agreement with theoretical predictions. Simultaneously, in the classical cores, full C-band dense WDM coherent transmission is performed over the maximum transmission distance of 25.2 km, yielding a total throughput of 110 Tb/s estimated based on GMI and 99.3 Tb/s after FEC decoding.

Author's contribution: The author contributed to the formulation of the experimental concept, supported the implementation and calibration of the different experimental setups, and led the classical transmission, data acquisition, and processing.

C28 Q. Wu, D. Ribezzo, G. Di Sciullo, D. A. Shaji, T. Hayashi, R. S. Luís, D. Bacco, Y. Zhu, W. Hu, A. Mecozzi *et al.*, "Co-existence of Quantum Key Distribution and Classical Transmission in a Field-Deployed Uncoupled-Core Four-Core Fiber," in *50th European Conference on Optical Communication (ECOC 2024)*, Frankfurt, Germany, September 2024, paper W2A.178.[11]

This work investigates the coexistence of QKD and classical transmission in a field-deployed UC-MCF. The experimental analysis is carried out over a 4-core UC-MCF link field-deployed in an underground multi-service tunnel infrastructure located in downtown L'Aquila, Italy. The impact of IC-SpRS and inter-core crosstalk (IC-XT) is investigated, and the feasibility of coexisting QKD alongside dense WDM classical transmission is assessed when one core is dedicated to the quantum channel and the remaining three cores are used for classical data transmission.

[11] Part of this work was later incorporated into [J9].

Author's contribution: The author contributed marginally to the formulation of the experimental concept and supported the implementation and calibration of the experimental setup.

J17 M. van den Hout, G. Di Sciullo, R. S. Luís, B. J. Puttnam, N. K. Fontaine, R. Ryf, H. Chen, M. Mazur, D. T. Neilson, P. Sillard *et al.*, "Transmission of 273.6 Tb/s Over 1001 km of 15-Mode Multi-Mode Fiber Using C-Band Only 16-QAM Signals," in *Journal of Lightwave Technology*, vol. 42, no. 3, pp. 1136-1142, 1 Feb, 2024.

This work demonstrates a recirculating-loop-based C-band transmission over a 15-mode MMF. By transmitting 184×24.5 Gbaud PDM-16QAM signals on each of the 15 fiber modes, a total capacity of 312.6 Tb/s estimated from the GMI and 273.6 Tb/s after FEC decoding is achieved at a transmission distance of 1001 km. This result represents the highest reported data rate for long-distance MMF transmission. Furthermore, with 273.9 Pb/s·km (273.6 Tb/s×1001 km), it also represents a record capacity-distance product for MMF transmission.

Author's contribution: The author contributed to the formulation of the experimental concept, participated in the implementation and calibration of the experimental setup, and assisted in the data acquisition process.

C36 B. J. Puttnam, M. van den Hout, G. Di Sciullo, R. S. Luís, G. Rademacher, J. Sakaguchi, C. Antonelli, C. Okonkwo, and H. Furukawa, "22.9 Pb/s data-rate by extreme space-wavelength multiplexing," in *49th European Conference on Optical Communications (ECOC 2023)*, Glasgow, UK, October 2023, paper Th.C.2.1. [Post-deadline paper]

This work demonstrates extreme WDM and SDM by transmitting a 19 THz-wide optical spectrum over a 38-core 3-mode multi-core multi-mode fiber (MC-MMF) system. By transmitting 750×24.5 Gbaud PDM-256QAM signals across the S-, C-, and L-bands over 114 spatial channels, a total data rate of 24.7 Pb/s estimated from GMI and 22.9 Pb/s after FEC decoding is achieved. This result represents the highest throughput ever reported over a single optical fiber, making a two-fold increase compared to the previously reported record of 10.66 Pb/s after FEC decoding achieved using the same fiber.

Author's contribution: The author contributed to the implementation and calibration of the experimental setup.

C38 M. van den Hout, B. J. Puttnam, G. Di Sciullo, R. S. Luís, G. Rademacher, C. Antonelli, C. Okonkwo, and H. Furukawa, "Transmission of 138.9 Tb/s over 12 345 km of 125µm cladding diameter 4-core fiber using signals spanning S, C, and L-band," in *49th European Conference on Optical Communications (ECOC 2023)*, Glasgow, UK, October 2023, paper M.A.5.5.

This work demonstrates recirculating loop transmission of S-, C-, and L-band signals over 12 345 km of 4-core UC-MCF. With 518×24.5 Gbaud signals transmitted on each core, a total throughput of 151.2 Tb/s estimated from GMI and 138.9 Tb/s after FEC decoding are achieved. The combination of high capacity and long transmission distance resulted in the highest reported capacity-distance product of 1714.7 Pb/s·km in a standard cladding diameter MCF at the time of manuscript publication.

Author's contribution: The author contributed to the implementation and calibration of the experimental setup.

C43 M. van den Hout, G. Di Sciullo, G. Rademacher, R. S. Luís, B. J. Puttnam, N. K. Fontaine, R. Ryf, H. Chen, M. Mazur, D. T. Neilson *et al.*, "273.6 Tb/s Transmission Over 1001 km of 15-Mode Fiber Using 16-QAM C-Band Signals," in *Optical Fiber Communication Conference (OFC) 2023*, San Diego (CA), USA, March 2023, paper Th4B.5.[12] [Post-deadline paper]

This work demonstrates a recirculating-loop-based C-band transmission over a 15-mode MMF. By transmitting 184×24.5 Gbaud PDM-16QAM signals on each of the 15 fiber modes, a total capacity of 312.6 Tb/s estimated from the GMI and 273.6 Tb/s after FEC decoding is achieved at a transmission distance of 1001 km. This result represents the highest reported data rate for long-distance MMF transmission. Furthermore, with 273.9 Pb/s·km (273.6 Tb/s×1001 km), it also represents a record capacity-distance product for MMF transmission.

Author's contribution: The author contributed to the formulation of the experimental concept, participated in the implementation and calibration of the experimental setup, and assisted in the data acquisition process.

C44 R. S. Luís, G. Di Sciullo, G. Rademacher, B. J. Puttnam, A. Marotta, R. Emmerich, N. Braig-Christophersen, R. Stolte, F. Graziosi, A. Mecozzi *et al.*, "Colorless and Directionless ROADM for Meshed Coupled-Core Multicore Fiber

[12] This work was later extended into [J17].

Networks," in *Optical Fiber Communication Conference (OFC) 2023*, San Diego (CA), USA, March 2023, paper Th4C.3. [Post-deadline paper]

This work demonstrates the first meshed spatial-super-channel switching SDM network using field-deployed CC-MCFs and UC-MCFs with a three line-side, colorless, and directionless reconfigurable optical add-drop multiplexer (ROADM). The CC-MCF links, field-deployed in an underground multi-service tunnel infrastructure located in downtown L'Aquila, Italy, have total lengths of approximately 69.3 km and 6.3 km, while the field-deployed UC-MCF link has a total length of 6.3 km. Nineteen network scenarios typical of meshed networks are investigated, including full add and drop, full express, optical bypass and grooming with 2 Tb/s spatial-super-channel tributaries. This work represents the first demonstration of a meshed SDM network using field-deployed CC-MCFs.

Author's contribution: The author contributed to the implementation and calibration of the experimental setup.

C45 A. Gatto, P. Parolari, R. S. Luís, G. Rademacher, B. J. Puttnam, R. Emmerich, C. Schubert, G. Ferri, F. Achten, P. Sillard, P. Martelli, G. Di Sciullo *et al.*, "Partial MIMO-based Mode Division Multiplexing Transmission over the First Field-Deployed 15-Mode Fiber in Metro Scenario," in *Optical Fiber Communication Conference (OFC) 2023*, San Diego (CA), USA, March 2023, paper M2B.3.[13]

This work investigates MMF transmission with partial MIMO equalization. The 15-mode MMF link, with a total length of 6.1 km, is deployed in an underground multi-service tunnel infrastructure located in downtown L'Aquila, Italy. The achievable throughput is evaluated as a function of the required partial-MIMO receiver resources, considering multiple combinations of mode groups (MGs) and various modulation formats.

Author's contribution: The author contributed to the implementation and calibration of the experimental setup.

C46 P. Parolari, A. Gatto, R. S. Luís, G. Rademacher, B. J. Puttnam, R. Emmerich, C. Schubert, G. Ferri, F. Achten, P. Sillard, P. Martelli, G. Di Sciullo *et al.*, "Demonstration of Multi-Hop Mode-Group Routing in a Field-Deployed Multi-Mode Fiber Network," in *Optical Fiber Communication Conference (OFC) 2023*, San Diego (CA), USA, March 2023, paper M4G.3.

[13] This work was later extended into [J15].

This work demonstrates SDM switching based on the routing of groups of degenerate spatial modes in a 15-mode MMF link in urban networks, improving network flexibility at the node level. The link, with a total length of 6.1 km, is deployed in an underground multi-service tunnel infrastructure located in downtown L'Aquila, Italy. The results show that inter-mode-group crosstalk (IG-XT) affects the performance in terms of maximum achievable throughput. However, the selection of suitable combinations of modes enables the routing of Tb/s data rates.

Author's contribution: The author contributed to the implementation and calibration of the experimental setup.

C47 R. S. Luís, G. Rademacher, B. J. Puttnam, G. Di Sciullo, A. Marotta, R. Emmerich, N. Braig-Christophersen, R. Stolte, F. Graziosi, A. Mecozzi *et al.*, "Demonstration of a Spatial Super Channel Switching SDM Network Node on a Field Deployed 15-Mode Fiber Network," in *48th European Conference on Optical Communications (ECOC 2022)*, Basel, Switzerland, September 2022, paper Th3C.5.[14] [Post-deadline paper]

This work demonstrates a high spatial spectral efficiency SDM ROADM operating on a field-deployed 15-mode MMF network. The link, with a total length of 6.1 km, is deployed in an underground multi-service tunnel infrastructure located in downtown L'Aquila, Italy. The switching fabric enabled 5 Tb/s tributaries, and full add and drop, full express and optical bypass scenarios were successfully demonstrated. This resulted in the highest mode-count ever reported on an SDM ROADM and the first implementation using a field-deployed fiber.

Author's contribution: The author contributed to the implementation and calibration of the experimental setup.

C48 G. Rademacher, R. S. Luís, B. J. Puttnam, G. Di Sciullo, R. Emmerich, N. Braig-Christophersen, A. Marotta, L. Dallachiesa, R. Ryf, A. Mecozzi *et al.*, "Characterization of the First Field-Deployed 15-Mode Fiber Cable for High Density Space-Division Multiplexing," in *48th European Conference on Optical Communications (ECOC 2022)*, Basel, Switzerland, September 2022, paper Th3B.1. [Post-deadline paper]

[14]This work was later extended into [J18].

This work reports the first experimental characterization of a deployed 15-mode fiber cable, installed in an underground multi-service tunnel infrastructure located in downtown L'Aquila, Italy. Fiber propagation characteristics including IIR duration (providing an estimates of MD), MDL, crosstalk (XT) and signal-to-noise ratio (SNR) for several WDM channels across the C-band are measured for transmission distances of 6.1 km and 48.8 km. Since MMF properties can change after field-deployment, these results demonstrate the high maturity of MMF-based SDM technologies for high-capacity transmission systems.

Author's contribution: The author contributed to the implementation and calibration of the experimental setup.

4.2.3 Publications with Marginal Contribution

The following publications or submitted manuscripts are not covered in the thesis but contain related materials and applications.

C2 A. Marotta, P. A. Robles, P. Gonzalez, L. D'Errico, I. Babiker, C. Centofanti, G. Di Sciullo, C. Antonelli, L. Velasco, S. Tennina *et al.*, "End-to-End Orchestration across MCF Infrastructure: Field Trial of Spatial PON and P2MP Metro Convergence with O-RAN for AR/VR Services with Edge Offload," in *Optical Fiber Communication Conference (OFC) 2026*, Los Angeles (CA), USA, March 2026, paper Th3E.4.

C3 D. A. Shaji, J. Schneck, L. A. Zischler, G. Di Sciullo, R. S. Luís, P. Sillard, H. Furukawa, G. Rademacher, A. Mecozzi, and C. Antonelli, "Raman Gain Profiling and Distributed Raman Amplification in a Field-Deployed 15-Mode Graded-Index Multimode Fiber," in *Optical Fiber Communication Conference (OFC) 2026*, Los Angeles (CA), USA, March 2026, paper M4E.3.

C4 C. Lasagni, L. A. Zischler, P. Serena, A. Bononi, G. Di Sciullo, A. Mecozzi, and C. Antonelli, "Investigation of Wide-band Nonlinear Effects Leveraging a Semi-analytical EGN Model," in *Optical Fiber Communication Conference (OFC) 2026*, Los Angeles (CA), USA, March 2026, paper Tu3A.3.

C5 M. Giacomin, J. M. Traktenberg, M. R. Bolaños, G. Di Sciullo, T. Hayashi, C. Antonelli, G. Vallone, P. Villoresi, and C. Agnesi, "Demonstration of a Cross-Encoded RFI QKD system in a field-deployed multi-core fiber," in *Optical Fiber Communication Conference (OFC) 2026*, Los Angeles (CA), USA, March 2026, paper M1K.5.

C6 M. Ibrahimi, G. S. Sticca, M. Tibaldini, M. Milione, F. Musumeci, G. Di Sciullo, A. Marotta, C. Antonelli, and M. Tornatore, "A Network-Wide Power Analysis of Cladding-Pumped Amplification in Multi-Core Optical Networks," in *Optical Fiber Communication Conference (OFC) 2026*, Los Angeles (CA), USA, March 2026, paper W1H.4.

J4 D. A. Shaji, R. S. Luís, D. Orsuti, L. A. Zischler, B. J. Puttnam, M. S. Neves, B. Boriboon, G. Di Sciullo, Q. Wu, M. Tan *et al.*, "Experimental Evaluation of Transmission of C+L+U bands over an Unrepeatered Link," in *Journal of Lightwave Technology*, vol. 44, no. 4, pp. 1249-1258, 15 Feb, 2026.

J5 D. A. Shaji, R. S. Luís, B. J. Puttnam, D. Orsuti, M. S. Neves, B. Boriboon, G. Di Sciullo, Q. Wu, S. Gross, A. Ross-Adams *et al.*, "Experimental Demonstration of a Low-Cost Petabit-per-Second SDM Network Node," submitted to *Optics Express* (Under Revision).

J6 L. A. Zischler, C. Lasagni, P. Serena, A. Bononi, G. Di Sciullo, D. A. Shaji, A. Mecozzi, and C. Antonelli, "Closed-form Expression for the Power Profile in Wideband Systems with Inter-channel Stimulated Raman Scattering," in *Journal of Lightwave Technology*, vol. 44, no. 1, pp. 115-124, 1 Jan, 2026.

C7 D. A. Shaji, B. J. Puttnam, R. S. Luís, D. Orsuti, N. K. Fontaine, M. Mazur, L. Dallachiesa, G. Di Sciullo, L. A. Zischler, R. Ryf *et al.*, "Impact of Distributed Raman Amplification on OSNR in Unrepeatered ESCL Transmission," in *2025 IEEE Photonics Conference (IPC)*, Singapore, November 2025, paper WE3.1.

C8 L. A. Zischler, J. Schneck, G. Di Sciullo, D. A. Shaji, B. Kalla, S. Gaiani, R. S. Luís, D. Orsuti, P. Sillard, C. Okonkwo *et al.*, "Evaluation of Inter-Mode-Group Stimulated Raman Scattering on Multi-Mode Fibers," in *2025 IEEE Photonics Conference (IPC)*, Singapore, November 2025, paper MF1.4.

C9 A. Marotta, G. Di Sciullo, C. Antonelli, M. Ibrahimi, G. S. Sticca, F. Musumeci, and M. Tornatore, "Experimental Insights on Fault Localization and Energy Efficiency in Multi-Core Fiber Systems," in *2025 Asia Communications and Photonics Conference (ACP)*, Suzhou, China, November 2025, paper ACP2025-0801-6. [Invited paper]

J7 L. A. Zischler, Ç. Özkan, T. Vosshenrich, Q. Wu, G. Di Sciullo, D. Shaji, C. Lasagni, P. Serena, A. Bononi, A. Ghazisaeidi *et al.*, "Accurate and Effective

Model for Coexistence of Classical and Quantum Signals In Optical Fibers," in *arXiv*, arXiv:2510.02807 [quant-ph], 2025.

C12 C. Lasagni, P. Serena, A. Bononi, G. Di Sciullo, L. A. Zischler, R. S. Luís, A. Mecozzi, and C. Antonelli, "Nonlinear Interference Investigation in Coupled-Core Multi-Core Fibers with Stimulated Raman Scattering and Mode Dispersion," in *51st European Conference on Optical Communication (ECOC 2025)*, Copenhagen, Denmark, September 2025, paper Tu.01.05.2.

C13 D. A. Shaji, B. J. Puttnam, R. S. Luís, D. Orsuti, N. K. Fontaine, M. Mazur, L. Dallachiesa, G. Di Sciullo, L. A. Zischler, R. Ryf *et al.*, "Experimental Evaluation of Throughput Gains from Distributed Raman Amplification in Ultra-Wideband ESCL Transmission," in *51st European Conference on Optical Communication (ECOC 2025)*, Copenhagen, Denmark, September 2025, paper Tu.04.05.2.

C15 Q. Wu, G. Di Sciullo, D. A. Shaji, D. Ribezzo, D. Bacco, R. S. Luís, T. Hayashi, L. A. Zischler, A. Marotta, F. Graziosi *et al.*, "Co-existence of Quantum-Key Distribution and Classical Transmission in Space-Division Multiplexed Fiber-Optic Systems: Modelling and Validation over Field-Deployed Multi-Core Fibers," in *51st European Conference on Optical Communication (ECOC 2025)*, Copenhagen, Denmark, September 2025, paper W.02.01.183.[15]

C18 R. S. Bravo Ospina, A. Ghazisaeidi, S. Gaiani, R. S. Luís, D. Orsuti, B. Kalla, M. van den Hout, P. Sillard, F. Achten, G. Di Sciullo *et al.*, "Rate-Adaptive Partial MIMO Equalization for Mode-Group Selective Transmission over Few Mode Fibers," in *51st European Conference on Optical Communication (ECOC 2025)*, Copenhagen, Denmark, September 2025, paper Th.02.04.5.

J8 L. A. Zischler, C. Lasagni, P. Serena, A. Bononi, G. Di Sciullo, D. Shaji, A. Mecozzi, and C. Antonelli, "Closed-form Expression for the Power Profile in Wideband Systems with Inter-channel Stimulated Raman Scattering," in *arXiv*, arXiv:2508.00093 [eess.SP], 2025.

C19 A. Marotta, C. Centofanti, G. Di Sciullo, C. Antonelli, F. Graziosi and L. Valcarenghi, "A Resilient Passive Optical Network Architecture Based on Dynamic Spatial Aggregation," in *2025 25th Anniversary International Conference on*

[15] This work is based on results previously reported in [J9].

Transparent Optical Networks (ICTON), Barcelona, Spain, July 2025, paper Mo.C7.6.

C21 C. Antonelli, A. Mecozzi, A. Marotta, F. Graziosi, G. Di Sciullo, D. A. Shaji, L. A. Zischler, Q. Wu, M. Mazur, N. K. Fontaine *et al.*, "Space-Division Multiplexed Transmission in Deployed Fibers," in *2025 30th OptoElectronics and Communications Conference (OECC) and 2025 International Conference on Photonics in Switching and Computing (PSC)*, Sapporo, Japan, June 2025, paper WD1-1. [Invited paper]

C22 D. A. Shaji, R. S. Luís, B. J. Puttnam, D. Orsuti, M. S. Neves, B. Boriboon, G. Di Sciullo, Q. Wu, S. Gross, A. Ross-Adams *et al.*, "Experimental Demonstration of a Low-Cost Petabit-Per-Second SDM Network Node," in *2025 Conference on Lasers and Electro-Optics Europe & European Quantum Electronics Conference (CLEO/Europe-EQEC)*, Munich, Germany, June 2025, paper CI-1.2.[16] [Invited paper]

J10 N. Hoghooghi, M. Mazur, N. K. Fontaine, Y. Liu, D. Lee, C. McLemore, T. Nakamura, T. Hayashi, G. Di Sciullo, D. Shaji *et al.*, "Ultrastable optical frequency transfer and attosecond timing in deployed multicore fiber," in *Optica*, vol. 12, pp. 894-899 (2025).

C24 H. Chen, N. K. Fontaine, R. Ryf, G. Di Sciullo, L. Dallachiesa, K. Kim, C. Tran, M. Mazur, X. Xu, J. E. Simsarian *et al.*, "Reconfigurable Multi-Port Multi-Wavelength Coherent Receiver," in *Optical Fiber Communication Conference (OFC) 2025*, San Francisco (CA), USA, March 2025, paper M2D.1. [Top-scored paper]

J11 M. van den Hout, R. S. Luís, B. J. Puttnam, G. Di Sciullo, T. Hayashi, A. Inoue, T. Nagashima, S. Gross, A. Ross-Adams, M. J. Withford *et al.*, "Reaching the pinnacle of high-capacity optical transmission using a standard cladding diameter coupled-core multi-core fiber," in *Nature Communications*, vol. 16, no. 3833 (2025).

J12 D. Orsuti, B. J. Puttnam, R. S. Luís, M. S. Neves, M. van den Hout, G. Di Sciullo, D. A. Shaji, B. Boriboon, G. Rademacher, J. Sakaguchi *et al.*, "S/C/L-Band Transmission in Few-Mode MCF With Optical Frequency Comb Regen-

[16] This work was later extended into [J5].

eration via Single-Mode Core Seed Distribution," in *Journal of Lightwave Technology*, vol. 43, no. 4, pp. 1786-1793, 15 Feb, 2025.

C27 Q. Wu, D. Ribezzo, G. Di Sciullo, D. A. Shaji, T. Hayashi, R. S. Luís, D. Bacco, Y. Zhu, W. Hu, A. Mecozzi *et al.*, "Integration of Quantum Key Distribution and Classical Communications Over Field-Deployed Uncoupled-Core Four-Core Fiber," in *2024 IEEE Photonics Conference (IPC)*, Rome, Italy, November 2024, paper ME4.3.[17]

C29 M. van den Hout, G. Di Sciullo, R. S. Luís, B. J. Puttnam, N. K. Fontaine, R. Ryf, H. Chen, M. Mazur, D. T. Neilson, P. Sillard *et al.*, "Long-Distance Space-Division-Multiplexed Transmission Using High-Mode-Count Multi-Mode Fibers," in *50th European Conference on Optical Communication (ECOC 2024)*, Frankfurt, Germany, September 2024, paper W3B.3. [Invited paper]

C30 C. Antonelli, A. Mecozzi, A. Marotta, F. Graziosi, G. Di Sciullo, D. A. Shaji, Q. Wu, D. Ribezzo, M. Mazur, N. K. Fontaine *et al.*, "Space-Division Multiplexed Transmission from the Lab to the Field," in *50th European Conference on Optical Communication (ECOC 2024)*, Frankfurt, Germany, September 2024, paper Tu3B.4. [Invited paper]

J13 N. Hoghooghi, M. Mazur, N. K. Fontaine, Y. Liu, D. Lee, C. McLemore, T. Nakamura, T. Hayashi, G. Di Sciullo, D. A. Shaji *et al.*, "Enabling a multifunctional telecommunications fiber optic network: Ultrastable optical frequency transfer and attosecond timing in deployed multicore fiber," in *arXiv*, arXiv:2410.13801 [physics.optics], 2024.

C31 B. J. Puttnam, D. Orsuti, R. S. Luís, M. S. Neves, M. van den Hout, G. Di Sciullo, G. Rademacher, J. Sakaguchi, C. Antonelli, C. Okonkwo *et al.*, "Wideband S, C, + L-Band Comb Regeneration in Large-Scale Few-Mode MCF Link with Single-Mode Seed Channel," in *Optical Fiber Communication Conference (OFC) 2024*, San Diego (CA), USA, March 2024, paper Th4A.6.[18] [Post-deadline paper]

C32 N. Hoghooghi, M. Mazur, N. K. Fontaine, Y. Liu, T. Hayashi, G. Di Sciullo, D. A. Shaji, A. Mecozzi, C. Antonelli, and F. Quinlan, "Towards international

[17] Part of this work was later incorporated into [J9].
[18] This work was later extended into [J12].

clock comparisons on a telecom network: ultrastable optical frequency transfer over deployed multi-core fiber," in *Optical Fiber Communication Conference (OFC) 2024*, San Diego (CA), USA, March 2024, paper Th4A.5.[19] [Post-deadline paper]

C33 C. Antonelli, A. Mecozzi, A. Marotta, F. Graziosi, G. Di Sciullo, D. Ribezzo, M. Mazur, N. K. Fontaine, L. Dallachiesa, R. Ryf *et al.*, "Field Transmission Performance of Multi-core and Few-Mode Fibers," in *Optical Fiber Communication Conference (OFC) 2024*, San Diego (CA), USA, March 2024, paper W3J.1. [Invited paper]

C35 M. van den Hout, R. S. Bravo Ospina, R. S. Luís, B. J. Puttnam, G. Di Sciullo, T. Hayashi, A. Inoue, T. Nagashima, S. Gross, A. Ross-Adams *et al.*, "Experimental Analysis of Receiver Failure For 19-Core Randomly Coupled Core Fibre Transmission," in *Optical Fiber Communication Conference (OFC) 2024*, San Diego (CA), USA, March 2024, paper W2A.28.

J14 B. J. Puttnam, R. S. Luís, D. Orsuti, G. Rademacher, G. Di Sciullo, M. van den Hout, J. Sakaguchi, C. Antonelli, C. Okonkwo, L. Palmieri *et al.*, "Experimental demonstration of a multi-core fiber seeded comb optical network (MCF-SCON)," in *Journal of Optical Communications and Networking*, vol. 16, no. 7, pp. C69-C75, July 2024.

J15 A. Gatto, P. Parolari, R. S. Luís, G. Rademacher, B. J. Puttnam, R. Emmerich, C. Schubert, G. Ferri, F. Achten, P. Sillard, P. Martelli, G. Di Sciullo *et al.*, "Partial-MIMO Based Mode-Group Transmission and Routing in a Field-Deployed 15-Mode Network: Throughput, DSP Resources and Network Flexibility," in *Journal of Lightwave Technology*, vol. 42, no. 14, pp. 4720-4732, 15 July, 2024.

J16 R. S. Luís, B. J. Puttnam, G. Rademacher, M. van den Hout, G. Di Sciullo, D. Orsuti, C. Okonkwo, C. Antonelli, J. Sakaguchi, and H. Furukawa, "Wideband Unrepeatered Transmission Using Doped Tellurite-Fiber Amplifiers," in *Journal of Lightwave Technology*, vol. 42, no. 13, pp. 4410-4416, 1 July, 2024.

C39 B. J. Puttnam, R. S. Luís, G. Rademacher, G. Di Sciullo, M. van den Hout, J. Sakaguchi, C. Antonelli, C. Okonkwo, and H. Furukawa, "C + L-band seeded comb regeneration for MCF networks," in *49th European Conference on Optical*

[19] This work was later extended into [J10] and [J13].

Communications (ECOC 2023), Glasgow, UK, October 2023, paper Th.B.2.5.[20] [Top-scored paper]

C40 R. S. Luís, B. J. Puttnam, G. Rademacher, M. van den Hout, G. Di Sciullo, C. Okonkwo, C. Antonelli, J. Sakaguchi, and H. Furukawa, "40.5 Tb/s, 312.9 km, unrepeatered transmission using erbium-doped tellurite fiber amplifiers," in *49th European Conference on Optical Communications (ECOC 2023)*, Glasgow, UK, October 2023, paper Th.B.6.5.[21]

J18 R. S. Luís, G. Rademacher, B. J. Puttnam, G. Di Sciullo, A. Marotta, R. Emmerich, N. Braig-Christophersen, R. Stolte, F. Graziosi, A. Mecozzi *et al.*, "Demonstration of a 15-Mode Network Node Supported by a Field-Deployed 15-Mode Fiber," in *Journal of Lightwave Technology*, vol. 41, no. 12, pp. 3695-3703, 15 June, 2023.

C42 G. Rademacher, M. van den Hout, R. S. Luís, B. J. Puttnam, G. Di Sciullo, T. Hayashi, A. Inoue, T. Nagashima, S. Gross, A. Ross-Adams *et al.*, "Randomly Coupled 19-Core Multi-Core Fiber with Standard Cladding Diameter," in *Optical Fiber Communication Conference (OFC) 2023*, San Diego (CA), USA, March 2023, paper Th4A.4.[22] [Post-deadline paper]

[20] This work was later extended into [J14].
[21] This work was later extended into [J16].
[22] This work was later extended into [J11].

Part II

Appended Papers

Conference C1

Petabit-per-Second C+L Band Transmission Over a Field-deployed 15-Mode Fiber Link

G. Di Sciullo, R. S. Luís, M. van den Hout, Q. Wu, P. Sillard, F. Achten, R. Emmerich, N. Braig-Christophersen, B. J. Puttnam, D. A. Shaji, L. A. Zischler, A. Marotta, F. Graziosi, C. Lasagni, P. Serena, A. Bononi, G. Rademacher, C. Okonkwo, C. Schubert, R. Freund, J. Sakaguchi, A. Mecozzi, H. Furukawa, and C. Antonelli

in

Optical Fiber Communication Conference (OFC) 2026, Los Angeles (CA), USA, March 2026, paper M1C.2

Abstract

We demonstrate the first C+L band transmission over a field-deployed 6.1 km-long 15-mode fiber, achieving a record decoded throughput of 1.06 Pb/s. This marks the first petabit-per-second-class transmission over any field-deployed fiber.

C1.1 Introduction

Space-division multiplexing (SDM) over multi-mode fiber (MMF) has been shown to achieve the highest spatial density in optical transmission [7, 45], enabling data rates well above 1 Pb/s [43, 44], while maintaining the standard 125 µm cladding diameter and ensuring similar mechanical reliability as single-mode fiber (SMF) [42]. Although MMF transmission has been extensively addressed in laboratory conditions [43, 45, 115, 140–142], and it has been shown that MMF transmission properties can differ significantly after installation [143], petabit-per-second transmission in field-deployed fibers remains to be demonstrated.

Here, we demonstrate the first petabit-per-second-class transmission over a field-deployed MMF. We transmit 266×35 GBaud, 15-mode spatial super channels, across a bandwidth of 88.5 nm covering the C+L band. The transmission is performed over a 6.1 km-long, 15-mode fiber link, deployed in the city of L'Aquila, Italy, as part of the INCIPICT project [144]. By evaluating signal performance for all channels, we achieve a data rate of 1.13 Pb/s, estimated from the generalized mutual information (GMI), and 1.06 Pb/s after forward error correction (FEC) decoding. This represents the highest throughput ever reported over any field-deployed fiber [145], and the first demonstration of petabit-per-second-class transmission over such fibers, also exceeding the previously reported record throughput achieved with the same fiber in laboratory settings [43].

C1.2 Experimental Setup

The experimental transmission setup is shown in Fig. C1.1. A single-channel test band tunable across the C+L band was obtained by modulating the carrier of a tunable laser source (TLS) through a dual-polarization IQ modulator (DP-IQM) designed for operation in the C-band. This was driven by a 100 GSa/s, 4-channel arbitrary waveform generator (AWG) to produce a 35 GBaud, polarization-division multiplexing 64-ary quadrature-amplitude modulated (PDM-64QAM) signal in the C-band, and a 35 GBaud, PDM-16QAM signal in the L-band. A channel spacing of 40 GHz and a root-raised cosine pulse shape with a roll-off factor of 1% were employed in both bands. A noise-loaded dummy band covering the C+L band was also generated by spectrally flattening the amplified spontaneous emission (ASE) noise produced by C- and L-band erbium-doped fiber amplifiers (EDFAs). The C-band ranged between 1526.5 nm and 1568.5 nm, while the L-band was split into the lower

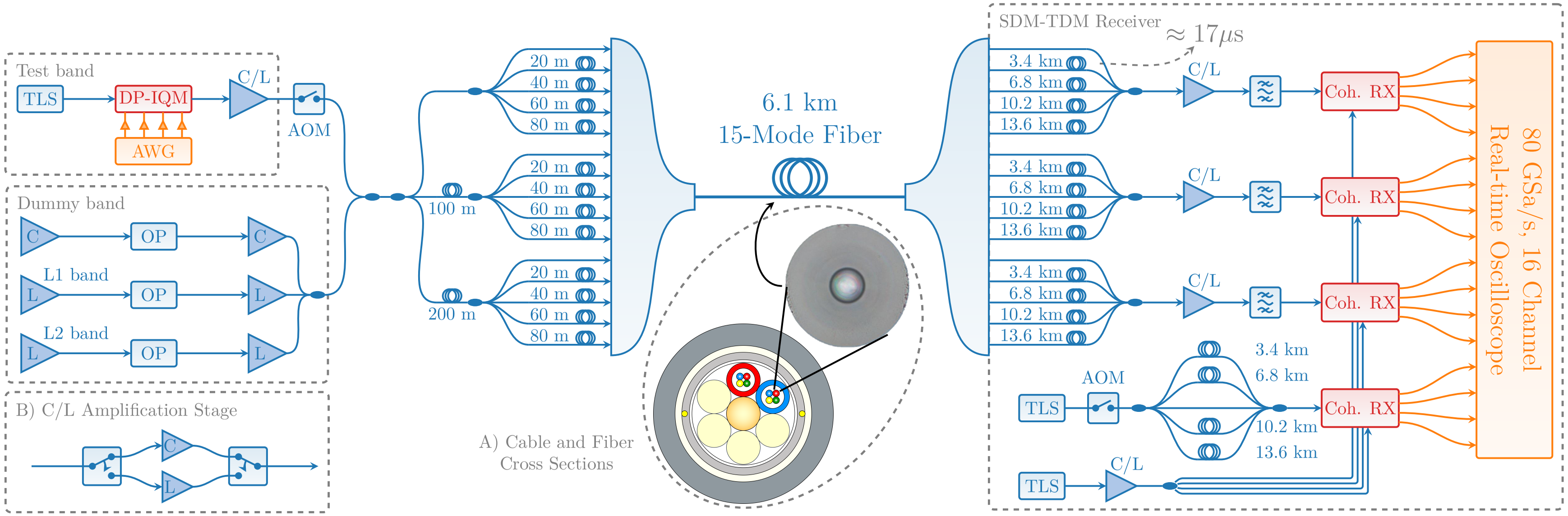

Figure C1.1: Experimental setup of the 15-mode-fiber transmission system. Inset A shows the multi-mode fiber cable and the multi-mode fiber cross sections. Inset B illustrates the C/L amplification stage implementation.

L1-band, ranging between 1569.5 nm and 1585.0 nm, and the upper L2-band, ranging between 1585.0 nm and 1615.0 nm. Spectral flatness was achieved using band-specific optical processors (OPs), which were also programmed to shape the flattened noise into ASE-based wavelength-division multiplexing (WDM) channels as illustrated in Fig. C1.2(a). The OPs were also used to remove the ASE channel corresponding to the test band. The transmission signal consisting of the test and dummy bands was split and delayed to generate 15 uncorrelated copies of the same signal with relative delays of 100 ns, which were then fed into a multi-plane light converter (MPLC)-based mode-multiplexer (MUX). The total per-mode power across both C- and L-bands at the input of the MUX was approximately 18 dBm. The multi-mode field at the MUX output propagated over a field-deployed 6.1 km-long, graded-index 15-mode fiber with a standard cladding diameter [38, 146], before being converted back into single-mode fields by the mode-demultiplexer (DeMUX). The fiber cross section is shown in inset A of Fig. C1.1.

A time-division multiplexing (TDM) receiver was implemented to receive all 15 modes by sharing three coherent receivers (Coh. RXs) [147]. The 15 single-mode outputs of the DeMUX were divided into three groups of 5 modes each. Within each group, the 5 signals were optically delayed by multiples of approximately 17 µs, corresponding to fiber spools of multiples of 3.4 km. To avoid time-domain interference between signals from different modes, an acousto-optic modulator (AOM) operating with a duty-cycle of 16.6% on a time period of 100 µs was used at the transmitter side to cut the test-band signal prior to its combination with the dummy band. The three TDM signals arriving at the receiver were amplified using C- or L-band EDFAs, that were manually selected as illustrated in inset B of Fig. C1.1, depending on the wavelength of the channel under test (CUT). Both the L1- and L2-bands were collectively amplified by a single L-band EDFA. The CUT was then selected by optical filters covering the C+L band, and detected by means of Coh. RXs designed for operation in the C-band. The local oscillator (LO), which was a TLS with a linewidth of less than 10 kHz, was shared among the three Coh. RXs. To detect the relative phase and frequency changes of the LO across the five different time slots, a similar TDM setup was implemented. Specifically, the output from a different TLS of the same kind as the LO was passed through an AOM operating under the same conditions as that at the transmitter side, and was then split, delayed and combined again prior to detection by a fourth Coh. RX [148]. The electrical signals from the Coh. RXs were digitized using an 80-GSa/s, 16 channels real-time oscilloscope (RTO), storing traces for offline digital signal processing (DSP). The DSP consisted of stages for time-division demultiplexing, frequency recovery, and TDM-related phase-change compensation, followed by a time-domain 30×30 multiple-input multiple-output (MIMO) equalizer. The MIMO equalizer operated with 1201 half-symbol-spaced taps, corresponding to a temporal memory of approximately 17.2 ns, which were initially updated in a data-aided mode before switching into decision-directed operation after convergence, for signal performance estimation. Carrier recovery was implemented within the equalizer loop. Data rates were calculated based on GMI and by implementing an FEC coding scheme as described in more details in [43]. This coding scheme relied on codes from the digital video broadcasting (DVB-S2) standard in conjunction with code-rate puncturing to guarantee error-free transmission [149]. Signal performance estimation was performed on all the 266 spatial super channels. We note that the main limitation in achieving longer distances was not due to fiber-related impairments, despite a fiber cut that was repaired with negligible splicing loss, nor to the complexity of the DSP. Instead, the predominant constraint arose from the high loss associated with the split-and-delay stage before the 15-mode fiber, the MPLC MUX/DeMUX pair, and the TDM combining stage prior to signal detection.

C1.3 Results and Discussions

Figure C1.2(b) illustrates the throughput for all the 266 15-mode spatial super channels spanning the C+L band, estimated using GMI (circles) and after FEC decoding (diamonds). In the C-band, we report decoded data rates exceeding 3.5 Tb/s for all wavelength channels, with the exception of the channel at the longest wavelength of 1568.28 nm. Nearly uniform performance can be observed across the band, with the gradual decrease in data rates at longer wavelengths attributed to the operational bandwidth limitations of the C-band EDFAs. The reported aggregate C-band decoded throughput is 564.1 Tb/s. In the L-band, signals were modulated using PDM-16QAM, mainly due to limitations imposed by the Coh. RXs used in the experiment, which were designed for operation in the C-band only, and consequently degraded the signal performance at longer wavelengths. The minor performance difference between the L1- and L2-bands, marked by a small step in throughput at 1585.5 nm, can be attributed to the difference in channel transmit power between the two bands, as seen in Fig. C1.2(a). This power difference arises from using two L-band amplifiers to generate the L-dummy-band, with the dual objective of maximizing the total output power and reducing the power gap with the C-band. On the other hand, the substantial performance difference between the C- and L-bands

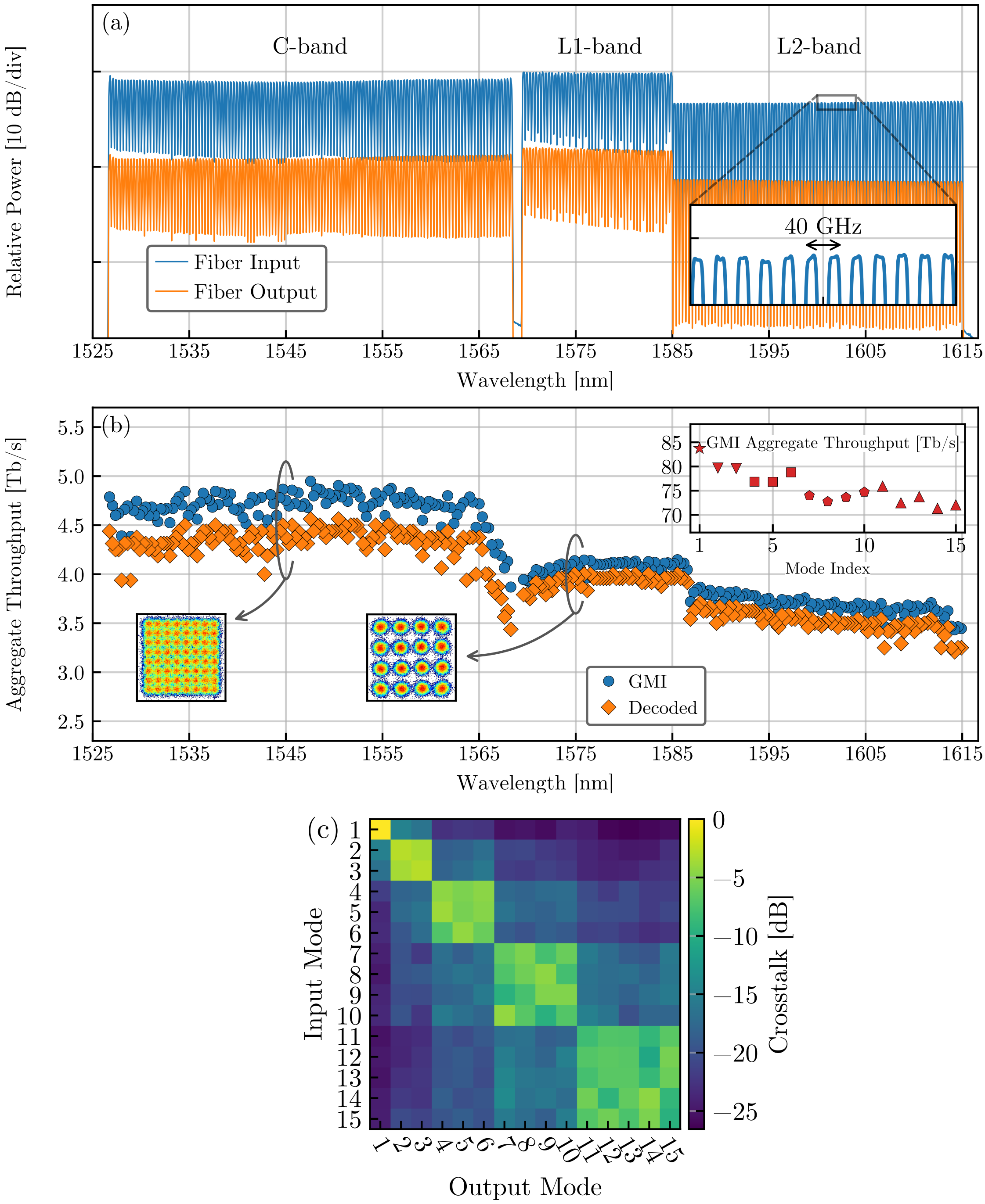

Figure C1.2: (a) Signal spectrum of the fundamental mode at the multiplexer input and demultiplexer output. (b) Spatially aggregated generalized mutual information and forward error correction-decoded throughput of the 266 wavelength-division multiplexing channels transmitted in the deployed 15-mode fiber. (c) Crosstalk matrix of the 15-mode fiber at 1547.56 nm.

follows directly from the poor performance of the transmitter/receiver equipment, which was designed for operation in the C-band. The reported aggregate L-band decoded throughput is 495.8 Tb/s. The top-right inset in Fig. C1.2(b) illustrates the spectrally-aggregated GMI throughput contribution from each mode (different markers refer to different mode groups). Figure C1.2(c) shows the polarization-averaged crosstalk matrix of the 15-mode fiber for the wavelength channel at 1547.56 nm, obtained from the MIMO equalizer taps. The diagonal nature of the matrix highlights the high mode selectivity of the MUX/DeMUX pair and the efficient mode-group confinement of the 15-mode fiber, with strong coupling occurring only between modes belonging to the same mode group. We speculate that similar or superior performance could be achieved with concatenated fiber strands if a more substantial power budget and more suitable equipment for L-band operation were available.

C1.4 Conclusion

We successfully demonstrated the first C+L band transmission over a field-deployed, 6.1 km-long 15-mode fiber link, achieving a total decoded throughput of 1.06 Pb/s. This was obtained by transmitting 266×35 GBaud PDM-64QAM and PDM-16QAM 15-mode spatial super channels across a spectral range extending from 1526.5 nm to 1615.0 nm. This represents the highest transmission capacity ever achieved over any field-deployed fiber, and marks the first petabit-per-second-class transmission over such fibers. Moreover, this achievement exceeds previously reported throughputs obtained with the same MMF type in laboratory environments.

Journal J1

Characterization of Stimulated Raman Scattering in Field-Deployed Coupled-Core Multi-Core Fibers

G. Di Sciullo, L. A. Zischler, D. A. Shaji, Q. Wu, R. S. Luís, R. Emmerich, M. van den Hout, B. J. Puttnam, G. Rademacher, C. Lasagni, P. Serena, A. Bononi, T. Hayashi, C. Schubert, C. Okonkwo, R. Ryf, L. Palmieri, M. Shtaif, A. Marotta, A. Mecozzi, and C. Antonelli

in

Journal of Lightwave Technology, vol. 44, no. 2, pp. 550-557, 15 Jan, 2026

Abstract

We report the first experimental characterization of stimulated Raman scattering (SRS) in coupled-core multi-core fibers (MCFs). The experiment was performed using field-deployed fibers, with two complementary methodologies. First, the effective Raman gain coefficient was directly measured over a bandwidth of 120 nm – covering the upper S-, C- and lower L-bands – with the Raman pump being injected into different combinations of fiber cores and using either co- or counter-propagating signal. Second, we analyzed the spectral power tilt induced by SRS when transmitting a wavelength-division multiplexed signal spanning the entire C-band from 1529.4 nm to 1564.2 nm, which was found to be in agreement with the Raman gain coefficient measurements. Measurements performed on a co-deployed standard single-mode fiber (SMF) produced similar results. This observation, together with the notion that the Raman gain coefficient should be similar in MCFs and SMFs, validates our earlier derived model of SRS in fibers with strong mode mixing.

J1.1 Introduction

Standard single-mode fibers (SMFs) are approaching their theoretical transmission capacity limits [19], while fiber-optic networks continue to face an exponential growth in the demand for higher data rates [33]. To counteract this ever-increasing demand for capacity, multi-band wavelength-division multiplexing (WDM) offers a cost-effective solution to enhance the capacity of existing fiber infrastructures [150, 151]. Indeed, recent experiments have demonstrated data rates exceeding 400 Tb/s when fully exploiting the 38 THz low-loss window of silica fibers, covering the O-, E-, S-, C-, L-, and U-bands [9, 34, 152, 153]. However, while multi-band WDM can temporarily extend the capacity of existing SMF-based infrastructures [154], to further scale the capacity of future fiber-optic systems will require combining multi-band WDM with space-division multiplexing (SDM), employing both multi-core and multi-mode fibers (MCFs and MMFs, respectively) [7]. Recent short-reach experiments in this domain reported data-rates exceeding 22 Pb/s over a 13 km-long, 312 µm cladding diameter, 38-core, 3-mode fiber using the S-, C-, and L-bands [155]. Alternatively, when considering fibers with a standard 125 µm cladding diameter – a feature that ensures compatibility with existing manufacturing processes and preserves fibers' mechanical reliability [99, 156] – data-rates exceeding 3.5 Pb/s were reported over 12.5 km of 55-mode MMF using the C- and L-bands [45]. Long-haul experiments reported to date demonstrated data-rates exceeding 1 Pb/s over more than 1800 km using the C- and L-bands over a standard cladding diameter, 19-core coupled-core multi-core fiber (CC-MCF) [108]. Unlocking this potential poses several challenges, especially in terms of signal amplification and mitigation of fiber nonlinearities [157]. In particular, stimulated Raman scattering (SRS) – a nonlinear optical process where incident photons interact with the vibrational modes of the fiber material, transferring power to lower-frequency photons [82] – can significantly impact the performance of multi-band WDM systems [89]. Stimulated Raman scattering causes a unidirectional power transfer from higher- to lower-frequency channels, resulting in a tilt in the spectral power distribution [87, 88] and, consequently, in a degradation of the overall system performance [9, 34, 88, 158]. Nevertheless, SRS can be leveraged for broad-band amplification at any frequency suitable for propagation in an optical fiber, by simply ensuring that the pump and signal frequencies are separated by the so-called Stokes shift [85, 159] – making it highly attractive for multi-band WDM systems. Stimulated Raman scattering has been extensively studied in WDM systems over standard SMFs [82, 84–91]. In SDM systems, the impact of SRS in multi-band WDM transmission over weakly-coupled multi-core fibers (WC-MCFs) has been found to be similar in magnitude to that observed in SMFs [92, 93], and some preliminary investigations have also been conducted in MMF systems [94]. However, its impact in multi-band WDM transmission over CC-MCFs has received only limited attention [160, 161].

In this work, expanding on our previous works in [160] and [161], we present the first experimental characterization of SRS in CC-MCFs. The experiment was conducted over a 69.2 km-long, coupled-core four-core fiber (CC-4CF), with a standard 125 µm cladding diameter, field-deployed in an underground tunnel infrastructure in the city of L'Aquila, Italy [101, 144, 162, 163]. The effective Raman gain coefficient – defined as the ratio between the Raman gain coefficient and the effective mode area of the fiber cores – was measured under two different Raman-pump-injection schemes, differing in how the pump power was distributed across the fiber cores. In the first scheme, the total pump power was launched into a single core of the CC-4CF, whereas in the second, it was equally distributed across all four cores. The signal was simultaneously injected into all cores in both schemes, with both co- and counter-propagating configurations with respect to the pump. The measured effective gain coefficient was nearly identical in all the cases, as expected in the strong random inter-core coupling regime typical of CC-MCFs. In addition, the same CC-4CF was used to evaluate the power spectral tilt induced by SRS in WDM transmission over the C-band. This was performed by measuring the spectral power distribution at the input and output of each of the four fiber cores, while systematically varying the launch power into the fiber. Both the effective Raman gain coefficient and the SRS-induced gain tilt of the CC-4CF were found to be similar in magnitude to those measured in a reference SMF deployed in the same infrastructure, in agreement with the theory of SRS in SDM fibers with strongly-coupled modes. Notably, the remarkable agreement between the two results – which can be directly compared, as the SRS-induced gain tilt allows estimating the frequency derivative of the effective Raman gain coefficient – further confirms the validity and accuracy of our experimental findings. The remainder of the paper is organized as follows: Section J1.2 provides the theoretical background and presents both the experimental setup and experimental results related to the characterization of the effective Raman gain coefficient of the CC-4CF. Section J1.3 focuses on the characterization of the SRS-induced gain tilt in the same fiber and highlights the convergence between the two independently measured quantities. Finally, the conclusions are drown in Section J1.4.

J1.2 Effective Raman Gain Characterization

In this section, we present the characterization of the effective Raman gain coefficient of the CC-4CF, expanding on the work presented in [161]. Section J1.2.1 provides the necessary theoretical background related to the modeling of SRS in SDM systems with strongly coupled modes, Section J1.2.2 describes the experimental setup used to evaluate the Raman on-off gain over the CC-4CF, and Section J1.2.3 presents the related experimental results.

J1.2.1 Theoretical Background

The reference framework used to model SRS in wide-band SDM systems was previously introduced in [164]. The propagation equations derived therein address multiple non-degenerate mode groups and can be applied to the case of CC-MCFs with N cores. In this case, the signal power evolution in the presence of SRS is described by the following differential equation:

$$\pm\frac{\mathrm{d}P_s}{\mathrm{d}z} = -\alpha_s(z)P_s + \frac{g_\mathrm{R}}{2NA_\mathrm{eff}}P_pP_s, \tag{J1.1}$$

where P_s and P_p represent the optical powers across the N coupled cores at the signal and pump frequencies f_s and f_p, respectively, A_eff denotes the effective area of the pump-signal interaction in the fundamental mode of the fiber cores [165], and α_s is the fiber loss coefficient at the signal frequency f_s. The Raman gain coefficient $g_\mathrm{R} = g_\mathrm{R}(f_s, f_p)$ represents the key parameter describing the efficiency of power transfer from the pump to the signal frequencies, and its experimental characterization is the main objective of this work. The plus and minus signs on the left-hand side of (J1.1) relate to the cases of co- and counter-propagating signal and pump, respectively. In the undepleted-pump regime – where the depletion of pump power due to energy transfer to the signal is negligible – the pump power evolution is given by

$$P_p(z) = P_p(0)e^{-\int_0^z \alpha_p(z')\mathrm{d}z'}, \tag{J1.2}$$

where $\alpha_p(z)$ denotes to the position-dependent fiber loss coefficient at the pump frequency f_p, accounting for both distributed fiber attenuation and lumped splice losses at the fan-in and along the field-deployed link. By applying (J1.1) and (J1.2), the Raman on-off gain, defined as the ratio between the output signal powers with and without the presence of the pump, expressed in decibels, is given by

$$
\begin{aligned}
G_{\mathrm{R}} &= 10\log_{10}(e)\frac{g_{\mathrm{R}}}{2NA_{\mathrm{eff}}}\int_0^L P_p(z)\mathrm{d}z \\
&= 10\log_{10}(e)\frac{g_{\mathrm{R}}}{2NA_{\mathrm{eff}}}P_p(0)L_{\mathrm{eff}}^{(p)},
\end{aligned}
\tag{J1.3}
$$

where L is the total fiber length, and $L_{\mathrm{eff}}^{(p)} = \int_0^L \exp\left[-\int_0^z \alpha_p(z')\mathrm{d}z'\right]\mathrm{d}z$. Provided that the loss profile $\alpha_p(z)$ is known, the measurement of G_{R} yields the effective gain coefficient $g_{\mathrm{R}}/A_{\mathrm{eff}}$, whose experimental evaluation is one of this paper's goals.

J1.2.2 Experimental Setup

The experimental setup used to evaluate the Raman on-off gain of the CC-4CF is illustrated in Fig. J1.1. An Ando AQ8201-13B external cavity laser (ECL), tunable from 1500 nm to 1620 nm and with a linewidth of 5 MHz, was used as a probe signal. To suppress stimulated Brillouin scattering (SBS), the coherence control function of the ECL was enabled, increasing the optical signal bandwidth to approximately 100 MHz. The laser output was first passed through an optical isolator to prevent the Raman pump light from reaching and potentially damaging the device, and then split using a 1×4 power coupler to produce four replicas that simultaneously fed all four fiber cores. These replicas were passed through an array of variable optical attenuators (VOAs), used to reduce the probe signal launch power to approximately −35 dBm per core, ensuring that pump depletion due to Raman-induced power transfer to the signal was negligible [82]. The outputs of the four parallel VOAs were then delayed using the available (although much longer than necessary) SMF spools of multiples of 3.4 km to decorrelate the signals before launching them into a 69.2 km-long CC-4CF link, field deployed in an underground tunnel infrastructure in the city of L'Aquila, Italy [51, 101, 144, 163]. The fiber had a standard 125 µm cladding diameter, and its cross section is shown in the top-right inset in Fig. J1.1(a). More details on the fiber characteristics are provided in [51]. After propagation through the fiber, the signals from the four cores were further delayed using fiber spools of multiples of 40 m prior to being combined with a 4×1 power coupler. The decorrelation at the fiber output was necessary to prevent coherent interference among the signals from the four cores. Moreover, the use of a 4×1 power coupler at the fiber output enabled performing an accurate estimate of the average per-core signal power at the fiber output. The power of the combined signal was then measured using an optical spectrum analyzer (OSA).

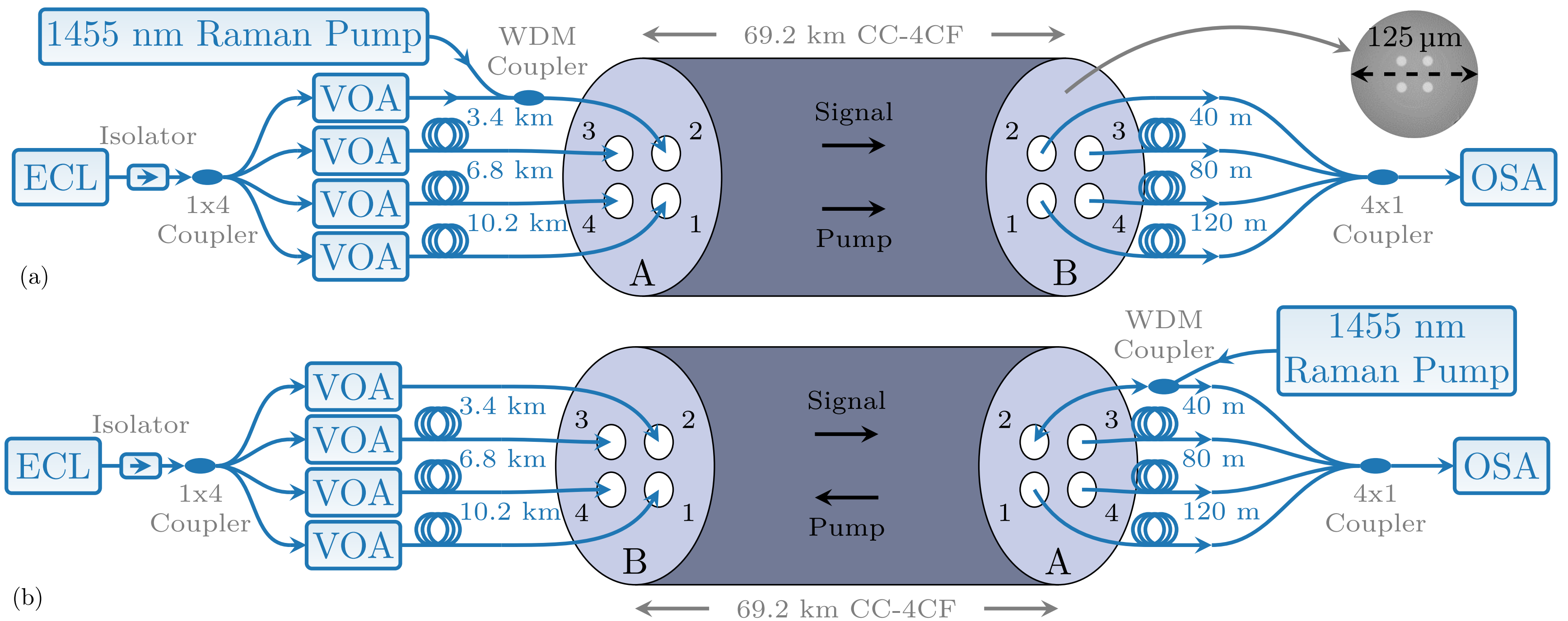

Figure J1.1: Experimental setup to measure the Raman gain over the 69.2 km-long, field-deployed coupled-core four-core fiber link in co-popagating (a) and counter-propagating (b) configurations. The probe signal is simultaneously injected into all four fiber cores at fiber end “A” in the co-propagating configuration, and at fiber end “B” in the counter-propagating configuration. In both cases, the Raman pump is injected into fiber core *2* (SC1) at fiber end “A”. In SC2, the fiber connections to cores 2 and 4 were physically swapped at fiber end “A”.

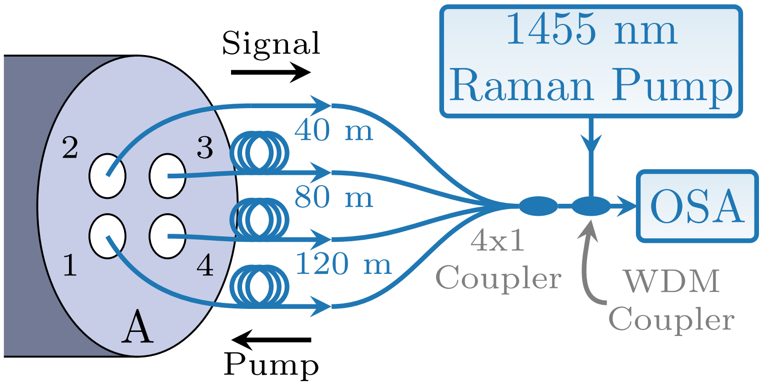

Figure J1.2: Raman pump injection in counter-propagating configuration for SC3. The WDM coupler is placed between the 4×1 power coupler and the optical spectrum analyzer, with the pump being injected into all four fiber cores at fiber end "A".

A Raman pump at 1455 nm with a power of approximately 30 dBm was injected at the fiber end labeled as "A" using a WDM coupler, in both co- and counter-propagating configurations, as illustrated in Figs. J1.1(a) and J1.1(b), respectively. Due to splices between different MCF cable sections field-deployed in the tunnel infrastructure, the CC-4CF link was found to exhibit a slight directional asymmetry. As a result, keeping the Raman pump injection location fixed in both configurations (at fiber end "A") ensured that the Raman pump experienced the same loss profile, enabling a fair comparison of the Raman gain measured in the two cases. Moreover, to assess the dependence of the Raman gain on the specific pump injection configuration, two different scenarios were considered based on how the Raman pump was injected into the fiber. In the first measurement scenario (SC1), the Raman pump was injected into core 2, while in the second scenario (SC2), it was injected into the diagonally opposite core 4, both at fiber end "A". In counter-propagating configuration, an additional scenario (SC3) was considered, in which the Raman pump was split and simultaneously injected into all of the four fiber cores, again at fiber end "A", as illustrated in Fig. J1.2. This configuration was only considered in the counter-propagating configuration due to limited availability of WDM couplers, and was implemented by changing the position of the WDM coupler in the setup of Fig. J1.1(b), placing it in between the 4×1 coupler and the OSA.

J1.2.3 Experimental Results

Figure J1.3 illustrates the experimental results in the co-propagating configuration. The experimental Raman on-off gain, G_{R}, is plotted versus wavelength (bottom horizontal axis) in Fig. J1.3(a), while the top horizontal axis shows the frequency offset

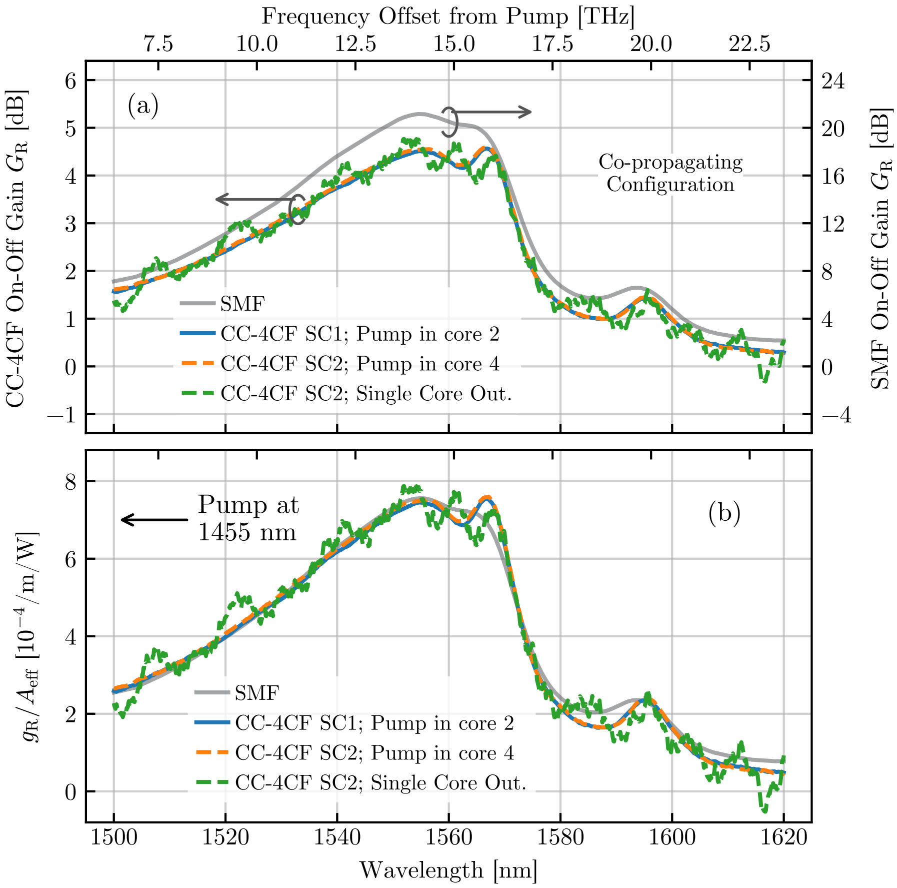

Figure J1.3: (a) On-off Raman gain and (b) Effective Raman gain coefficient in the co-propagating configuration over the coupled-core four-core fiber and a reference single-mode fiber. The probe signal is simultaneously injected into all four fiber cores, while the Raman pump is injected in the core specified in the legend.

from the pump centered at 1455 nm, expressed in THz. The left vertical axis refers to the Raman on-off gain measured over the 69.2 km-long CC-4CF link, whereas the right vertical axis refers to the gain measured over a reference 73.2 km-long SMF link with a similar effective area (~75 μm^2 for the SMF versus ~80 μm^2 for the CC-4CF [51]), both deployed in the same tunnel infrastructure. The solid blue line corresponds to scenario SC1 (pump injected into core 2), while the two dashed lines refer to scenario SC2 (pump injected into core 4) under two different measurement conditions. In the first (orange dashed line), the measured power is taken as the sum of the powers from all four fiber cores (see Fig. J1.3(a)), while in the second (green dashed line), the power is measured from a single output core. Each trace in the figure shows the peak-power difference in dB scale of the probe signal measured with and without the Raman pump, after carefully subtracting the contribution of spontaneous Raman scattering (SpRS), measured with the pump on and the probe signal off. The Raman on-off gain measured in the CC-4CF is approximately four times lower than that in the SMF. This reduction is a direct consequence of the pump power being evenly distributed among all four cores of the CC-4CF after a short propagation distance, reducing the average per-core pump power by a factor of four. Moreover, the fluctuations observed in the Raman on-off gain for SC2 when measured from a single output core can be attributed to the temporal dynamics of the random inter-core coupling. This phenomenon is greatly reduced when the aggregate output power from all the fiber cores is measured using a 4×1 coupler. Figure J1.3(b) illustrates the effective Raman gain coefficient, $g_{\mathrm{R}}/A_{\mathrm{eff}}$, extracted from (J1.3) using the Raman on-off gain traces shown in Fig. J1.3(a) for scenarios SC1 and SC2, as well as for the reference SMF, with the normalization ensuring that the plotted quantities are independent of the effective area of the fiber cores. The Raman pump power after the WDM coupler was approximately 29.4 dBm, with the WDM coupler adding an insertion loss of 0.6 dB to the nominal 30 dBm pump power at the output of the Raman module. (with the WDM coupler adding an insertion loss of 0.6 dB), while the actual launch power into the CC-4CF link was further reduced to approximately 29 dBm due to an additional 0.4 dB insertion loss at the fan-in spliced to the fiber. Specifically, 0.2 dB were coming from the fan-in's nominal insertion loss (as indicated in the manufacturer's calibration report) and 0.2 dB were coming from the splice loss between the fan-in and the CC-4CF link. The good agreement with the results presented in Section J1.3 further supports the validity of these assumptions. The total span loss of the 69.2 km-long CC-4CF link at the pump wavelength of 1455 nm was approximately 21.7 dB, with approximately 2.9 dB being attributed to splice losses. These splices were performed in the field following a fiber cut and are therefore spaced by 6.3 km starting 3.4 km away from fiber-end "A". The estimated insertion losses of each splice are estimated to be 0.17 dB, 0.27 dB, 0.25 dB, 0.22 dB, 0.3 dB, 0.21 dB, 0.38 dB, 0.48 dB, 0.12 dB, 0.2 dB and 0.29 dB. The fiber effective length was approximately 14.04 km. The 73.2 km-long SMF link had a span loss at 1455 nm of approximately 21.3 dB and an effective length of 14.79 km. The effective Raman gain coefficient in the CC-4CF shows two adjacent peaks of similar height, located at 1556.1 nm (14.31 THz shift from the pump) and 1567 nm (15.86 THz shift from the pump). In contrast, in the SMF case the first peak coincides with the first peak in the CC-4CF case, whereas the second peak is significantly suppressed. This difference may be attributed to variations in the doping profile between the CC-4CF and the SMF [166]. No noticeable difference is observed between the curves for scenarios SC1 and SC2, confirming that the strong random inter-core coupling in the fiber ensures pump power equalization

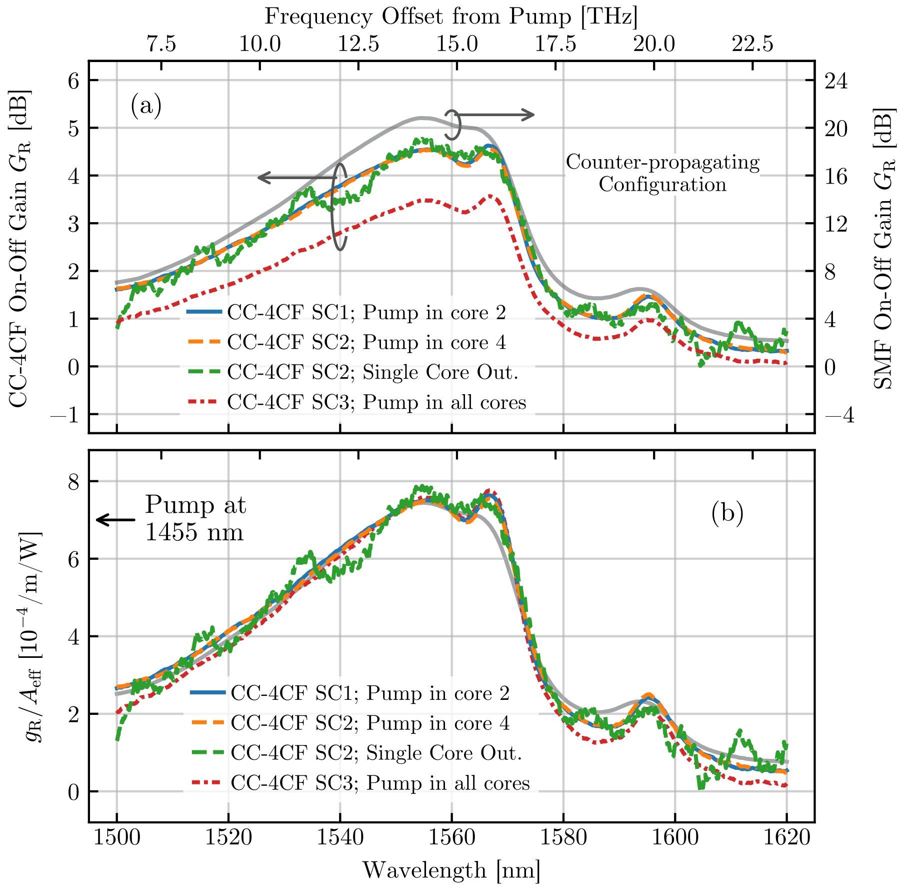

Figure J1.4: (a) On-off Raman gain and (b) Effective Raman gain coefficient in the counter-propagating configuration over the coupled-core four-core fiber and a reference single-mode fiber. The probe signal is simultaneously injected into all four fiber cores, while the Raman pump is injected in the core specified in the legend.

among the cores during propagation. The fluctuations observed in the Raman gain for SC2 when measured from a single output core remains evident. However, they are centered around an average value that is consistent with the results obtained from the other measurement configurations.

Figure J1.4 illustrates the experimental results in the counter-propagating configuration. As for the co-propagating configuration, the measured power for SC2 is taken both as the sum of the powers from all four fiber cores and from a single output core. The effective Raman gain coefficient, g_R/A_{eff}, for all scenarios and for the reference SMF are shown in Fig. J1.4(b). The results for SC1 and SC2, along with those for the reference SMF, are in remarkable agreement with the measurements shown in Fig. J1.3(a), with the two peaks appearing at the same frequency offsets from the pump and with very similar heights. However, the Raman on-off gain measured over the CC-4CF in scenario SC3 (pump in all cores) is slightly lower than that measured in the other two scenarios. This reduction is a direct consequence of an additional 1.2 dB loss introduced to the pump at the 4×1 power coupler. Specifically, the total insertion loss from the single input to all of the four coupler outputs was approximately 7.2 dB, comprising 6 dB due to the 25% power split and 1.2 dB due to the device's additional insertion loss. The effective Raman gain coefficient for scenario SC3 is similar to those obtained for the other scenarios, with a minor deviation visible only in the tails of the spectrum. The reason for this small difference requires further investigation. We note that Figs. J1.3(b) and J1.4(b) show the co-polarized Raman gain coefficient, which is twice as large as the polarization-averaged (link) Raman gain coefficient measured in some other works [167, 168].

Although the effective Raman gain coefficient was measured only for the specific pump wavelength of 1455 nm, its value is not expected to change noticeably when the pump is shifted by a few tens of nanometers. The reason is that the wavelength dependence of the Raman gain coefficient is mostly due to the weak wavelength dependence of the effective area of the pump-signal interaction [165].

J1.3 SRS-induced Spectral Tilt Characterization

In this section, we present the characterization of the spectral distortion induced by SRS in WDM transmission over the CC-4CF, as discussed in [160]. Section J1.3.1 describes our model for the SRS-induced spectral tilt in CC-MCFs; Section J1.3.2 describes the experimental setup used to evaluate such tilt in our deployed CC-4CF; Section J1.3.3 presents the experimental results[1] and includes a comparison of the Raman gain coefficient estimated on the basis of the tilt measurements with the results presented in Section J1.2.3.

J1.3.1 Theoretical Background

As discussed in Section J1.2.1, signal power evolution in the presence of SRS is described by (J1.1). Here we focus on a WDM system, where the transmitted signal with power spectral density (PSD) $S(z, f)$ occupies the full C-band. The PSDs $S(z, f)$ represents the total power at frequency f and distance z across all fiber cores. We examine the effect of a component of the signal spectrum at frequency f_p on another component at frequency f. In this configuration, denoting the smallest and largest

[1] The results presented in Section J1.3 differ from those presented in [160], as they were entirely retaken after a fiber cut that occurred prior to the experiment reported in Section J1.2.

frequencies of the transmitted spectrum by $f_{\min}$ and $f_{\max}$, respectively, (J1.1) yields [84]

$$\frac{\partial S}{\partial z} = -\alpha S + \int_{f_{\min}}^{f_{\max}} \frac{g_{\mathrm{R}}'(f_p - f)}{2NA_{\mathrm{eff}}} S(z, f_p) S(z, f)\, \mathrm{d}f_p, \tag{J1.4}$$

where g_{R}' is the Raman gain coefficient slope, defined by using a linear expansion of the Raman gain coefficient $g_{\mathrm{R}}(f_p, f)$ with respect to the frequency offset as $g_{\mathrm{R}}(f_p, f) \simeq g_{\mathrm{R}}' \times (f_p - f)$. In addition, the approximation $f_p/f \simeq 1$ within the band of interest is used. Solving (J1.4) yields

$$\log\left[\frac{S_\alpha(L, f)}{S(0, f)}\right] = \int_0^L \int_{f_{\min}}^{f_{\max}} \frac{g_{\mathrm{R}}'(f_p - f)}{2NA_{\mathrm{eff}}} S(z, f_p)\, \mathrm{d}f_p \mathrm{d}z, \tag{J1.5}$$

where $S_\alpha(L, f) = S(L, f) \exp\left[\int_0^L \alpha(z, f) \mathrm{d}z\right]$ is the output signal after factoring out the linear link loss, and $S(0, f)$ is the input spectrum. By evaluating (J1.5) at $f = f_{\max}$ and $f = f_{\min}$, and by assuming the input spectrum $S(0, f)$ to be flat across frequency, one obtains the following expression for the power tilt (in Neper)

$$\log\left[\frac{S_\alpha(L, f_{\max})}{S_\alpha(L, f_{\min})}\right] = \frac{g_{\mathrm{R}}'(f_{\min} - f_{\max})}{2NA_{\mathrm{eff}}} \int_0^L \int_{f_{\min}}^{f_{\max}} S(z, f_p) \mathrm{d}f_p \mathrm{d}z. \tag{J1.6}$$

Introducing the total power $P_t(z) = \int_{f_{\min}}^{f_{\max}} S(z, f_p) \mathrm{d}f_p$ yields

$$\log\left[\frac{S_\alpha(L, f_{\max})}{S_\alpha(L, f_{\min})}\right] = \frac{g_{\mathrm{R}}'(f_{\min} - f_{\max})}{2NA_{\mathrm{eff}}} \int_0^L P_t(z) \mathrm{d}z. \tag{J1.7}$$

The evolution equation for $P_t(z)$ is obtained by integrating (J1.4) with respect to f, with the result

$$\frac{\mathrm{d}P_t}{\mathrm{d}z} = -\int_{f_{\min}}^{f_{\max}} \alpha(z, f) S(z, f) \mathrm{d}f \simeq -\bar{\alpha} P_t, \tag{J1.8}$$

where we assume that the frequency-dependent loss coefficient $\alpha(z, f)$ is adequately replaced with its frequency average $\bar{\alpha}(z)$, so that $P_t(z) = P_0 \exp\left[-\int_0^z \bar{\alpha}(z') \mathrm{d}z'\right]$, where P_0 is the total input power across all cores. Finally, we obtain

$$\log\left[\frac{S_\alpha(L, f_{\max})}{S_\alpha(L, f_{\min})}\right] = \frac{g_{\mathrm{R}}' \Delta f}{2NA_{\mathrm{eff}}} P_0 L_{\mathrm{eff}}, \tag{J1.9}$$

where $L_{\mathrm{eff}} = \int_0^L \exp\left[-\int_0^z \bar{\alpha}(z') \mathrm{d}z'\right] \mathrm{d}z$ and $\Delta f = f_{\max} - f_{\min}$. From the above we can extract the frequency derivative of the Raman gain coefficient normalized by the effective area as

$$\frac{g_{\mathrm{R}}'}{A_{\mathrm{eff}}} = \frac{2N}{10 \log_{10}(e) P_0 L_{\mathrm{eff}}} \frac{-\mathrm{Tilt}_{\mathrm{dB}}}{\Delta f}, \tag{J1.10}$$

where $\mathrm{Tilt}_{\mathrm{dB}} = 10 \log_{10}\left[S_\alpha(L, f_{\max})/S_\alpha(L, f_{\min})\right]$ is the spectral tilt induced by SRS, defined as the difference (in decibels) between the highest- and shortest-frequency power levels, after factoring out the frequency-dependent link loss.

J1.3.2 Experimental Setup

The experimental setup used to evaluate the SRS-induced spectral distortion in the CC-4CF is illustrated in Fig. J1.5. A fully-loaded WDM transmission system spanning the entire C-band from 1529.4 nm to 1564.2 nm was emulated by spectrally flattening the amplified spontaneous emission (ASE) noise generated by a C-band erbium-doped fiber amplifier (EDFA) through the use of an optical processor (OP). The spectrally shaped ASE noise seed was passed through an isolator and split using a 1×4 power coupler. Each output of the coupler was further amplified using an array of four EDFAs, each equipped with an internal VOA to adjust the launch power into the fiber cores. Spectral flattening of the ASE noise was performed by monitoring the output port of one of the four EDFAs. Due to the use of a single OP for all four fiber cores, the spectral flatness at the fiber input was within approximately 1 dB. The signals from the four EDFAs propagated over the same 69.2 km-long, field-deployed CC-4CF link used in the Raman gain coefficient characterization described in Section J1.2. As discussed in Section J1.2.2, due to a slight asymmetry of the CC-4CF link, the WDM signals were injected at fiber end "A", consistently with the Raman pump injection location. At the fiber output, one core at a time was manually connected to the OSA for PSD measurement, as shown in the right-hand side of Fig. J1.5.

J1.3.3 Experimental Results

Figure J1.6 illustrates the experimental results of the SRS-induced spectral distortion of the CC-4CF. Figure J1.6(a) shows the input and output spectra versus wavelength (bottom horizontal axis) and frequency (top horizontal axis), averaged across all four fiber cores, for input power levels of approximately 20 dBm, 18 dBm, 16 dBm, and 14 dBm per core. At the fiber output, minor differences in the spectral tilt can be observed among the four traces. These variations are shown more clearly in Fig. J1.6(b), which illustrates the SRS-induced excess gain (and loss) across the WDM spectrum for all the considered input power levels, ranging from 20 dBm down to 2 dBm in steps of 2 dB. Each trace in the figure is obtained by subtracting the core-averaged output spectrum to the core-averaged input spectrum, in decibels, for all power levels, and by then subtracting the fiber loss, estimated as the difference between the input and output spectra at a launch power of 0 dBm.

Figure J1.7 shows the spectral tilt induced by SRS, in decibels, as a function of the per-core input power, in Watts, for both the 69.2 km-long CC-4CF link and the

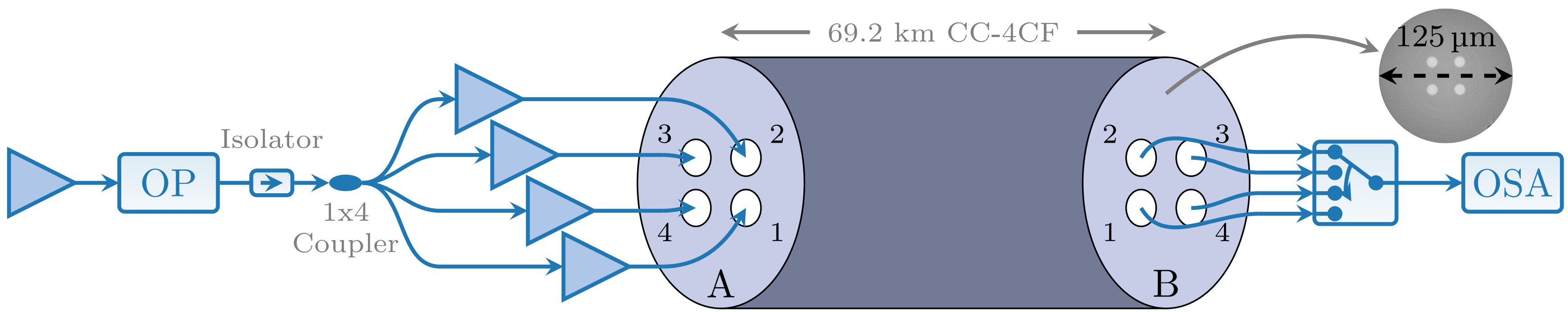

Figure J1.5: Experimental setup to evaluate the stimulated Raman scattering-induced gain tilt after propagation over the 69.2 km-long, field-deployed coupled-core four-core fiber link. The seed noise signal is spectrally flattened using an optical processor, split and amplified before being injected into the fiber with varying power levels. At the fiber output, the spectral power distribution is measured by manually connecting each output core to the optical spectrum analyzer.

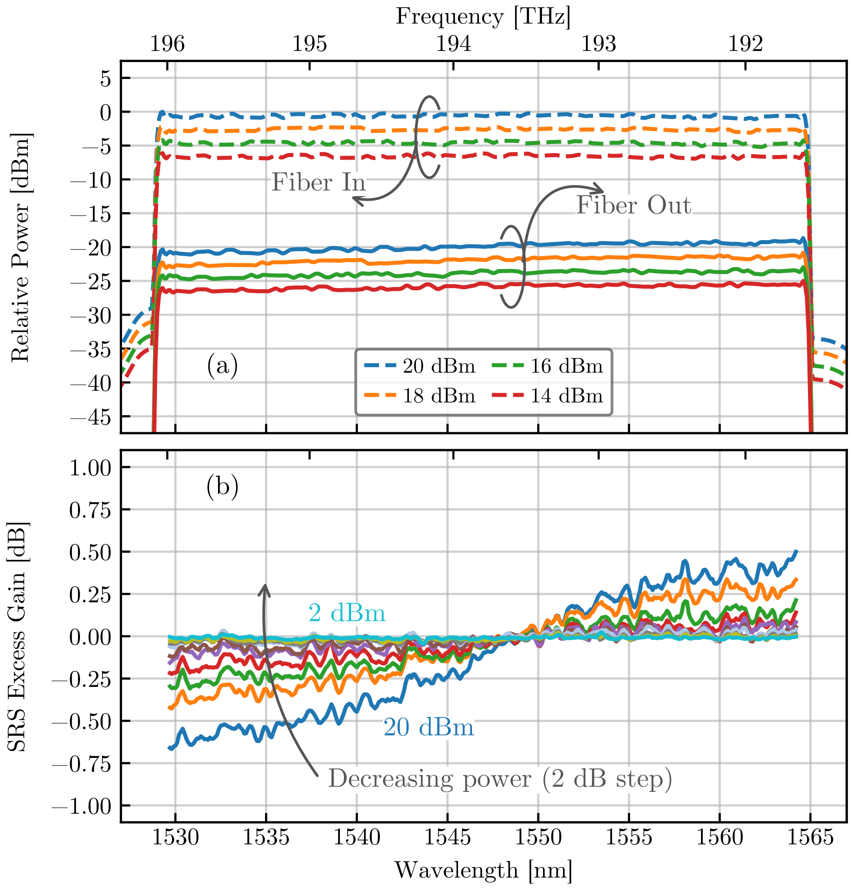

Figure J1.6: (a) Input and output spectra of the coupled-core four-core fiber, averaged over all cores, for four different launch power levels. (b) Measured stimulated Raman scattering-induced excess gain (in dB) for decreasing input power levels (decreasing with a step of 2 dB).

reference 73.2 km-long SMF link. A linear dependence of the SRS tilt on the per-core input power can be observed for both fibers [88]. A maximum tilt of approximately 1.06 dB is measured with a per-core input power of around 20 dBm in the CC-4CF, while a tilt of approximately 1 dB is measured with an input power of around 20.1 dBm in the SMF. The angular coefficient between SRS-induced tilt and per-core input power for the two fibers are 10.8 dB/W and 9.4 dB/W, respectively, as indicated with colored arrows in Fig. J1.7. By substituting the measured tilt values into (J1.10), we obtain values of the frequency derivative of the Raman gain coefficient, $g'_{\mathrm{R}}/A_{\mathrm{eff}}$, of $6.11{\times}10^{-17}$/m/W/Hz for the CC-4CF and $6.58{\times}10^{-17}$/m/W/Hz for the SMF.

A comparison between the two complementary approaches for the characterization of SRS is performed by comparing the frequency derivative of the Raman gain coefficient, $g'_{\mathrm{R}}/A_{\mathrm{eff}}$, directly obtained from (J1.10), with that of the slopes of the effective Raman gain coefficient curves, $g_{\mathrm{R}}/A_{\mathrm{eff}}$, depicted in Figs. J1.3(b) and J1.4(b).

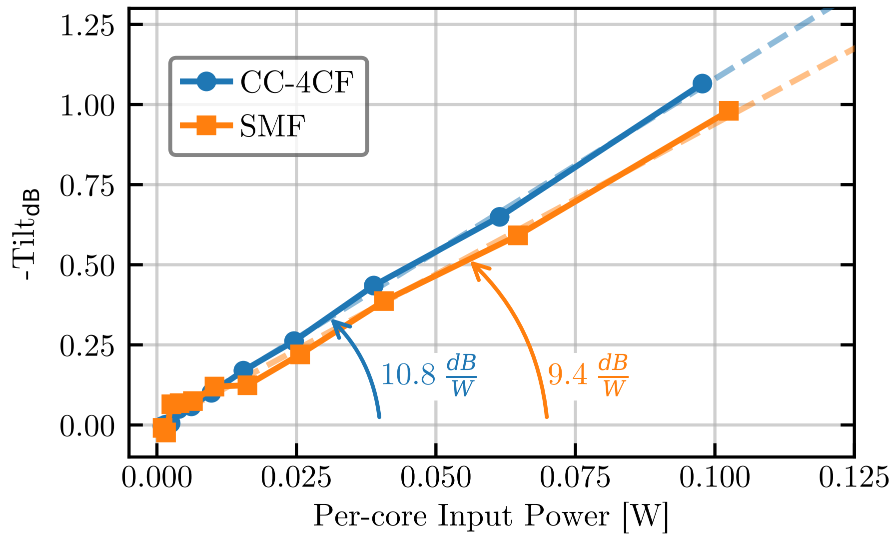

Figure J1.7: Measured stimulated Raman scattering-induced gain tilt as a function of per-core input power for both the coupled-core four-core fiber link and the reference single-mode fiber. Dashed lines represent a linear regression on the data, with the corresponding angular coefficients indicated by the colored arrows.

In all the considered scenarios (SC1, SC2, and SC3), and for both co- and counter-propagating configurations, the frequency derivative of the slope of the Raman gain coefficient yield values between 6.1×10^{-17}/m/W/Hz and 7×10^{-17}/m/W/Hz for the CC-4CF and between 6.4×10^{-17}/m/W/Hz and 6.5×10^{-17}/m/W/Hz for the SMF. The remarkable agreement between these results provides a strong validation of the accuracy and consistency of our experimental findings.

J1.4 Conclusion

We presented an experimental characterization of stimulated Raman scattering in a field-deployed, standard 125 µm cladding diameter, coupled-core four-core fiber using two complementary methodologies. First, we characterized the effective Raman gain coefficient – defined as the ratio between the Raman gain coefficient and the effective area of the pump-signal interaction in the fundamental mode of the fiber cores – by measuring the Raman on-off gain over an 120 nm bandwidth, from 1500 nm to 1620 nm, in both co- and counter-propagating configurations. Nearly identical results were observed across different Raman-pump-injection scenarios, confirming the strong inter-core coupling taking place in the field-deployed coupled-core four-core fiber under analysis. We then characterized the spectral power tilt induced by stimulated

Raman scattering by emulating a C-band wavelength-division multiplexed transmission system spanning from 1529.4 nm to 1564.2 nm. In both approaches, the effective Raman gain coefficient of the multi-core fiber was found to be similar in magnitude to that of a reference standard single-mode fiber deployed in the same tunnel infrastructure. The remarkable agreement between the results obtained with the two independent measurement approaches provided a strong validation of the accuracy and consistency of our experimental findings.

Journal J2

45.7 Tb/s Over 12 053 km Transmission in an All-Multi-Core-Amplified Recirculating Loop

G. Di Sciullo, B. J. Puttnam, M. van den Hout, R. S. Luís, D. A. Shaji, G. Rademacher, C. Okonkwo, A. Mecozzi, C. Antonelli, and H. Furukawa

in

Journal of Lightwave Technology, vol. 43, no. 10, pp. 4635-4641, 15 May, 2025

Abstract

We present a recirculating-loop-based long-haul transmission system that achieves the longest reach ever reported in multi-core fiber transmissions relying on a fully integrated multi-core amplification scheme without the use of fan-in/fan-out devices. Our system successfully transmits 45.7 Tb/s using 4×175×24.5 GBd polarization-division multiplexing (PDM) 4-quadrature-amplitude modulated (QAM) signals over 12 053 km of weakly-coupled four-core fiber (WC-4CF), enabled by multi-core C-band erbium-doped fiber amplifiers (EDFAs) and distributed Raman amplification (DRA). Additionally, we evaluate the performance of 16-QAM and 64-QAM signals within the same recirculating loop, estimating total decoded throughputs of 90.8 Tb/s after 3161.6 km and 137 Tb/s after 395.2 km, respectively.

J2.1 Introduction

As data rates are expected to continue their exponential increase in optical fiber networks and single-mode optical fibers are reaching their transmission limits [7, 33], space-division multiplexing (SDM) has emerged as a highly promising technology to address the impending information capacity crunch and to meet the ever-increasing demand for transmission capacity. Despite the potential for implementing SDM using a variety of new optical fiber types [7], such as multi-core fibers (MCFs), including both randomly coupled (RC) and weakly coupled (WC), multi-mode fibers (MMFs), and hybrid multi-core multi-mode fibers (MC-MMFs), recent developments show a trend towards the adoption of low-core-count WC-MCFs in SDM systems [135, 139]. Furthermore, these fibers have a standard 125 µm cladding diameter, aligning with existing manufacturing, cabling and connectorization processes for standard single-mode fibers (SMFs). This characteristics not only makes them compatible with current processes, but also reduces their vulnerability to mechanical failures [99]. Although data rate enhancement is a primary aim for SDM systems, another significant factor pushing their development is the demand for hardware integration and reduced power consumption [7]. Specifically, the availability of efficient SDM amplifiers plays a key role in advancing SDM systems. In fact, these amplifiers not only enhance the performance of SDM systems but also play a crucial role in optimizing the integration of hardware components within the system, while reducing energy consumption. The overwhelming majority of transmission experiments over SDM fibers reported to date still rely on single-mode amplifier, requiring the demultiplexer (DeMUX) and multiplexer (MUX) of all the spatial modes at every stage of amplification [141, 169, 170]. Some experiments utilizing various types of SDM erbium-doped fiber amplifiers (EDFAs) for inline amplification, including both multi-mode (MM) [171, 172] and multi-core (MC) [173–183] EDFAs, stand out as notable exceptions. Nevertheless, it is important to highlight that even in these experiments, single-mode amplifiers have still been employed as boosters or pre-amplifiers, or to compensate for the losses introduced by the loop components during recirculating transmission. This approach can significantly impact gain tilt and transmission performance, potentially leading to an inaccurate assessment of fan-in/fan-out (FIFO)-less SDM amplifiers' suitability for long-haul transmission. A notable exception is [184], where FIFO-less MC-EDFAs were used to amplify the signal of RC-MCFs without single-mode amplifiers in the loop. While the aforementioned work focuses on RC-MCFs, whereas our study involves WC-MCFs, we note that this work extends the total transmission reach by a factor of two.

In this work, expanding on [109] and [185], we report the first trans-Pacific-equivalent transmission distance using an MCF system that relies on an all-MCF amplification strategy, seamlessly integrating core-pumped MC-EDFAs and distributed Raman amplification (DRA). We use weakly-coupled 4-core C-band EDFAs to simultaneously amplify 4×175 polarization-division multiplexing (PDM) 4-, 16-, and 64-quadrature-amplitude modulated (QAM) signals across a spectral range of approximately 35 nm, extending from 1528.8 nm to 1563.5 nm. These signals are transmitted through a recirculating loop consisting of two spans of 4-core WC-MCFs. Additionally, to mitigate the extra losses introduced by the recirculating-loop-circuit components, a 4-core EDFA with a gain profile matching those used for fiber loss compensation is employed. Unlike previous experiments, this approach enables a more accurate analysis of the MC-EDFAs' effectiveness for long-haul transmission. Remarkably, this is the first experiment in which no single-mode amplifiers are used in a recirculating-loop-based transmission over WC-MCFs. System performance is evaluated in terms of generalized mutual information (GMI) and post-decoding using forward error correction (FEC) codes. In the case of 4-QAM signal transmission, total throughputs of 49.9 Tb/s based on GMI and 45.7 Tb/s after FEC decoding over a transmission distance of 12 053 km are reported, achieving a per-spatial-mode capacity-distance product of 137.8 Pb/s·km. To the best of our knowledge, this represents the longest reach ever reported in SDM transmission experiments utilizing only SDM amplifiers. System performance estimation is also assessed when transmitting 16-QAM and 64-QAM signals through the same 4-core MCF-based recirculating loop. Extrapolation from measurements taken in a single core of the fully-loaded 4-core MCF yield total throughputs of 99.70 Tb/s (GMI) and 90.8 Tb/s (FEC decoding) after 3161.6 km, and 149.6 Tb/s (GMI) and 137 Tb/s (FEC decoding) after 395.2 km for 16-QAM and 64-QAM signals, respectively.

The remainder of the paper is organized as follows: Section J2.2 outlines the experimental setup used in this work, while Section J2.3 discusses the multi-core amplification strategy. The results are presented in Section J2.4, and the conclusions are drawn in Section J2.5.

J2.2 Experimental Setup

Figure J2.1 illustrates the experimental transmission setup. To generate a three-channel sliding test band, carriers from three tunable laser sources (TLSs) were mod-

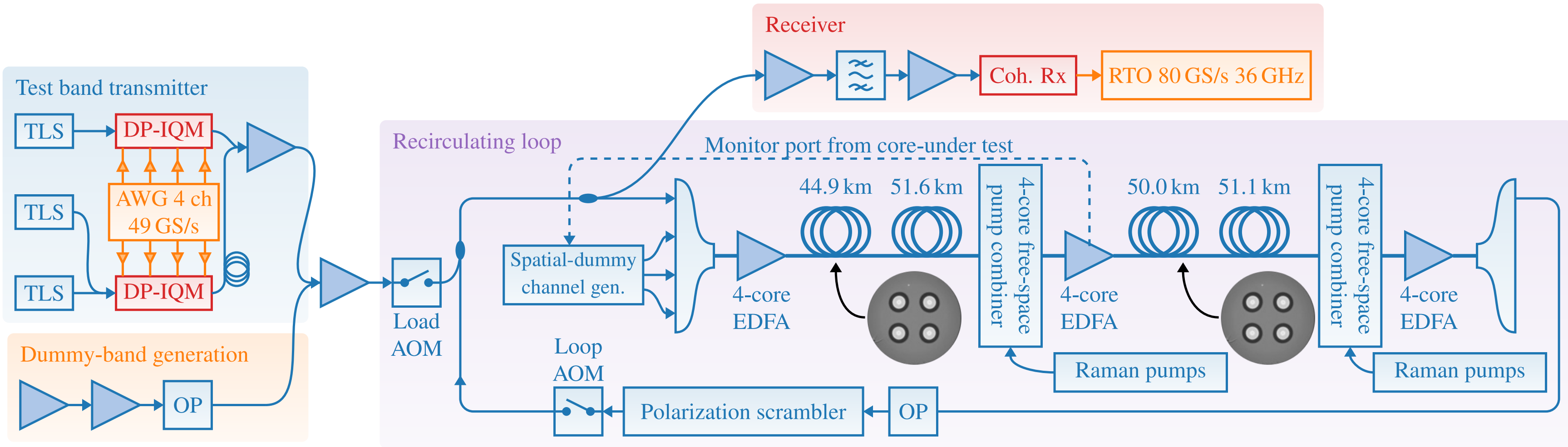

Figure J2.1: Experimental setup of the 4-core multi-core fiber system with an all-multi-core-amplified recirculating loop.

ulated using two dual-polarization IQ modulators (DP-IQMs). One DP-IQM was dedicated to the central test channel, while the other was shared between the two adjacent channels. Both modulators were driven by a single 49 GS/s 4-channel arbitrary waveform generator (AWG), producing 24.5 GBd PDM 4-QAM, 16-QAM, and 64-QAM signals with a 1% roll-off root-raised-cosine pulse shape. Furthermore, a dummy band was created by utilizing an optical processor (OP) to spectrally flatten the amplified spontaneous emission noise generated by two EDFAs. The OP was also employed to carve a notch in the spectrum to accommodate the test band. The wavelength-division multiplexing (WDM) system comprised 175 25-GHz-spaced channels, spanning the spectral range from 1528.8 nm to 1563.5 nm. While this configuration adhered to the International Telecommunication Union – Telecommunication Standardization Bureau (ITU-T) 25 GHz channel grid, it was tailored to the spectral range used in our experiment, with the three-channel test band being dynamically positioned within this range. The combined signal was amplified and passed through an acousto-optic modulator (AOM), which was used to load a 4-core recirculating loop containing two spans of low-loss, standard-cladding diameter, 4-core WC-MCF and three 4-core EDFAs. Spatial dummy channels were generated from a copied version of the signal propagating in the core under test, obtained from the monitor output port of the second-stage MC-EDFA. This ensured that the signals in all cores had propagated the same distance as the test signal during each recirculation. The signals in the four fiber cores were simultaneously amplified using two 4-core EDFAs preceding two fiber spans of 96.5 km and 101.1 km. Both spans were obtained by connecting two spools of weakly-coupled four-core fibers (WC-4CFs), with the second fiber section of each span being a zero-water-peak fiber, enabling more efficient Raman amplification, similar to what was done in [170]. Both fiber types had a core pitch of 40 µm and exhibited inter-core crosstalk (XT) levels below −50 dB/km [100]. Specifically, for the first fiber type, the XT level was measured to be approximately −50 dB/km, while for the zero-water-peak fiber, the XT level was around −55 dB/km at 1625 nm. The mode field diameter (MFD) was 8.5 µm at 1310 nm for both fiber types. The fiber loss is illustrated in Fig. J2.2, which shows the wavelength-dependent loss (WDL) of the individual cores for the two fiber types, expressed in dB/km. Free-space 4-core pump combiners were used to introduce Raman pumps into each core at the end of the two fiber spans. An additional 4-core EDFA, similar to the one preceding the two fiber spans, was used to simultaneously amplify the signal at the output of the second fiber span. The outputs of the dummy cores were terminated, while the signal in the core under test was routed back to the loop input. Before re-entering the loop,

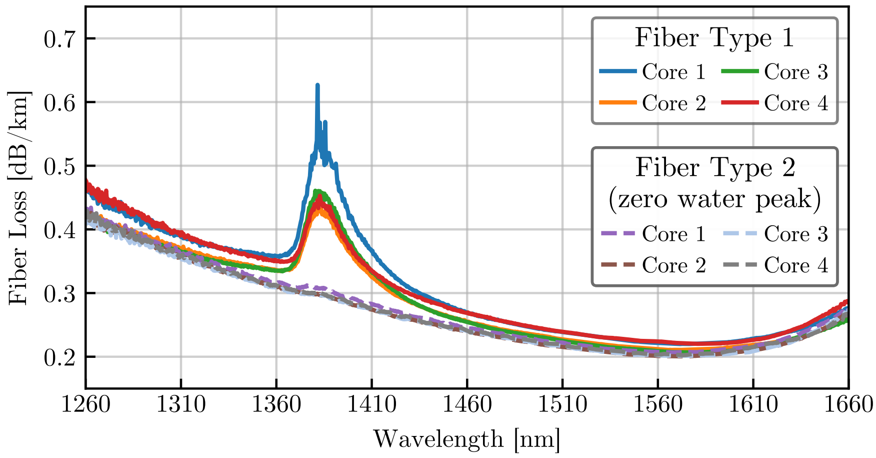

Figure J2.2: Per-core wavelength-dependent loss of the two 4-core weakly-coupled multi-core fiber types, expressed in dB/km.

the signal was passed through an OP, to compensate for the amplifiers' gain tilt, and a polarization scrambler, to prevent polarization-dependent effects and meet more realistic transmission conditions. These single-mode devices, together with the FIFO devices at the edges of the MCF spans, were essential for looping the signal back from the output to the input of the all-four-core-component two-span system.

For signal reception, the spatial channel under test was amplified, and the channel of interest (COI) was filtered out and amplified again before being detected with a coherent receiver (Coh. RX), using a local oscillator (LO) with a linewidth of less than 60 kHz. A 4-channel, 80-GS/s real-time oscilloscope was used to digitize the electrical signals from the Coh. RX. These traces were then stored for offline digital signal processing (DSP), which included a time-domain 2×2 multiple-input multiple-output (MIMO) equalizer operating at 2 samples per symbol (equivalent to a sampling rate of 49 GS/s), and employing 41 taps, corresponding to a temporal memory of approximately 0.84 ns. The equalizer was initially updated in a data-aided least-mean squares (DA-LMS) mode before switching to decision-directed (DD) operation, after convergence. Data rates were determined based on the GMI [186] and the implementation of an FEC coding scheme as described in [43]. The FEC scheme used codes from the digital video broadcasting (DVB-S2) standard [187], augmented with code-rate puncturing to achieve a bit-error ratio (BER) below $5{\times}10^{-5}$. An additional 10% hard-decision outer FEC was utilized to ensure error-free transmission, as discussed in [149]. Performance estimation was conducted individually on all 4×175 SDM and WDM channels.

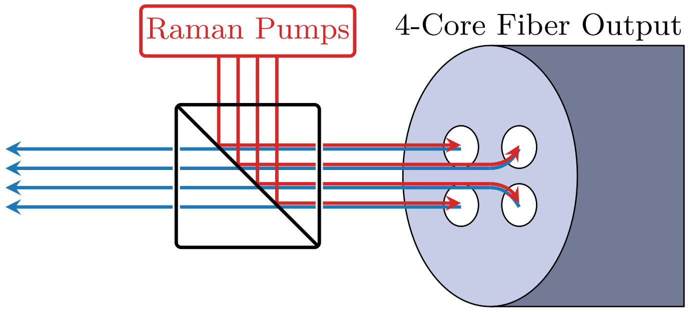

Figure J2.3: Schematic representation of the free-space 4-core pump combiners used in the experiment.

J2.3 Multi-Core Amplification

The all-multi-core-amplified recirculating loop used in the experiment relied on a hybrid amplification scheme that combined DRA and MC-EDFAs. These techniques enabled the simultaneous amplification of 4×175 SDM and WDM channels over distances up to 12 000 km of 4-core WC-MCF.

Raman pumps at 1410.8 nm and 1417.5 nm were injected into each core of the MCF spans with a power of 270 mW, while pumps at 1424.3 nm were set to 150 mW. Additionally, an extra pump at 1431 nm with a power of 80 mW was injected into each core at the end of the first fiber span. These pumps were introduced into each core using free-space 4-core pump combiners, as schematically illustrated in Fig. J2.3. These pump combiners enabled the injection of Raman pumps into each core, with an insertion loss of 0.5 dB per core for both the signal and pump paths. These pump configurations primarily amplified the shorter-wavelength region of the C-band, with Raman gain decreasing as the wavelength increases. Figure J2.4(a) illustrates the signal spectrum at the input and output of the first fiber span, both with and without Raman amplification. The Raman gain profile, estimated as the difference between the green and orange curves in the figure, was obtained in an effort to optimally compensate for the gain tilt of the multi-core amplifier.

The MC-EDFAs used in the experimental setup were 976 nm core-pumped 4-core EDFAs operating in the wavelength range between 1527 nm and 1564 nm [188]. The amplifier's noise figure (NF) was below 7.2 dB, and the inter-core XT values are reported in Table J2.1. These XT values were measured using a free-space 4-core MUX and DeMUX pair, of the kind employed in the experiment, on both sides of a 4-core EDFA. The XT values in parentheses refer to the back-to-back (B2B) MUX+DeMUX case. Figure J2.4(b) illustrates the gain spectra of a single core of the 4-core EDFA, with the gain spectra of the other cores remaining consistent. The

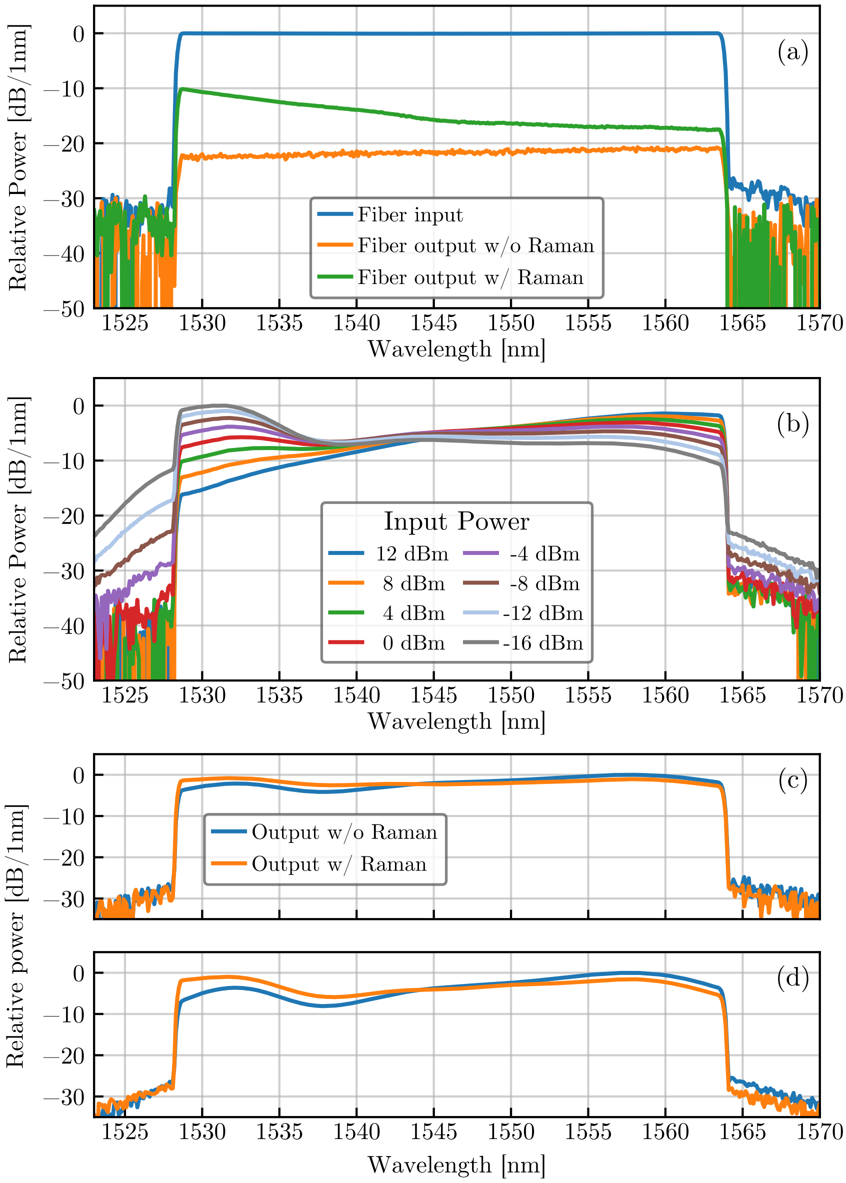

Figure J2.4: (a) Spectrum of the signal at the input and output of the first fiber span, with and without Raman amplification. (b) Gain profile of the 4-core erbium-doped fiber amplifiers at 19 dBm output power for frequency-flat input signals with the displayed power values. (c)-(d) Combined effect of multi-core erbium-doped fiber amplifiers and Raman amplification: output spectra of the first and second multi-core fiber spans, with and without Raman amplification.

output power level was set to 19 dBm – our optimum launch power level, as discussed in Section J2.4.1 – while the input power was systematically varied from 12 dBm down to -16 dBm in steps of 4 dB. As shown in the figure, the optimum input power level into the 4-core EDFA – corresponding to the amplifier's minimum gain tilt – was between 0 dBm and -4 dBm, represented by the red and purple lines, respectively.

Table J2.1: Cross-talk matrix of the 4-core erbium-doped fiber amplifiers. Values in parentheses refer to the back-to-back case.

XT [dB]	Core 1	Core 2	Core 3	Core 4
Core 1		-50.90 (-54.53)	-61.18 (LO)	-49.68 (-55.53)
Core 2	-51.26 (-53.85)		-51.61 (-54.95)	-58.13 (LO)
Core 3	-58.60 (-60.16)	-50.68 (-54.80)		-51.62 (-53.50)
Core 4	-48.86 (-55.80)	-57.81 (LO)	-52.46 (-56.10)	

The combined effect of MC-EDFAs and Raman amplification is illustrated in Figs. J2.4(c) and J2.4(d), which show the output spectra of the first and the second MCF spans, respectively, with and without Raman amplification. The Raman-amplification-induced tilt on the spectrum at the second MC-EDFA input (see Fig. J2.4(a)) reduced the spectral tilt at the same MC-EDFA output (Fig. J2.4(c)). This effect becomes even more pronounced at the output of the second fiber span within the loop (Fig. J2.4(d)), allowing for a reduction in the attenuation profile programmed in the OP to compensate for the residual gain tilt.

J2.4 Experimental Results

In this section, we present the transmission results obtained with the experimental setup discussed in the previous sections for 4-QAM, 16-QAM and 64-QAM signals. Section J2.4.1 details the transmission of 4-QAM signals, while Section J2.4.2 presents the results for the transmission of 16-QAM and 64-QAM signals.

J2.4.1 PDM 4-Quadrature Amplitude Modulation Signals

The optimal transmission power level is identified by performing a *launch-power sweep*, which involves systematically varying the launch power level into the fiber and observing the resulting Q-factors after signal reception. Figure J2.5(a) illustrates this analysis, showing Q-factors (in dB) versus launch power (in dBm) for different propagation distances in one of the fiber cores. Each data point corresponds to the average Q-factor across three WDM channels evenly distributed in the C band, with wavelengths at 1529.9, 1545.7 and 1561.8 nm. The shaded area indicates the range between the minimum and maximum values obtained at these wavelengths. An optimum launch power of 19 dBm for transmission distances above 5000 km is identified

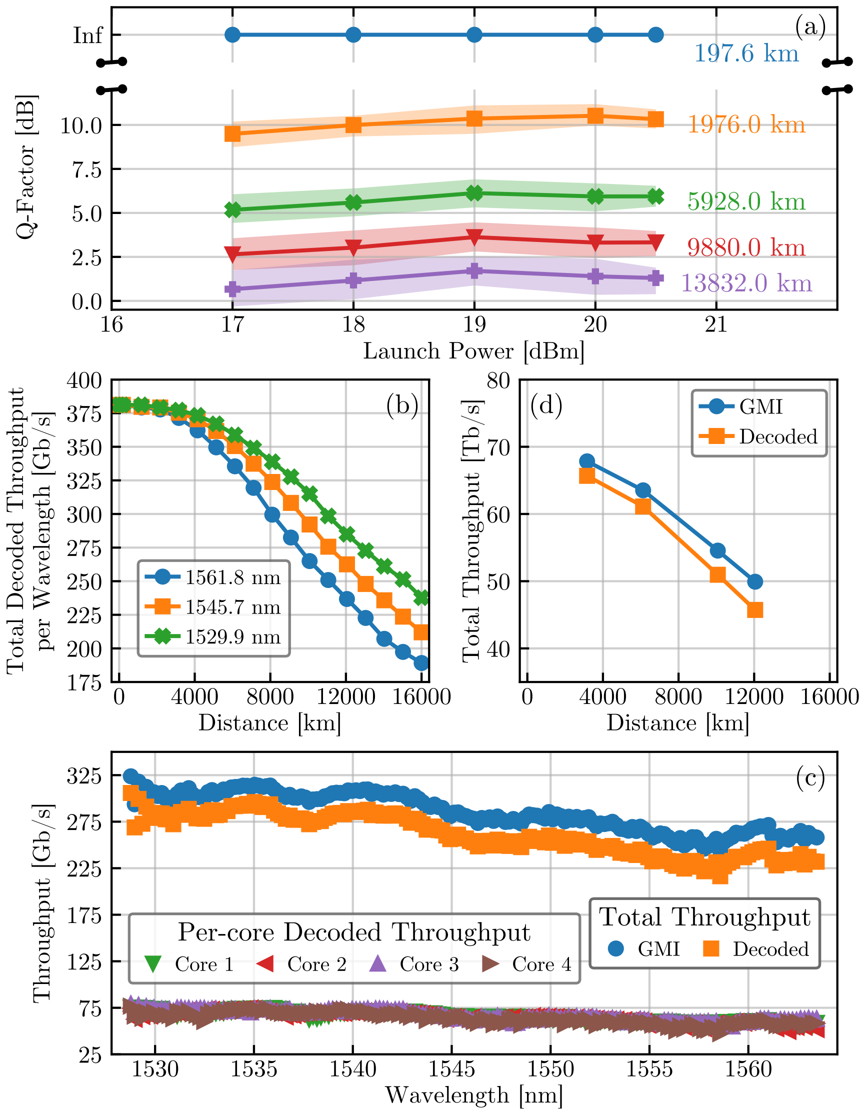

Figure J2.5: (a) Q-factors versus launch power level into each of the fiber cores at different propagation distances. Each data point represents the average across three wavelength channels in the C-band, measured over a single core of the fully-loaded 4-core multi-core fiber. (b) Total decoded throughput versus propagation distance for three wavelength-division multiplexing channels evenly distributed across the C-band, with wavelengths displayed in the legend. (c) Throughput of the 4×175 space-division multiplexing and wavelength-division multiplexing channels after 12 053 km transmission. Circles and squares show the generalized mutual information-based and decoded aggregate throughput, respectively. Triangles show the per-core decoded throughput. (d) Total achievable generalized mutual information-based and decoded throughput for full 4-core transmission versus propagation distance.

for all WDM channels. This optimization addresses the trade-off between signal-to-noise ratio (SNR) and nonlinear impairments. However, while the DSP chain includes a time-domain MIMO equalizer to compensate for linear impairments, and nonlinear phase noise is indirectly addressed in the carrier phase recovery stage, no explicit nonlinear compensation methods are applied in this experiment.

For each of the same three channels, we plot in Fig. J2.5(b) the total achievable throughput after FEC decoding. We remind that this is estimated by implementing an FEC coding scheme using codes from the DVB-S2 standard, as described in [43]. The code is augmented with code-rate puncturing to achieve a BER below 5×10^{-5}, and an additional 10% hard-decision outer FEC is utilized to ensure error-free transmission. The results of the figure suggest that shorter-wavelength channels outperform longer-wavelength ones due to two main factors. Firstly, shorter-wavelength channels benefit from greater Raman amplification compared to longer-wavelength ones, as illustrated in Fig. J2.4(a). Secondly, the OP in the loop, used to compensate for the amplifiers' gain tilt, imposes higher attenuation on longer wavelengths, causing a reduction in their throughput.

Figure J2.5(d) shows the per-core decoded data rates of all WDM channels after a transmission distance of 12 053 km. The same figure also shows the aggregate decoded troughput, as well as the achievable information rate estimated in terms of GMI [186]. The differences in total throughput among the wavelength channels is attributed to the wavelength-dependence of Raman and amplifier gains, as well as the filtering applied by the OP in the loop. In order to ensure a flat spectrum across the entire bandwidth at the input of the first fiber span in the recirculating loop, the OP penalizes longer-wavelength channels. No noticeable performance differences are observed between cores, with only a 0.5 Tb/s difference in total decoded throughput. The worst and best cores provide total throughputs of 12.2 Tb/s and 12.7 Tb/s based on GMI, and 11.2 Tb/s and 11.7 Tb/s after FEC decoding, respectively. This results in a total GMI-based throughput of 49.9 Tb/s and a total decoded throughput of 45.7 Tb/s over a transmission distance of 12 053 km. This represents the longest reach ever reported in SDM transmission experiments utilizing only SDM amplifiers.

Per-core data rates for all WDM channels are also measured at intermediate distances of 3161.6 km, 6125.6 km, and 10 077.6 km. Figure J2.5(c) illustrates the total throughput obtained by transmitting 4×175 SDM and WDM channels, estimated with GMI and after decoding, for the considered propagation distances.

J2.4.2 PDM 16-QAM and 64-QAM Signals

System performance assessment is also conducted with 16-QAM and 64-QAM modulated signals for the same launch power level. Figure J2.6(a) shows the decoded data rates as a function of transmission distance for both modulation formats. Here too,

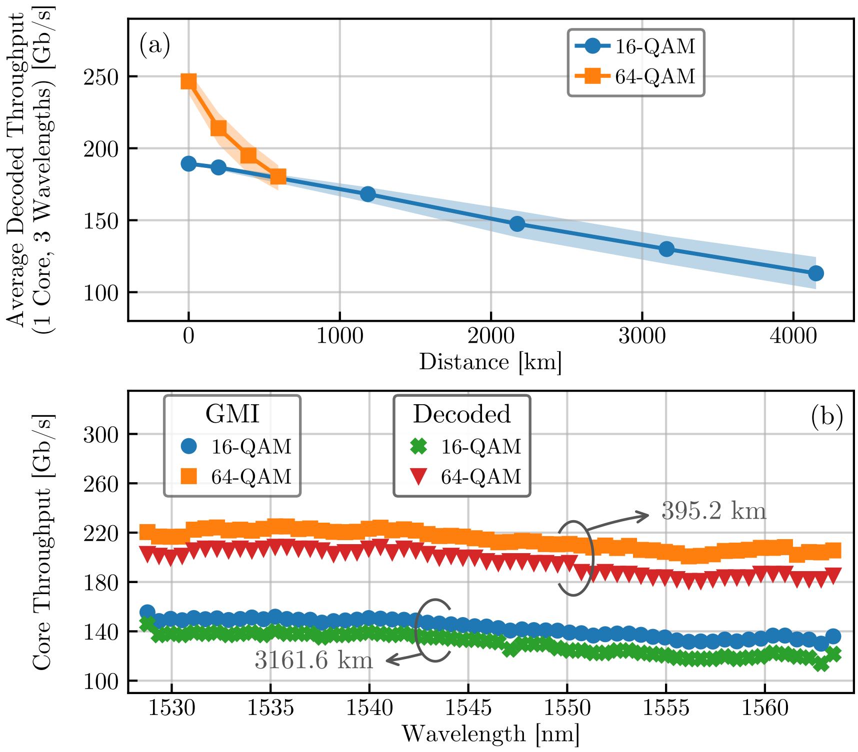

Figure J2.6: (a) Decoded throughput versus transmission distance, averaged across three wavelength channels in the C-band, measured for a single core of the fully-loaded 4-core multi-core fiber. (b) Per-core decoded throughput for 175 wavelength-division multiplexing channels on a single core of the fully-loaded 4-core multi-core fiber, estimated using both generalized mutual information and forward error correction decoding.

each data point represents the average data-rate for three WDM channels distributed across the C band, with wavelengths at 1529.9, 1545.7 and 1561.8 nm. The shaded area indicates the range between the minimum and maximum values obtained at these wavelengths. We stress that although performance assessment was conducted on only one core of the 4-core fiber, the fiber was fully loaded, with signals simultaneously transmitted across all four cores, just like in the case of 4-QAM transmission.

Figure J2.6(b) illustrates the throughput for 175 WDM channels in the same core of the 4-core MCF, estimated using both GMI and after FEC decoding, after transmission over 3161.6 km and 395.2 km for 16-QAM and 64-QAM signals, respectively. Similar to the case of 4-QAM signals, the differences in throughput among the wavelength channels are mainly attributed to the wavelength-dependence of Raman and amplifier gains, as well as the filtering applied by the OP in the loop. For 16-QAM signals, single-core throughputs of 25 Tb/s based on GMI and 22.7 Tb/s after FEC decoding are reported over a transmission distance of 3161.6 km. Similarly, for 64-QAM

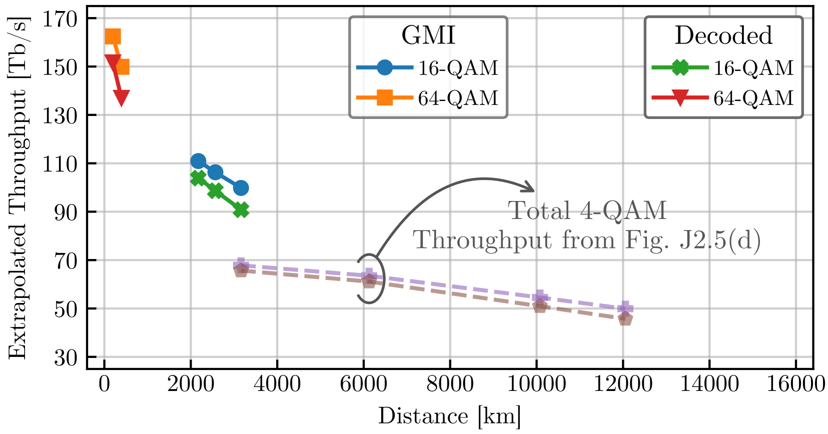

Figure J2.7: Total data rates, estimated in terms of generalized mutual information and after decoding, extrapolated from the 16-quadrature-amplitude modulated and 64-quadrature-amplitude modulated throughputs measured over a single core of the fully-loaded 4-core multi-core fiber. Total data rates obtained for 4-quadrature-amplitude modulated signals are shown in shaded colors for comparison.

signals, single-core throughputs of 37.5 Tb/s based on GMI and 34.3 Tb/s after FEC decoding are obtained over a transmission distance of 395.2 km. Given the negligible performance differences observed between cores for 4-QAM transmission, we expect extrapolated aggregate data rates of approximately 90.8 Tb/s after 3161.6 km with 16-QAM, and 137 Tb/s after 395.2 km with 64-QAM signals. These values are calculated after FEC decoding, utilizing all four cores of the MCF. Figure J2.7 illustrates the extrapolated data rates for these modulation formats – estimated using GMI and after decoding – versus propagation distance. The total throughputs obtained with 4-QAM signals, from Fig. J2.5(b), are shown in shaded colors for comparison.

J2.5 Conclusion

We demonstrated a trans-Pacific transmission distance of 12 053 km using an all-multi-core-amplified, 4-core WC-MCF system, supported by a hybrid amplification scheme integrating 4-core EDFAs and DRA. A total decoded throughput of 45.7 Tb/s was achieved by transmitting 4×175 PDM 4-QAM SDM and WDM channels ranging from 1528.8 nm to 1563.5 nm. A performance comparison between 4-QAM, 16-QAM, and 64-QAM was conducted over the same transmission system, showing significant variations in throughput and transmission reach across modulation formats. Data rates for 16-QAM and 64-QAM were extrapolated from measurements taken over a single core of the 4-core fiber while the fiber was fully loaded. Extrapolated total decoded throughputs of 90.8 Tb/s after 3161.6 km and 137 Tb/s after 395.2 km are reported for 16-QAM and 64-QAM, respectively. This analysis, performed on the first all-multi-core-amplified recirculating-loop-based transmission system, highlights the importance of modulation scheme selection in balancing total throughput and transmission reach, especially in the absence of constellation shaping. Furthermore, this work represents the longest reach ever demonstrated in spatially multiplexed transmission experiments relying entirely on SDM amplifiers.

Journal J3

Enhancing Long-Haul 15-Mode Fiber Performance: Mode Permutation for Reduced Modal Dispersion

G. Di Sciullo, D. A. Shaji, M. van den Hout, G. Rademacher, R. S. Luís, B. J. Puttnam, N. K. Fontaine, R. Ryf, H. Chen, M. Mazur, D. T. Neilson, P. Sillard, F. Achten, J. Sakaguchi, C. Okonkwo, A. Mecozzi, and C. Antonelli

in

Journal of Lightwave Technology, vol. 43, no. 2, pp. 481-491, 15 Jan, 2025

Abstract

We explore the efficacy of mode permutation (MP) to mitigate the impact of modal dispersion in a 15-mode fiber link for long-haul space-division multiplexed transmission. By introducing strong coupling between all the fiber modes, mode permutation reduces the growth rate of the link's intensity impulse response (IIR) with transmission distance, yielding a reduction in the receiver multiple-input multiple-output (MIMO)-digital signal processing (DSP) complexity. Using a recirculating fiber-loop configuration, we experimentally compare four permutation schemes and find that they are similarly effective in reducing the increase of the IIR duration from proportional to the square-root of propagation distance. At the reach of 530 km – the largest achievable with the time-domain MIMO window of 71.4 ns available in the experiment in the absence of mode permutation – the IIR duration is seen to reduce from almost 40 ns to less than 15 ns, while the maximum reach achieved with the use of mode permutation increases to 1178 km. We also devise a simple model to simulate propagation in realistic multi-mode fiber (MMF) links with independent fiber spans, whose parameters can be conveniently extracted from the data. In achieving good agreement between the simulated and experimental results, the model suggests that the effectiveness of mode permutation in a realistic 15-mode fiber link, composed of independent fiber spans, is only slightly greater than in the experimental recirculating-loop configuration.

J3.1 Introduction

As demand for higher data rates is expected to continue its exponential increase in optical fiber networks, and single-mode optical fibers are reaching their transmission limits [33], space-division multiplexing (SDM) has gained traction as a promising alternative to address the impending capacity crunch [22]. Proposed SDM fibers include multi-core fibers (MCFs), multi-mode fibers (MMFs) and hybrid multi-core multi-mode fibers (MC-MMFs) [7]. Specifically, MMFs, wherein discrete data signals are multiplexed across distinct spatial modes can support a substantial quantity of spatial channels within the same 125 µm cladding diameter as standard single-mode fibers (SMFs). This characteristic ensures similar fiber mechanical reliability and compatibility with current cabling and manufacturing processes [99]. Nonetheless, the accumulation of modal dispersion (MD) has a direct impact on the required memory length for the multiple-input multiple-output (MIMO) equalizer [140], imposing constraints on both mode count and transmission reach. Indeed, while short-distance transmission utilizing MMFs with up to 55 modes has been recently reported [43, 44, 148], experiments targeting long-haul transmission have only used up to 15 fiber modes [113–117, 189, 190]. In addressing the accumulation of MD, a strategic approach involves intentionally inducing strong mode coupling within the MMF link. This method is grounded in the understanding that modal dispersion increases proportionally to the square root of the propagation distance under conditions of strong mode mixing, as opposed to a proportional increase with propagation distance in situations marked by no-to-weak mode coupling [191–193]. In pursuit of robust mode coupling to counteract the accumulation of MD, a practical implementation involves the incorporation of lumped mode scramblers along the fiber link. This method stands as a viable scheme, strategically implemented to enhance mode mixing and mitigate MD effects, offering a solution to optimize the performance of the MMF link [193]. It is scalable for arbitrary mode counts, thereby providing a practical approach for future MMF system deployments. Recent advancements in this scheme include the proposals of cyclic mode permutation (C-MP) and cyclic mode-group permutation (C-MGP), demonstrating evolving techniques to further refine and improve the effectiveness of the mode coupling strategy [113–117].

In this work we examine the efficacy of four distinct mode permutation (MP) schemes within a recirculating-loop-based, long-haul 15-mode fiber link, expanding on [194]. Employing these permutation schemes allowed extending the transmission reach from 530 km to 1178 km while significantly reducing the complexity of the receiver MIMO digital signal processing (DSP). Notably, at 530 km, there was a reduction exceeding 65% in the duration of the MMF link intensity impulse response (IIR). An important supplement to the original work in [194] is the study of mode-dependent loss (MDL) in the MMF system, which shows that MP does not affect MDL accumulation with transmission distance. We also developed a simple model for the simulation of multi-mode propagation to assess the effectiveness of MP in realistic links with independent fiber spans, as opposed to the recirculating-loop scheme used in the experiment. The model relies on a handful of parameters that can be conveniently extracted from the experimental data. Despite its simplicity, the model demonstrated accuracy in reproducing the experimental results. Numerical results obtained for a link composed of independent fiber spans showed only a modest improvement in the performance of MP compared to the recirculating-loop configuration, further supporting the reliability and applicability of the experimental findings. Finally, the model was used to explain the observed independence of MDL accumulation on MP.

The remainder of this paper is organized as follows. Section J3.2 delves into the concept of mode permutation and introduces the schemes examined in the experiment. Section J3.3 outlines the experimental setup and presents the obtained results. In Section J3.4, a simulation framework complementing the experimental results is introduced and the corresponding findings are presented. The conclusions of this work are drawn in Section J3.5.

J3.2 Mode Permutation Schemes

Graded-index-core multi-mode fiber are characterized by the existence of non-degenerate mode groups, such that modes within the same group couple strongly during propagation, whereas modes belonging to different groups are weakly coupled and the extent to which they mix increases with propagation distance. In short-reach applications, where the inter-mode-group coupling is negligible, the individual mode groups can be addressed independently with a considerable simplification of the receiver MIMO [195, 196]. However, in metro-to-long-haul applications that are of interest for this work, a full-MIMO approach (where all the fiber modes are processed jointly) becomes necessary, in spite of the fact that non-degenerate mode groups may remain only partially coupled. In this regime MD, which is typically quantified in terms of the link's IIR duration, increases linearly with propagation distance at first, transiting to some sub-linear growth when inter-mode-group coupling becomes substantial.

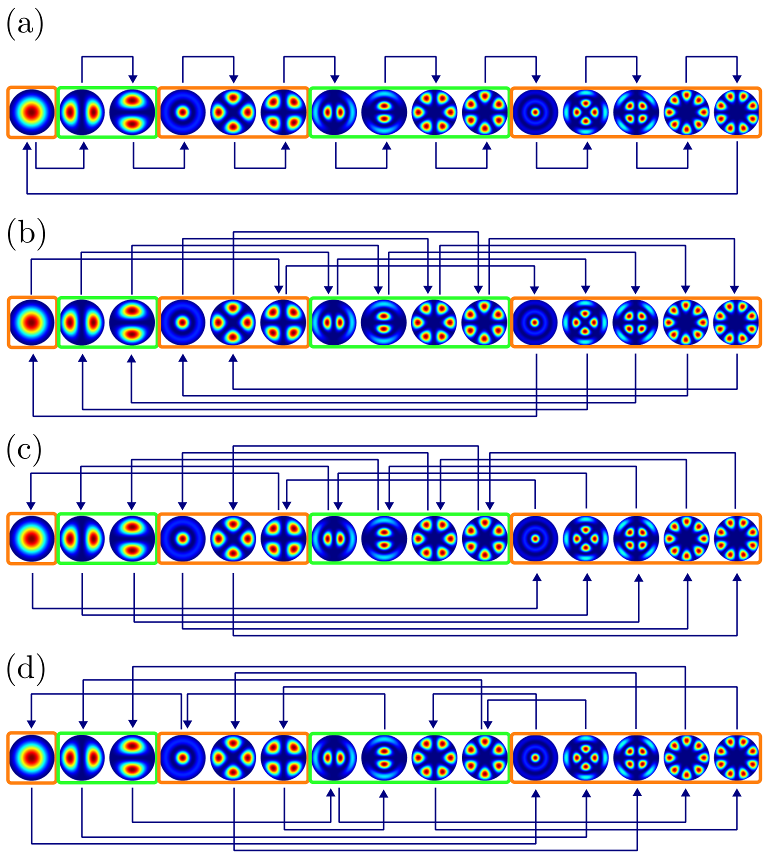

Figure J3.1: Sketch of the considered mode permutation schemes: (a) cyclic mode permutation, (b) Clockwise cyclic mode-group permutation, (c) Counter-clockwise cyclic mode-group permutation and (d) non-cyclic mode-group permutation.

The complexity of the receiver MIMO-DSP grows accordingly. In this scenario, strong coupling between all modes is preferred. In fact, in the regime of strong mode mixing, MD is known to grow only proportionally to the square root of propagation distance [191–193], implying a drastic reduction in the MIMO-DSP complexity compared to the regime of partial mode coupling.

A practical approach to induce strong coupling between modes belonging to different groups involves the introduction of lumped mode scramblers along the MMF link. In this study, we investigate the effectiveness of four distinct MP schemes in introducing strong mode mixing along a multi-span MMF link, where MP is implemented through a demultiplexer/multiplexer (DeMUX/MUX) device pair at the end of each span. The first device serves to separate the multi-mode field at the output of the MMF into individual single-mode fields. These are subsequently cross-connected to the single-mode sections of the recirculating loop, which guide the signal back to the input of the second device. Figure J3.1 illustrates the mode permutation schemes

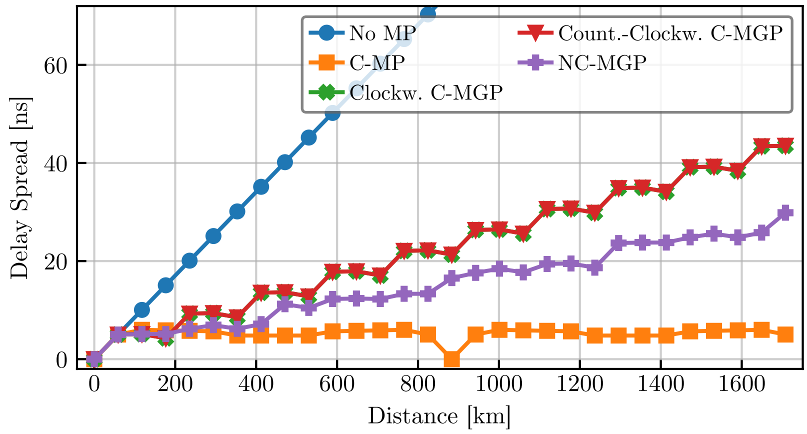

Figure J3.2: Delay spread versus propagation distance in the absence of mode coupling in the multi-mode fiber spans, with and without mode permutation, as obtained through numerical simulation.

under consideration for the 15-mode fiber used in the experiment. The first scheme [113] (Fig. J3.1(a)), employs unitary C-MP. In this method, the 15 spatial modes undergo a cyclic shift, moving one position towards higher-order modes at each permutation stage. The second [116, 117] and third schemes, involve the cyclic clockwise (clockwise C-MGP, Fig. J3.1(b)) and counter-clockwise (counter-clockwise C-MGP, Fig. J3.1(c)) shifts of the 15 spatial modes by five positions, corresponding to the largest mode-group size. These schemes exhibit a periodic pattern, where spatial modes revert to their initial configuration after either 15 or 3 permutation stages, respectively. Introducing a novel approach in our work [194], the fourth scheme (Fig. J3.1(d)), referred to as non-cyclic mode-group permutation (NC-MGP), breaks away from periodicity by implementing controlled inter-mode-group permutation. In this scheme, spatial modes within a given mode group are mapped onto other spatial modes of the remaining mode groups, with careful consideration to minimize multiple mappings between any two mode groups. We note that the proposed scheme is one of the many possible schemes that are non-periodic for practical numbers of recirculations. Additionally, the proposed approach can easily be generalized to construct non-cyclic permutation schemes for multi-mode fibers supporting arbitrary number of modes.

It is instructive noting that in the ideal case where no coupling occurs during propagation in the MMF spans, the C-MP scheme would be optimal in terms of delay management. This is illustrated in Fig. J3.2, where we plot the *delay spread* (that is, the largest differential delay between any two modes) versus propagation distance both in the absence of MP and for each of the considered permutation schemes, under the assumption of uncoupled MMF propagation. For the plot we assumed numerical values extracted from the experiment. In particular, we assumed a 15-mode fiber link with a span length of 58.9 km and the differential mode-group delays (DMGDs) relative to the fundamental mode measured at 1557.8 nm. These are listed in Table J3.1, which is discussed in Section J3.4, along with other parameters that are not used in this section. The plot shows that, as expected, in the absence of MP the delay spread grows linearly with propagation distance (blue dots), and it coincides with the differential delay between the slowest and the fastest modes. In the case of C-MGP (crosses and triangles) and NC-MGP (plus symbols), it also grows linearly with propagation distance, yet with a lower growth rate. In contrast, the delay spread is bounded and periodic in the case of C-MP (squares), as a result of the fact that each mode accumulates the same propagation delay after a number of permutation stages equal to the number of modes.

This picture changes completely in the presence of random mode coupling. Indeed, the experimental and simulation results presented in the following sections show that in realistic regimes of intra-group and inter-group coupling all permutation schemes have similar performance. In simulations, the C-MP scheme is even slightly lower performing than the others, which aligns with the observation that this scheme is the least effective in enhancing inter-mode-group coupling, as it only couples a single mode of each group into a mode of an adjacent mode group.

J3.3 Experiment

J3.3.1 Experimental Setup

Figure J3.3 illustrates the experimental setup employed to validate the efficacy of the examined mode permutation schemes. To generate a three-channel sliding test band, carriers from three tunable laser sources (TLSs) were modulated using two dual-polarization IQ modulators (DP-IQMs). These modulators were driven by the same 65 GS/s 4-channel arbitrary waveform generator (AWG). The resulting modulated signals adopted the form of polarization-division multiplexing quadrature phase-shift keying (PDM-QPSK) signals with a 1% roll-off root-raised cosine pulse shape, transmitted at a rate of 24.5 GBd. A dummy-band was generated by utilizing an optical processor (OP) to spectrally flatten the amplified spontaneous emission noise originating from an erbium-doped fiber amplifier. The composite signal, encompassing both the test and dummy bands, was passed through a loading acousto-optic modulator (AOM), acting as an optical switch, before undergoing a split and delay procedure

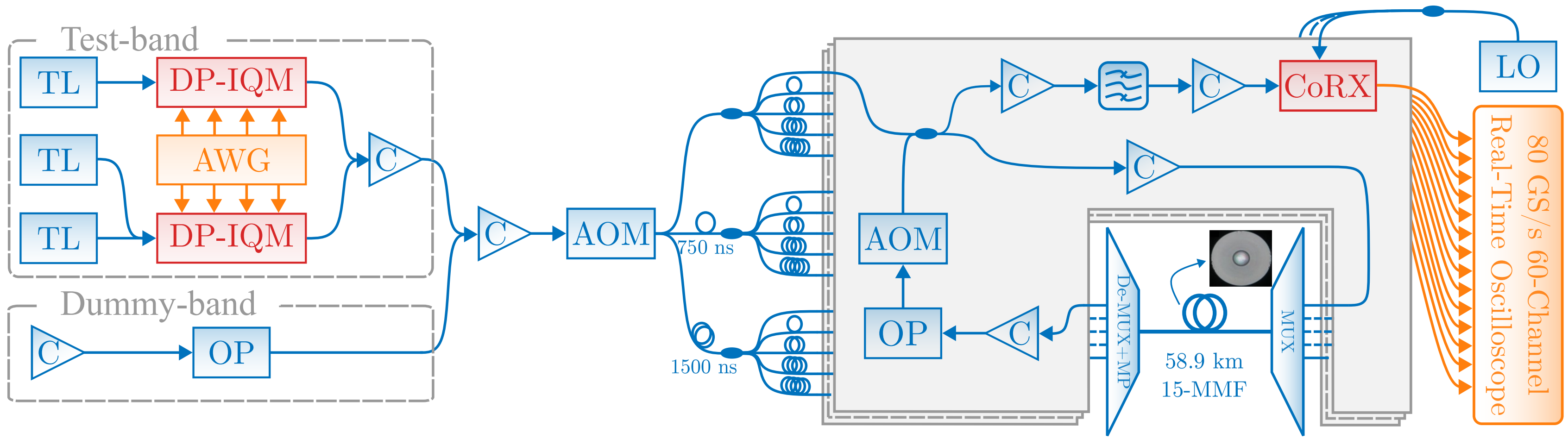

Figure J3.3: Experimental setup of the recirculating-loop-based long-haul 15-mode fiber link. Mode permutation is performed at the demultiplexer stage.

to generate 15 uncorrelated replicas of the same signal. These replicas, characterized by a relative delay of 150 ns, were subsequently directed into 15 parallel recirculating loops with precisely aligned path lengths. The alignment of the 15 parallel recirculating loops was executed with a precision within the tolerance range of ±1 cm, corresponding to a differential offset on the order of approximately ±50 ps. The signals associated with each of the 15 loops were amplified and subsequently multiplexed using a multi-plane light converter (MPLC) [122]. Following the multiplexing process, the combined signal was launched into a 58.9 km long span of 15-mode MMF with low loss (between 0.21 dB/km and 0.24 dB/km for the 15 spatial modes at 1550 nm) and inherently low DMGD (< 100 ps/km at 1550 nm) [38]. The outputs of the MPLC demultiplexer were connected to the single-mode loops based on the prescribed permutation schemes. Subsequently, the signals entered a second amplification stage, followed by OPs to rectify amplifier gain tilts as well as fiber and component loss profiles, and looping AOMs to implement recirculating-loop transmission. Regarding signal reception, the 15 outputs from the parallel loops were first amplified. Subsequently, the channel of interest (COI) was filtered and amplified once more before being received by 15 coherent receivers (Coh. RXs) that shared a common path-length aligned local oscillator (LO). The electrical signals were captured using an 80-GS/s 60-channel real-time oscilloscope, with the recorded traces intended for offline DSP, mainly involving a time-domain 30×30 MIMO equalizer. This required a time-domain equalizer window of 71.4 ns in the absence of MP, and of only 38.8 ns when MP was present in the case of recirculating-loop transmission.

J3.3.2 Experimental Results

J3.3.2.1 Modal Dispersion Accumulation

Figures J3.4(a) and J3.4(b) show how the shape of the IIR measured at 1557.8 nm evolves as propagation distance increases in the absence of MP and when NC-MGP is applied, respectively. Here, the IIR is defined as the sum of the absolute square values of the equalizer taps, normalized with respect to their maximum value. The isolated peaks seen in the first case are an indication of weak inter-group coupling occurring in the MMF spans, while their disappearance after a few spans in the second case is clearly a consequence of MP. Moreover, the Gaussian-shaped profile of the IIR at 1178 km is a signature of the strong mode coupling regime achieved in the presence of MP [192, 197].

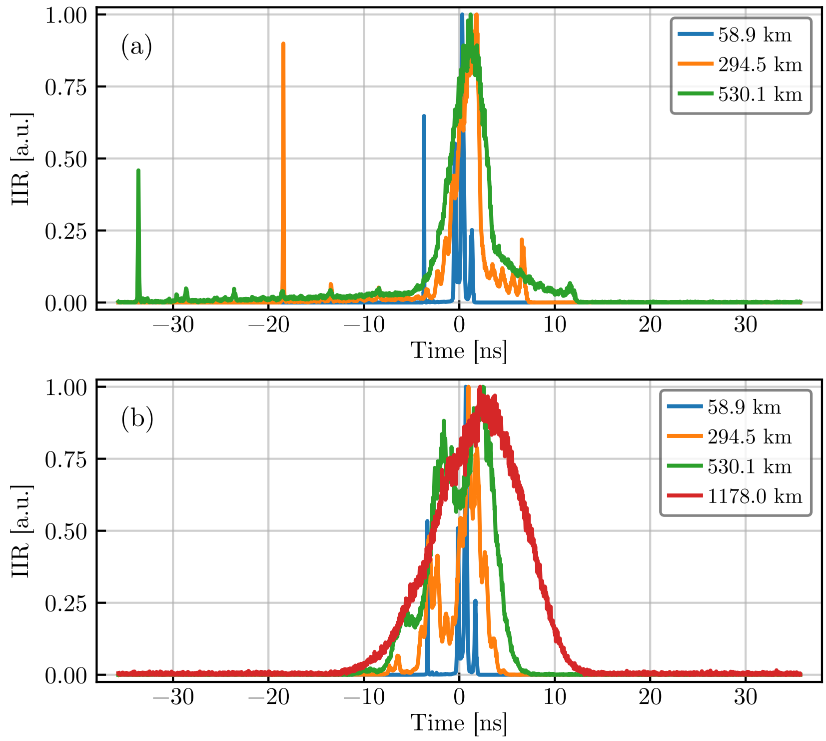

Figure J3.4: Intensity impulse response for various transmission distances at 1557.8 nm (a) in the absence of mode permutation and (b) with non-cyclic mode-group permutation.

In Fig. J3.5(a) we plot the duration of the IIR versus propagation distance for all permutation schemes, as well as in the absence of MP. Here, we define the IIR duration as the time interval encompassing 98% of the IIR energy, and each data point is obtained by averaging the IIR duration of the MMF link across five different wavelength channels spanning the C-band, specifically at 1533.9, 1539.8, 1545.7, 1553.7, and 1557.8 nm. The dots are obtained in the absence of MP and the straight line is a linear fit to the data, showing that in this case the IIR duration starts increasing linearly with propagation distance, as a result of the weak inter-mode-group coupling.[1] As inter-group coupling becomes non-negligible, a transition to a sub-linear growth of the IIR duration is seen, at approximately 400 km. The markers, complemented by a square-root data fit growing at a rate of approximately 496 ps/$\sqrt{\text{km}}$, refer to the considered permutation schemes. The remarkable alignment between the data and the square-root fit indicates that the MMF link is operating in the strong mode

[1] We acknowledge that the observed linear increase in the IIR duration with propagation distance, in the absence of mode permutation, may be attributed in part to certain loop artifacts—such as path-length misalignment between single-mode loops—that are inherently present in practical transmission systems. If this assumption holds true, our findings demonstrate the effective mitigation of these artifacts' impact through the implementation of mode permutation.

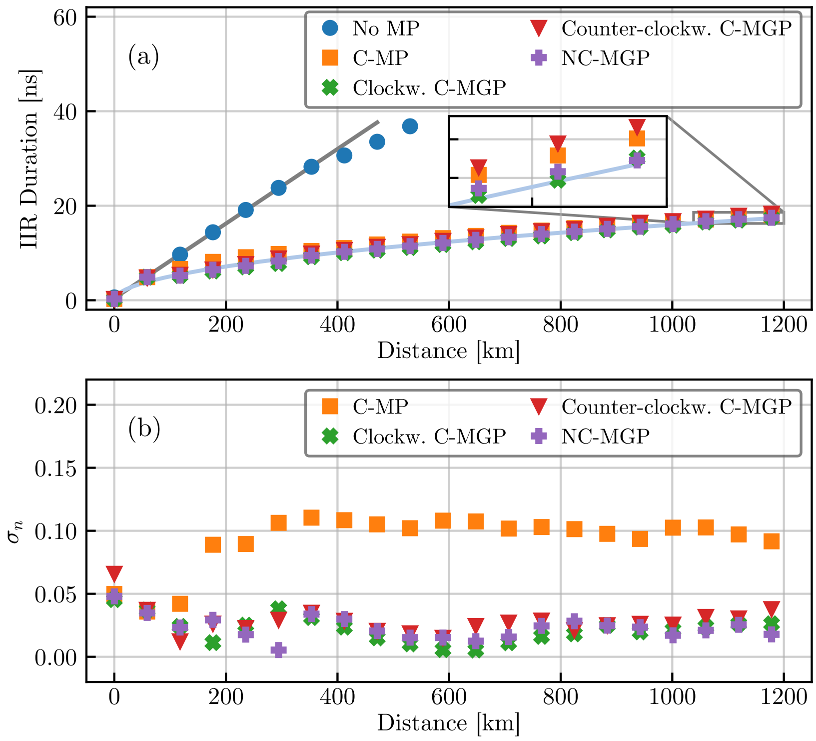

Figure J3.5: (a) Wavelength-averaged intensity impulse response duration versus transmission distance in the absence of mode permutation and for the considered permutation schemes and (b) normalized standard deviation of the intensity impulse response duration versus transmission distance for the considered permutation schemes. The line spacing in the inset of (a) is 2 ns.

coupling regime, underscoring the efficacy of the considered permutation schemes in facilitating inter-mode-group coupling. The performance among the schemes exhibits no significant differences, while an impressive reduction of approximately 65% in the IIR duration is obtained at 530.1 km. The fact that C-MP performs similar to the other schemes is in contrast with what was observed in [114]. We attribute this discrepancy to the fact that, in our case, C-MP always maps LP_{01} into LP_{11}, which are the fastest and the slowest mode groups,[2] respectively, at all wavelengths used in the experiment, therefore implementing a delay-management scheme that remains somewhat effective also in the presence of random mode coupling, beyond the ideal case of no-coupling illustrated in Fig. J3.2. However, this result would change if the first and the second mode groups were not the fastest and the slowest, respectively.

We also examined the wavelength dependence of the IIR duration. To this end, we calculated the normalized standard deviation of the IIR duration measured across the five distinct wavelength channels spanning the C-band for each permutation scheme.

[2]For the channel at 1558.8 nm, this can be seen in Table J3.1.

This is obtained by normalizing the actual standard deviation of the IIR duration with respect to its average value, namely $\sigma_n = \frac{1}{\mu}\sqrt{\frac{1}{N_{\rm ch}}\sum_{i=1}^{N_{\rm ch}}(T_i - \mu)^2}$, where T_i is the i-th wavelength-channel's IIR duration, and $\mu = \frac{1}{N_{\rm ch}}\sum_{i=1}^{N_{\rm ch}} T_i$ is the average duration across all channels. In Fig. J3.5(b), σ_n is plotted versus propagation distance for each permutation scheme. The plot shows that all permutation schemes have similar wavelength dependence,[3] with the exception of the C-MP scheme, which exhibits a stronger dependence on wavelength. We speculate that the larger deviation is due to the fact that the C-MP scheme is less effective in achieving strong mode coupling than the other schemes, which makes the profile and duration of the IIR not as deterministic as it would be expected [192].

J3.3.2.2 MDL Accumulation

Modal dispersion is a unitary effect with no direct implications on the achievable data transmission capacity. In contrast, MDL is non-unitary and it fundamentally limits the achievable transmission performance [198–201]. We characterize the link's MDL by using two metrics. The first metric is the ratio in dB between the largest and smallest eigenvalues of $\mathbf{H}(\omega)\mathbf{H}^{\dagger}(\omega)$, where by $\mathbf{H}(\omega)$ we denote the frequency-dependent transfer matrix of the MMF link and by $\mathbf{H}^{\dagger}(\omega)$ its hermitian adjoint. We refer to this metric as Max/Min MDL. The frequency-dependent transfer matrix $\mathbf{H}(\omega)$ is derived as the inverse of the Fourier transform of the time-domain MIMO equalization matrix. The second metric is the standard deviation of the natural logarithm of all of the eigenvalues of the same matrix, also expressed in dB [199]. We refer to this metric as Std-MDL. The frequency dependence of the so-evaluated quantities is then eliminated by performing a frequency average across the WDM channel bandwidth.

In Fig. J3.6, we plot the MDL of the 15-mode fiber link versus propagation distance for all the considered permutation schemes, as well as in the absence of MP. It is worth noting that the results in the absence of MP are hidden by the presence of the other data points. Similarly to what was done for the IIR duration, each data point is obtained by averaging the MDL of the MMF link across the five channel wavelengths. The vertical axis on the left refers to the Max/Min MDL, while the vertical axis on the right refers to the Std-MDL. The results in the latter figure show no substantial differences among the various permutation scenarios, indicating that MP does not affect the accumulation of MDL, in agreement with what was observed in [202]. An interesting feature that emerges from the results of Fig. J3.6 is that

[3] Specifically, in [141], the IIR duration is seen to increase as a function of wavelength.

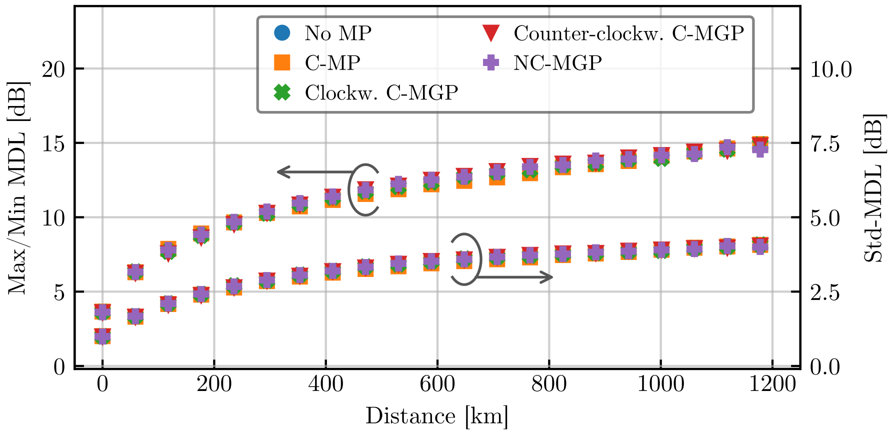

Figure J3.6: Wavelength-averaged Max/Min MDL and Std-MDL versus propagation distance in the absence of mode permutation and for the considered permutation schemes.

MDL accumulates proportionally to the square root of propagation distance not only in the presence of MP, but also when no MP is implemented. This result comes as a surprise, as one would expect to see a linear growth of MDL with propagation distance. A possible explanation of this behavior is that MDL is dominated by some intra-mode-group MDL, possibly arising from the in-span fiber splices, rather than by inter-mode-group MDL. In particular, we have verified that the MDL values extracted from the channel-transfer-matrix blocks describing the fourth and fifth mode groups after one fiber span are comparable in magnitude to the overall MDL. On the other hand, MDL measurements performed on a deployed 48 km-long fiber of the same kind used in this work have shown that when addressing only the fourth fiber mode-group [203] or all the fiber modes [146], the measured MDL values are quite similar. These evidences provide a qualitative explanation of why MDL grows proportionally with the square root of propagation distance, namely because its accumulation is dominated by strong coupling within a group of quasi-degenerate modes.

We also characterized the wavelength dependence of MDL. To this end, we computed the normalized standard deviation of the MDL measured across the five distinct wavelength channels spanning the C-band for each permutation scheme. Figure J3.7 shows the resulting values of the normalized standard deviation plotted versus the transmission distance in the absence of MP and for all the considered permutation schemes, with Fig. J3.7(a) referring to the Max/Min MDL, and Fig. J3.7(b) to the Std-MDL. The absence of substantial difference between the considered scenarios is consistent with the argument that MDL accumulation is dominated by intra-mode-group dynamics.

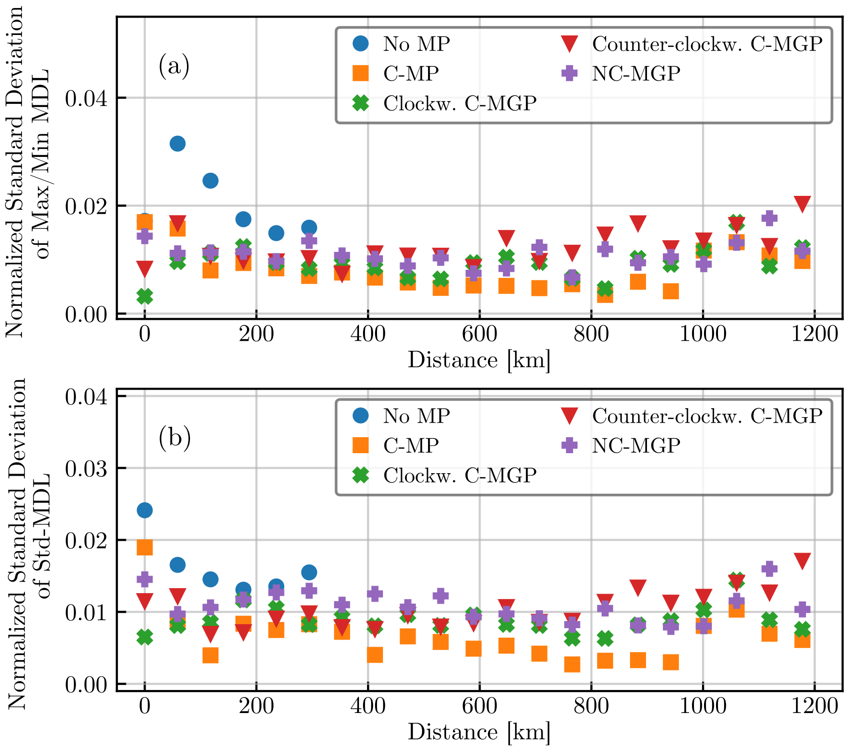

Figure J3.7: Normalized standard deviation of (a) Max/Min MDL and (b) Std-MDL versus transmission distance in the absence of mode permutation and for the considered permutation schemes.

J3.4 Simulations

In this section we perform simulations in support of the experimental results, with two main goals. On the one hand, we aim to assess whether the similarity in performance between the considered permutation schemes is consistent with some simple and fully-controllable model or results from practical implementation aspects. On the other hand, we aim to assess whether the performance of MP improves in real systems, where the signal propagates in uncorrelated fiber spans, as compared to the case where it propagates in the same fiber span in a recirculating-loop configuration.

J3.4.1 Model for Distributed Coupling and Parameter Extraction

We start by considering two non-degenerate mode groups a and b, which we describe by means of generalized Jones vectors $\vec{E}_a$ and $\vec{E}_b$ [191], whose evolution along the fiber obeys the following set of coupled equations,

$$\begin{aligned}\frac{\mathrm{d}\vec{E}_a}{\mathrm{d}z} &= i\beta_a\vec{E}_a + i\omega\beta'_a\vec{E}_a + i\frac{\vec{V}_a\cdot\vec{\Lambda}}{2N_a}\vec{E}_a \\ &+ i\omega\frac{\vec{W}_a\cdot\vec{\Lambda}}{2N_a}\vec{E}_a - \frac{\vec{\alpha}_a\cdot\vec{\Lambda}}{2} + i\mathbf{C}\vec{E}_b \end{aligned} \quad \text{(J3.1)}$$

$$\begin{aligned}\frac{\mathrm{d}\vec{E}_b}{\mathrm{d}z} &= i\beta_b\vec{E}_b + i\omega\beta'_b\vec{E}_b + i\frac{\vec{V}_b\cdot\vec{\Lambda}}{2N_b}\vec{E}_b \\ &+ i\omega\frac{\vec{W}_b\cdot\vec{\Lambda}}{2N_b}\vec{E}_b - \frac{\vec{\alpha}_b\cdot\vec{\Lambda}}{2} + i\mathbf{C}^\dagger\vec{E}_a. \end{aligned} \quad \text{(J3.2)}$$

Here β_u and β'_u, with $u \in \{a, b\}$, are the propagation constant and its derivative with respect to the angular frequency ω, respectively, for mode group u, while N_u is the number of degenerate spatial modes in the same group. By $\vec{V}_u$ we denote a generalized Stokes vector of dimension $D_u = 4N_u^2 - 1$, while by $\vec{\Lambda}_u$ we denote a vector whose elements are $2N_u \times 2N_u$ generalized Pauli matrices, so that $\vec{V}_u \cdot \vec{\Lambda}_u = \sum_{n=1}^{D_u} V_{u,n}\Lambda_{u,n}$ [191]. This term describes intra-group random mode coupling in mode groups u. The vector $\vec{W}_u$ is also a generalized Stokes vector and it describes intra-group modal dispersion [191]. The matrix $\mathbf{C}$ and its Hermitian adjoint $\mathbf{C}^\dagger$ account for random inter-group coupling. The vectors $\vec{\alpha}_a$ and $\vec{\alpha}_b$ are the local MDL vectors, which we also model as independent white-noise processes of suitable strength [200]. In what follows, we model both intra-group and inter-group random coupling by means of white noise processes, with the result that the mismatch in propagation constant becomes immaterial and the terms proportional to β_u can be dropped [204]. A further simplification is obtained by establishing a reference frame that follows intra-group coupling in each mode group. This yields the following simplified equations

$$\frac{\mathrm{d}\vec{E}_a}{\mathrm{d}z} = i\omega\beta'_a\vec{E}_a + i\omega\frac{\vec{W}_a\cdot\vec{\Lambda}}{2N_a}\vec{E}_a - \frac{\vec{\alpha}_a\cdot\vec{\Lambda}}{2} + i\mathbf{C}\vec{E}_b \quad \text{(J3.3)}$$

$$\frac{\mathrm{d}\vec{E}_b}{\mathrm{d}z} = i\omega\beta'_b\vec{E}_b + i\omega\frac{\vec{W}_b\cdot\vec{\Lambda}}{2N_b}\vec{E}_b - \frac{\vec{\alpha}_b\cdot\vec{\Lambda}}{2} + i\mathbf{C}^\dagger\vec{E}_a, \quad \text{(J3.4)}$$

with

$$\langle W_{u,i}(z)W_{u,j}(z')\rangle = \gamma_u^2\delta_{i,j}\delta(z-z') \quad \text{(J3.5)}$$

$$\langle \alpha_{u,i}(z)\alpha_{u,j}(z')\rangle = \zeta_u^2\delta_{i,j}\delta(z-z') \quad \text{(J3.6)}$$

$$\langle C_{i,j}(z)C^*_{i',j'}(z')\rangle = \eta^2\delta_{i,i'}\delta_{j,j'}\delta(z-z') \quad \text{(J3.7)}$$

$$\langle C_{i,j}(z)C_{i',j'}(z')\rangle = 0, \quad \text{(J3.8)}$$

where the coefficients involved are to be extracted from the experimental data. The inverse group velocities β'_u are obtained by inspecting the peaks of the measured IIR after propagation in the first fiber span.

The MD coefficients γ_u^2 are known to be related to the duration of the intra-group intensity impulse responses through the relation $T_u^2(z) = \gamma_u^2 D_u / 4N_u^2\, z$ [192]. This allows to extract them by fitting the intensity impulse responses of the individual mode groups at the output of the first fiber span with a Gaussian-shaped waveform with root-mean-square width equal to T_u.

We set $\vec{\alpha}_a = \vec{\alpha}_b = 0$ in the following discussion. We leave the analysis of MDL accumulation to Section J3.4.4.

The extraction of the inter-group coupling coefficients is more involved. Here we proceed by evaluating the evolution of the mean optical powers in the individual mode groups, as these quantities can be extracted from the experimental crosstalk matrix. To this end we make use of the Ito calculus [205], by first expressing Eqs. (J3.3) and (J3.4) in the Stratonovich form, namely,

$$\mathrm{d}\vec{E}_a = i\omega\beta'_a\vec{E}_a\mathrm{d}z + i\omega\frac{\mathrm{d}\vec{W}_a\cdot\vec{\Lambda}}{2N_a}\vec{E}_a + i\mathrm{d}\mathbf{C}\vec{E}_b \tag{J3.9}$$

$$\mathrm{d}\vec{E}_b = i\omega\beta'_b\vec{E}_b\mathrm{d}z + i\omega\frac{\mathrm{d}\vec{W}_b\cdot\vec{\Lambda}}{2N_b}\vec{E}_b + i\mathrm{d}\mathbf{C}^\dagger\vec{E}_a. \tag{J3.10}$$

The Ito-corrected equations are obtained in the following form with the use of Eqs. (J3.5), (J3.7) and (J3.8),

$$\begin{aligned}\mathrm{d}\vec{E}_a = {} & i\omega\beta'_a\vec{E}_a\mathrm{d}z + i\omega\frac{\mathrm{d}\vec{W}_a\cdot\vec{\Lambda}}{2N_a}\vec{E}_a + i\mathrm{d}\mathbf{C}\vec{E}_b \\ & -\omega^2\frac{\gamma_a^2 D_a}{8N_a^2}\vec{E}_a\mathrm{d}z - \frac{1}{2}\eta^2 2N_b\vec{E}_a\mathrm{d}z\end{aligned} \tag{J3.11}$$

$$\begin{aligned}\mathrm{d}\vec{E}_b = {} & i\omega\beta'_b\vec{E}_b\mathrm{d}z + i\omega\frac{\mathrm{d}\vec{W}_b\cdot\vec{\Lambda}}{2N_b}\vec{E}_b + i\mathrm{d}\mathbf{C}^\dagger\vec{E}_a \\ & -\omega^2\frac{\gamma_b^2 D_b}{8N_b^2}\vec{E}_b\mathrm{d}z - \frac{1}{2}\eta^2 2N_a\vec{E}_b\mathrm{d}z.\end{aligned} \tag{J3.12}$$

The equations for the average powers carried by each mode group $I_a = \langle\vec{E}_a^\dagger\vec{E}_a\rangle$ and $I_b = \langle\vec{E}_b^\dagger\vec{E}_b\rangle$ are then obtained in the following form,

$$\mathrm{d}I_a = \eta^2 2N_a I_b\mathrm{d}z - \eta^2 2N_b I_a\mathrm{d}z \tag{J3.13}$$

$$\mathrm{d}I_b = \eta^2 2N_b I_a\mathrm{d}z - \eta^2 2N_a I_b\mathrm{d}z, \tag{J3.14}$$

or, equivalently,

$$\frac{\mathrm{d}}{\mathrm{d}z}\begin{bmatrix} I_a \\ I_b \end{bmatrix} = \begin{bmatrix} -2\eta^2 N_b & 2\eta^2 N_a \\ 2\eta^2 N_b & -2\eta^2 N_a \end{bmatrix}\begin{bmatrix} I_a \\ I_b \end{bmatrix} = \mathbf{K}\begin{bmatrix} I_a \\ I_b \end{bmatrix}. \tag{J3.15}$$

The solution to the above,

$$\begin{bmatrix} I_a(z) \\ I_b(z) \end{bmatrix} = \exp(\mathbf{K}z)\begin{bmatrix} I_a(0) \\ I_b(0) \end{bmatrix} = \mathbf{X}_g\begin{bmatrix} I_a(0) \\ I_b(0) \end{bmatrix}, \tag{J3.16}$$

can be mapped into experimental data, by establishing a relation between the matrix $\mathbf{X}_g$, which describes inter-mode-group crosstalk, and the experimentally measurable crosstalk matrix $\mathbf{X}$. This relation is not straightforward and is discussed in what follows. Prior to doing so, however, we note that the expression of $\mathbf{K}$ can be readily generalized to the case of more than two mode groups. For instance, in the case of three mode groups a, b, and c, it takes the following form

$$\begin{bmatrix} -2(\eta_{ab}^2 N_b + \eta_{ac}^2 N_c) & 2\eta_{ab}^2 N_a & 2\eta_{ac}^2 N_a \\ 2\eta_{ab}^2 N_b & -2(\eta_{ab}^2 N_a + \eta_{bc}^2 N_c) & 2\eta_{bc}^2 N_b \\ 2\eta_{ac}^2 N_c & 2\eta_{bc}^2 N_c & -2(\eta_{ac}^2 N_a + \eta_{bc}^2 N_b) \end{bmatrix} \tag{J3.17}$$

where η_{uv}^2 is the coefficient that describes coupling between mode groups u and v. Figure J3.8 illustrates the relation between $\mathbf{X}_g$, which is a $N_g \times N_g$ matrix (with N_g denoting the number of non-degenerate mode groups), and $\mathbf{X}$, which is an $N \times N$ matrix (with N denoting the total number of modes), in the case of a three-mode-group fiber. The figure relies on the fact that the simple model used in this work yields a crosstalk matrix $\mathbf{X}$ that is symmetric and made of blocks with identical elements[4] (the elements in each block are identical owing to the strong intra-group mixing). Therefore, each element in the mode-group crosstalk matrix $\mathbf{X}_g$ corresponding to a specific pair of mode groups is obtained by summing the elements of any one column of $\mathbf{X}$ that also corresponds to the same pair of mode groups. For instance, the (b, c) element of $\mathbf{X}_g$ can be obtained by summing the second and third elements of the sixth column of $\mathbf{X}$ (or, equivalently, the second and third elements of the fourth or the fifth column of $\mathbf{X}$). Note that all the elements in each column (or row) of $\mathbf{X}$ sum to unity, as a result of unitary propagation assumed in the model.

Extracting the 5×5 matrix $\mathbf{X}_g$ from the experimental 15×15 crosstalk matrix $\mathbf{X}_{\mathrm{exp}}$ is not as straightforward, as in practice $\mathbf{X}_{\mathrm{exp}}$ never takes the highly symmetric form illustrated in Fig. J3.8. Note that by $\mathbf{X}_{\mathrm{exp}}$ we denote the time- and polarization-averaged absolute square fiber impulse response matrix, measured for a single MMF

[4]Symmetry emerges immediately in the special case $N_a = N_b = N_c = 1$, where $\mathbf{X}$ and $\mathbf{X}_g$ coincide.

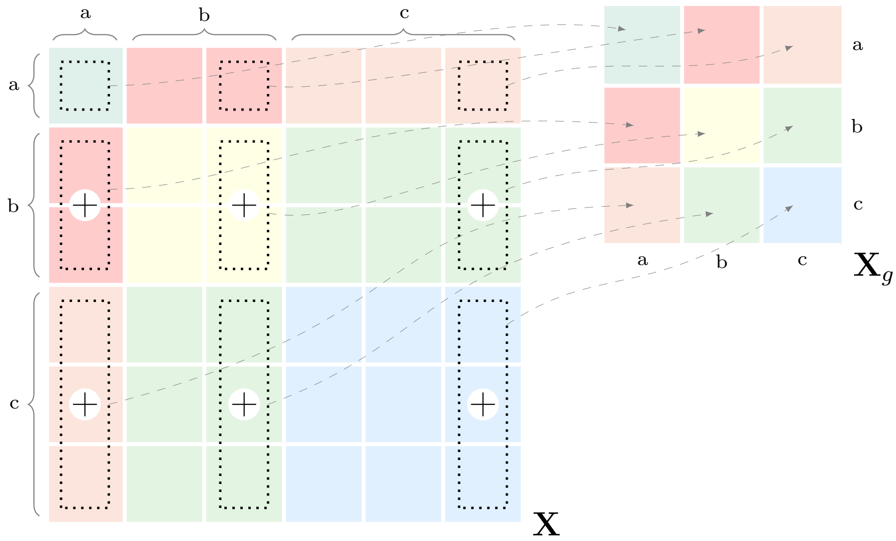

Figure J3.8: Relation between the $N \times N$ crosstalk matrix $\mathbf{X}$ and the $N_g \times N_g$ matrix $\mathbf{X}_g$ describing inter-mode-group crosstalk, in the example of a three-mode-group fiber, where $N = 6$ and $N_g = 3$.

span. The first step towards extracting the ten coupling coefficients (one per each pair of mode groups) is therefore enforcing this form into $\mathbf{X}_{\text{exp}}$, which is done as follows. The matrix $\mathbf{X}_{\text{exp}}$ is first normalized so that the sum of each column's elements equals one. The obtained matrix (that in practice is slightly asymmetric) is then symmetrized into $\tilde{\mathbf{X}}_{\text{exp}} = (\mathbf{X}_{\text{exp}} + \mathbf{X}^t_{\text{exp}})/2$. To shape $\tilde{\mathbf{X}}_{\text{exp}}$ into the form depicted in Fig. J3.8, all the elements within each of the off-diagonal blocks are replaced with their respective averages. Subsequently, normalization of each column is re-enforced by setting the elements in each diagonal square box with identical values so that the sum of the elements in each column equals one. The resulting matrix can then be used to extract $\mathbf{X}_g$ as illustrated in Fig. J3.8, and the ten coupling coefficients are obtained from the off-diagonal elements of $\log(\mathbf{X}_g)/L_s$, where L_s is the span length.

J3.4.2 Numerical Simulation

In the numerical simulation, propagation is modeled based on Eqs. (J3.3) and (J3.4), generalized for five mode groups. A 15-mode fiber span of length $L_s = 58.9\,\text{km}$ (consistent with the experiment) is emulated. It is implemented as a concatenation of $\mathcal{N} = 400$ wave-plates of width $\Delta z = L_s/\mathcal{N}$. The transfer matrix of each wave-plate

Table J3.1: Dispersion coefficients at 1557.8 nm used for simulation.

	$\mathbf{MG}_a$	$\mathbf{MG}_b$	$\mathbf{MG}_c$	$\mathbf{MG}_d$	$\mathbf{MG}_e$
MD γ_u (ps/km$^{1/2}$)	2.1369	13.304	8.0916	9.8246	16.952
DMGD β'_u (ps/km) (w.r.t. $\mathbf{MG}_a$)	–	-85.236	-67.219	-54.399	-68.951

$\mathbf{U}_{\rm wp}$ is then characterized by $\exp(i\mathbf{M}\Delta z)$, with

$$\mathbf{M} = \begin{bmatrix} \frac{\vec{W}_a\cdot\vec{\Lambda}_a}{2N_a}\omega & \mathbf{C}_{ab} & \mathbf{C}_{ac} & \mathbf{C}_{ad} & \mathbf{C}_{ae} \\ \mathbf{C}^\dagger_{ab} & \frac{\vec{W}_b\cdot\vec{\Lambda}_b}{2N_b}\omega & \mathbf{C}_{bc} & \mathbf{C}_{bd} & \mathbf{C}_{be} \\ \mathbf{C}^\dagger_{ac} & \mathbf{C}^\dagger_{bc} & \frac{\vec{W}_c\cdot\vec{\Lambda}_c}{2N_c}\omega & \mathbf{C}_{cd} & \mathbf{C}_{ce} \\ \mathbf{C}^\dagger_{ad} & \mathbf{C}^\dagger_{bd} & \mathbf{C}^\dagger_{cd} & \frac{\vec{W}_d\cdot\vec{\Lambda}_d}{2N_d}\omega & \mathbf{C}_{de} \\ \mathbf{C}^\dagger_{ae} & \mathbf{C}^\dagger_{be} & \mathbf{C}^\dagger_{ce} & \mathbf{C}^\dagger_{de} & \frac{\vec{W}_e\cdot\vec{\Lambda}_e}{2N_e}\omega \end{bmatrix}. \quad \text{(J3.18)}$$

As discussed in the previous section, the terms in the main diagonal describe intra-group mode dispersion. The vectors $\vec{W}_u$ ($u \in \{a,b,c,d,e\}$) are all independently generated and their components are independent Gaussian random variables with zero mean and standard deviation equal to $\gamma_u/\sqrt{\Delta z}$, consistent with Eq. (J3.5). The matrix $\mathbf{C}_{uv}$ ($u,v \in \{a,b,c,d,e\}$) describes coupling between mode groups u and v. The coupling matrices are generated independently of one another and, in accordance with Eqs. (J3.7) and (J3.8), their elements are independent complex-valued Gaussian random variables with zero mean, uncorrelated real and imaginary parts, and standard deviation equal to $\eta_{uv}/\sqrt{\Delta z}$. Consistently with the experimental settings, the fiber-span transfer matrix $\mathbf{T}_s(\omega)$ is calculated in a frequency band of 24.5 GHz. Multiple recirculations are described in the frequency domain by the matrix $\mathbf{T}_s(\omega)\mathbf{P}\mathbf{T}_s(\omega)\cdots\mathbf{P}\mathbf{T}_s(\omega)$, where by $\mathbf{P}$ we denote a 30×30 matrix that implements ideal MP. The inverse Fourier transform of the accumulating matrix is used to evaluate the intensity impulse response at every recirculation. The parameters used in the simulations for the wavelength channel at 1557.8 nm are listed in Table J3.1 and Table J3.2.

J3.4.3 Simulation Results: Modal Dispersion

Figure J3.9 shows a plot of the simulated IIR of the wavelength channel at 1557.8 nm, for the same propagation distances and MP settings as in Fig. J3.4. A qualitative

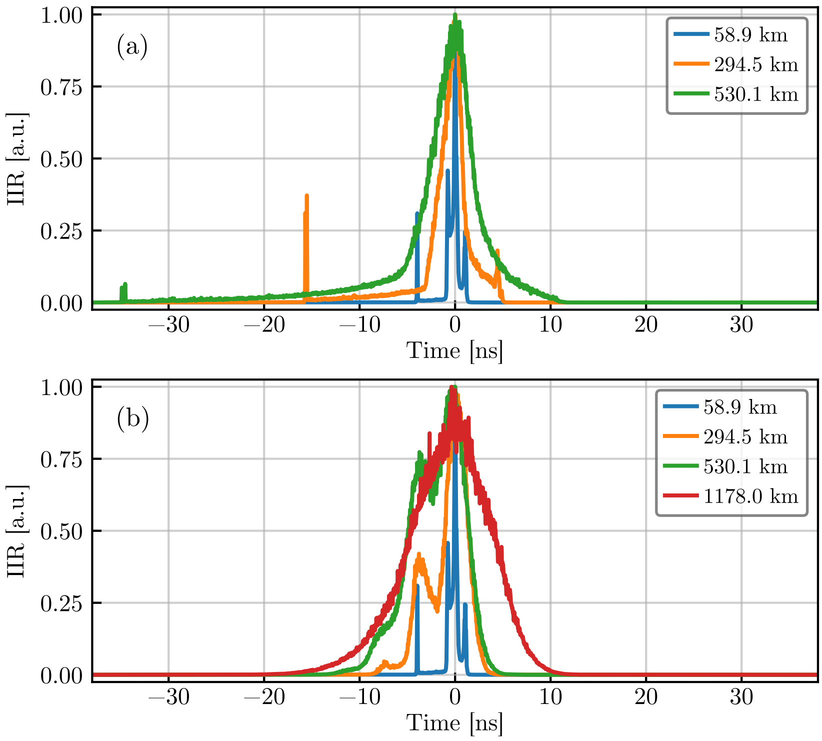

Figure J3.9: Simulated intensity impulse response for various transmission distances at 1557.8 nm (a) in the absence of mode permutation and (b) with non-cyclic mode-group permutation.

similarity between the two figures can be noticed.

Figure J3.10(a) shows the plot of the IIR duration versus propagation distance for the same wavelength channel (the duration of the simulated IIR is calculated to be the period of time which encompasses 98% of the IIR energy, as in the experiment). Similarly, Fig. J3.10(b) illustrates the extension of the same analysis to all five channels, with their average IIR duration plotted versus propagation distance. In both figures, a square-root fit is also plotted for comparison. The plot indicates that, on average, all permutation schemes yield similar results in remarkable agreement with

Table J3.2: Coupling coefficients at 1557.8 nm used for simulation.

Coefficient	**Value** ($km^{-1/2}$)	**Coefficient**	**Value** ($km^{-1/2}$)
η_{ab}	0.0296	η_{bd}	0.0144
η_{ac}	0.0130	η_{be}	0.0129
η_{ad}	0.0297	η_{cd}	0.0150
η_{ae}	0.0129	η_{ce}	0.0302
η_{bc}	0.0147	η_{de}	0.0325

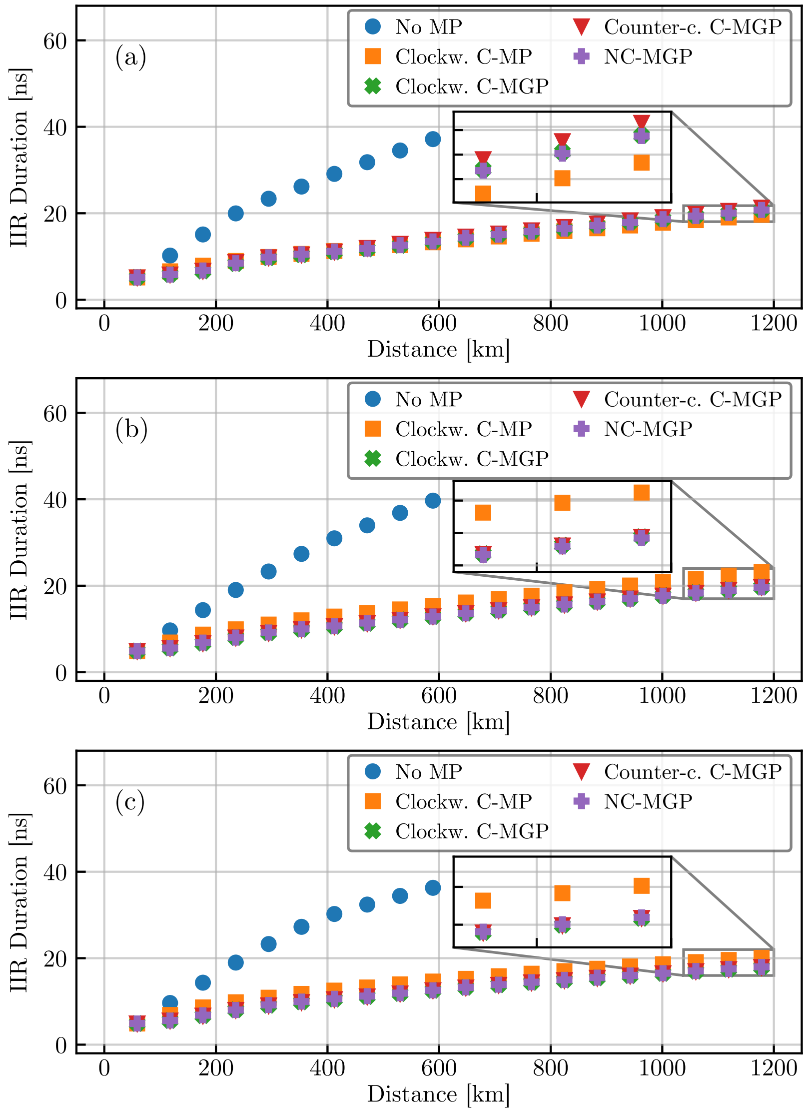

Figure J3.10: (a) Simulated intensity impulse response duration of the wavelength channel at 1557.8 nm versus propagation distance in the recirculating-loop configuration. (b) Simulated intensity impulse response duration averaged over the five wavelength channels used in the experiment versus propagation distance in the recirculating-loop configuration. (c) Same as in (b) for a link with independent fiber spans. The line spacings in the insets of (b) and (c) are 2 ns.

the experiment, with the C-MP scheme, performing slightly lower than the others. Specifically, at 1178 km, it results in an IIR duration approximately 2 ns greater than for the other schemes. This suggests that in the propagation regime of our experiment, inter-group coupling is more critical than delay management in implementing MP. The fact that no difference in performance between the C-MP scheme and the other schemes is observed experimentally, must be ascribed to additional coupling introduced in the experimental setup. Indeed, in our model we assume that coupling occurs only during fiber propagation, whereas multiplexing, de-multiplexing and MP are implemented ideally, that is by introducing no additional crosstalk.

We used the model developed for propagation in the 15-mode fiber, to evaluate the performance of the permutation schemes in a realistic multi-span fiber system, where permutation is performed between independent fiber spans. To this end, we simulated a fiber link composed of 20 fiber spans, where each span was generated independently as described above. Figure J3.10(c) illustrates the IIR duration evaluated at the end of each span for all permutation schemes. Note that, similar to Fig. J3.10(b), each data point in the figure is obtained by averaging the IIR duration of the MMF link across the five wavelength channels spanning the C-band. Compared to the recirculating-loop configuration, only a small additional reduction in the IIR duration is observed, which further supports the reliability of our experimental findings in predicting the performance of MP in field-deployed multi-span fiber links.

It is worth stressing that the effectiveness of the C-MP scheme is strongly influenced by the fact that the fastest mode (LP_{01}) is always mapped into the slowest mode group (LP_{11}). This suggests a dependence on the details of the MMF design for this scheme's performance. Indeed, we verified through simulations that exchanging the group velocities of the five mode groups may substantially deteriorate the performance of the C-MP scheme, while having negligible practical impact on the performance of the other schemes.

J3.4.4 Simulation Results: Mode-Dependent Loss

As observed in Section J3.3.2.2, MDL accumulates with propagation distance in the same way with and without MP. A possible explanation for this evidence is that MDL accumulates within groups of strongly coupled modes as a result of random and distributed local MDL, compatible with multiple fiber splices, thereby growing proportionally to the square root of propagation distance even in the absence of MP. Independence of the MDL accumulation on the mode permutation scheme has also been reported in [202], where it was argued that this might follows from the fact that MDL is mainly introduced by the single-mode stages connecting two recirculating loops.

To assess which one of the two assumptions is consistent with the experimental observations, we describe the accumulation of distributed MDL at the center frequency by simply setting $\omega = 0$ in Eqs. (J3.3) and (J3.4). Conversely, we account for the case of MDL introduced by the single-mode stage by adding independent gain

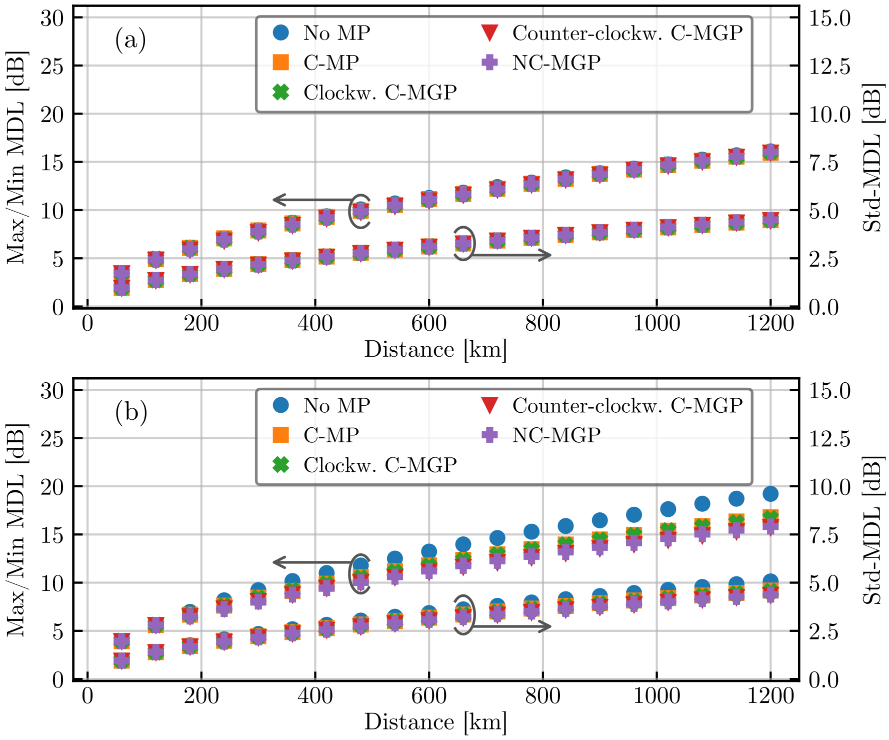

Figure J3.11: Simulated Max/Min MDL and Std-MDL for the wavelength channel at 1557.8 nm versus propagation distance in the recirculating-loop configuration assuming (a) Distributed mode-dependent loss, and (b) Single-mode gain fluctuations.

fluctuations with a Gaussian distribution and suitable strength to the propagating space and polarization modes between two recirculations, while assuming that the multi-mode fiber itself is unitary, that is, assuming $\alpha_a = \alpha_b = 0$ in Eqs. (J3.3) and (J3.4). In both cases, a random phase is applied to each space and polarization mode between two recirculations, in order to account for the effect of the AOMs that are used in the loop as optical switches (the AOMs apply an 80 MHz frequency shift when they route the impinging signal towards the next circulation). Note that while the local MDL and the gain fluctuations are *frozen* from recirculation to recirculation, the random phases change from recirculation to recirculation as a result of the linewidth (resulting from frequency fluctuations) of the modulation applied by the AOMs. It is worth noting that the AOMs play an important role in shaping the growth of MDL with propagation distance. In fact, this approaches a quasi-linear accumulation if no phase fluctuation is introduced, as is the case when electro-optic modulators are used as optical switches [206].

The simulation results are shown in Fig. J3.11, where we plot the average MDL versus propagation distance in the absence of mode permutation and for the considered MP schemes. The averaging is performed over 1000 link transfer matrices obtained for as many independent instantiations of the random quantities involved. Figure J3.11(a) refers to the case of distributed MDL, and Fig. J3.11(b) to the case of single-mode gain fluctuations. Intra-group coupling was introduced so as to enforce a decorretalation length of 1 km in each mode group [204]. For the inter-mode group coupling we assumed the coefficient values in Table J3.2. For the local MDL strength, which is characterized by the coefficients ζ_u defined through Eq. (J3.6), we assumed one of the many sets of numerical values that are compatible with an accumulated mean MDL of approximately 15 dB after 1200 km, as observed in the experiment. Finally, for the gain fluctuations, based on the same criterion, we assumed a standard deviation of 0.5 dB.

Inspection of Fig. J3.11 suggests that while MDL accumulation is similar across all considered schemes in both models, the model based on distributed MDL is more consistent with the experimental finding. Therefore, we conclude that distributed random MDL, possibly arising from fiber splices (seven in the experiment, one every less than 8 km in the loop), may be the predominant (yet not the only one) mechanism contributing to MDL accumulation in MMF links.

J3.5 Conclusion

We experimentally investigated the effectiveness of four mode permutation schemes in reducing the accumulation of modal dispersion in a long-haul 15-mode fiber link. We found that with mode permutation, the duration of the intensity impulse response of the MMF link increased proportionally to the square root of transmission distance, rather than linearly with it, as is the case in the absence of mode permutation. This reduced considerably the complexity of the receiver MIMO-DSP. We estimated an extension of the system reach from 530 km to 1178 km, enabled by a reduction in the time-domain equalizer window from 71.4 ns to 38.8 ns. Although no transmission results are shown in this work, such an extension has been demonstrated with a full C-band transmission in [141]. The considered permutation schemes exhibited comparable performance with little wavelength dependence across the C-band. We also developed a simple model to simulate propagation in multi-mode fibers, whose parameters can be conveniently extracted from the experimental data. Simulations indicate negligible difference between the experimental results obtained in a recirculating-loop configuration and the performance of mode permutation in a realistic fiber link composed of independent fiber spans.

Part III

Conclusion

Concluding remarks and future directions

Research on optical fiber communication systems has supported the exponential growth in data traffic observed in optical communication networks for decades. For many years, the capacity offered by optical fibers was thought to be unlimited, and research efforts focused primarily on enabling emerging bandwidth-intensive applications such as high-definition video streaming and cloud services. The adoption of a wide set of novel technologies allowed network operators to scale their capacities without incurring in the large costs of deployment of new fiber-optic cables. For instance, operators could simply install additional transceivers to support wavelength-division multiplexing (WDM) over existing fibers, or replace older transceivers with new, more advanced ones capable of supporting higher data rates. However, more than twenty years ago, around the early 2000s, both theoretical and experimental studies began to formalize the capacity limit of single-mode fibers (SMFs). Modern optical links now operate close to these fundamental limits. Although the required capacity of optical networks continues to grow exponentially, albeit at a slightly lower pace compared to previous years, network operators will soon be forced to deploy new optical fiber cables. One potential solution is the adoption of multi-band WDM, extending operation beyond the conventional C-band. While this approach can provide up to a twelve-fold increase in available bandwidth, the actual increase in fiber-optic capacity is expected to be only four to five times that of systems operating in the C-band. This discrepancy arises from the use of immature technologies, as well as from fundamental wavelength-dependent physical properties of silica fibers, such as fiber loss. Moreover, multi-band operation does not significantly reduce the cost-per-bit, which is primarily achieved through integration and mass production. Since the deployment of new optical fibers would still be required, the research community has also focused on determining what type of fiber should be deployed. In this context, novel optical fiber types capable of supporting multiple spatial channels within a single cladding have been proposed and extensively studied over the past decade. Although a somewhat riskier approach, these fibers for space-division multiplexing (SDM) have the potential to enable petabit-per-second transmission capacities per fiber, while reducing the cost per bit. In this thesis, we focused on transmission and characterization challenges that must be addressed in designing and operating multi-band WDM systems over SDM fibers.

The first problem addressed is the accumulation of modal dispersion (MD) in long-haul multi-mode fiber (MMF) transmission systems, which directly impacts the required memory length for multiple-input multiple-output (MIMO) equalization. Modes belonging to different mode groups (MGs) travel with slightly different velocities and experience partial coupling, causing MD to accumulate linearly with propagation distance, at least initially. This is impractical to handle, as a dispersion of 100 ps/km would require at least 100 ns of system memory to undo the coupling occurring over a 1000 km transmission. To mitigate this, strong coupling between MGs can be intentionally introduced using lumped mode permutation (MP) strategies. Operating in this regime is advantageous because the channel memory grows only with the square-root of propagation distance. The effectiveness of four distinct MP schemes in reducing the growth rate of the channel memory is examined using a recirculating-loop-based 15-mode MMF link. Additionally, the accumulation of mode-dependent loss (MDL) is analyzed, showing a square-root dependence on propagation distance. Finally, a simple model for simulating multi-mode propagation in realistic links with multiple fiber spans is developed. The effectiveness of MP is also validated using the model, which relies on a set of parameters that can be conveniently extracted from experimental data.

The second problem concerns long-haul uncoupled-core multi-core fiber (UC-MCF) transmission with fan-in/fan-out (FIFO)-less amplification. The overwhelming majority of transmission experiments over SDM fibers reported to date still rely on single-mode amplification, requiring demultiplexing and multiplexing of all spatial modes at every amplification stage. In this thesis, we report the first trans-Pacific-equivalent transmission-distance demonstration using multi-core erbium-doped fiber amplifiers (MC-EDFAs) and distributed Raman amplification (DRA). We transmitted 175 polarization-division multiplexing (PDM)-quadrature-amplitude modulated (QAM) channels per core of a four-core UC-MCF, achieving a total decoded throughput of 45.7 Tb/s over 12 053 km. This represented the longest reach ever demonstrated in SDM transmission experiments relying entirely on SDM amplifiers.

Another aspect addressed in this thesis is the characterization of stimulated Raman scattering (SRS) in coupled-core multi-core fibers (CC-MCFs). On the one hand, SRS can directly impact the performance of multi-band WDM systems. On the other hand, it can be leveraged for broad-band amplification at any frequency suitable for transmission by simply ensuring that pump and signal are separated by approximately 13 THz. The impact of SRS in SDM fibers has not been properly investigated. To date, experimental transmission over UC-MCFs suggests that SRS in such fibers is similar to that observed in SMFs, and only some preliminary studies have considered MMFs. In this thesis, we presented the first experimental characterization of SRS in CC-MCFs, conducted over a coupled-core four-core fiber (CC-4CF), field-deployed in the city of L'Aquila. A theoretical model describing SRS in the presence of strong coupling was also developed. The remarkable agreement between the CC-4CF measurements and those obtained from a reference SMF validated both our model and the experimental results.

The final problem addressed is that of petabit-per-second short-reach transmission over MMFs. Transmission demonstrations above 3 Pb/s have been demonstrated in laboratory settings. However, since MMF transmission properties have been shown to differ even significantly after installation, petabit-per-second transmission in field-deployed fibers remain to be demonstrated. A 6.1 km long, 15-mode MMF link, field-deployed in the city of L'Aquila was loaded with WDM signals spanning the C- and L-bands. By transmitting and successfully receiving 266 polarization-multiplexed spatial super-channels, each modulated with QAM signals, a total decoded throughput of 1.06 Pb/s was demonstrated. This resulted in the highest transmission throughput ever reported over any field-deployed fiber, and marked the first petabit-per-second-class transmission over such fibers.

Although significant research is still required for SDM to reach its full potential, its successful adoption will ultimately depend on the techno-economic assessments made by network operators and system vendors. Only time will tell when the ever-growing demand for data transmission capacity will make large-scale deployment of SDM unavoidable. Nevertheless, with the announcement of the first commercial deployment of two-core fibre, it is clear that the era of SDM has finally begun.

References

[1] G. P. Agrawal, “Chapter 2 - Optical Fibers,” in *Fiber-Optic Communication Systems (Fifth Edition)*, John Wiley & Sons, Ltd, 2010, pp. 24–78, ISBN: 978-0-470-91852-4. DOI: https://doi.org/10.1002/9780470918524.ch2.

[2] J. Nicolette, *Corning Celebrates its 1 Billionth Kilometer of Optical Fiber*, https://www.corning.com/worldwide/en/about-us/news-events/news-releases/2017/09/corning-celebrates-its-1-billionth-kilometer-of-optical-fiber.html, Corning Incorporated, Sep. 28, 2017. Accessed: Sep. 24, 2025.

[3] *TeleGeography Website, Submarine Cable Map*, https://www.submarinecablemap.com/, TeleGeography. Accessed: Sep. 24, 2025.

[4] B. Mukherjee, I. Tomkos, M. Tornatore, et al., Eds., *Springer Handbook of Optical Networks*. Cham: Springer International Publishing, 2020, ISBN: 978-3-030-16249-8. DOI: 10.1007/978-3-030-16250-4.

[5] P. J. Winzer and D. T. Neilson, “From Scaling Disparities to Integrated Parallelism: A Decathlon for a Decade,” *Journal of Lightwave Technology*, vol. 35, no. 5, pp. 1099–1115, 2017. DOI: 10.1109/JLT.2017.2662082.

[6] E. Agrell, M. Karlsson, A. R. Chraplyvy, et al., “Roadmap of optical communications,” *Journal of Optics*, vol. 18, no. 6, p. 063 002, May 2016. DOI: 10.1088/2040-8978/18/6/063002.

[7] B. J. Puttnam, G. Rademacher, and R. S. Luís, “Space-division multiplexing for optical fiber communications,” *Optica*, vol. 8, no. 9, pp. 1186–1203, Sep. 2021. DOI: 10.1364/OPTICA.427631.

[8] B. J. Puttnam, R. S. Luís, Y. Huang, et al., “321 Tb/s E/S/C/L-Band Transmission With E-Band Bismuth-Doped Fiber Amplifier and Optical Processor,” *Journal of Lightwave Technology*, vol. 42, no. 11, pp. 4006–4012, 2024. DOI: 10.1109/JLT.2024.3379676.

[9] B. J. Puttnam, R. S. Luis, I. Phillips, et al., “402 Tb/s GMI Data-Rate OESCLU-Band Transmission,” in *Optical Fiber Communication Conference (OFC) 2024*, Optica Publishing Group, 2024, Th4A.3. DOI: 10.1364/OFC.2024.Th4A.3.

[10] P. J. Winzer, “Scaling Optical Fiber Networks: Challenges and Solutions,” *Opt. Photon. News*, vol. 26, no. 3, pp. 28–35, Mar. 2015. DOI: 10.1364/OPN.26.3.000028.

[11] P. J. Winzer, D. T. Neilson, and A. R. Chraplyvy, “Fiber-optic transmission and networking: the previous 20 and the next 20 years [Invited],” *Opt. Express*, vol. 26, no. 18, pp. 24 190–24 239, Sep. 2018. DOI: 10.1364/OE.26.024190.

[12] M. van den Hout, “Ultra-wideband and Space-division Multiplexed Optical Transmission Systems,” Phd Thesis, Electrical Engineering, Eindhoven University of Technology, Feb. 2024, ISBN: 978-90-386-5909-1. DOI: 10.6100/jnxx-6t19.

[13] D. Che, X. Chen, C. Deakin, et al., “2.4-Tb/s single-wavelength coherent transmission enabled by 114-GHz all-electronic digital-band-interleaved DACs,” *IET Conference Proceedings*, vol. 2023, pp. 1706–1709, 34 2023. DOI: 10.1049/icp.2023.2672.

[14] *ICE7 1.2Tb/s high-performance coherent optics*, https://www.nokia.com/optical-networks/ice7/, Nokia. Accessed: Oct. 6, 2025.

[15] H. Sun, K.-T. Wu, and K. Roberts, “Real-time measurements of a 40 Gb/s coherent system,” *Opt. Express*, vol. 16, no. 2, pp. 873–879, Jan. 2008. DOI: 10.1364/OE.16.000873.

[16] S. Hardy, *Ciena introduces single-carrier 1.6-Tbps WaveLogic 6 coherent optical engines*, https://www.lightwaveonline.com/optical-tech/transmission/article/14290118/ciena-introduces-single-carrier-16-tbps-wavelogic-6-coherent-optical-engines, Ciena, Feb. 21, 2023. Accessed: Oct. 6, 2025.

[17] P. P. Mitra and J. B. Stark, “Nonlinear limits to the information capacity of optical fibre communications,” *Nature*, vol. 411, no. 6841, pp. 1027–1030, Jun. 2001, ISSN: 1476-4687. DOI: 10.1038/35082518.

[18] R.-J. Essiambre, G. Kramer, P. J. Winzer, et al., “Capacity Limits of Optical Fiber Networks,” *Journal of Lightwave Technology*, vol. 28, no. 4, pp. 662–701, 2010. DOI: 10.1109/JLT.2009.2039464.

[19] R.-J. Essiambre, G. J. Foschini, G. Kramer, et al., “Capacity Limits of Information Transport in Fiber-Optic Networks,” *Phys. Rev. Lett.*, vol. 101, p. 163 901, 16 Oct. 2008. DOI: 10.1103/PhysRevLett.101.163901.

[20] M. Shtaif, C. Antonelli, A. Mecozzi, et al., “Challenges in Estimating the Information Capacity of the Fiber-Optic Channel,” *Proceedings of the IEEE*, vol. 110, no. 11, pp. 1655–1678, 2022. DOI: 10.1109/JPROC.2022.3197188.

[21] E. B. Desurvire, “Capacity Demand and Technology Challenges for Lightwave Systems in the Next Two Decades,” *Journal of Lightwave Technology*, vol. 24, no. 12, pp. 4697–4710, 2006. DOI: 10.1109/JLT.2006.885772.

[22] A. Chraplyvy, “Plenary paper: The coming capacity crunch,” in *35th European Conference on Optical Communication (ECOC) 2009*, 2009, Plenary Session.

[23] R. S. Tucker, “Green Optical Communications—Part I: Energy Limitations in Transport,” *IEEE Journal of Selected Topics in Quantum Electronics*, vol. 17, no. 2, pp. 245–260, 2011. DOI: 10.1109/JSTQE.2010.2051216.

[24] T. Kamiya and Y. Awaji, "Toward Extremely Advanced Transmission (EXAT) technology," in *2010 Photonics Global Conference*, 2010, pp. 1–2. DOI: 10.1109/PGC.2010.5706086.

[25] D. Richardson, "Progress on European Union Project MODEGAP," in *2014 IEEE Photonics Society Summer Topical Meeting Series*, 2014, pp. 162–163. DOI: 10.1109/SUM.2014.90.

[26] "ITU-T Recommendation G.Sup39: Optical system design and engineering considerations," International Telecommunication Union Telecommunication Standardization Sector (ITU-T), Recommendation G.Sup39, Mar. 2025.

[27] R. Ryf, S. Randel, A. H. Gnauck, et al., "Space-division multiplexing over 10 km of three-mode fiber using coherent 6 × 6 MIMO processing," in *Optical Fiber Communication Conference/National Fiber Optic Engineers Conference 2011*, Optica Publishing Group, 2011, PDPB10. DOI: 10.1364/OFC.2011.PDPB10.

[28] J. Sakaguchi, Y. Awaji, N. Wada, et al., "109-Tb/s (7×97×172-Gb/s SDM/WDM/PDM) QPSK transmission through 16.8-km homogeneous multi-core fiber," in *Optical Fiber Communication Conference/National Fiber Optic Engineers Conference 2011*, Optica Publishing Group, 2011, PDPB6. DOI: 10.1364/OFC.2011.PDPB6.

[29] B. Zhu, T. Taunay, M. Fishteyn, et al., "Space-, Wavelength-, Polarization-Division Multiplexed Transmission of 56-Tb/s over a 76.8-km Seven-Core Fiber," in *Optical Fiber Communication Conference/National Fiber Optic Engineers Conference 2011*, Optica Publishing Group, 2011, PDPB7. DOI: 10.1364/OFC.2011.PDPB7.

[30] A. Li, A. A. Amin, X. Chen, et al., "Reception of Mode and Polarization Multiplexed 107-Gb/s CO-OFDM Signal over a Two-Mode Fiber," in *Optical Fiber Communication Conference/National Fiber Optic Engineers Conference 2011*, Optica Publishing Group, 2011, PDPB8. DOI: 10.1364/OFC.2011.PDPB8.

[31] M. Salsi, C. Koebele, D. Sperti, et al., "Transmission at 2×100Gb/s, over Two Modes of 40km-long Prototype Few-Mode Fiber, using LCOS-based Mode Multiplexer and Demultiplexer," in *Optical Fiber Communication Conference/National Fiber Optic Engineers Conference 2011*, Optica Publishing Group, 2011, PDPB9. DOI: 10.1364/OFC.2011.PDPB9.

[32] C. E. Shannon, "A mathematical theory of communication," *The Bell System Technical Journal*, vol. 27, no. 3, pp. 379–423, 1948. DOI: 10.1002/j.1538-7305.1948.tb01338.x.

[33] P. J. Winzer and D. T. Neilson, "From Scaling Disparities to Integrated Parallelism: A Decathlon for a Decade," *Journal of Lightwave Technology*, vol. 35, no. 5, pp. 1099–1115, Mar. 2017, ISSN: 1558-2213. DOI: 10.1109/JLT.2017.2662082.

[34] B. J. Puttnam, R. S. Luís, I. Phillips, et al., "High Data-Rate OESCLU-Band Transmission," *Journal of Lightwave Technology*, pp. 1–9, 2025. DOI: 10.1109/JLT.2025.3543448.

[35] R. Dar, P. J. Winzer, A. R. Chraplyvy, et al., "Cost-Optimized Submarine Cables Using Massive Spatial Parallelism," *Journal of Lightwave Technology*, vol. 36, no. 18, pp. 3855–3865, 2018. DOI: 10.1109/JLT.2018.2841810.

[36] O. V. Sinkin, A. V. Turukhin, W. W. Patterson, et al., "Maximum Optical Power Efficiency in SDM-Based Optical Communication Systems," *IEEE Photonics Technology Letters*, vol. 29, no. 13, pp. 1075–1077, 2017. DOI: 10.1109/LPT.2017.2701148.

[37] O. V. Sinkin, A. V. Turukhin, Y. Sun, et al., "SDM for Power-Efficient Undersea Transmission," *Journal of Lightwave Technology*, vol. 36, no. 2, pp. 361–371, 2018. DOI: 10.1109/JLT.2017.2771315.

[38] P. Sillard, D. Molin, M. Bigot-Astruc, et al., "Low-Differential-Mode-Group-Delay 9-LP-Mode Fiber," *J. Lightwave Technol.*, vol. 34, no. 2, pp. 425–430, Jan. 2016.

[39] P. Sillard, D. Molin, M. Bigot-Astruc, et al., "50 µm Multimode Fibers for Mode Division Multiplexing," *Journal of Lightwave Technology*, vol. 34, no. 8, pp. 1672–1677, 2016. DOI: 10.1109/JLT.2015.2507442.

[40] P. Sillard, M. Bigot, K. de Jongh, et al., "55-Spatial-Mode Fiber for Space Division Multiplexing," in *2023 Optical Fiber Communications Conference and Exhibition (OFC)*, 2023, pp. 1–3. DOI: 10.1364/OFC.2023.M4B.5.

[41] D. Gloge and E. A. J. Marcatili, "Multimode theory of graded-core fibers," *The Bell System Technical Journal*, vol. 52, no. 9, pp. 1563–1578, 1973. DOI: 10.1002/j.1538-7305.1973.tb02033.x.

[42] P. Sillard, "Few-Mode Fibers for Space Division Multiplexing," in *Optical Fiber Communication Conference*, Optica Publishing Group, 2016, Th1J.1. DOI: 10.1364/OFC.2016.Th1J.1.

[43] G. Rademacher, B. J. Puttnam, R. S. Luís, et al., "Peta-bit-per-second optical communications system using a standard cladding diameter 15-mode fiber," *Nature Communications*, vol. 12, no. 1, p. 4238, 2021. DOI: 10.1038/s41467-021-24409-w.

[44] G. Rademacher, R. S. Luís, B. J. Puttnam, et al., "1.53 Peta-bit/s C-Band Transmission in a 55-Mode Fiber," in *48th European Conference on Optical Communication (ECOC) 2022*, Optica Publishing Group, 2022, Th3C.3.

[45] G. Rademacher, R. S. Luís, B. J. Puttnam, et al., "3.56 peta-bit/s C+L band transmission over a 55-mode multi-mode fiber," in *49th European Conference on Optical Communications (ECOC) 2023*, IET, 2023, We.A.1.1. DOI: 10.1049/icp.2023.1834.

[46] S. Inao, T. Sato, M. Ogai, et al., "High Density Multicore-Fiber Cable," in *International Wire and Cable Symposium (28th)*, 1979, pp. 370–384.

[47] S. Inao, T. Sato, S. Sentsui, et al., "Multicore optical fiber," in *Optical Fiber Communication*, Optica Publishing Group, 1979, WB1. DOI: 10.1364/OFC.1979.WB1.

[48] K. Saitoh and S. Matsuo, "Multicore Fiber Technology," *Journal of Lightwave Technology*, vol. 34, no. 1, pp. 55–66, 2016. DOI: 10.1109/JLT.2015.2466444.

[49] T. Matsui, P. L. Pondillo, and K. Nakajima, "Weakly Coupled Multicore Fiber Technology, Deployment, and Systems," *Proceedings of the IEEE*, vol. 110, no. 11, pp. 1772–1785, 2022. DOI: 10.1109/JPROC.2022.3202812.

[50] G. L. Noane, D. Boscher, P. Grosso, et al., "Ultra High Density Cables Using a New Concept of Bundled Multicore Monomode Fibers: a Key for the Future FTTH Networks," in *International Wire and Cable Symposium (43th)*, 1994, pp. 203–210.

[51] T. Hayashi, T. Nagashima, T. Nakanishi, et al., "Field-Deployed Multi-Core Fiber Testbed," in *2019 24th OptoElectronics and Communications Conference (OECC) and 2019 International Conference on Photonics in Switching and Computing (PSC)*, 2019, pp. 1–3. DOI: 10.23919/PS.2019.8818058.

[52] T. Hayashi, T. Sakamoto, Y. Yamada, et al., "Randomly-Coupled Multi-Core Fiber Technology," *Proceedings of the IEEE*, vol. 110, no. 11, pp. 1786–1803, 2022. DOI: 10.1109/JPROC.2022.3182049.

[53] K.-P. Ho and J. M. Kahn, "Statistics of Group Delays in Multimode Fiber With Strong Mode Coupling," *Journal of Lightwave Technology*, vol. 29, no. 21, pp. 3119–3128, 2011. DOI: 10.1109/JLT.2011.2165316.

[54] C. Antonelli, A. Mecozzi, and M. Shtaif, "Delay spread in strongly coupled multi-core fibers for SDM transmission," in *Optical Fiber Communication Conference*, Optica Publishing Group, 2015, Th4C.2. DOI: 10.1364/OFC.2015.Th4C.2.

[55] R. Ryf, A. Sierra, R.-J. Essiambre, et al., "Coherent 1200-km 6 × 6 MIMO Mode-Multiplexed Transmission over 3-core Microstructured Fiber," in *37th European Conference on Optical Communication (ECOC) 2011*, Optica Publishing Group, 2011, Th.13.C.1. DOI: 10.1364/ECOC.2011.Th.13.C.1.

[56] C. Antonelli, A. Mecozzi, M. Shtaif, et al., "Stokes-Space Analysis of Modal Dispersion of SDM Fibers With Mode-Dependent Loss: Theory and Experiments," *Journal of Lightwave Technology*, vol. 38, no. 7, pp. 1668–1677, 2020. DOI: 10.1109/JLT.2019.2959191.

[57] K.-P. Ho and J. M. Kahn, "Mode-dependent loss and gain: statistics and effect on mode-division multiplexing," *Opt. Express*, vol. 19, no. 17, pp. 16 612–16 635, Aug. 2011. DOI: 10.1364/OE.19.016612.

[58] M. Arikawa, K. Nakamura, K. Hosokawa, et al., "Long-Haul WDM/SDM Transmission Over Coupled 4-Core Fiber With Coupled 4-Core EDFA and Its Mode Dependent Loss Characteristics Estimation," *Journal of Lightwave Technology*, vol. 40, no. 6, pp. 1664–1671, 2022. DOI: 10.1109/JLT.2021.3118684.

[59] D. B. Keck, "Chapter 1 - optical fiber waveguides," in *Fundamentals of Optical Fiber Communications (Second Edition)*, M. K. Barnoski, Ed., Second Edition, Academic Press, 1981, pp. 1–107, ISBN: 978-0-12-079151-4. DOI: https://doi.org/10.1016/B978-0-12-079151-4.50005-4.

[60] D. Gloge, "Weakly guiding fibers," *Appl. Opt.*, vol. 10, no. 10, pp. 2252–2258, Oct. 1971. DOI: 10.1364/AO.10.002252.

[61] F. Mitschke, ""Chromatic Dispersion"," in *"Fiber Optics: Physics and Technology"*. Berlin, Heidelberg: Springer Berlin Heidelberg, 2016, pp. 55–85, ISBN: 978-3-662-52764-1. DOI: 10.1007/978-3-662-52764-1_4.

[62] J. S. Toll, "Causality and the dispersion relation: Logical foundations," *Phys. Rev.*, vol. 104, pp. 1760–1770, 6 Dec. 1956. DOI: 10.1103/PhysRev.104.1760.

[63] R. Ryf and C. Antonelli, "Chapter 10 - space-division multiplexing," in *Springer Handbook of Optical Networks*, B. Mukherjee, I. Tomkos, M. Tornatore, et al., Eds., Cham: Springer International Publishing, 2020, pp. 353–393. DOI: 10.1007/978-3-030-16250-4_10.

[64] J. P. Gordon and H. Kogelnik, "Pmd fundamentals: Polarization mode dispersion in optical fibers," *Proceedings of the National Academy of Sciences*, vol. 97, no. 9, pp. 4541–4550, 2000. DOI: 10.1073/pnas.97.9.4541.

[65] *Visualizing the geometric phase of light*, https://skullsinthestars.com/2020/02/05/visualizing-the-geometric-phase-of-light/, Skulls in the Stars, Feb. 5, 2020. Accessed: Nov. 19, 2025.

[66] C. Antonelli, G. Riccardi, T. Hayashi, et al., "Role of polarization-mode coupling in the crosstalk between cores of weakly-coupled multi-core fibers," *Opt. Express*, vol. 28, no. 9, pp. 12 847–12 861, Apr. 2020. DOI: 10.1364/OE.391092.

[67] M. Karlsson and J. Brentel, "Autocorrelation function of the polarization-mode dispersion vector," *Opt. Lett.*, vol. 24, no. 14, pp. 939–941, Jul. 1999. DOI: 10.1364/OL.24.000939.

[68] C. Antonelli, A. Mecozzi, and M. Shtaif, "The delay spread in fibers for SDM transmission: dependence on fiber parameters and perturbations," *Opt. Express*, vol. 23, no. 3, pp. 2196–2202, Feb. 2015. DOI: 10.1364/OE.23.002196.

[69] A. Mecozzi and M. Shtaif, "The statistics of polarization-dependent loss in optical communication systems," *IEEE Photonics Technology Letters*, vol. 14, no. 3, pp. 313–315, 2002. DOI: 10.1109/68.986797.

[70] A. Galtarossa and L. Palmieri, "The exact statistics of polarization-dependent loss in fiber-optic links," *IEEE Photonics Technology Letters*, vol. 15, no. 1, pp. 57–59, Jan. 2003, ISSN: 1941-0174. DOI: 10.1109/LPT.2002.805799.

[71] L. E. Nelson, C. Antonelli, A. Mecozzi, et al., "Statistics of polarization dependent loss in an installed long-haul wdm system," *Opt. Express*, vol. 19, no. 7, pp. 6790–6796, Mar. 2011. DOI: 10.1364/OE.19.006790.

[72] S. Zarkosvky and M. Shtaif, "Statistical distribution of polarization-dependent loss in systems characterized by the hinge model," *Opt. Lett.*, vol. 45, no. 5, pp. 1224–1227, Mar. 2020. DOI: 10.1364/OL.385525.

[73] G. Agrawal, "Chapter 1 - Introduction," in *Nonlinear Fiber Optics (Fifth Edition)*, ser. Optics and Photonics, G. Agrawal, Ed., Fifth Edition, Boston: Academic Press, 2013, pp. 1–25. DOI: https://doi.org/10.1016/B978-0-12-397023-7.00001-2.

[74] G. Agrawal, "Chapter 2 - Pulse Propagation in Fibers," in *Nonlinear Fiber Optics (Fifth Edition)*, ser. Optics and Photonics, G. Agrawal, Ed., Fifth Edition, Boston: Academic Press, 2013, pp. 27–56. DOI: https://doi.org/10.1016/B978-0-12-397023-7.00002-4.

[75] S. V. Manakov, "On the theory of two-dimensional stationary self-focusing of electromagnetic waves," *Soviet Journal of Experimental and Theoretical Physics*, vol. 65, pp. 505–516, Aug. 1973.

[76] P. Wai and C. Menyak, "Polarization mode dispersion, decorrelation, and diffusion in optical fibers with randomly varying birefringence," *Journal of Lightwave Technology*, vol. 14, no. 2, pp. 148–157, 1996. DOI: 10.1109/50.482256.

[77] C. Antonelli, M. Shtaif, and A. Mecozzi, "Modeling of Nonlinear Propagation in Space-Division Multiplexed Fiber-Optic Transmission," *Journal of Lightwave Technology*, vol. 34, no. 1, pp. 36–54, 2016. DOI: 10.1109/JLT.2015.2510511.

[78] A. Mecozzi, C. Antonelli, and M. Shtaif, "Coupled Manakov equations in multimode fibers with strongly coupled groups of modes," *Opt. Express*, vol. 20, no. 21, pp. 23 436–23 441, Oct. 2012. DOI: 10.1364/OE.20.023436.

[79] S. Mumtaz, R.-J. Essiambre, and G. P. Agrawal, "Nonlinear Propagation in Multimode and Multicore Fibers: Generalization of the Manakov Equations," *Journal of Lightwave Technology*, vol. 31, no. 3, pp. 398–406, 2013. DOI: 10.1109/JLT.2012.2231401.

[80] P. Poggiolini, "The GN Model of Non-Linear Propagation in Uncompensated Coherent Optical Systems," *Journal of Lightwave Technology*, vol. 30, no. 24, pp. 3857–3879, 2012. DOI: 10.1109/JLT.2012.2217729.

[81] R. Dar, M. Feder, A. Mecozzi, et al., "Inter-Channel Nonlinear Interference Noise in WDM Systems: Modeling and Mitigation," *Journal of Lightwave Technology*, vol. 33, no. 5, pp. 1044–1053, 2015. DOI: 10.1109/JLT.2014.2384998.

[82] G. Agrawal, "Chapter 8 - Stimulated Raman Scattering," in *Nonlinear Fiber Optics (Fifth Edition)*, ser. Optics and Photonics, G. Agrawal, Ed., Fifth Edition, Boston: Academic Press, 2013, pp. 295–352. DOI: https://doi.org/10.1016/B978-0-12-397023-7.00008-5.

[83] D. Hollenbeck and C. D. Cantrell, "Multiple-vibrational-mode model for fiber-optic raman gain spectrum and response function," *J. Opt. Soc. Am. B*, vol. 19, no. 12, pp. 2886–2892, Dec. 2002. DOI: 10.1364/JOSAB.19.002886.

[84] M. Zirngibl, "Analytical model of Raman gain effects in massive wavelength division multiplexed transmission systems," *Electronics Letters*, vol. 34, 789–790(1), 8 Apr. 1998, ISSN: 0013-5194. DOI: 10.1049/el:19980555.

[85] R. H. Stolen and E. P. Ippen, "Raman gain in glass optical waveguides," *Applied Physics Letters*, vol. 22, no. 6, pp. 276–278, Mar. 1973. DOI: 10.1063/1.1654637.

[86] R. Stolen, "Polarization effects in fiber Raman and Brillouin lasers," *IEEE Journal of Quantum Electronics*, vol. 15, no. 10, pp. 1157–1160, 1979. DOI: 10.1109/JQE.1979.1069913.

[87] D. Christodoulides and R. Jander, "Evolution of Stimulated Raman Crosstalk in Wavelength Division Multiplexed Systems," *IEEE Photonics Technology Letters*, vol. 8, no. 12, pp. 1722–1724, 1996. DOI: 10.1109/68.544731.

[88] S. Bigo, S. Gauchard, A. Bertaina, et al., "Experimental Investigation of Stimulated Raman Scattering Limitation on WDM Transmission Over Various Types of Fiber Infrastructures," *IEEE Photonics Technology Letters*, vol. 11, no. 6, pp. 671–673, 1999. DOI: 10.1109/68.766780.

[89] D. Semrau, R. I. Killey, and P. Bayvel, "The Gaussian Noise Model in the Presence of Inter-Channel Stimulated Raman Scattering," *Journal of Lightwave Technology*, vol. 36, no. 14, pp. 3046–3055, Jul. 2018. DOI: 10.1109/JLT.2018.2830973.

[90] K. Rottwitt and J. Povlsen, "Analyzing the fundamental properties of Raman amplification in optical fibers," *Journal of Lightwave Technology*, vol. 23, no. 11, pp. 3597–3605, 2005. DOI: 10.1109/JLT.2005.857776.

[91] D. A. Shaji, R. S. Luis, D. Orsuti, et al., "Characterizing Raman Gain Efficiencies and SRS Induced Tilt in C+L+U bands," in *2024 IEEE Photonics Conference (IPC)*, 2024, MA2.2. DOI: 10.1109/IPC60965.2024.10799592.

[92] B. J. Puttnam, R. S. Luis, G. Rademacher, et al., "1 Pb/s Transmission in a 125um diameter 4-core MCF," in *Conference on Lasers and Electro-Optics*, Optica Publishing Group, 2022, JTh6B.1. DOI: 10.1364/CLEO_AT.2022.JTh6B.1.

[93] M. van den Hout, B. J. Puttnam, G. Di Sciullo, et al., "Transmission of 138.9 Tb/s over 12 345 km of 125um cladding diameter 4-core fiber using signals spanning S, C, and L-band," in *49th European Conference on Optical Communications (ECOC) 2023*, 2023, pp. 294–297. DOI: 10.1049/icp.2023.2063.

[94] M. Esmaeelpour, R. Ryf, N. K. Fontaine, et al., "Transmission over 1050-km few-mode fiber based on bidirectional distributed raman amplification," *Journal of Lightwave Technology*, vol. 34, no. 8, pp. 1864–1871, 2016. DOI: 10.1109/JLT.2016.2526908.

[95] G. D. Sciullo, L. A. Zischler, D. A. Shaji, et al., "Characterization of Stimulated Raman Scattering in Field-Deployed Coupled-Core Multi-Core Fibers," *Journal of Lightwave Technology*, pp. 1–8, 2025. DOI: 10.1109/JLT.2025.3633510.

[96] G. Agrawal, "Chapter 9 - Stimulated Brillouin Scattering," in *Nonlinear Fiber Optics (Fifth Edition)*, ser. Optics and Photonics, G. Agrawal, Ed., Fifth Edition, Boston: Academic Press, 2013, pp. 353–396. DOI: https://doi.org/10.1016/B978-0-12-397023-7.00009-7.

[97] K. Komatsu, S. Beppu, D. Soma, et al., "126-Tb/s C+L-Band 2-Core Fiber Transmission Over 114.6 km × 5 Spans," *Journal of Lightwave Technology*, vol. 43, no. 16, pp. 7656–7662, 2025. DOI: 10.1109/JLT.2025.3577337.

[98] Y. Sasaki, K. Takenaga, K. Aikawa, et al., "Single-Mode 37-Core Fiber with a Cladding Diameter of 248 μm," in *Optical Fiber Communication Conference*, Optica Publishing Group, 2017, Th1H.2. DOI: 10.1364/OFC.2017.Th1H.2.

[99] S. Matsuo, K. Takenaga, Y. Sasaki, et al., "High-Spatial-Multiplicity Multicore Fibers for Future Dense Space-Division-Multiplexing Systems," *Journal of Lightwave Technology*, vol. 34, no. 6, pp. 1464–1475, 2016. DOI: 10.1109/JLT.2015.2508928.

[100] T. Matsui, T. Kobayashi, H. Kawahara, et al., "118.5 Tbit/s transmission over 316 km-long multi-core fiber with standard cladding diameter," in *2017 Opto-Electronics and Communications Conference (OECC) and Photonics Global Conference (PGC)*, 2017, pp. 1–2. DOI: 10.1109/OECC.2017.8115049.

[101] C. Antonelli, D. Cassioli, F. Franchi, et al., "The City of L'Aquila as a Living Lab: the INCIPICT Project and the 5G Trial," in *2018 IEEE 5G World Forum (5GWF)*, 2018, pp. 410–415. DOI: 10.1109/5GWF.2018.8517089.

[102] T. Nakanishi, T. Hayashi, O. Shimakawa, et al., "Spatial-spectral-efficiency-enhanced multi-core fiber," in *2015 Optical Fiber Communications Conference and Exhibition (OFC)*, 2015, pp. 1–3. DOI: 10.1364/OFC.2015.Th3C.3.

[103] T. Hayashi and T. Sasaki, "Design strategy of uncoupled multicore fiber enabling high spatial capacity transmission," in *2013 IEEE Photonics Society Summer Topical Meeting Series*, 2013, pp. 78–79. DOI: 10.1109/PHOSST.2013.6614461.

[104] T. Hayashi and T. Nakanishi, "Bandwidth density as a figure of merit for few-mode multi-core fibers," *Opt. Express*, vol. 25, no. 21, pp. 24 983–24 990, Oct. 2017. DOI: 10.1364/OE.25.024983.

[105] J. M. Gené and P. J. Winzer, "A Universal Specification for Multicore Fiber Crosstalk," *IEEE Photonics Technology Letters*, vol. 31, no. 9, pp. 673–676, 2019. DOI: 10.1109/LPT.2019.2903717.

[106] B. J. Puttnam, R. S. Luís, T. A. Eriksson, et al., "Impact of Intercore Crosstalk on the Transmission Distance of QAM Formats in Multicore Fibers," *IEEE Photonics Journal*, vol. 8, no. 2, pp. 1–9, 2016. DOI: 10.1109/JPHOT.2016.2523993.

[107] M. van den Hout, R. S. Luís, B. J. Puttnam, et al., "Reaching the pinnacle of high-capacity optical transmission using a standard cladding diameter coupled-core multi-core fiber," *Nature Communications*, vol. 16, no. 1, p. 3833, 2025, ISSN: 2041-1723. DOI: 10.1038/s41467-025-59037-1.

[108] R. S. Luis, M. v. d. Hout, S. Gaiani, et al., "1.02 petabit/s transmission over 1,808.1 km in a 19-core randomly-coupled multicore fiber," in *Optical Fiber Communication Conference (OFC) Postdeadline Papers 2025*, Optica Publishing Group, 2025, Th4A.1. DOI: 10.1364/OFC.2025.Th4A.1.

[109] G. Di Sciullo, B. J. Puttnam, M. van den Hout, et al., "45.7 Tb/s over 12 053 km Transmission with an All-Multi-Core Recirculating-Loop 4-Core-Fiber System," in *Optical Fiber Communication Conference (OFC) 2024*, Optica Publishing Group, 2024, Th3E.2. DOI: 10.1364/OFC.2024.Th3E.2.

[110] G. Di Sciullo, B. J. Puttnam, M. v. d. Hout, et al., "45.7 Tb/s Over 12053 km Transmission in an All-Multi-Core-Amplified Recirculating Loop," *Journal of Lightwave Technology*, vol. 43, no. 10, pp. 4635–4641, 2025. DOI: 10.1109/JLT.2025.3541842.

[111] M. Giacomin, J. M. Traktenberg, M. R. Bolaños, et al., "Demonstration of a Cross-Encoded RFI QKD System in a Field-Deployed Multi-Core Fiber," in *2026 Optical Fiber Communication Conference (OFC)*, 2026, pp. 1–3.

[112] P. Sillard, D. Molin, M. Bigot-Astruc, et al., "Micro-bend-Resistant Low-Differential-Mode-Group-Delay Few-Mode Fibers," *Journal of Lightwave Technology*, vol. 35, no. 4, pp. 734–740, 2017. DOI: 10.1109/JLT.2016.2594586.

[113] K. Shibahara, T. Mizuno, D. Lee, et al., "DMD-Unmanaged Long-Haul SDM Transmission Over 2500-km 12-Core × 3-Mode MC-FMF and 6300-km 3-Mode FMF Employing Intermodal Interference Canceling Technique," *J. Lightwave Technol.*, vol. 37, no. 1, pp. 138–147, Jan. 2019.

[114] K. Shibahara, T. Mizuno, H. Ono, et al., "Long-Haul DMD-Unmanaged 6-Mode-Multiplexed Transmission Employing Cyclic Mode-Group Permutation," in *Optical Fiber Communication Conference (OFC) 2020*, Optica Publishing Group, 2020, Th3H.3. DOI: 10.1364/OFC.2020.Th3H.3.

[115] K. Shibahara, M. Hoshi, and Y. Miyamoto, "10-Spatial-Mode 1300-Km Transmission Over 6-LP Graded Index Few-Mode Fiber With 36-Ns Modal Dispersion," *J. Lightwave Technol.*, vol. 42, no. 4, pp. 1257–1264, Feb. 2024.

[116] M. van den Hout, G. Di Sciullo, G. Rademacher, et al., "273.6 Tb/s Transmission Over 1001 km of 15-Mode Fiber Using 16-QAM C-Band Signals," in *2023 Optical Fiber Communications Conference and Exhibition (OFC)*, 2023, Th4B.5. DOI: 10.1364/OFC.2023.Th4B.5.

[117] G. Di Sciullo, M. van den Hout, G. Rademacher, et al., "Modal Dispersion Mitigation in a long-haul 15-Mode Fiber link through Mode Permutation," in *2023 IEEE Photonics Society Summer Topicals Meeting Series (SUM)*, 2023, WC1.3. DOI: 10.1109/SUM57928.2023.10224367.

[118] A. M. Velázquez-Benítez, J. E. Antonio-López, J. C. Alvarado-Zacarías, et al., "Scaling photonic lanterns for space-division multiplexing," *Scientific Reports*, vol. 8, no. 1, p. 8897, 2018. DOI: 10.1038/s41598-018-27072-2.

[119] N. K. Fontaine, J. Carpenter, S. Gross, et al., "Photonic Lanterns, 3-D Waveguides, Multiplane Light Conversion, and Other Components That Enable Space-Division Multiplexing," *Proceedings of the IEEE*, vol. 110, no. 11, pp. 1821–1834, 2022. DOI: 10.1109/JPROC.2022.3207046.

[120] G. Labroille, B. Denolle, P. Jian, et al., "Efficient and mode selective spatial mode multiplexer based on multi-plane light conversion," *Opt. Express*, vol. 22, no. 13, pp. 15 599–15 607, Jun. 2014. DOI: 10.1364/OE.22.015599.

[121] N. K. Fontaine, H. Chen, M. Mazur, et al., "Hermite-Gaussian mode multiplexer supporting 1035 modes," in *Optical Fiber Communication Conference (OFC) 2021*, Optica Publishing Group, 2021, p. M3D.4. DOI: 10.1364/OFC.2021.M3D.4.

[122] N. K. Fontaine, M. Mazur, R. Ryf, et al., "Broadband 15-Mode Multiplexers based on Multi-Plane Light Conversion with 8 Planes in Unwrapped Phase Space," in *European Conference on Optical Communication (ECOC) 2022*, Optica Publishing Group, 2022, We3A.2.

[123] B. Mukherjee, *Optical WDM Networks* (Optical Networks). Springer, 2006, ISBN: 978-0-387-29055-3.

[124] D. M. Marom, Y. Miyamoto, D. T. Neilson, et al., "Optical Switching in Future Fiber-Optic Networks Utilizing Spectral and Spatial Degrees of Freedom," *Proceedings of the IEEE*, vol. 110, no. 11, pp. 1835–1852, 2022. DOI: 10.1109/JPROC.2022.3207576.

[125] D. M. Marom, P. D. Colbourne, A. D'Errico, et al., "Survey of Photonic Switching Architectures and Technologies in Support of Spatially and Spectrally Flexible Optical Networking," *J. Opt. Commun. Netw.*, vol. 9, no. 1, pp. 1–26, Jan. 2017. DOI: 10.1364/JOCN.9.000001.

[126] P. Boffi, N. Sambo, P. Martelli, et al., "Mode-Group Division Multiplexing: Transmission, Node Architecture, and Provisioning," *Journal of Lightwave Technology*, vol. 40, no. 8, pp. 2378–2389, 2022. DOI: 10.1109/JLT.2021.3135636.

[127] A. Gatto, P. Parolari, R. S. Luis, et al., "Partial-mimo based mode-group transmission and routing in a field-deployed 15-mode network: Throughput, dsp resources and network flexibility," *Journal of Lightwave Technology*, vol. 42, no. 14, pp. 4720–4732, 2024. DOI: 10.1109/JLT.2024.3383290.

[128] R. Ryf and N. K. Fontaine, "Wavelength-Selective Switches for Multimode Fiber Systems," in *Frontiers in Optics 2014*, Optica Publishing Group, 2014, FTh4B.1. DOI: 10.1364/FIO.2014.FTh4B.1.

[129] M. Nakazawa, "Evolution of EDFA from single-core to multi-core and related recent progress in optical communication," *Optical Review*, vol. 21, no. 6, pp. 862–874, 2014, ISSN: 1349-9432. DOI: 10.1007/s10043-014-0139-1.

[130] G. Lopez-Galmiche, Z. S. Eznaveh, J. E. Antonio-Lopez, et al., "Few-mode erbium-doped fiber amplifier with photonic lantern for pump spatial mode control," *Opt. Lett.*, vol. 41, no. 11, pp. 2588–2591, Jun. 2016. DOI: 10.1364/OL.41.002588.

[131] N. K. Fontaine, B. Huang, Z. S. Eznaveh, et al., "Multi-mode optical fiber amplifier supporting over 10 spatial modes," in *2016 Optical Fiber Communications Conference and Exhibition (OFC)*, 2016, Th5A.4.

[132] R. Ryf, A. Sierra, R.-J. Essiambre, et al., "Mode-Equalized Distributed Raman Amplification in 137-km Few-Mode Fiber," in *37th European Conference and Exposition on Optical Communications*, Optica Publishing Group, 2011, Th.13.K.5. DOI: 10.1364/ECOC.2011.Th.13.K.5.

[133] C. Antonelli, A. Mecozzi, and M. Shtaif, "Modeling Raman amplification in multimode and multicore fibers," in *Optical Fiber Communication Conference*, Optica Publishing Group, 2014, W3E.1. DOI: 10.1364/OFC.2014.W3E.1.

[134] A. Kawai, K. Shibahara, M. Hoshi, et al., "389.3-Tb/s 1017-km C-band transmission over field-installed 12-coupled-core fiber cable with >12-Tb/s spatial MIMO channels," in *50th European Conference on Optical Communications (ECOC) 2025*, ITG/VDE, 2024, Th3B.1.

[135] "Document N: TR-23288A," Sumitomo Electric Industries, Ltd., Japan, Datasheet, 2023.

[136] *Sumitomo Electric Launches World's First Mass-produced Ultra-low Loss, Multi-core Fiber*, https://sumitomoelectric.com/press/2023/09/prs049, Sumitomo Electric Industries, Ltd., Sep. 22, 2023. Accessed: Dec. 5, 2025.

[137] *Advanced Optical Communication Testbed*, https://www.aoctestbed.in/, Indian Institute of Technology Madras. Accessed: Jan. 7, 2026.

[138] *Lisbon Underground Multi-core Fiber Ring (LUMIRing)*, https://lumiring.iscte-iul.pt/, Instituto Universitário de Lisboa. Accessed: Jan. 7, 2026.

[139] B. Quigley and M. Cantono, *Delivering Multi-Core Fiber Technology in Subsea Cables | Google Cloud Blog — cloud.google.com*, https://cloud.google.com/blog/products/infrastructure/delivering-multi-core-fiber-technology-in-subsea-cables, 2023.

[140] R. Ryf, S. Randel, A. H. Gnauck, et al., "Mode-Division Multiplexing Over 96 km of Few-Mode Fiber Using Coherent 6 $\times$ 6 MIMO Processing," *Journal of Lightwave Technology*, vol. 30, no. 4, pp. 521–531, 2012. DOI: 10.1109/JLT.2011.2174336.

[141] M. van den Hout, G. Di Sciullo, R. S. Luís, et al., "Transmission of 273.6 Tb/s Over 1001 km of 15-Mode Multi-Mode Fiber Using C-Band Only 16-QAM Signals," *J. Lightwave Technol.*, vol. 42, no. 3, pp. 1136–1142, Feb. 2024.

[142] G. Di Sciullo, D. A. Shaji, M. v. d. Hout, et al., “Enhancing Long-Haul 15-Mode Fiber Performance: Mode Permutation for Reduced Modal Dispersion,” *Journal of Lightwave Technology*, vol. 43, no. 2, pp. 481–491, 2025. DOI: 10.1109/JLT.2024.3453553.

[143] M. Mazur, N. K. Fontaine, L. Dallachiesa, et al., “Broadband characterization of field-deployed 15-mode graded-index multi-mode fiber cable,” in *49th European Conference on Optical Communications (ECOC) 2023*, IET, 2023, Th.B.3.5. DOI: 10.1049/icp.2023.2409.

[144] C. Antonelli, A. Mecozzi, A. Marotta, et al., “Field Transmission Performance of Multi-core and Few-Mode Fibers,” in *Optical Fiber Communication Conference (OFC) 2024*, Optica Publishing Group, 2024, W3J.1. DOI: 10.1364/OFC.2024.W3J.1.

[145] R. Luis, G. Di Sciullo, M. van den Hout, et al., “19.2 THz S+C+L Transmission in a Field Deployed, Randomly-Coupled, Multicore Fiber,” in *51st European Conference on Optical Communications (ECOC) 2025*, 2025, p. M.03.05.2.

[146] G. Rademacher, R. S. Luís, B. J. Puttnam, et al., “Characterization of the First Field-Deployed 15-Mode Fiber Cable for High Density Space-Division Multiplexing,” in *48th European Conference on Optical Communication (ECOC) 2022*, Optica Publishing Group, 2022, Th3B.1.

[147] R. G. H. van Uden, C. M. Okonkwo, H. Chen, et al., “Time domain multiplexed spatial division multiplexing receiver,” *Opt. Express*, vol. 22, no. 10, pp. 12 668–12 677, May 2014. DOI: 10.1364/OE.22.012668.

[148] N. K. Fontaine, R. Ryf, H. Chen, et al., “30×30 MIMO Transmission over 15 Spatial Modes,” in *Optical Fiber Communication Conference Post Deadline Papers*, Optica Publishing Group, 2015, Th5C.1. DOI: 10.1364/OFC.2015.Th5C.1.

[149] D. S. Millar, R. Maher, D. Lavery, et al., “Design of a 1 Tb/s Superchannel Coherent Receiver,” *Journal of Lightwave Technology*, vol. 34, no. 6, pp. 1453–1463, 2016. DOI: 10.1109/JLT.2016.2519260.

[150] J. K. Fischer, M. Cantono, V. Curri, et al., “Maximizing the Capacity of Installed Optical Fiber Infrastructure Via Wideband Transmission,” in *2018 20th International Conference on Transparent Optical Networks (ICTON)*, 2018, Tu.B3.3. DOI: 10.1109/ICTON.2018.8473994.

[151] L. Rapp, “Increasing Capacity of Installed Fiber Links by Wideband Optical Amplification,” in *Optica Advanced Photonics Congress 2022*, Optica Publishing Group, 2022, NeTh1C.2. DOI: 10.1364/NETWORKS.2022.NeTh1C.2.

[152] D. Soma, T. Kato, S. Beppu, et al., “25-THz O+S+C+L+U-band digital coherent DWDM transmission using a deployed fibre-optic cable,” in *49th European Conference on Optical Communications (ECOC) 2023*, vol. 2023, 2023, pp. 1658–1661. DOI: 10.1049/icp.2023.2660.

[153] B. J. Puttnam, R. S. Luis, Y. Huang, et al., "301 Tb/s E, S, C+L-band transmission over 212 nm bandwidth with E-band bismuth-doped fiber amplifier and gain equalizer," in *49th European Conference on Optical Communications (ECOC) 2023*, vol. 2023, 2023, pp. 1674–1677. DOI: 10.1049/icp.2023.2664.

[154] A. Ferrari, A. Napoli, J. K. Fischer, et al., "Assessment on the Achievable Throughput of Multi-Band ITU-T G.652.D Fiber Transmission Systems," *Journal of Lightwave Technology*, vol. 38, no. 16, pp. 4279–4291, 2020. DOI: 10.1109/JLT.2020.2989620.

[155] B. J. Puttnam, M. van den Hout, G. Di Sciullo, et al., "22.9 Pb/s data-rate by extreme space-wavelength multiplexing," in *49th European Conference on Optical Communications (ECOC) 2023*, vol. 2023, 2023, Th.C.2.1. DOI: 10.1049/icp.2023.2665.

[156] P. Sillard, K. Benyahya, D. Soma, et al., "Few-Mode Fiber Technology, Deployments, and Systems," *Proceedings of the IEEE*, vol. 110, no. 11, pp. 1804–1820, 2022. DOI: 10.1109/JPROC.2022.3207012.

[157] G. Di Rosa and L. Rapp, "Opportunities, challenges and requirements for introducing space division multiplexing in fibre optical networks," *IET Optoelectronics*, vol. 19, no. 1, e12130, 2025. DOI: https://doi.org/10.1049/ote2.12130.

[158] B. J. Puttnam, R. S. Luís, G. Rademacher, et al., "S-, C- and L-band transmission over a 157 nm bandwidth using doped fiber and distributed Raman amplification," *Optics Express*, vol. 30, no. 6, pp. 10 011–10 018, Mar. 2022. DOI: 10.1364/OE.448837.

[159] J. Bromage, "Raman amplification for fiber communications systems," *Journal of Lightwave Technology*, vol. 22, no. 1, pp. 79–93, 2004. DOI: 10.1109/JLT.2003.822828.

[160] G. Di Sciullo, Q. Wu, R. S. Luís, et al., "Stimulated Raman scattering in WDM transmission over randomly-coupled multi-core fibers," in *2024 IEEE Photonics Conference (IPC)*, 2024, ThG2.5. DOI: 10.1109/IPC60965.2024.10799658.

[161] G. Di Sciullo, D. A. Shaji, L. A. Zischler, et al., "Experimental Characterization of Stimulated Raman Scattering in Field-Deployed Coupled-Core Multi-Core Fibers," in *51st European Conference on Optical Communications (ECOC) 2025*, 2025, W.02.01.01.

[162] T. Hayashi, T. Nagashima, T. Nakanishi, et al., "Field-Deployed Multi-Core Fiber Testbed," in *2019 24th OptoElectronics and Communications Conference (OECC) and 2019 International Conference on Photonics in Switching and Computing (PSC)*, Jul. 2019, pp. 1–3. DOI: 10.23919/PS.2019.8818058.

[163] C. Antonelli, A. Mecozzi, A. Marotta, et al., "Space-Division Multiplexed Transmission from the Lab to the Field," in *50th European Conference on Optical Communication (ECOC) 2024*, 2024, Tu3B.4.

[164] C. Antonelli, A. Mecozzi, and M. Shtaif, “Raman amplification in multimode fibers with random mode coupling,” *Optics Letters*, vol. 38, no. 8, pp. 1188–1190, Apr. 2013. DOI: 10.1364/OL.38.001188.

[165] K. Rottwitt, J. Bromage, A. Stentz, et al., “Scaling of the Raman gain coefficient: applications to germanosilicate fibers,” *Journal of Lightwave Technology*, vol. 21, no. 7, pp. 1652–1662, 2003. DOI: 10.1109/JLT.2003.814386.

[166] Y. Kang, “Calculations and Measurements of Raman Gain Coefficients of Different Fiber Types,” M.S. Thesis, Virginia Polytechnic Institute and State University, 2002.

[167] E. Pincemin, D. Grot, L. Bathany, et al., “Raman gain efficiencies of modern terrestrial transmission fibers in S-, C- and L-band,” in *Nonlinear Guided Waves and Their Applications*, Optica Publishing Group, 2002, NLTuC2. DOI: 10.1364/NLGW.2002.NLTuC2.

[168] S. Jiang, B. Bristiel, Y. Jaouën, et al., “Full characterization of modern transmission fibers for Raman amplified-based communication systems,” *Opt. Express*, vol. 15, no. 8, pp. 4883–4892, Apr. 2007. DOI: 10.1364/OE.15.004883.

[169] B. J. Puttnam, R. S. Luís, G. Rademacher, et al., “319 Tb/s Transmission over 3001 km with S, C and L band signals over 120nm bandwidth in 125 μm wide 4-core fiber,” in *Optical Fiber Communication Conference (OFC) 2021*, Optica, 2021, F3B.3. DOI: 10.1364/OFC.2021.F3B.3.

[170] M. van den Hout, B. J. Puttnam, G. Di Sciullo, et al., “Transmission of 138.9 Tb/s over 12 345 km of 125um cladding diameter 4-core fiber using signals spanning S, C, and L-band,” in *49th European Conference on Optical Communications (ECOC 2023)*, vol. 2023, 2023, pp. 294–297. DOI: 10.1049/icp.2023.2063.

[171] V. Sleiffer, Y. Jung, V. Veljanovski, et al., “73.7 Tb/s (96 x 3 x 256-Gb/s) mode-division-multiplexed DP-16QAM transmission with inline MM-EDFA,” *Opt. Express*, vol. 20, no. 26, B428–B438, Dec. 2012. DOI: 10.1364/OE.20.00B428.

[172] E. Ip, M.-J. Li, K. Bennett, et al., “146λ $\times$ 6 $\times$ 19-Gbaud Wavelength-and Mode-Division Multiplexed Transmission Over 10 $\times$ 50-km Spans of Few-Mode Fiber With a Gain-Equalized Few-Mode EDFA,” *Journal of Lightwave Technology*, vol. 32, no. 4, pp. 790–797, 2014. DOI: 10.1109/JLT.2013.2290434.

[173] H. Takahashi, T. Tsuritani, E. L. T. de Gabory, et al., “First demonstration of MC-EDFA-repeatered SDM transmission of 40 x 128-Gbit/s PDM-QPSK signals per core over 6,160-km 7-core MCF,” *Opt. Express*, vol. 21, no. 1, pp. 789–795, Jan. 2013. DOI: 10.1364/OE.21.000789.

[174] K. Igarashi, T. Tsuritani, I. Morita, et al., “1.03-Exabit/skm Super-Nyquist-WDM transmission over 7,326-km seven-core fiber,” in *European Conference on Optical Communication (ECOC) 2013*, 2013, pp. 1–3. DOI: 10.1049/cp.2013.1690.

[175] K. Takeshima, T. Tsuritani, Y. Tsuchida, et al., "51.1-Tbit/s MCF Transmission over 2,520 km Using Cladding Pumped 7-core EDFAs," in *Optical Fiber Communication Conference (OFC) 2015*, Optica, 2015, W3G.1. DOI: 10.1364/OFC.2015.W3G.1.

[176] T. Kobayashi, M. Nakamura, F. Hamaoka, et al., "1-Pb/s (32 SDM/46 WDM/768 Gb/s) C-band Dense SDM Transmission over 205.6-km of Single-mode Heterogeneous Multi-core Fiber using 96-Gbaud PDM-16QAM Channels," in *Optical Fiber Communication Conference (OFC) 2017*, Optica, 2017, Th5B.1. DOI: 10.1364/OFC.2017.Th5B.1.

[177] S. Jain, C. Castro, Y. Jung, et al., "32-core erbium/ytterbium-doped multicore fiber amplifier for next generation space-division multiplexed transmission system," *Opt. Express*, vol. 25, no. 26, pp. 32 887–32 896, Dec. 2017. DOI: 10.1364/OE.25.032887.

[178] D. Soma, S. Beppu, K. Maeda, et al., "Long-Haul MCF Transmission Using Full C+L-Band 19-Core Cladding-Pumped EDFA," in *European Conference on Optical Communication (ECOC) 2018*, 2018, pp. 1–3. DOI: 10.1109/ECOC.2018.8535291.

[179] B. J. Puttnam, G. Rademacher, R. S. Luís, et al., "0.715 Pb/s Transmission over 2,009.6 km in 19-core cladding pumped EDFA amplified MCF link," in *Optical Fiber Communication Conference Postdeadline Papers 2019*, Optica Publishing Group, 2019, Th4B.1. DOI: 10.1364/OFC.2019.Th4B.1.

[180] B. J. Puttnam, G. Rademacher, R. S. Luís, et al., "8007 km C + L band transmission over MCF with 19-core cladding-pumped EDFA," in *45th European Conference on Optical Communication (ECOC 2019)*, 2019, pp. 1–4. DOI: 10.1049/cp.2019.0798.

[181] B. J. Puttnam, G. Rademacher, R. S. Luís, et al., "Transmission and Crosstalk Measurements in MC-EDFA amplified 19-core link," in *2019 24th OptoElectronics and Communications Conference (OECC) and 2019 International Conference on Photonics in Switching and Computing (PSC)*, 2019, pp. 1–3. DOI: 10.23919/PS.2019.8818060.

[182] B. J. Puttnam, G. Rademacher, R. S. Luís, et al., "High Data-Rate and Long Distance MCF Transmission With 19-Core C+L band Cladding-Pumped EDFA," *Journal of Lightwave Technology*, vol. 38, no. 1, pp. 123–130, 2020. DOI: 10.1109/JLT.2019.2946879.

[183] M. Arikawa, K. Nakamura, K. Hosokawa, et al., "Long-Haul WDM/SDM Transmission Over Coupled 4-Core Fiber With Coupled 4-Core EDFA and Its Mode Dependent Loss Characteristics Estimation," *Journal of Lightwave Technology*, vol. 40, no. 6, pp. 1664–1671, 2022. DOI: 10.1109/JLT.2021.3118684.

[184] H. Yan, H. Liu, S. Yuan, et al., "56.3 Tb/s $\times$ 6030 km Transmission over Randomly Coupled MCF with FIFO-less Weakly-Coupled MCF EDFA," in *2023 Opto-Electronics and Communications Conference (OECC)*, 2023, pp. 1–4. DOI: 10.1109/OECC56963.2023.10209969.

[185] G. Di Sciullo, M. van den Hout, B. J. Puttnam, et al., "Performance Comparison of QAM Modulation Formats on an All-4-Core Recirculating Loop," in *2024 IEEE Photonics Conference (IPC)*, 2024, ThG2.4. DOI: 10.1109/IPC60965.2024.10799625.

[186] A. Alvarado, E. Agrell, D. Lavery, et al., "Replacing the Soft-Decision FEC Limit Paradigm in the Design of Optical Communication Systems," *Journal of Lightwave Technology*, vol. 33, no. 20, pp. 4338–4352, 2015. DOI: 10.1109/JLT.2015.2450537.

[187] "ETSI EN 302 307-1," European Telecommunications Standards Institute (ETSI), France, Standard, 2014.

[188] T. Ohtsuka, H. Sakuma, T. Suganuma, et al., "Optical Amplifiers Using Multicore Erbium Doped Optical Fibers," Tech. Rep., 2022.

[189] X. Liu, Y. Wang, Q. Huang, et al., "A Joint Mode Permutation Architecture for 10-Mode-Multiplexed Long-haul Transmissions," in *2024 Optical Fiber Communications Conference and Exhibition (OFC)*, 2024, Th1H.3.

[190] Y. Wang, X. Liu, Q. Huang, et al., "10-mode PM-QPSK Transmission over 2320 km Enabled by Optimized Mode Permutation Strategies," in *2024 Optical Fiber Communications Conference and Exhibition (OFC)*, 2024, Th1H.7.

[191] C. Antonelli, A. Mecozzi, M. Shtaif, et al., "Stokes-space analysis of modal dispersion in fibers with multiple mode transmission," *Opt. Express*, vol. 20, no. 11, pp. 11 718–11 733, May 2012. DOI: 10.1364/OE.20.011718.

[192] A. Mecozzi, C. Antonelli, and M. Shtaif, "Intensity impulse response of SDM links," *Opt. Express*, vol. 23, no. 5, pp. 5738–5743, Mar. 2015. DOI: 10.1364/OE.23.005738.

[193] S. Ö. Arik, K.-P. Ho, and J. M. Kahn, "Group Delay Management and Multi-input Multioutput Signal Processing in Mode-Division Multiplexing Systems," *J. Lightwave Technol.*, vol. 34, no. 11, pp. 2867–2880, May 2016.

[194] G. Di Sciullo, M. van den Hout, G. Rademacher, et al., "Reduction of modal dispersion in a long-haul 15-mode fiber link by means of mode permutation," in *49th European Conference on Optical Communications (ECOC 2023)*, vol. 2023, 2023, We.A.1.2. DOI: 10.1049/icp.2023.2052.

[195] A. Gatto, P. Parolari, R. S. Luis, et al., "Partial MIMO-based Mode Division Multiplexing Transmission over the First Field-Deployed 15-Mode Fiber in Metro Scenario," in *2023 Optical Fiber Communications Conference and Exhibition (OFC)*, 2023, M2B.3. DOI: 10.1364/OFC.2023.M2B.3.

[196] P. Parolari, A. Gatto, R. S. Luis, et al., "Demonstration of Multi-Hop Mode-Group Routing in a Field-Deployed Multi-Mode Fiber Network," in *2023 Optical Fiber Communications Conference and Exhibition (OFC)*, 2023, M4G.3. DOI: 10.1364/OFC.2023.M4G.3.

[197] R. Ryf, R.-J. Essiambre, A. H. Gnauck, et al., “Space-Division Multiplexed Transmission over 4200-km 3-Core Microstructured Fiber,” in *National Fiber Optic Engineers Conference*, Optica Publishing Group, 2012, PDP5C.2. DOI: 10.1364/NFOEC.2012.PDP5C.2.

[198] P. J. Winzer and G. J. Foschini, “MIMO capacities and outage probabilities in spatially multiplexed optical transport systems,” *Opt. Express*, vol. 19, no. 17, pp. 16 680–16 696, Aug. 2011. DOI: 10.1364/OE.19.016680.

[199] K.-P. Ho and J. M. Kahn, “Mode-dependent loss and gain: statistics and effect on mode-division multiplexing,” *Opt. Express*, vol. 19, no. 17, pp. 16 612–16 635, Aug. 2011. DOI: 10.1364/OE.19.016612.

[200] A. Andrusier, M. Shtaif, C. Antonelli, et al., “Assessing the Effects of Mode-Dependent Loss in Space-Division Multiplexed Systems,” *Journal of Lightwave Technology*, vol. 32, no. 7, pp. 1317–1322, 2014. DOI: 10.1109/JLT.2014.2303931.

[201] C. Antonelli, A. Mecozzi, M. Shtaif, et al., “Modeling and performance metrics of MIMO-SDM systems with different amplification schemes in the presence of mode-dependent loss,” *Opt. Express*, vol. 23, no. 3, pp. 2203–2219, Feb. 2015. DOI: 10.1364/OE.23.002203.

[202] K. Shibahara, T. Mizuno, H. Kawakami, et al., “Full C-Band 3060-km DMD-Unmanaged 3-Mode Transmission With 40.2-Tb/s Capacity Using Cyclic Mode Permutation,” *Journal of Lightwave Technology*, vol. 38, no. 2, pp. 514–521, 2020. DOI: 10.1109/JLT.2019.2950430.

[203] L. Dallachiesa, R. Ryf, N. K. Fontaine, et al., “Mode-Group-Division Multiplexing over a Deployed 15-Mode-Fiber Cable,” in *2023 Optical Fiber Communications Conference and Exhibition (OFC)*, Mar. 2023, M2B.4. DOI: 10.1364/OFC.2023.M2B.4.

[204] C. Antonelli, A. Mecozzi, M. Shtaif, et al., “Random coupling between groups of degenerate fiber modes in mode multiplexed transmission,” *Opt. Express*, vol. 21, no. 8, pp. 9484–9490, Apr. 2013. DOI: 10.1364/OE.21.009484.

[205] C. W. Gardiner, *Stochastic methods for physics, chemistry and natural sciences.* NY: Springer-Verlag, 1983.

[206] R. Ryf, A. Marotta, M. Mazur, et al., “Transmission over Randomly-Coupled 4-Core Fiber in Field-Deployed Multi-Core Fiber Cable,” in *2020 European Conference on Optical Communications (ECOC)*, 2020, pp. 1–4. DOI: 10.1109/ECOC48923.2020.9333277.

Tesi redatta con il cofinanziamento dell'Unione europea-*NextGeneration EU*
Piano Nazionale di Ripresa e Resilienza Missione 4 – Componente 1 –
Investimento 4.1. del PNRR – "Ricerca PNRR" – CUP E11I22000470001

Finanziato dall'Unione europea NextGenerationEU
Ministero dell'Università e della Ricerca
Italiadomani PIANO NAZIONALE DI RIPRESA E RESILIENZA
UNIVERSITÀ DEGLI STUDI DELL'AQUILA